ANNUAL REPORT

Center for Experimental Nuclear Physics and Astrophysics
University of Washington
April, 2014

Sponsored in part by the United States Department of Energy
under Grant #DE-FG02-97ER41020.

Cover design by Gary Holman. The background image on the front and back cover is a photo of the CENPA tandem insulating gas storage tanks (photo by Greg Harper). In the top photo, the Muon $g-2$ ring is attached to the barge at the Smith Point Marina on Long Island, preparing for its sea voyage (Sec. 4.2) (Credit: Brookhaven National Laboratory). The bottom left photo depicts grad student Julieta Gruszko working on the MAJORANA detector strings for the MAJORANA experiment (Sec. 1.9) in Sanford Underground Research Facility (photo by Alan Poon). In the bottom right photo, grad student Timothy Major is calibrating the laser for measuring the scintillator formulations for the SNO+ experiment (Sec. 1.17) (photo by Gary Holman).

INTRODUCTION

The Center for Experimental Nuclear Physics and Astrophysics, CENPA, was established in 1998 at the University of Washington as the institutional home for a broad program of research in nuclear physics and related fields. Research activities are conducted locally and at remote sites. The research program emphasis is fundamental symmetries and neutrinos. In neutrino physics, CENPA is the lead US institution in the KATRIN tritium-beta-decay experiment, the institutional home for Project 8, and a collaborating institution in the MAJORANA ^{76}Ge and the SNO+ ^{130}Te double-beta-decay experiments. The Muon Physics group is developing the MuSun experiment to measure muon capture in deuterium at the Paul Scherrer Institute in Switzerland. The group has a leadership role in the new project to measure the anomalous magnetic moment of the muon at Fermilab to even higher precision than it is presently known from the collaboration's previous work at Brookhaven. The fundamental symmetries program also includes "in-house" research using the local tandem Van de Graaff accelerator with an experiment to measure the electron-neutrino correlation and Fierz interference in ^{6}He decay, and neutron physics at other locations. We conduct user-mode research on relativistic heavy ions at the Relativistic Heavy Ion Collider at Brookhaven.

The DOE Office of Nuclear Physics carried out in the summer of 2013 a Comparative Review of grantees and subcontractors. CENPA placed at or near the top of some 20 grantees in the Fundamental Symmetries and Neutrinos category, a very exciting outcome for us. Another affirmation came in the form of the US News and World Report number 2 ranking of the University of Washington in nuclear physics in the nation. The combination of CENPA, the Institute for Nuclear Theory, and the Nuclear Theory group in the Department of Physics has clearly been effective.

Assistant Professor Jason Detwiler was the recipient of a DOE Early Career Award. Jason leads the MAJORANA project at UW and is the MAJORANA Data Analysis Coordinator.

Our master instrument maker, Hank Simons, took retirement in December. He is promising to remain active and will be helping us about one day a week. Tom Burritt has stepped into Hank's role in managing the CENPA shops, and still designs and builds all kinds of intricate equipment for our projects.

Jaromir (Jarek) Kaspar, a postdoctoral fellow, was appointed UW detector systems Project Manager for the muon $g-2$ project in February, 2014, with the academic rank of Acting Assistant Professor. This was one of many changes that accompanied the award of Major Research Instrumentation funding to UW and Cornell for the new muon $g-2$ project. MRI funding is keenly contested, and the success is a signal achievement for the muon group.

Four new postdoctoral fellows joined us in the past year. Clara Cuesta arrived in June, 2013, from the University of Zaragoza, where she had completed her dissertation work on the ANAIS dark matter experiment. Matthew Sternberg joined us in July from the University of Chicago, bringing his experience in trapping ions in order to measure the electron-neutrino correlation in ^{8}Li. Jason Crnkovic arrived as a graduate student with the muon group from Illinois and has stayed on as a postdoc since May, 2013, to complete some analysis of data from

Belle for the $g-2$ program. Martin Fertl arrived in February, 2014, from ETH, Switzerland, where he had developed a laser based mercury NMR magnetometer for electric-dipole-moment searches.

Ted Cook and David Kettler successfully defended their theses, Ted in June and David in December 2013. We congratulate them, and also Julieta Gruszko, who won a highly competitive NSF Graduate Fellowship.

Our Advisory Committee has been reconstituted with Dan McKinsey, Bob McKeown, and Michael Ramsey-Musolf. The Committee will be coming to Seattle in early May 2014. We take this opportunity to express our gratitude to Baha Balantekin, Russell Betts, Barbara Jacak, Bill Zajc, and the late Stuart Freedman for their thoughtful help over many years.

The DOE Office of Nuclear Physics, which provides operating support through programs in Low Energy Nuclear Physics and Heavy Ion Physics, renewed our grant DE-FG02-97ER41020 for FY12-14. The continued support of CENPA by the Office of Nuclear Physics is greatly appreciated. In the following paragraphs we record some of the highlights of our past year in research.

- The $g-2$ Experiment received CD-1 approval. The BNL superconducting storage ring was successfully relocated to Fermilab and the new home for the ring and experiment, the MC-1 building, is nearly complete.

- The UW-led MRI proposal to NSF was funded. It supports the capital costs for the $g-2$ calorimeter, electronics, and DAQ systems that will measure the anomalous precession frequency. The PbF_2 crystals have been ordered, a major test-beam run at SLAC using prototypes has been completed, and the data from that run have been analyzed.

- The MuSun detector was significantly upgraded with CENPA built TPC components and new cryogenic preamplifiers. The resulting 3-fold improved resolution allowed us to monitor *in situ* the TPC purity at the required part-per-billion level, as demonstrated in the 2013 production run.

- After successfully passing an Operational Readiness Review in March 2013 (the first subsystem to do so), the KATRIN detector system was connected to the main spectrometer. The detector system was then used for an extensive series of measurements for the KATRIN main spectrometer commissioning carried out from May to September last year. The whole detector system including the DAQ system worked stably and reliably throughout the measurement period, despite some troubles with misalignment, reduced pinch magnetic field, and lower post-acceleration voltage. Ten papers on the measurement results are currently in preparation by the KATRIN collaboration for publication in a few months.

- The real-time and near-time analysis tools developed by UW for our detector commissioning were also used for the spectrometer commissioning measurements with some significant extensions. The tools produced almost-final-quality results immediately after every measurement, making for efficient operation and timely planning of the next day's measurements. The tools became a *de facto* standard KATRIN analysis platform, and UW offered assistance in data analysis to everyone who works on it, placing UW as the resource for the entire KATRIN analysis.

- After the spectrometer commissioning, it was recognized that higher DAQ readout performance and the ability to count incident electrons precisely with correction for pile-up effects and DAQ dead-time were needed. An FPGA upgrade design proposed by UW in 2012 was implemented in November 2013 and is awaiting verification.

- UW personnel have been participating in the construction of the MAJORANA DEMONSTRATOR. In addition to detector deployment at the experimental site in Lead, SD, we pushed through a local R&D effort to design and prototype custom ultra-low background signal cable connectors using miniature brass pins and sockets held in a high-purity Vespel housing. We also built and operated a vacuum high-voltage test stand to validate DEMONSTRATOR HV components and connections, and to measure microdischarge rates in MAJORANA's miniature "pico-coax" HV cables.

- Work on MAJORANA DEMONSTRATOR Simulations and Analysis, which is led by UW personnel, proceeded at a rapid pace over the past year as detector characterization moved forward and prototype detector systems have been brought online. We also spearheaded a major update to the background model for the experiment, which projects a total background rate near the original technical goal based on upper limits on radiopurity indicated by assay.

- The Project 8 proof-of-concept experiment has been completely rebuilt around a 'new' Bruker NMR magnet provided by UCSB. An upgraded vacuum system, low-noise amplifiers, and electronics provide much improved sensitivity and reliability.

- The ^{199}Hg electric-dipole-moment experiment began data collection. The statistical sensitivity of the new data set, less than half complete, already surpasses the most recent published result by more than a factor of 2.

- All detector systems for the ^{6}He experiment have been developed and tested. In addition, many improvements to the laser systems allow for a determination of the electron-neutrino correlation parameter at the level of 1%, which we plan to accomplish during 2014.

- The analysis of data from a spin-polarized torsion balance rotating in proximity to spin-polarized sources was completed. New limits on exotic long-range spin-spin interactions between electrons were obtained for interactions mediated by spin-1 bosons with axial and vector couplings and for pseudoscalar interactions.

- Used results from a previous polarized ^{3}He experiment at Princeton, plus Eöt-Wash equivalence-principle tests, to constrain long-ranged parity-violating interactions of neutrons up to 11 orders of magnitude more tightly than those obtained from the parity-violating spin-precession of neutrons transmitted through liquid ^{4}He.

- We have developed a universal four-parameter model for inclusive jet spectra from p-p collisions that describes accurately all jet spectrum data below $\sqrt{s} = 1$ TeV collision energy and down to a 3-GeV jet-energy lower bound (ISR and Sp$\bar{p}$S data) but reveals substantial inconsistencies among data sets and data-Monte Carlo comparisons above 1 TeV (Tevatron and LHC data).

- We have applied a two-component (soft + hard) hadron spectrum model (TCM) to recent mean-p_t measurements for p-p, p-Pb and Pb-Pb collisions at the LHC. In contrast to several popular Monte Carlo models the TCM describes all of the mean-p_t data precisely and reveals that the p-p hard-component energy trend from RHIC to LHC energies is consistent with the jet-spectrum-width energy trend as expected if the hadron spectrum hard component is minimum-bias jet fragments.

- We have derived a quantitative correspondence between jet fragmentation functions obtained from p-p and $e^+ - e^-$ collisions and the hard component of minimum-bias trigger-associated hadron correlations from p-p collisions, providing further differential evidence that the hard component of hadron production in nuclear collisions is minimum-bias jet fragments.

As always, we encourage outside applications for the use of our facilities. As a convenient reference for potential users, the table on the following page lists the capabilities of our accelerators. For further information, please contact Greg Harper, Associate Director (gharper@u.washington.edu) or Eric Smith, Research Engineer (esmith66@u.washington.edu) CENPA, Box 354290, University of Washington, Seattle, WA 98195; (206) 543 4080. Further information is also available on our web page: `http://www.npl.washington.edu`.

We close this introduction with a reminder that the articles in this report describe work in progress and are not to be regarded as publications or to be quoted without permission of the authors. In each article the names of the investigators are listed alphabetically, with the primary author underlined in the case of multiple authors, to whom inquiries should be addressed.

Hamish Robertson, Director
Gary Holman, Editor

Victoria Clarkson, Assistant Editor
Greg Harper, Associate Director

TANDEM VAN DE GRAAFF ACCELERATOR

Our tandem accelerator facility is centered around a High Voltage Engineering Corporation Model FN purchased in 1966 with NSF funds, with operation funded primarily by the U.S. Department of Energy. See W. G. Weitkamp and F. H. Schmidt, "The University of Washington Three Stage Van de Graaff Accelerator," *Nucl. Instrum. Methods* **122**, 65 (1974). The tandem was adapted in 1996 to an (optional) terminal ion source and a non-inclined tube #3, which enables the accelerator to produce high intensity beams of hydrogen and helium isotopes at energies from 100 keV to 7.5 MeV.

Some Available Energy Analyzed Beams

Ion	Max. Current (particle μA)	Max. Energy (MeV)	Ion Source
^{1}H or ^{2}H	50	18	DEIS or 860
^{3}He or ^{4}He	2	27	Double Charge-Exchange Source
^{3}He or ^{4}He	30	7.5	Tandem Terminal Source
^{6}Li or ^{7}Li	1	36	860
^{11}B	5	54	860
^{12}C or ^{13}C	10	63	860
*^{14}N	1	63	DEIS or 860
^{16}O or ^{18}O	10	72	DEIS or 860
F	10	72	DEIS or 860
* Ca	0.5	99	860
Ni	0.2	99	860
I	0.001	108	860

*Negative ion is the hydride, dihydride, or trihydride.

Several additional ion species are available including the following: Mg, Al, Si, P, S, Cl, Fe, Cu, Ge, Se, Br and Ag. Less common isotopes are generated from enriched material. We recently have been producing positive ion beams of the noble gases He, Ne, Ar, and Kr at ion source energies from 10 keV to 100 keV for implantation, in particular the rare isotopes ^{21}Ne and ^{36}Ar. We have also produced a separated beam of 15-MeV ^{8}B at 6 particles/second.

Contents

1 Neutrino Research

KATRIN

1.1 Overview of the KATRIN experiment

J. F. Amsbaugh, J. Barrett*, A. Beglarian†, T. Bergmann†, L. I. Bodine, T. H. Burritt, T. J. Corona§, P. J. Doe, S. Enomoto, J. A. Formaggio*, F. M. Fränkle†, D. L. Furse*, F. Harms†, G. C. Harper, A. Kopmann†, E. L. Martin, A. Müller†, N. S. Oblath*, D. S. Parno, D. A. Peterson, L. Petzold†, A. W. P. Poon¶, R. G. H. Robertson, M. Steidl†, J. Schwarz†, D. Tcherniakhovski†, B. A. VanDevender‖, T. D. Van Wechel, B. L. Wall**, K. J. Wierman§, J. F. Wilkerson§, and S. Wüstling†

The KATRIN neutrino experiment will make a direct, model-independent probe of the neutrino mass to a sensitivity of 200 meV. The experiment uses the well established technique of an electrostatic retarding spectrometer to precisely map the endpoint of the electron spectrum from tritium beta decay. A distortion at the endpoint of the spectrum would provide a measure of the neutrino mass. The experimental technique and apparatus of KATRIN has been described in earlier Annual Reports.

In 2001, the University of Washington (UW), the lead US institute, and the Massachusetts Institute of Technology (MIT) were among the founding institutes of the five country collaboration. The primary US responsibility was to provide the electron detection system and data acquisition system for KATRIN.

The detector system was commissioned at UW then shipped to the experimental site at the Karlsruhe Institute of Technology (KIT) in June 2011 where it was installed and re-commissioned. After a successful Operational Readiness Review in March 2013, the detector system underwent its first real test with the Spectrometer-Detector Section (SDS-I) commissioning. Operating close to 24/7 for 116 days demonstrated that the system was technically sound, robust, and user-friendly. There were some problems related to two shorted pixels on the detector wafer (a manufacturing problem) and mis-alignment of the detector system which resulted in "shadowing" of the detector wafer (a procedures problem). A more serious problem was the eventual failure of the pinch magnet to run at the design field of 6T. A replacement pinch magnet has been ordered, with delivery expected in August, 2014.

As a result of the SDS-I experience, and in preparation for the second phase of spectrometer commissioning (SDS-II), a suite of detector upgrades are underway. These are described below and will be completed by August, 2014, when SDS-II begins. This will be followed

*Massachusetts Institute of Technology, Cambridge, MA.
†Karlsruhe Institute of Technology, Karlsruhe, Germany.
§University of North Carolina, Chapel Hill, NC.
¶Lawrence Berkeley National Laboratory, Berkeley, CA.
‖Pacific Northwest National Laboratory, Richland, WA.
**Graduated March, 2013.

in January, 2015, by the commissioning of the new pinch magnet. Following this is a long commissioning period for the tritium source and transport system until, in July, 2016, the first neutrino mass tritium data will be taken.

Since 2001 the US participation and responsibilities have expanded considerably. In 2008 the University of North Carolina, Chapel Hill, (UNC) joined the KATRIN collaboration when John Wilkerson moved from UW to UNC, which is now the center of DAQ maintenance and development. In 2009 the Lawrence Berkeley National Laboratory (LBNL) joined KATRIN and, under the leadership of Alan Poon, is a leading institute in the development of the KATRIN analysis task. In 2009 the University of California at Santa Barbara (UCSB), led by Ben Monreal, assumed responsibility for supplying much of the rear system used for monitoring and diagnostics of the KATRIN source and electron transport.

Another major US contributions is the electromagnetic modeling tool Kassiopeia, developed jointly by MIT and UNC. This program models electron transport through the entire KATRIN experiment. The software is now available in the public domain. Under the leadership of UW's Sanshiro Enomoto an innovative and user-friendly set of analysis tools has been developed. The tools essentially remove the need for detailed coding, allowing a wider group of people to focus on the physics. This is key to a speedy commissioning of KATRIN.

A major source of systematic error in the KATRIN probe of the neutrino mass is related to uncertainties associated with molecular final states following tritium decay. To better understand these final states, construction of the TRIMS (Sec. 1.8) experiment is well under way at UW.

Simulations have shown that the run time, statistical precision and possibly mass sensitivity of KATRIN can be improved by running the spectrometer in time-of-flight mode. To this end, an innovative way of detecting the passage of individual electrons entering the spectrometer is being investigated at UW[1].

1.2 Status of the KATRIN experiment

P. J. Doe

The KATRIN experiment is in an intense construction phase which is expected to last for another 2 years before tritium data taking begins in July, 2016. KATRIN has been described in detail elsewhere and can be thought to consist of the tritium source and electron transport section and the spectrometer and detector section. Overseeing these two sections is the rear section used to monitor the entire chain and control systematic effects.

- Source and transport systems
  The KATRIN source is of the windowless, gaseous type, essentially an open-ended

[1] "Neutrino mass sensitivity by MAC-E-Filter based time-of-flight spectroscopy with the example of KATRIN," Nicholas Steinbrink, Volker Hannen, Eric L. Martin, R. G. Hamish Robertson, Michael Zacher and Christian Weinheimer, New J. Phys. 15 113020 (2013).

tube into which tritium is injected at 1.8 mbar l/sec, resulting in an intense source of 1.7 x 10^{11} Bq. To control systematics the temperature is stable to $<$ 10mK. To constrain and transport the electrons the source tube is surrounded by seven superconducting magnets. The tritium injection, temperature stability, and magnets have all been demonstrated to work independently. The entire apparatus is now being assembled by Research Instruments. Factory acceptance tests are expected to be complete in July, 2015, after which the entire assembly will be shipped to KIT for installation. Preparation of the Tritium Laboratory infrastructure at KIT has begun. It is the schedule for installation and commissioning of this complex component that sets the critical path for the KATRIN experiment.

The job of the transport section is to guide the electrons to the spectrometers while reducing the flow of tritium by 14 orders of magnitude. The first transport stage is the Differential Pumping System (DPS) which uses turbomolecular pumps to return the tritium to the source. A version of this component was delivered to KIT in 2011 but because of flaws in the superconducting magnets was abandoned. A second design, using independent magnets made in the US by Cryomagnetics Inc., is well underway. Three of the six magnets have been delivered to KIT with the remaining three expected by June, 2014. The DPS is scheduled to undergo an Operational Readiness Review in October, 2014.

The second stage of the transport system is the Cryogenic Pumping System (CPS). The "pumping" consists of trapping tritium on the walls of the beam tube which is coated with argon frost to enhance tritium capture and retention, the efficiency of which has been demonstrated. Currently under construction, the CPS is facing some challenges in part due to the inadequate quality control of the manufacturer. Steps are being taken to rectify this and factory acceptance tests are currently expected in November, 2014, after which the system will be shipped to KIT for installation and commissioning.

- Spectrometer and detector systems
  The transport system delivers the electrons to two spectrometers. The first is the pre-spectrometer. Delivered to KIT in 2006, this spectrometer was the workhorse for the design and understanding of the main spectrometer. The UW provided the internal electric-field-shaping structure for this spectrometer. The pre-spectrometer reduces event rates by rejecting electrons below the region of interest. It is ready to be attached to the main spectrometer.

  The main spectrometer is a triumph of vacuum engineering, 1,400 m^3 at 10^{-11} mbar. Another challenge is the homogeneity of the electric fields required to achieve the 0.93-eV resolution and the required suppression of backgrounds. This is achieved by a structure of wire-electrode planes that conforms to the walls of the spectrometer vessel. These wire planes, which was fabricated and installed under cleanroom conditions, successfully passed the bake-out test. However, the CuBe rods that make the electrical connections between the wire plane modules deformed and shorted out during bake-out. A scheme has been worked out to repair the central 60% of the wire planes from outside the spectrometer vessel. This level of repair is sufficient to test the wire planes' efficacy for suppressing backgrounds - a major goal of SDS-II. Repair of the remaining 40% of the wire planes is more challenging and may require reentering the main spectrometer.

The UW-led detector system, as noted above, had a very successful SDS-I run. The detector-system design is robust. Some weaknesses were revealed and these are the subject of the upgrades discussed below. The US-supplied data acquisition system, ORCA, performed well and the suite of analysis tools was found to be both user-friendly and crucial for a fast turn-around in data interpretation during the commissioning process. Some rate limitations in the DAQ system appeared. This mainly was a concern during the high rate calibration of the system and has since been corrected through firmware and modifications.

One disappointment is the pinch magnet. This is designed to run at 6 T, which it does when operated by itself. However, in the presence of the detector magnetic field of 3.6 T, it is no longer possible to operate the pinch above 5 T without it quenching. Thus all SDS-I data was taken with the pinch at 5 T. For his undergraduate thesis, Axel Müller studied the field of the pinch magnet both with and without the detector magnet and demonstrated that the coil of the pinch magnet moves several mm under the influence of the detector magnet. This movement is unexpected and is very likely the explanation of the pinch magnet symptoms. It is not cost-effective to repair the pinch magnet and consequently a new magnet has been ordered and is expected be available in July, 2014, too late for SDS-II, which begins in August, 2014. All SDS-II data will be taken with the pinch at 5 T. This will not detract from the main goals of SDS-II. It is expected that the new pinch magnet will be commissioned and installed starting in January, 2015 and will be ready for commissioning of the fully repaired main spectrometer.

- Rear system
  The rear system, located upstream of the gaseous source, is independent from the rest of the KATRIN systems except for the very important fact that it establishes the potential of the tritium source. UC Santa Barbara is a key player in designing and procuring the rear system. Fabrication of the rear system is almost complete and it is expected to be delivered to KIT as soon as the Design Review is complete. The electron gun of the rear system, although primarily a diagnostic tool during tritium data taking, will be essential in commissioning the entire chain of KATRIN hardware.

- Future activities
  The detector system is expected to be much in demand for commissioning until July, 2016, when regular tritium data taking begins. SDS-II, which will study spectrometer backgrounds, will take place from August through December, 2014. An SDS-III will be required when the repair of the spectrometer wire planes is complete. With the installation and commissioning of the source and transport sections, using the electron gun of the rear system, electrons can be transported the length of KATRIN. The exact procedure for commissioning the system for tritium is still being developed.

The extensive installation and commissioning activities planned for 2015 make the date of July, 2016, for tritium data-taking a challenge. To ensure success a rigorous project-management program has been implemented at KIT.

1.3 Analysis tools

S. Enomoto

For the commissioning measurements of the KATRIN Spectrometer-Detector Section (SDS) carried out in 2013, UW has provided a suite of analysis tools which is based on the toolkit originally developed for the detector commissioning analysis in 2011-2012. The toolset was developed for near-time analysis of the detector commissioning with a design goal of a very short turn-around time (time from a measurement to a physics result, which is usually dominated by code development time). With a recent extension to general offline analysis, it became a very handy and versatile toolset for the SDS commissioning measurements: most of the measurement analyses were completed on the same day, and the results were used to plan the next day's measurements. Even after the commissioning measurements, the same toolset has been being used for further analysis by virtually everyone in KATRIN. This shows that the toolset is useful not only for quick near-time data examinations but also for detailed physics investigations. One typical user analysis code with the toolset is $\sim$50 lines long, while the core part of the UW-provided toolset consists of $\sim$40000 lines; this might be an indication of that the toolset has reduced the users' load and time.

The toolset consists of several components as described below:

BEANS

BEANS (Building ... Analysis ... Sequence) is a C++ toolkit to construct user analysis logic by a simple combination of reusable analysis elements. Each analysis element is configurable, and user analysis logic is described as a linear sequence of analysis elements. Since the final analysis description is just a line of elements with configuration parameters, it is very simple as a software program as it does not use any programming concepts such as variables, if-branches and while-loops. It is so simple that the logic can be described by a configuration file without any C++ coding: the configuration file can be easily generated by a GUI design tool with a drag-and-drop interface. The GUI interface is particularly useful for near-time analysis because compiling code and inserting it into the data processing chain is often too much trouble for a one-time data investigation. Even without the GUI, describing the linear sequence with C++ is straightforward and one can now perform data analysis without programming skills.

The conceptual structure of BEANS is similar to *functional programming* which is very mathematical and is in a different paradigm from *imperative programming* such as C++. This helps allow this simple linear structure to describe all the complicated physics analysis logic.

ROAST

ROAST (Realtime Orca Analysis ...) is an interface between the BEANS analysis logic and the ORCA data acquisition system. It enables users to run BEANS logic in real-time while data taking is ongoing. ROAST is a web application, and by connecting it to the BEANS GUI tool which is also a web application, users can design their analysis logic and execute it during data taking within a web browser. Because ROAST can accept any BEANS logic, full offline analysis can be performed in real-time by drag-and-drop methods without making any changes to the analysis code.

DRIPS
DRIPS (Detector Readout ... Simulation) is the detector simulation tool that starts from an energy deposit in the FPD wafer and traces the entire signal processing chain including the preamp, analog filters, A/D converter, trapezoidal filter the FPGA, and digital elements. DRIPS can be connected to the KATRIN field and track simulation tool (KASSIOPEIA), providing the BEANS analysis logic with unified access to both real data and simulated data.

KAFFEE
KAFFEE (Katrin Automation Framework ...) is a work-flow automation framework that can launch any software tasks automatically based on the contents of the incoming data. Users can easily configure their analysis logic to be executed automatically for specific types of measurements. The output, input, and description of tasks, are automatically classified and placed into the KAFFEE Catalog, which is accessible through the web interface. By preinstalling several common analyses, it worked as an in-line data processor, near-time data monitor, and run catalog. By dynamically adding analysis logic, typically with the BEANS GUI, users can also perform interactive data analysis on their web browsers.

1.4 Detector performance during SDS-I commissioning

S. Enomoto, F. Harms*, and J. Schwarz*

The KATRIN Spectrometer-Detector Section (SDS) was commissioned for the first time during summer 2013. This included 116 days of data taking with the detector system attached to the main spectrometer. In preparation for these measurements the detector system was connected to the main spectrometer for the first time in May, 2013. In the following, details about the connection process, misalignments in the detector system and the detector performance during the SDS-I commissioning are given.

Connection process and misalignments: During the connection process of the detector system and the main spectrometer several issues with the alignment hardware arose. It turned out that it was not possible to adjust the detector alignment after the connection to the main spectrometer was established. Therefore, the Focal-Plane Detector (FPD) system was tilted against the axis of the main spectrometer during the whole SDS-I commissioning. In combination with the lowered magnetic field of the pinch magnet (5 T), the magnetic flux tube was blocked at several points within the detector system. Thus, 24 pixels of the detector wafer did not "see" inside the main spectrometer. Fig. 1.4-1 gives an overview of the affected segments.

*Karlsruhe Institute of Technology, Karlsruhe, Germany.

Several measurement techniques were used to investigate the misalignment between the FPD system and the main spectrometer. These included mechanical measurements, background measurements with the main spectrometer, and line scans with an electron gun across the detector wafer. In the latter case, the electron gun was attached on the opposite side of the main spectrometer. Using these techniques it was possible to detect misalignments in the millimeter range within the 25-meter SDS apparatus.

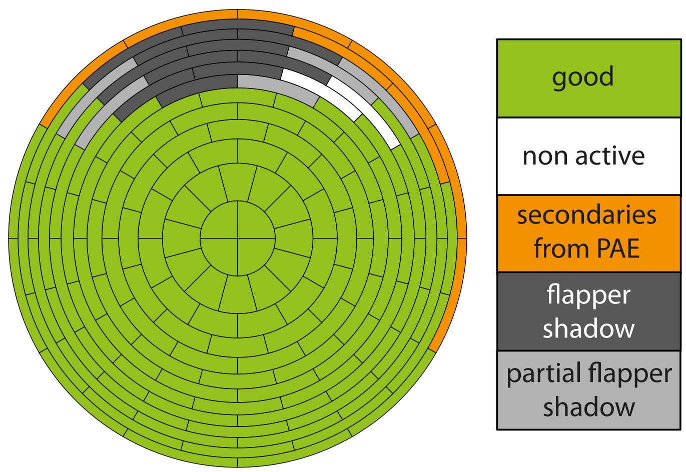

Figure 1.4-1. View of FPD segments with reasons for shadowing indicated.

General performance: The detector system ran at nearly 100% duty cycle during the 116 days of SDS-I commissioning and more than 4000 measurement runs were taken with the system. It can be stated that the system did not cause any major interruptions of data-taking during the entire period. The performance of some important detector components are listed below:

- **Shorted detector segments:** During the SDS-I commissioning measurements, two of the 148 detector segments were found to be shorted on the backside of the detector wafer (marked in white in Fig. 1.4-1). Therefore, only 146 segments were used during the data-taking.

- **Post acceleration:** While designed for up to 30-kV potential, the post acceleration electrode (PAE) of the FPD system was only capable of 10-kV post acceleration during the SDS-I commissioning. At higher potentials it has shown high-voltage break downs. Nevertheless, a 10-kV post acceleration was still high enough to allow for measurements with the main spectrometer at zero potential, as the detector threshold was around 5 keV.

- **Pulcinella:** The Pulcinella disc of the FPD system was used in a non-standard mode during the SDS-I commissioning. With a small positive voltage applied to the disc it acted as a Faraday cup in front of the detector. In this way it was possible to protect the wafer when new measurement configurations in the main spectrometer were tested for the first time. If for example, a high-voltage break down had occurred in the spectrometer creating a burst of electrons guided towards the detector, Pulcinella would have measured that current while the wafer was protected against damages. Nevertheless, since no discharges were observed during SDS-I commissioning, Pulcinella did not measure any electron bursts.

- **Calibration:** During the SDS-I commissioning, the FPD was calibrated twice a week with the use of a ^{241}Am-source, adding up to 22 calibration runs in total. An analysis of these calibrations showed no major fluctuations of the detector calibration apart from a negligible temperature dependence during the SDS-I commissioning.

- **User friendliness:** Operator training which took place before the SDS-I commissioning[1] paid off and the detector system worked as a user facility. Students were able to take their data without having an FPD-system expert present all the time. In addition, the analysis software developed by S. Enomoto allowed easy access and analysis of the data taken (Sec. 1.3).

- **Background:** To allow for a detailed background study with the main spectrometer, the intrinsic FPD background had to be low during the SDS-I commissioning. Therefore, background studies with the stand-alone detector system were carried out at the beginning of the measurement phase. Fig. 1.4-2 shows the energy spectrum of the intrinsic FPD background.

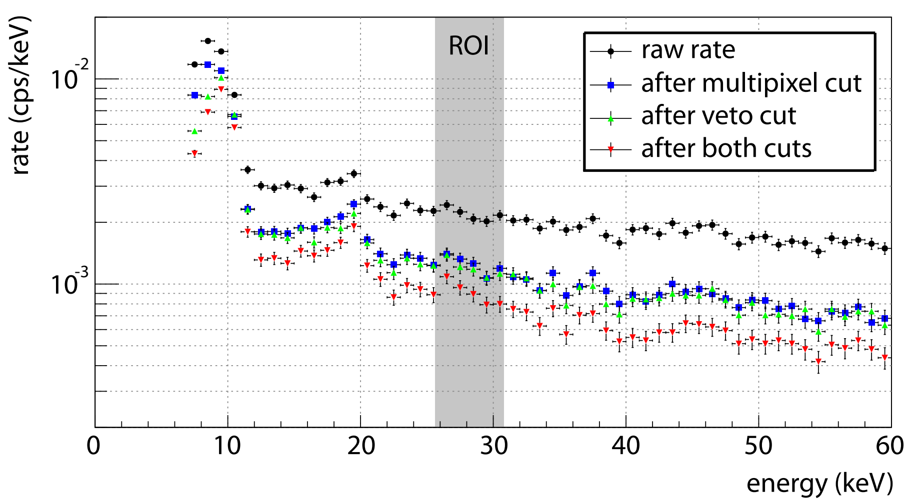

Figure 1.4-2. Intrinsic detector background during SDS-I commissioning. The SDS region of interest (ROI) is marked as a gray band. The background spectrum was taken in a stand-alone mode of the FPD system with a post-acceleration potential of 10 kV applied.

Two different kinds of cuts have been applied here. First, a veto cut is applied which excludes detector events that are coincident with veto events within a $\pm 2\ \mu$s coincidence window and are assumed to be due to muons. Secondly, a multi pixel cut is applied

[1]CENPA Annual Report, University of Washington (2013) p. 8.

where events with arrival times less than 2 μs apart are excluded as they are expected to be due to charge sharing and cross-talk effects. With both of these cuts applied, a detector background of less than 5 mcps has been measured within the SDS-I region of interest. With the background from the main spectrometer at several hundred mcps during the SDS-I commissioning, the small background contribution from the detector system could be neglected in the data analysis.

1.5 System upgrades and changes to the detector system

J. F. Amsbaugh, A. Beglarian*, T. H. Burritt, P. J. Doe, S. Enomoto, F. Harms*, L. La Cascio*, E. L. Martin, A. Müller*, D. S. Parno, R. G. H. Robertson, and J. Schwarz*

We continue to improve the performance of the detector system. Based on our SDS-I experiences we are implementing the following upgrades:

- **The Pulcinella solar panel:**
  The Pulcinella meter measures the current leaving the electron-source disk. Its primary use is to measure the efficiency of the electron detector by comparing the current leaving the electron source to the current measured by the detector. In addition, the electron-source disk may be used as a safety check on excess charge coming from the main spectrometer before exposing the detector to the spectrometer.

  To allow Pulcinella to float at the electron-source voltage, power to the meter is supplied by an array of LEDs at low voltage illuminating a solar panel floating at the electron-source voltage. The LED array light output was found to drop drastically over the first few days of operation, which resulted in insufficient power for proper meter operation. The Pulcinella solar panel is being upgraded to a more efficient panel. The new panel was tested with a new set of LEDs over a two-month burn-in period. After the first couple of days the light output of the LEDs decreased gradually, and it was estimated that the power setup using the new solar panel would supply sufficient power for proper operation for 3 years of continuous use, which is compatible with KATRIN operations.

- **In-line valve:**
  The DN250 isolation valve between the detector system and the main spectrometer is located between the pinch magnet and the detector magnet. As a result one cannot remove the pinch magnet without first breaking vacuum on the main spectrometer to remove the isolation valve. A custom designed in-line valve, which fits inside the bore of the pinch magnet, was installed between the isolation valve and the main spectrometer. The pneumatically operated isolation valve is used for rapidly isolating the detector system from the main spectrometer and the new manually operated detector in-line valve is used to allow removal of the pinch magnet without breaking vacuum.

  The detector in-line valve was originally sealed using a Kalrez O-ring in a half dove-tail groove. When the main spectrometer was baked out, the in-line valve was in the open

*Karlsruhe Institute of Technology, Karlsruhe, Germany.

position, and the Kalrez O-ring expanded enough for part of it to pop out of the groove, resulting in the inability to properly seat the valve. A new valve disk, with a narrower groove width and a double dove-tail, was constructed. The new disk was tested by heating to bake-out temperature in the open valve position and the O-ring was found to remain properly seated inside the groove. The in-line valve located at the entrance of the main spectrometer has also had its O-ring groove modified.

To assist in aligning the detector system an additional bellows has been installed in the detector-side in-line valve.

- **Electron source illumination:**
  The previous upgrade to the electron-source UV illumination supplied too much light, requiring the device to be operated just above the LED turn-on to achieve a low enough source rate, making fine control difficult. Neutral-density filters are being added between the UV LEDs and the illumination port to allow easier control of electron-source rate. Integrated into the electron-source illumination device is a red LED pulser used to measure detector linearity. Previously, the drive current of the red LED was stabilized by optical feedback in an attempt to make the output of the LED proportional to the drive signal. The linearity was intended to be determined by comparing detector response to the amplitude of the drive signal. However, the driver produced a slow LED-current rise time which was significant compared to the shaping time of the filters used for the focal plane detector, so detector response was instead compared to the LED current. A new driver board is being developed which rapidly pulses the red LED, and instead of using optical feedback to stabilize the LED current it simply measures the light output of the red LED for comparison to detector response.

- **Detector alignment:**
  Electronic calipers and inclinometers have been installed to assist in aligning the detector system. When subject to loading from atmospheric pressure the detector system was seen to move slightly in the direction of the spectrometer. To prevent this, additional bracing has been incorporated into the XHVac support structure. These upgrades, in addition to revised alignment procedures, will eliminate the detector alignment problems experienced in SDS-I.

- **Cooling system:**
  The detector system relies on the house chilled-water supply to cool the magnet, cryopump and electronics cooling compressors as well as the veto readout. Inside the detector hall the chilled-water plumbing is all stainless steel to ensure no magnetic disturbance. Unfortunately the rest of the chilled-water plumbing is mild steel. As a result there is significant corrosion that resulted in failure of the electronics cooling compressor with subsequent overheating of the electronics. A permanent solution is being sought. Until then we will rely on an air-cooled chiller unit as emergency backup.

- **Firmware Upgrades for High-Rate Measurements:**
  At high rates, signals interfere with each other and the recorded energies and rates differ from incident energies and rates. If the time interval between two electrons is short compared to the trapezoidal filter-shaping length, they make only one event trigger

(peak pile-up). The energy estimated by the trapezoidal filter depends on the interval, making a plateau-shaped spectrum rather than peak shaped. If the interval between two electrons is short compared to the preamp discharge time constant, then the tail from the first signal affects the energy estimation of the second signal (tail pile-up). If the average time interval between incident electrons is short compared to this time scale, tail pile-up accumulates. The accumulation of tail pile-up lowers the average recorded energy and fluctuation of pile-up processes on a long time scale causes fluctuation of event-by-event recorded energies.

DRIPS simulation (Sec. 1.3) shows that the tail pile-up effects can be largely suppressed by using bipolar energy estimation, which does not have single-side accumulation. The peak-to-valley time of the bipolar shape also provides us with information about the signal rise-time, which is used to identify and separate peak pile-up events. The bipolar logic is implemented into the field-programmable gate array (FPGA) by simply adding one more trapezoidal-shaping stage to the existing dual-trapezoidal logic; this has an advantage that we will not lose the present, verified working, system. The bipolar energy has worse noise, due to the additional differentiation stage, but with this approach we still have the monopolar energy, therefore, we do not sacrifice performance at low-rates.

The above upgrades are currently being implemented in preparation for SDS-II beginning in August, 2014. Described in section 1.6 is a detector wafer testing unit that will allow the wafers to be assessed prior to installation in the detector system. This avoids the possibility of installing a faulty wafer, as was the case in SDS-I where two pixels were shorted together.

1.6 Si wafer tester

E. L. Martin

The KATRIN Focal Plane Detector (FPD) uses a silicon wafer separated into pixels, a guard ring, and a bias ring, with connections made to the back of the wafer by 184 pogo pins. The silicon wafer is mounted on a feedthrough flange used to connect the wafer in the ultra-high vacuum system to the amplifiers, located in the high vacuum system. After installing the silicon wafer on the feedthrough flange each connection must be checked. This process takes a few hours and requires carefully connecting to the delicate pins on the feedthrough flange, which presents a high risk for damage. To make testing quicker, and to reduce the risk of damage to the feedthrough pins, a FPD wafer tester was constructed.

The pins of the feedthrough flange are aligned with the sockets on the FPD-wafer test board by a Lexan piece which has conical openings for the pins to guide them in to the sockets. A second Lexan piece is used to press the FPD-wafer test board on to the pins, to prevent excessive flexing of the PCB. Large test pads on the FPD-wafer test board which mimic the layout of the pixels on the FPD wafer can be used to make electrical connection to the pins without risk of damage.

Two sets of multiplexers allow connecting two test pins to any two pins on the feedthrough flange. An Arduino board was programmed to automatically test a mounted FPD wafer for problems.

Tests include:

- Forward bias check from each pin to the bias ring.
- Reverse bias check from the bias ring to each pin.
- Connection check between all pins connected to the bias ring.
- Connection check between all pins connected to the guard ring.
- Check for shorts between all adjacent pixels as well as shorts to the guard ring for pixels adjacent to the guard ring.

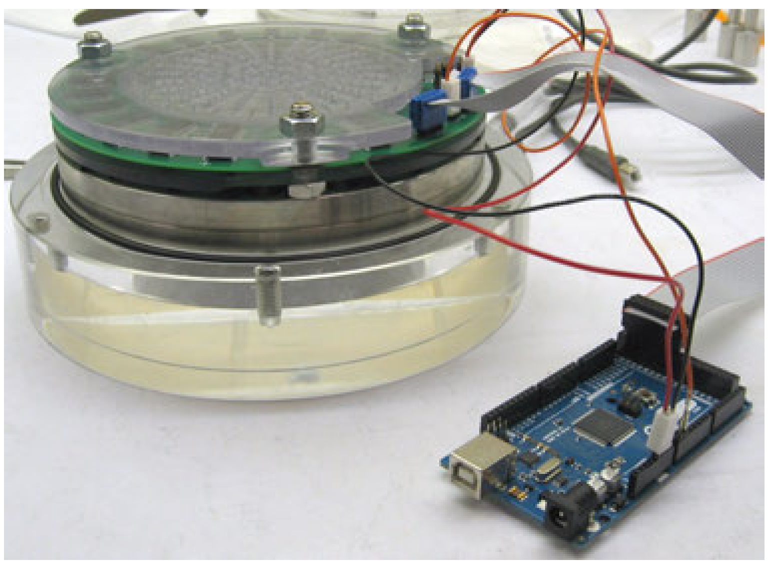

Figure 1.6-1. Wafer tester mounted on feedthrough flange, with controller board attached.

1.7 Final state distribution workshop

L. I. Bodine and D. S. Parno

The first KATRIN Final State Distribution (FSD) Workshop was held March 3-4, 2014, at the Karlsruhe Institute of Technology. The goals of the workshop were: a) identifying ways in which the theory of tritium molecular effects, including the FSD, will affect the KATRIN neutrino mass measurement and extensions of the KATRIN experiment; and b) defining actions and responsible persons to quantify and reduce KATRINs systematic uncertainties related to the molecular effects.

In order to achieve the workshop goals we brought together KATRIN analysts, FSD theorists and FSD experimentalists to engage in face-to-face discussions. Roughly 30 people attended the workshop and participated in discussions focused on the physics involved in determining the FSD, how the FSD calculations are done, how the machinery for FSD calculation can be tested, and how the impact on KATRIN can be quantified.

The relevance of the FSD to KATRIN was presented and provided along with a phenomenological view of the FSD and its relation to zero-point motion. Alejandro Saenz and Christoph Roll of the University of Berlin-Humboldt presented the theoretical framework of the calculations and discussed their plans for new calculations of the FSD with extensions to the energy region and time scales relevant to TRIMS (Sec. 1.8).

Ideas for FSD-related measurements were presented including TRIMS, proposed laser excitation experiments, ortho-para measurements and measurements of the electronically excited states in KATRIN. The strong relationship between the TRIMS experiment calculations and the FSD calculations were emphasized.

Plans for potential measurement of the branching ratio to the electronically excited states using KATRIN were discussed at length. While in principle KATRIN can see the kink in the spectrum at roughly 20 eV below the endpoint, achieving precision results will require a keen understanding of scattering in the source. Low-density runs would be necessary in order to reduce the rate at the detector and to examine the scattering effects. The measurement could potentially be done in conjunction with low-density WGTS test runs already planned.

Studies of the ortho-para ratio in KATRIN and the effect on the measurement were presented with results that are favorable for KATRIN. Simulations show the ortho-para ratio to be that of room temperature gas, confirming that the source is non-thermal. The effect on the neutrino-mass sensitivity was shown to be negligible due to the relative stability of the ratio over time.

The workshop succeeded in raising awareness of FSD-related issues in KATRIN. A workshop proceedings is in preparation for distribution to the collaboration. A KATRIN mailing list and internal website have been constructed to facilitate further discussions.

1.8 Update on the Tritium Recoil-Ion Mass Spectrometer

L. I. Bodine, D. S. Parno, and R. G. H. Robertson

The Tritium Recoil-Ion Mass Spectrometer (TRIMS) is designed to measure the molecular tritium beta decay branching ratio to the bound ^{3}HeT$^+$ molecule. The experiment is now under construction and aims to take data in summer 2014.

The ultra-high vacuum system was assembled in the cleanroom in the Physics Astronomy Building. Initial leak tests were successful with no leaks at the 10^{-12} mbar-l/s level. The system is being upgraded to provide electrical isolation between the pumps and front-end electronics.

The 60-kV high-voltage system has been tested in conjunction with the 2-kG uniform magnetic field provided by a set of four copper coils. Initially small high-voltage conditioning currents were observed and increased in the presence of the magnetic field. A post-conditioning disassembly of the system revealed no distinctive markings on the glass chamber or potential-defining plates. The detector mounts have been redesigned to allow shielding of the detectors during high-voltage conditioning. The upgraded hardware is currently being fabricated in the Cyclotron shop.

The custom preamplifiers and fiber-optic boards have been optimized to balance energy and timing resolution. Extensive testing of the 250-MS/s digitizer revealed a firmware bug that has been fixed by CAEN. The digitizer is being added to the ORCA data acquisition system. Slow controls data from the high-voltage supplies, magnet power supplies and vacuum gauges is taken using LabJack ADCs readout in ORCA. The data is stored in an SQL database for analysis.

A gaseous krypton-83m calibration has been designed for the TRIMS experiment and will be produced at the CENPA tandem van de Graaff. The 17.8-keV conversion electron from the krypton isomer is a standard calibration for tritium endpoint experiments. Following the transition the krypton ion can be highly charged due to an Auger cascade. The time-of-flight and energy of the ion can be used to extract the charge state in a similar manner to the extraction of the mass state in the main TRIMS measurement. The results of the krypton analysis will be used to determine the functionality of the spectrometer and whether any modifications are necessary prior to tritium data-taking.

The necessary utilities upgrades in the Hot Lab have been completed. Four closed-circuit water lines from the cooling tower have been plumbed. Additional 120-Vac power outlets have been installed to accommodate the high temperature bake-out of the vacuum system. Two 208-Vac power outlets were installed for the magnet power supplies. Ethernet is provided by a patch cable between the ATHENA server room and the Hot Lab as well as lab-wide wireless.

Majorana

1.9 Overview of the Majorana Demonstrator

T. H. Burritt, M. Buuck, C. Cuesta, J. A. Detwiler, P. J. Doe, J. Gruszko, I. Guinn, G. C. Harper, J. Leon, D. A. Peterson, R. G. H. Robertson, and T. D. Van Wechel

The Majorana Demonstrator is a ∼40-kg array of high-purity germanium (HPGe) detectors enriched in ^{76}Ge that is under construction at the Sanford Underground Research Facility (SURF) in Lead, SD. The detectors are arranged in strings of 4-5 on low-background copper supports which are then placed in two cryogenic lead- and copper-shielded modules (see Fig. 1.9-1). The primary technical goal of the Demonstrator is the achievement of a radioactive background of 4.1 counts/ton/year within a 4-keV region of interest surrounding the 2039-keV Q-value for ^{76}Ge neutrinoless double-beta ($0\nu\beta\beta$) decay. Such a low background level would justify deeper investment in a much larger ton-scale experiment with sufficient sensitivity to definitively search for $0\nu\beta\beta$ decay for inverted hierarchical neutrino masses. In the process, the DEMONSTRATOR will simultaneously perform a sensitive test of a claimed observation of $0\nu\beta\beta$ decay[1], and will also perform searches for low-mass WIMP dark matter, solar axions, and other physics signals.

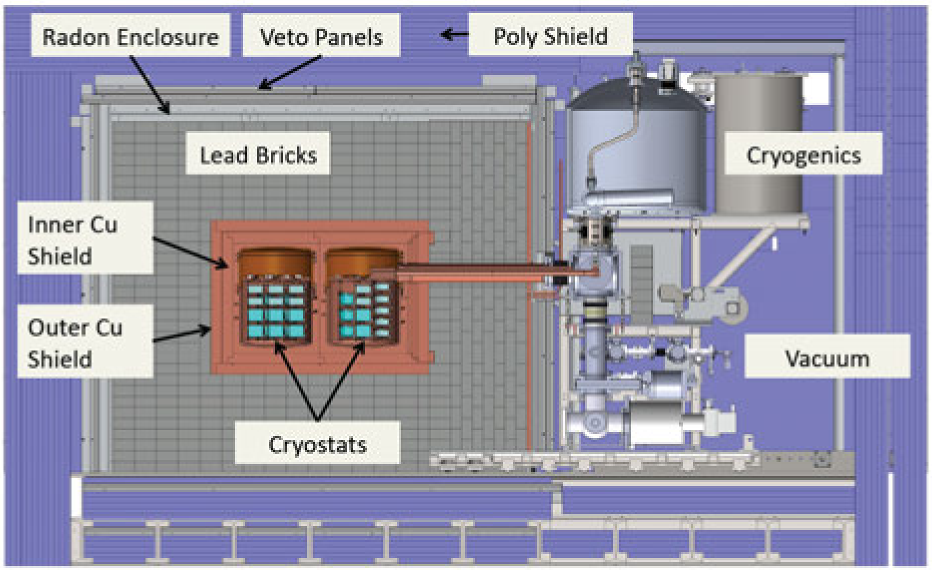

Figure 1.9-1. MAJORANA DEMONSTRATOR schematic

The UW MAJORANA group leads the simulations and analysis effort within the collaboration, and contributes significantly to efforts in software development, data analysis techniques, background modeling, geometrical models for Monte Carlo simulations, data handling and storage issues, database implementation, and feedback to design teams on background impact of proposed modifications. We are also responsible for the design and prototyping of the low-mass signal cable connectors to be used in the experiment, and for the testing of the high-voltage (HV) Picocoax® cables that deliver the bias voltage to the detectors. In addition to these responsibilities, our group at the University of Washington is also contributing to the ongoing construction efforts at SURF of the Cryo 1 module.

1.10 Construction of the MAJORANA DEMONSTRATOR Prototype Cryostat

T. H. Burritt, M. Buuck, C. Cuesta, J. A. Detwiler, P. J. Doe, J. Gruszko, I. Guinn, J. Leon, D. A. Peterson, R. G. H. Robertson, and T. D. Van Wechel

During the last year, a big effort has been carried out at Sanford Underground Research Facility (SURF) constructing the MAJORANA DEMONSTRATOR: installation of the shielding, characterization of the high-purity germanium (HPGe) detectors, and commissioning of

[1] H. V. Klapdor-Kleingrothaus *et al.*, Phys. Lett. B **586**, 198 (2004).

the Prototype Cryostat. The Prototype Cryostat is an initial cryostat fabricated from commercially produced copper with the following goals: debug and validate the cryostat design, vacuum system, cables and connectors, string insertion procedure, string cooling and readout, infrared shielding, and operation procedures. The Prototype Cryostat is currently acquiring data with two strings of detectors produced from natural germanium.

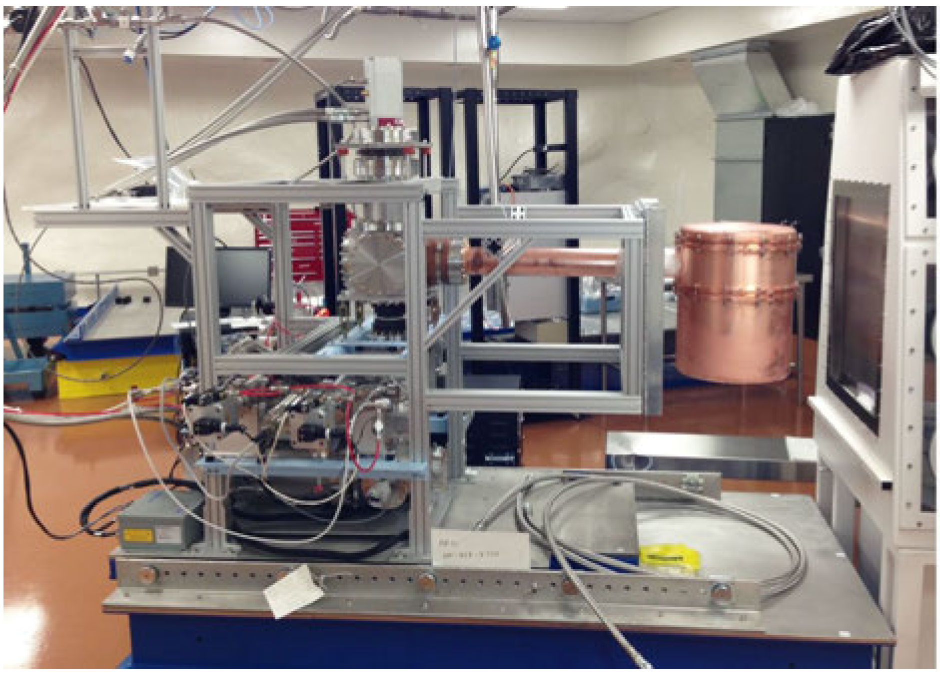

Figure 1.10-1. The Prototype Cryostat, including its vacuum and pulse-tube cooler cryogenic systems. It is used for the research and development of parts and techniques that are now being implemented in Module 1 of the MAJORANA DEMONSTRATOR.

The UW MAJORANA members have contributed on-site to this work, particularly in the construction and installation of detector strings. As changes to the strings have been introduced, especially in the cabling and connections, members have worked to rebuild detector units and strings with the new parts, and train other researchers in their use. Members have also worked on diagnosing and resolving problems with the Prototype Cryostat. For instance, UW MAJORANA members worked with others to conduct cold-pack tests, which allowed the diagnosis of high leakage current in the detectors as originating from IR shine. Members have worked on commissioning tasks, including preparing and operating the post-amplification electronics box and onboard pulser for the Prototype Cryostat, and optimizing data taking using the Prototype Cryostat. Preparation for the construction of the Module 1 strings has begun on-site and at UW, with local focus on the high-voltage and signal-cable connector tasks.

1.11 Simulations and analysis activities for the MAJORANA DEMONSTRATOR

M. Buuck, C. Cuesta, J. A. Detwiler, J. Gruszko, and I. Guinn

The UW MAJORANA group leads the simulations and analysis effort within the MAJORANA collaboration. Much of the low-level software for data I/O, event building, data processing, and simulation were written by CENPA personnel. Members of our group have played a central role in the building and validation of the background model for the MAJORANA DEMONSTRATOR, which informs the radiopurity criteria upon which the experimental design is evaluated. We also participate in the development and implementation of data analysis techniques, geometrical models for Monte Carlo simulations, data handling, storage, and database technologies.

Our efforts over the past year have focused on background model updates and validation, supporting detector acceptance and characterization activities, and preparation for and analysis of data taken with the prototype cryostat. A major update of the background model was performed taking into account design changes made since 2012, and using new assay information obtained since that time as well. Fig. 1.11-1 shows the full simulated spectrum, including the effect of analysis cuts. The total projected background rate in the 4-keV region of interest surrounding the 2039 keV Q-value for double-beta decay of ^{76}Ge is 4.1 counts/ton-year.

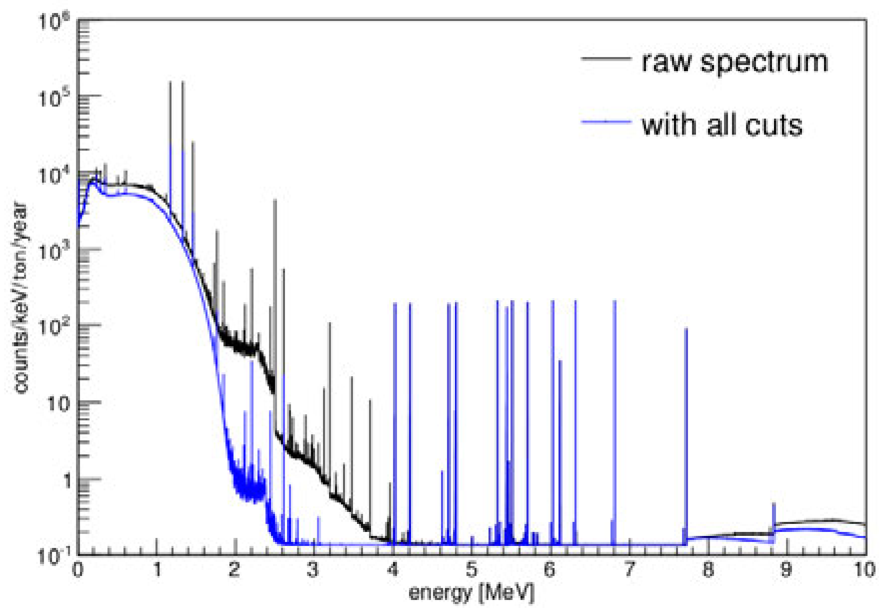

Figure 1.11-1. Full-spectrum background model for the MAJORANA DEMONSTRATOR, with and without analysis cuts.

We worked with collaborators at Lawrence Berkeley National Laboratory and Oak Ridge National Laboratory to implement, execute, and refine the software tools for detector acceptance tests at the detector manufacturer in Oak Ridge, TN, and were able to provide a timely response on detector acceptance criteria. The tools were modified and augmented to accommodate acceptance tests taken when the detectors arrive at the experimental site. We helped further to develop a suite of tools required to support detector characterization data taken after the detectors have been re-mounted in their MAJORANA-style detector mounts and loaded into a detector string test cryostat. We have also worked closely with the DAQ and electronics groups to tune the hardware to maximize the performance of our signal-processing routines.

Our primary attention is now focused on analysis of the first data from the DEMONSTRATOR prototype cryostat. Major activities include data production, refinement of event-building routines, optimization of energy estimation and pulse-shape parameter extraction algorithms, data monitoring and cleaning routines, software quality assurance tests, database implementation of run information recording, automatic data workflow management.

1.12 Low-background cable connectors for MAJORANA

T. H. Burritt, M. Buuck, C. Cuesta, J. A. Detwiler, P. J. Doe, J. Gruszko, I. Guinn, J. Leon, D. A. Peterson, R. G. H. Robertson, and T. D. Van Wechel

The UW MAJORANA group performed research and development for the coaxial signal cable connectors for the MAJORANA DEMONSTRATOR. Detector signals are carried from the low-mass front-end (LMFE) preamplifiers through a 24" Picocoax® cable to the signal connector, then through another 61" Picocoax® cable to the vacuum feedthrough that leads to the post-amplifier. The signal connectors allow detector strings to be deployed in the cryostat without having to re-route the cables through the confined cross-arm tube that runs to the outside of the shield.

Each detector requires four Picocoax® cables and their ground braids to be connected, leading to eight required connections for each of the four or five detectors in each detector string. Due to the low-background requirements of the MAJORANA DEMONSTRATOR, the connector must use extremely radio-pure materials and low-mass design. These factors preclude the use of commercially available solutions. The connector must also survive repeated temperature cycles to 80 K, and it must be vacuum compatible. Connectors must be easy to use once they are in place, since they are manipulated inside a glovebox.

The original connector design used silica wafer paddles with Au traces on a Cr adhesion layer, which were pressed together in a Cu garage to make the connections for an entire string of detectors. The signal-cable central conductor and ground braid were attached to the trace using Ag epoxy.[1] This design was found to be insufficiently robust. During assembly, the Ag epoxy used to attach the cables was found to have an approximately 10% failure rate when temperature-cycled, leading to a failure rate of about 50% for a board with 8 such joints. Furthermore, this known failure mode made the connection unreliable when in use inside the cryostat. The silica paddles themselves were prone to chipping and breaking during shipping and use. Finally, the garage connections were difficult to make *in situ* inside the

[1] CENPA Annual Report, University of Washington (2013) p. 20.

glove box, and when a single problem was found, an entire string of detectors would have to be disconnected to debug the problem.

To resolve these problems, the UW MAJORANA group proceeded with two parallel development tracks for new designs. The first of these tracks was an attempt to preserve the paddle design, but correct its flaws. The other track aimed for an entirely new design, potentially using a commercially available connector.

To change the existing paddle design, the connections of the cables to the paddle were changed to from Ag epoxy to low-background Sn-Bi eutectic solder. The heat of the solder led to evaporation of the Au traces, so they were changed to Au over a layer of Cu. Due to their differing thermal contraction rates, the solder joint broke the silica paddle when cooled. Therefore, the paddle material was switched to a 0.03" sapphire wafer, which had the additional advantage of being a stronger material, making paddle breakage during handling less likely. So that the connections would be easier to make, a new Cu garage was designed. The comb garage, shown in Fig. 1.12-1, allowed each connection to be made separately. The connections were made by applying pressure on a pair of paddles with a tapered Vespel peg. This design was modified to use with the existing silica paddles, and was used with some success in the prototype cryostat. When using it with the sapphire paddles, however, it was found that a connection would occasionally fail to form properly at the garage. This was attributed to the fact that the thinner sapphire was not as flat as the silica had been, and that the connectivity was very sensitive to the shape of the Vespel pegs. After some attempts to correct for this via changes in the garage and peg design, the paddle design was shelved.

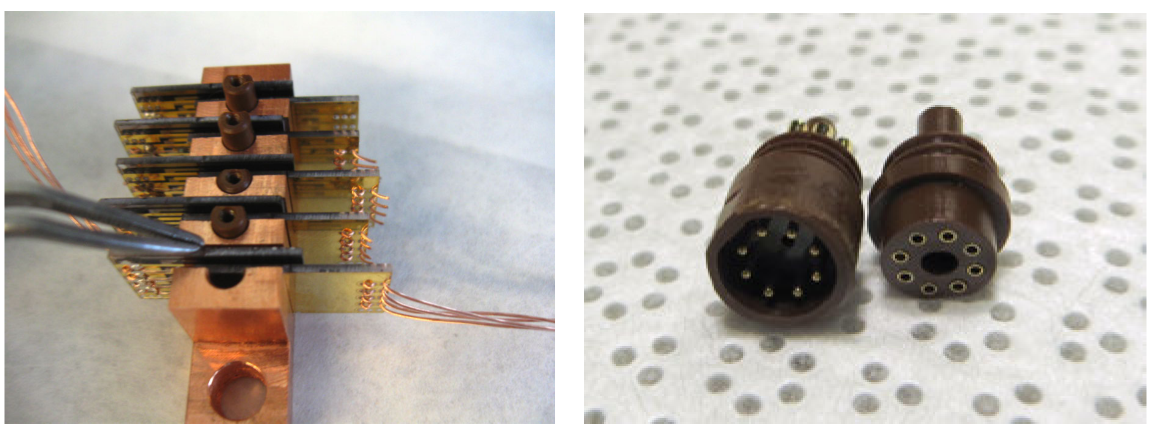

Figure 1.12-1. *Left:* The Cu comb garage was developed to resolve the problems found in the previous garage design. *Right:* The new signal cable connector design uses commercially available pins housed in a Vespel plug.

A new design was developed using small Au-plated brass sockets, ordered from Mill-Max. The reverse of a slightly larger socket is used as a male pin. Since the beryllium-copper springs used in the commercial versions of these sockets are too radioactive to be used in the DEMONSTRATOR, versions without the springs are used. The spring force for making the connection is instead supplied via the fit of the connector itself, via flexion of the pins. Therefore, the design of the pin housing is of utmost importance to ensuring that the connection is still reliable. The housing, made of Vespel plastic, places the male pins at slightly larger radius than the female pins, forcing them into contact when the plug is connected. Though the housing design relies on very low-tolerance machining of small parts, leading to some unreliability in production, preliminary use in the Prototype Cryostat indicates that the design, shown in Fig. 1.12-1, is robust and easy to use, a significant improvement over the previous paddle-and-garage designs.

Production of these connectors for Module 1 is now beginning, with the plug housings and covers being made in the clean machine shop at Sanford Underground Research Facility (SURF). The plastic pieces are leached and the Mill-Max pins are sonicated in the SURF wet lab, and then the pins are pressed into the housings. Following preliminary mechanical and connectivity tests, the connectors are sent to UW, where the cables are prepared and soldered to the pins using low-background Sn-Bi eutectic solder and radiopure abietic acid flux. The connectors are tested at room temperature and at 77 K, and then working connectors are sent to Lawrence Berkeley National Laboratory (LBNL) where MAJORANA collaborators integrate them with the detector electronic readout and vacuum feedthrough connectors.

1.13 High-voltage cable and vacuum feedthrough flange testing

T. H. Burritt, M. Buuck, C. Cuesta, J. A. Detwiler, P. J. Doe, J. Gruszko, I. Guinn, J. Leon, D. A. Peterson, R. G. H. Robertson, and T. D. Van Wechel

Due to the high material purities required for the MAJORANA DEMONSTRATOR, the selected high-voltage (HV) cables are extremely low-mass miniature coaxial cables. These cables must be capable of supplying high-purity germanium (HPGe) detector operating voltages as high as 5 kV without exhibiting discharges that can damage the front-end electronics or mimic detector signals. When the cables were first operated on-site, microdischarges and current fluctuations were observed. For this reason, a dedicated setup was designed and constructed at UW to accommodate testing of the cables under vacuum. The setup, shown in Fig. 1.13-1, reproduces as closely as possible the full HV cable path, using the same vacuum feedthroughs and HV connectors that will be used in the MAJORANA DEMONSTRATOR.

Different samples of HV cables have been tested, and the micro-discharge rates in all layouts have been compared. Cables were terminated with a corona ball for initial testing. At present cables are tested in a realistic configuration: the conductor is attached to a copper fork that is in contact with a copper ring of the same design as those used on MAJORANA HPGe detectors. The strip-back length between HV and ground has been investigated, and the optimum distance determined. The coiling of the cable was also found to be important, as a very tight coiling has proven to result in more frequent microdischarges. The cables operate under vacuum and are connected with the outer electronics through feedthroughs inserted in a flange. The first kind of feedthroughs showed current fluctuations, so new flanges with "*pee-wee*" and SHV connectors were tested. In addition, the deficiency of existing connectors was solved by potting the flange at Lawrence Berkeley National Laboratory, and tests at

UW have reported a very low rate of microdischarges. It is also worth mentioning that the systematics of the setup have been carefully investigated.

Figure 1.13-1. HV testing system at UW (left), and a cable attached to the HV copper fork and ring inside the vacuum chamber (right).

Finally, an optimum configuration where only random small microdischarges occur has been achieved. The cables are prepared at Lawrence Berkeley National Laboratory and, in view of historical problems, every cable to be installed at the MAJORANA DEMONSTRATOR will be verified to be free of gross breakdown and characterized in terms of microdischarges at UW prior to its installation underground.

1.14 Preamplifier with forward-biased reset for CoGeNT and MAJORANA

T. H. Burritt, J. A. Detwiler, J. Leon, D. A. Peterson, R. G. H. Robertson, and T. D. Van Wechel

The CoGeNT and MAJORANA projects both make use of hyperpure Ge detectors that are in principle sensitive to very low-energy nuclear recoil signals, such as those produced by coherent scattering of dark matter particles or neutrinos from Ge nuclei. However, this sensitivity can only be realized if sub-keV thresholds can be achieved. Development work continues at UW on a low-noise charge-sensitive preamplifier which is continuously reset by a forward-biased gate-to-source junction of the input tetrode JFET. Refer to previous reports for more information on the preamplifier's design principle and operation[1].

Several prototypes equipped with Moxtek MX-30 JFETs have been tested this past year. A LabVIEW program uses data from a digital oscilloscope to collect the noise power spectral density (PSD) at the output of the preamplifier, which is subsequently analyzed off-line. The noise PSD is used to fully characterize the preamplifier's noise performance in terms of three general noise sources: series, 1/f and parallel. It is crucial to correct the noise PSD for any poles or zeros in the closed-loop frequency response of the preamplifier in order to obtain reliable fits to the three-component noise model. As can be seen in Fig. 1.14-1, this

[1] CENPA Annual Report, University of Washington (2013) p. 24.

correction has a remarkable impact at low frequencies which translates to better estimates of the 1/f and parallel noise components.

The primary focus of testing this year has been to identify sources of 1/f noise and either reduce or remove their contributions. While the dissipation noise of the feedback capacitor has previously been identified as a major contributor, additional sources of 1/f noise have been discovered recently. In particular, tests of the preamplifier with an alternative configuration of the feedback loop reveal dissipation noise originating in the JFET's gate capacitance. This noise is exacerbated by lossy materials near the dissipative capacitance and this explains why low-loss substrate materials, such as fused silica, are necessary. So far best results have been achieved with a preamplifier with an MX-30 JFET and 'high-Q' feedback capacitor (from Passive Plus, Inc.) mounted on a low-loss Rogers circuit board. The feedback capacitor was mounted upright such that the input node was a small distance above the board and also away from other lossy materials. Tests with an open input show an equivalent noise charge (ENC) below 7 electrons RMS at a peaking time just below one hundred microseconds (see Fig. 1.14-1). The continuous curve is obtained via a fit of the noise PSD, while the points are obtained by direct integration of the noise PSD shaped by a trapezoidal filter of a given peaking time.

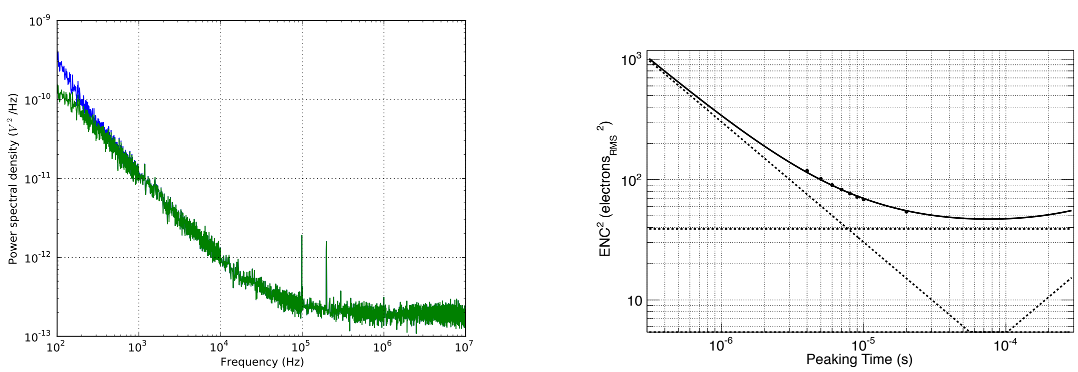

Figure 1.14-1. *Left:* Corrected (blue) versus uncorrected (green) noise power spectral density at output of the preamplifier. Peaks clearly visible at 100 kHz and 200 kHz due to external noise source are of little consequence in these measurements. *Right:* Equivalent noise charge squared as a function of peaking time for a preamplifier with MX-30 JFET and high-Q feedback capacitor. Series, 1/f and parallel noise components based on a fit of the corresponding noise PSD are drawn as black dashed and solid lines, respectively. Direct integrations of the shaped noise power spectral density at given peaking times are shown as black circles; error bars are too small to be visible.

The latest revision of the preamplifier calls for sub-mm-scale machined vacuum-gap capacitors on a fused silica board, which are features that are anticipated to further reduce the 1/f noise. Finite-element-method calculations using a COMSOL Multiphysics model have been instrumental in the design of this front-end board and the new feedback and test injection vacuum capacitors. Modifications to the post-amplification stage that drive down series noise have also been made in preparation for connecting to a p-type point contact germanium detector in the near future. Testing of this new preamplifier is scheduled to begin within the next month.

1.15 Low-background parylene coating and gasket production

J. A. Detwiler

The UW Majorana Group has helped lead the investigation of parylene technologies for use in low-background experiments. Parylene is a polymer with excellent dielectric properties whose raw materials have been demonstrated to have low natural radioactivity. Our past efforts included a promising implementation of ultra-low-mass, low-background ribbon cable to carry detector signals[1]. While ultimately the design was not able to achieve the impedance requirements of the low-mass front end being deployed in the Majorana Demonstrator, the cables remain a viable option for future detector systems.

Two other use-cases of parylene are being implemented in the Demonstrator. One of these is the use of parylene films as low-background gaskets for the large Majorana cryostats. The low-background requirements of the Demonstrator preclude the use of traditional cryostat sealing solutions such as indium. Parylene offers an alternative that uses a minimal amount of material that is already low in radioactivity. Films are produced in a clean room by parylene-coating large metal sheets polished to a mirror finish. The films are removed from the sheets and cut to size.

Parylene is also being used as a coating for ultra-pure electroformed copper (EFCu) parts. EFCu, which can be grown with exceedingly high radiopurity, is the primary structural component for the inner-most region of the Majorana Demonstrator apparatus. All internal metallic structures, including all nuts and bolts, are fabricated from this material. If left bare, these nuts and bolts run a significant risk of galling, which would result in poor fastening strength, and would make it difficult to non-destructively disassemble the apparatus. To prevent galling, all copper-on-copper interfaces are made with either the nuts or the bolts coated in parylene. Since parylene can be applied in thin coatings of the order of 1 mil or thinner, the coatings successfully eliminate the risk of galling with no impact on background or mechanical design.

Parylene film and copper-part coatings have been produced using the parylene coater in the UW clean room. These coatings are being successfully deployed in the Majorana Demonstrator Prototype Cryostat. For production of the films and part coatings required for the enriched detector cryostats, it is advantageous to be able to perform the coatings closer to the experimental site. In particular, it is desirable to reduce the duration that the EFCu components spend above ground, where they are exposed to cosmic rays that can activate long-lived radioisotopes, such as ^{60}Co, that pose a background risk for the Demonstrator. To achieve this, we relocated our coating apparatus to a surface facility at Sanford Underground Research Facility in South Dakota. We have trained collaborators to assist in the parylene coating production runs, and have consulted on technical issues with the coatings. We have also helped lead several assay efforts to constrain background sources originating in the parylene films.

[1] CENPA Annual Report, University of Washington (2012) p. 19.

SNO+

1.16 Overview of the SNO+ experiment and CENPA's contribution

J. Kaspar, L. Kippenbrock, T. J. Major, and N. R. Tolich

SNO+ is a large-volume underground liquid scintillator neutrino experiment presently under development at the SNOLAB facility in Sudbury, Ontario, Canada. It is a multi-purpose detector whose reach extends to the following areas of neutrino physics: neutrinoless double beta decay, geo-neutrinos, reactor neutrinos, and low-energy solar neutrinos. In addition, a large liquid scintillator detector serves as an excellent supernova neutrino monitor. We plan to load the scintillator with 0.3% Te, which would provide approximately 180 kg of ^{130}Te in a 3.5-m radius spherical fiducial volume. After one year of data this should give us a 90% confidence level (CL) sensitivity of approximately 4×10^{25} years (neutrino mass sensitivity of 70 to 100 meV). There is an R&D effort underway to increase the amount of Te loaded into the scintillator which could allow complete coverage of the inverted hierarchy.

SNO+ will use a lot of the infrastructure left behind by the completed Sudbury Neutrino Observatory (SNO) experiment including the acrylic vessel (AV), photomultiplier tubes, and most of the electronics. The main engineering work involved anchoring the AV to the floor which has been completed. The detector will be filled with water in the next few months and that will be replaced with liquid scintillator starting at the beginning of next year. Data-taking is scheduled to start in late-2015.

In SNO+ the data rate is expected to be two orders of magnitude higher than in SNO and therefore updates to the SNO electronics and data acquisition (DAQ) system are needed. CENPA is responsible for updating the DAQ into a faster, ORCA-based system compatible with the electronics upgrades that are being planned by the University of Pennsylvania. These include new XL3 cards for controlling the 19 data crates. Software for operating the XL3s through ORCA has been written and tested at the typical rates expected from SNO+. We continued to commission the full DAQ system this year collecting data with the detector empty for extended periods of a few days on multiple occasions. These test have resulted in many GUI feature requests and some low-level improvements that are currently being implemented. CENPA is also responsible for the SNO+ slow-control system, which monitors and records a large number of detector-related variables at a rate of $\sim$1 Hz. This system was installed and commissioned last year. This year we have extended the systems number of systems that this collects data from and have continued to refine the web based user interface.

To achieve the goals of the experiment it is imperative to understand the optical properties of the scintillator. At CENPA we developed an experiment to study scattering. This work is described in more detail (Sec. 1.17).

1.17 Measurement of light scattering in liquid scintillators considered for SNO+

T. J. Major and N. R. Tolich

The SNO+ experiment will use about 1000 tons of liquid scintillator solution loaded with tellurium in a search for neutrinoless double-beta decay. To facilitate this search, the scintillator formula will be optimized in terms of the concentration of tellurium, concentrations and types of fluorescent agents, and perhaps the presence and concentrations of other chemicals. A primary consideration is the amount and distribution of light scattering in the solution.

To measure the scattering characteristics of a given liquid, an apparatus (pictured on the cover of this report) was built that uses a selection of lasers to find the amount of light scattered in a given direction as a function of polarization and wavelength. The measurements were then fit to a model including absorption-reemission and Rayleigh scattering. Several scintillator formulations were characterized in this way.

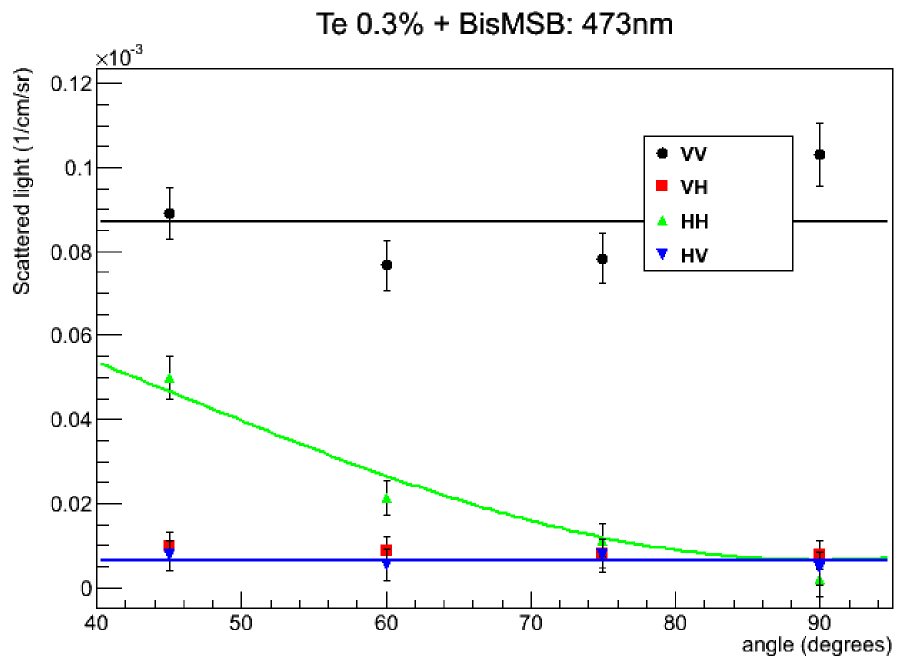

Figure 1.17-1. Scattering as a function of angle, at 473 nm, for a solution of PPO, Bis-MSB, and Te in linear alkyl benzene. Though not shown, the fit includes data at four other wavelengths. The black circles are vertically polarized incident and scattered light, the red squares are vertically polarized incident light but horizontally polarized scattered light, the green triangles are horizontally polarized incident and scattered light, and the blue inverted triangles are horizontally polarized incident but vertically polarized scattered light.

An example of a fit is shown in Fig. 1.17-1. This figure shows the fraction of incident light scattered per cm per steradian for a sample of linear alkyl benzene containing tellurium and the fluorescent agents PPO and Bis-MSB. While this plot only shows results at 473 nm, the fit included data at four other wavelengths, so the model looks reasonable for this sample.

Not all measured samples demonstrated behavior that fit the model well. Work has been done to extend the model to include Mie scattering and a previously neglected effect whereby Rayleigh scattering is enhanced near an absorption peak[1]. Successive improvements to the apparatus and procedure have also served to reduce systematic effects. Finally, a well-established standard, cyclohexane, is being measured to confirm our absolute scattering measurements are correct.

HALO

1.18 The HALO supernova detector

C. A. Duba*, T. H. Burritt, F. Duncan†‡, J. Farine‡, A. Habig§, A. Hime¶, M. Howe††, A. Kielbik‡, C. Kraus‡, S. Luoma‡, D. Peterson, R. G. H. Robertson, K. Scholberg‖, M. Schumaker‡, J. Secrest**, T. Shantz‡, J. Vasel§, T. D. Van Wechel, C. J. Virtue‡, B. von Krosigk§§, R. Wendell‖, J. F. Wilkerson††, S. Yen‡‡, and K. Zuber§§

The Helium And Lead Observatory, HALO, is a dedicated supernova neutrino detector at SNOLAB. The neutrino target material in HALO is 79 metric tons of lead, originally part of the Deep River Cosmic Ray Station. Charged- and neutral-current ν-Pb interactions produce neutron-unstable states and the subsequent emission of neutrons. A set of 128 ^{3}He proportional counters from CENPA, originally brought to Sudbury for the final phase of the SNO experiment, are arrayed throughout the target medium to detect the burst of neutrons that would signal the arrival of supernova neutrinos (Fig. 1.18-1). As a result, HALO is a low-cost, low-maintenance detector with unique capabilities because it is mainly sensitive to neutrino interactions rather than antineutrino interactions like water and scintillator detectors. It has been running since May, 2012.

The past year has seen a number of upgrades and changes designed to improve HALO's uptime and robustness. The data-acquisition system has been split across 2 independent VME crates, each serving half the detector. Two network switches, two high-voltage supplies, and two sets of low-voltage supplies provide further defenses against single-point failures. A test stand has been built to permit offline studies of up to 4 detectors and preamps at a time. GPS timing has been purchased by SNOLAB for general use, and HALO is presently the

*Digipen Institute of Technology, Redmond, WA.
†SNOLAB, Sudbury, ON, Canada.
‡Laurentian University, Sudbury, ON, Canada.
§University of Minnesota Duluth, Duluth, MN.
¶Pacific Northwest National Laboratory, Richland, WA.
††University of North Carolina, Chapel Hill, NC.
‖Duke University, Durham, NC.
**Armstrong Atlantic State University, Savannah, GA.
§§TU Dresden, Dresden, Germany.
‡‡TRIUMF, Vancouver, BC, Canada.

[1] S. G. Stanton, R. Pecora, B. S. Hudson, J. Chem. Phys. **75**(12), 5615 (1981).

Figure 1.18-1. The Helium And Lead Observatory (HALO), a dedicated supernova detector, at SNOLAB. The electronics, at left, has been extensively upgraded over the past year.

main beneficiary. Initial operation of HALO was subject to many interruptions but since September of 2013, it has been running essentially continuously. It is manned 2 shifts per day, 7 days a week. Data are monitored for rate spikes, but a supernova trigger is not yet perfected. The intention is to complete that this summer, 2014.

Project 8

1.19 Status of the Project 8 neutrino mass experiment

B. Clark*, P. J. Doe, M. Fertl, J. A. Formaggio†, D. Furse†, M. Jones‡, J. Kofron, B. H. LaRoque§, E. L. McBride, B. Monreal§, N. S. Oblath†, R. Patterson*, R. G. H. Robertson, L. J Rosenberg, G. Rybka, M. G. Sternberg, J. Tedeschi‡, and B. A. VanDevender‡

The neutrino is now known from neutrino oscillations to have a small but non-zero mass. There are 3 mass eigenstates with mixed active flavors, but to a good approximation the electron flavor is distributed in such a way that in experiments such as KATRIN (Sec. 1.1), the effects mimic those of a simple massive electron neutrino. KATRIN will reach a sensitivity of 0.2 eV and may observe a non-zero mass. If the mass is below this level another strategy is needed.

In Project 8 the energy of electrons is measured not in a high-resolution spectrometer like KATRIN's, but by precise measurement of the frequency of cyclotron radiation emitted

*California Institute of Technology, Pasadena, CA.
†Massachusetts Institute of Technology, Cambridge, MA.
‡Pacific Northwest National Laboratory, Richland, WA.
§University of California Santa Barbara, Santa Barbara, CA.

as βs spiral in a uniform magnetic field. Because a large source may be used, the region < 0.2 eV may then become accessible[1]. The first step for Project 8 is to demonstrate that the technique is feasible, and to this end a prototype apparatus is nearing completion at the University of Washington. Instead of tritium the initial tests are being made with ^{83m}Kr, which has narrow conversion-electron lines near 17 and 30 keV. The test volume is very small, a section of WR-42 waveguide.

With the granting of supplemental funds for Project 8 from DOE, radical improvements to the prototype became possible (Fig. 1.19-1). A 40-year-old cold-bore magnet has been replaced by an available Bruker '200' NMR magnet from our colleagues at UCSB. Tom Burritt and Lisa McBride traveled to Santa Barbara to stabilize the magnet mechanically for shipment, which went without a hitch July 19-22, 2013. The helium boil-off rate of this magnet is only 9 ml/hr and making changes to the warm-bore insert is very simple. A Cryomagnetics power supply with 12 shim-coil outputs was purchased and an interface box was constructed to drive the persistent-switch heaters in the new magnet. Assistance from KIT and Bruker GmbH was crucial in acquiring a charging kit for this magnet.

Figure 1.19-1. View of the new Project 8 experiment. The Bruker magnet is equipped with the NMR field mapper in this photo. Behind the magnet is the instrument platform with the Agilent RF sweeper, a spectrum analyzer, and the ^{83m}Kr gas system. In the background left are the NMR readout unit, computers, digitizers, and power supplies.

[1] B. Monreal and J. Formaggio, Phys. Rev. D **80**, 051301(R) (2009).

An NMR field mapper was designed and built. A map slice across the magnet bore is shown in Fig. 1.19-2. After setting the z and z^2 shims, a 2-ppm uniformity over 2 cm along the axis was achieved. The z^3 shim heater was found to be open, but this is not considered to be a significant problem. Vacuum hardware was built to allow evacuation of the bore. Our MIT colleagues built an elevated instrument platform and designed and supplied a vacuum chamber based on the ISO standard for ease of assembly and more internal space. All equipment has been moved from B027 in the Physics Building to the larger B037, and cable trays and chilled-water manifolds have been installed.

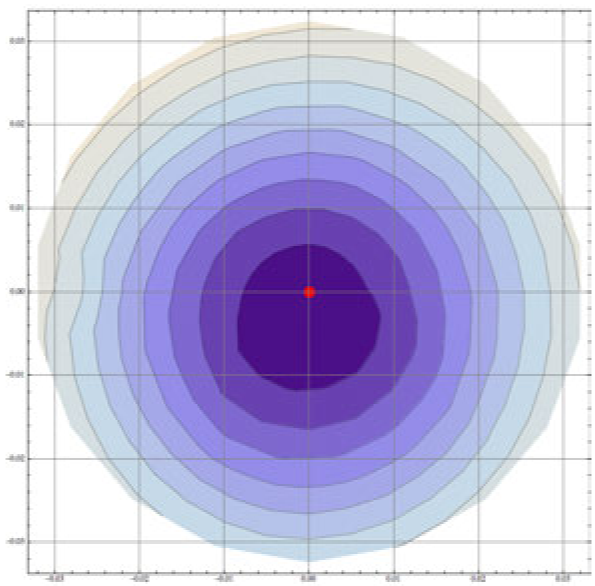

Figure 1.19-2. NMR field map across the bore of the Bruker 200 magnet. The grid lines are 1 cm apart. The central field is 0.946442 T and each contour is 15 ppm. The red dot marks the geometric center.

Low Noise Factory in Sweden built 2 new amplifiers operating at 30 K to amplify the 26-GHz cyclotron emission signal for digitization. These replace borrowed radio astronomy amplifiers that performed erratically. A new Agilent 31.8-GHz N5183B RF sweeper has been purchased to replace a failing unit that had been acquired 20 years ago from the SSC. A Planar Monolithics PIN diode switch with 120 db of isolation has been purchased to chop the signal provided by a voltage-controlled 26-GHz oscillator (VCO) made by our electronics group. It will provide the capability of realistic simulation of the chirping signal produced by an electron. A new Tektronix oscilloscope has been installed for diagnostics and observing calibration signals. New cabling with low-loss K-type connectors throughout has been purchased. A Herotek high-sensitivity power diode is now used to demodulate the absorption signal from 2,2-diphenyl-1-picrylhydrazyl (DPPH).

The first success with the new equipment has been the observation of the electron-spin-resonance absorption signal from DPPH in the magnet bore. This had never been achieved in the bore of the old magnet, but was completed in one hour with the new apparatus.

Slow-controls software has been written to automate the DPPH analysis and to supervise other calibrations. A complete analysis software tool has been developed at MIT to extract signal events from the digitized data. The software has initially been run on sample noise data and will soon be tested against sample pulses from the VCO and PIN switch as part of commissioning. With an 8-bit digitizer there are constraints on gain and bandwidth. With too little gain the bit resolution adds to the system noise, but with too much gain the system noise saturates the digitizer. Reduction of bandwidth and oversampling are mitigating strategies and work continues on this optimization. A computer-controlled stepped attenuator has been constructed and is interfaced through slow controls.

The gas system has been extensively reconfigured and a high-sensitivity MKS MicroPirani gauge was purchased to make a measurement of the background pressure in the waveguide cell. A virtual leak was found and eliminated and the residual gas analyzer shows a spectrum characteristic of a very clean, leak-tight system. A 7-zone bakeout controller designed by Laura Bodine for the TRIMS (Sec. 1.8) experiment will be pressed into service for Project 8 as well. A new ^{83}Rb source is being prepared at PNNL. At this writing some work on the insert remains but the apparatus is nearing completion and a search for the electron cyclotron-emission signal is not far off.

The assistance of undergraduate helpers Natasha Woods, Frank Sullivan, Megan Wachtendonk, and Dave Walt, as well as our professional staff Tom Burritt, Greg Harper, Peter Hirtle, David Peterson, Tim Van Wechel, and Doug Will, has been key to this progress.

2 Fundamental symmetries and non-accelerator-based weak interactions

Torsion-balance experiments

2.1 New-Wash rotating torsion balance upgrade

S. Fleischer, A. Kraft, J. G. Lee, H. E. Swanson, and T. A. Wagner

Work is continuing to bring the upgraded New-Wash rotating balance back online. The basis of smooth rotation is a 36000-line angle encoder. The turntable PID controller now determines the table's angle from a choice of either read head of the encoder or the average of both. The LabVIEW controller VI was completely re-written in more modular form using sub-VIs to facilitate future evolution of the controller's code. A software bridge connects the DAQ program with the PID controller allowing bidirectional communication.

A zero-moment pendulum was designed and built to track the turntable rotation rate as a function of turntable angle in the lab. As the turntable motion is locked to the angle encoder, this provides a check on the linearity of the encoder and the means to correct any discrepancies. A new torsion fiber was needed and the small crimp tubes used to fasten the fiber were in short supply. New copper tubes were located and used in making this fiber. We will be testing the long term stability of these replacement crimp pieces.

The gravity-gradient compensator is used as a winch when opening up the instrument in order to remove the outer vacuum vessel. It is positioned vertically by three lead screws. Over the years since the system was last operated the lubricant had deteriorated. In attempting to move the compensator one of the screws seized and this required some rebuilding and complete replacement of the old lubricant. The leg adjustment screws for the turntable support platform also required cleaning and re-lubrication for the same reason. Remote adjustment by stepping motors is now completely functional.

New AGI tilt sensors were installed with increased precision. Readout electronics were placed close to the sensors to reduce noise pickup that was observed in previous measurements. A sensitivity of 1, 10 or 100 may be selected as well as time constants for internal filters. The increased precision required new stages to level the sensors in the rotating frame with equally precise adjustment screws. We found adjustments were highly temperature-dependent and the time to reach thermal equilibrium made for slow progress. Small motors were added so these stages could be adjusted remotely without changing the thermal environment. Rotary contacts are used to provide power and control to the rotating frame but there were insufficient channels for the additional controls needed. A wireless communication system was built using XBee and Arduino technologies. The DAQ program accesses the XBee through a USB interface and is able to control both the adjustment motors and tilt-sensor electronics.

The ion pump that maintains vacuum in the rotating balance had developed a short circuit and could not be started. The pump is currently being refurbished.

2.2 Parallel-plate inverse-square-law test: data analysis

J. H. Gundlach, C. A. Hagedorn, M. D. Turner, and K. Venkateswara

The parallel-plate null test of Newton's inverse square law at submillimeter scales[1] is experimentally complete. Data analysis and writing are nearly complete.

This has been a year of software development. The analysis is automated using only open-source and freely available software (Octave, Gnuplot, git, make, LyX/LaTeX, and the GNU suite of Linux tools), and runs from raw data to finished paper without human involvement. This has several benefits:

1. The analysis may be repeated and audited in the future. The code and its development history is managed in a git repository, diagrammed[2] in Fig. 2.2-1.
2. To the extent that this is a blind measurement, unblinding is as simple as toggling a software flag. Direct integration of analysis output, both quantities and plots, into the LyX/LaTeX text means that the entire science document is generated at once.
3. Daily/hourly builds: a continuous build environment ensures that build-breaking errors are caught when changes are recent, not months or years later.
4. Automated testing: while crude, some of the critical libraries are internally-certified to yield correct results each time the analysis is run, reducing sensitivity to specific computer environments and external libraries.
5. The planned repetition/upgrade of the parallel-plate experiment with improved control of contact potentials and flatter test masses will be faster, as the analysis will be repeated almost exactly. Automated analysis is a prerequisite to a future fully-blind experiment.

Careful attention has been paid in the integration of systematic uncertainties to the conservative extraction of confidence intervals.

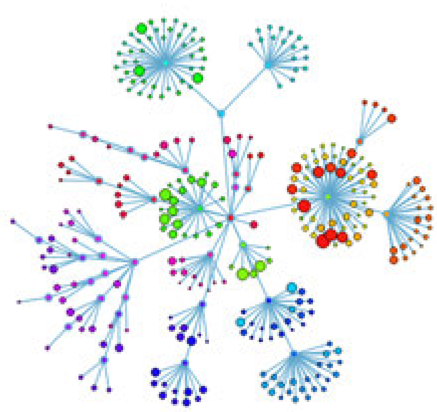

Figure 2.2-1. A CodeFlower diagramming the directory structure and relative file size of the analysis software git repository.

[1] CENPA Annual Report, University of Washington (2013) p. 40.

[2] F. Zaninotto, CodeFlower, `https://github.com/fzaninotto/CodeFlower`.

2.3 Progress on the upgrade of the wedge-pendulum experiment for testing short-range gravity

E. G. Adelberger, S. Fleischer, C. D. Hoyle*, J. G. Lee, H. F. Leopardi*, and H. E. Swanson

Our plans for a comprehensive upgrade of the Fourier-Bessel short-range experiment were described in the previous annual report[1]. We have now completed a substantial part of the upgrade. The in-situ alignment system for the electrostatic shield was built and tested, including development of an algorithm for parallel alignment at the smallest possible attractor-shield separation. The electrostatic shield itself was redesigned, fabricated, and checked using our SmartScope measuring microscope and profilometer. The results show that we have met our design goal: the entire area of about 66 mm diameter is flat within about $\pm 2\,\mu$m, and the central part directly relevant to the pendulum is within $\pm 1\,\mu$m. The larger-diameter replacement for the lower vacuum chamber and the corresponding support structures have been manufactured and are ready for assembly. All the necessary components for upgrading the pump line to a larger diameter have been acquired.

In order to improve the flatness of the pendulum and attractor, which initially showed surface-height variations of up to $50\,\mu$m and an overall conical deformation of $8-9\,\mu$m, we continued our research on possible fabrication methods. We ran an extensive series of tests of different strategies to glue the thin metal pattern to its flat glass substrate. We tried either to fill in the holes in the pattern with a low-viscosity epoxy or to remove the excess glue squeezed into these holes completely. Either option would avoid the irregular filling of the current implementation and allow an easier and more precise modeling of the mass distribution and capacitance. Ideally, we are aiming to achieve flatness on the 1-μm level. While the results are encouraging, we have not yet settled on a final solution. Despite the hope that a smooth and flat pendulum surface might also mitigate the excess-noise problem at small pendulum-shield separations, recent tests have not shown any improvement over the performance observed with the old pendulum at electrostatically favorable "sweet spots". The tests were performed using a pendulum with a gold-coated polished glass ring instead of the active pattern assembly in the old setup.

After discovering delamination problems with the tungsten foils in our tests, we have decided to switch to platinum foils. Its chemical inertness and even higher mass density compared to tungsten are additional advantageous qualities for our application. New wedge-pendulum and attractor patterns have been produced using the same EDM-based fabrication technique as previously used. The new foils were characterized using a high-precision lab scale and the SmartScope to quantify deviations from the design pattern.

In summary, the upgrade of the Fourier-Bessel experiment is well underway. It is expected to optimize the performance of the wedge-pendulum setup and to achieve significant improvements in testing the inverse-square law at even shorter distances.

---

*Humboldt State University, Arcata, CA.

[1] CENPA Annual Report, University of Washington (2013) p. 39.

2.4 Continued development of a low-drift gravity-gradiometer system

J. H. Gundlach, C. A. Hagedorn, M. D. Turner, and K. Venkateswara

We have continued work on a moving-mass gravity-gradiometer torsion-balance system, as introduced in previous Annual Reports[1,2]. The most notable achievement in the last year has been the development of a non-magnetic wirelessly powered rotary actuator. This actuator uses the thermally-driven contraction of shape-memory-alloy (SMA) wires to rotate a grooved wheel by discrete steps. The SMA wire is heated by electrical current from an inductive coil mounted on the torsion pendulum, which is powered by a surrounding coil fixed inside the vacuum chamber housing the device.

Although this new actuator overcomes limitations imposed by previous actuators (magnetic effects and positioning uncertainty), there remain some as yet unexplained effects that limit the sensitivity of the system. We are making progress in identifying the source of these problems and expect to resolve them in the coming months.

2.5 Progress on the development of a ground-rotation sensor for advanced LIGO

J. H. Gundlach, C. A. Hagedorn, M. D. Turner, and K. Venkateswara

Advanced LIGO (aLIGO) is a next-generation gravitational-wave-detector system expected to make first detections when turned on in 2015. Key among the improvements in the new detector is a better seismic isolation system to cancel the effect of ground motion on the suspended optics. This is done through an active-control system which measures the ground motion through seismometers and applies a corrective force on the optics platform. However, at low frequencies (10-500 mHz) seismometers and tiltmeters are unable to separate ground rotation and horizontal acceleration, which limits their ability to measure ground motion. Thus, aLIGO needs a ground-rotation sensor to accurately distinguish between horizontal ground acceleration and rotation. Such an instrument is not commercially available and the required sensitivity of the rotation sensor is challenging to reach.

Over the last three years, we have developed an instrument that meets a significant part of the requirement specified by the seismic-isolation team in aLIGO in the frequency range of 40 to 400 mHz. The device consists of a low-frequency flexure-beam balance. We measure its angle using a multi-slit autocollimator mounted to the platform. Above its resonance frequency, the balance remains inertial, thus the autocollimator measures ground rotation. Horizontal-ground motion is rejected by locating the center of mass at the pivot point of the flexure. The prototype beam consists of a 0.75-m aluminum tube with 1.8-kg brass weights attached at each end. It is suspended by two, 25-μm-thick, copper-beryllium flexures. The entire balance is surrounded by an aluminum heat shield and is placed in high vacuum to minimize thermal effects.

[1] CENPA Annual Report, University of Washington (2012) p. 39.
[2] CENPA Annual Report, University of Washington (2013) p. 47.

Over the last several months, we have built a second rotation sensor. Its design is similar to the first sensor, but it is enclosed in a compact vacuum can making it more suitable for field deployment. We have also built a new multi-slit autocollimator using mostly off-the-shelf components, thus reducing its cost and complexity. Having two rotation sensors allows us to subtract the rotation signal and measure the instrument noise directly.

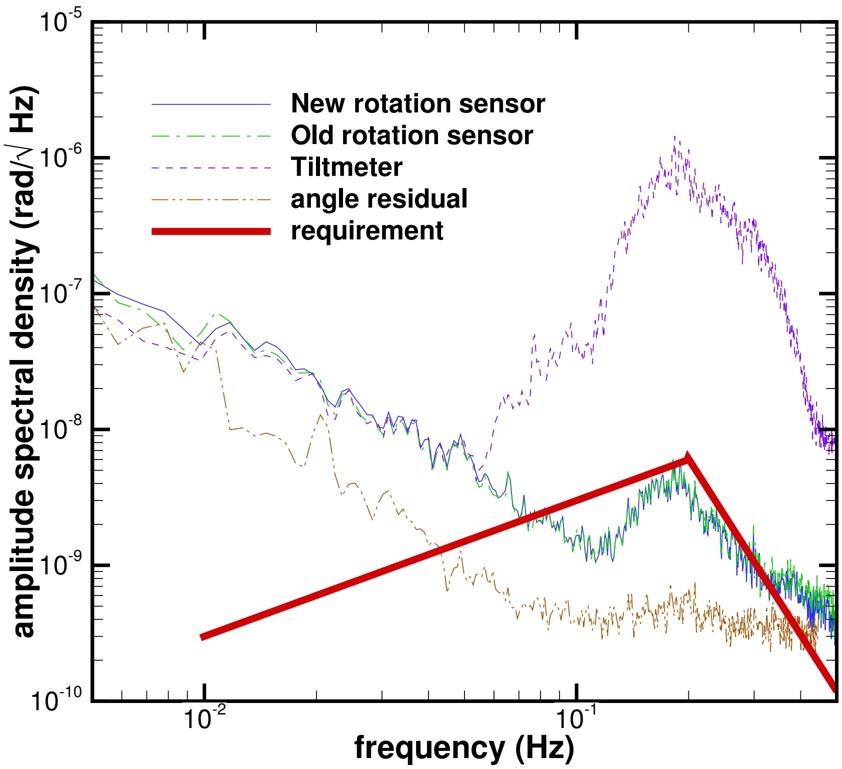

Figure 2.5-1. Plot showing the ground rotation recorded by our rotation sensors in comparison to a tiltmeter. Also shown are the rotation sensor residual and aLIGO requirement.

Fig. 2.5-1 shows an amplitude-spectral-density plot of 3000 seconds of data recorded simultaneously by three instruments — the two rotation sensors and a tiltmeter. The rotation-sensor curves lie nearly on top of each other over most of the frequency range, while the tiltmeter has good correlation at low frequencies but is affected by ground acceleration at higher frequencies. Also shown are the residual between the rotation-sensor measurements, which is indicative of the instrument noise, and the aLIGO requirement.

The new instrument is performing even better than the first and is expected to be installed at the LIGO-Hanford observatory in the near future. Measuring ground rotation at the site will allow us to measure the rotation-induced noise in the interferometer and improve its sensitivity.

2.6 Final data and preliminary results from a search for short-range spin-coupled forces

E. G. Adelberger, B. R. Heckel, and W.A. Terrano

We have finished taking data with the torsion pendulum designed to look for spin-coupled forces[1]. An issue with centering the pendulum was resolved by first centering the pendulum relative to the attractor rotation axis by maximizing the signal using the gravitational attractor (Fig. 2.6-1) and then installing the spin attractor for data taking.

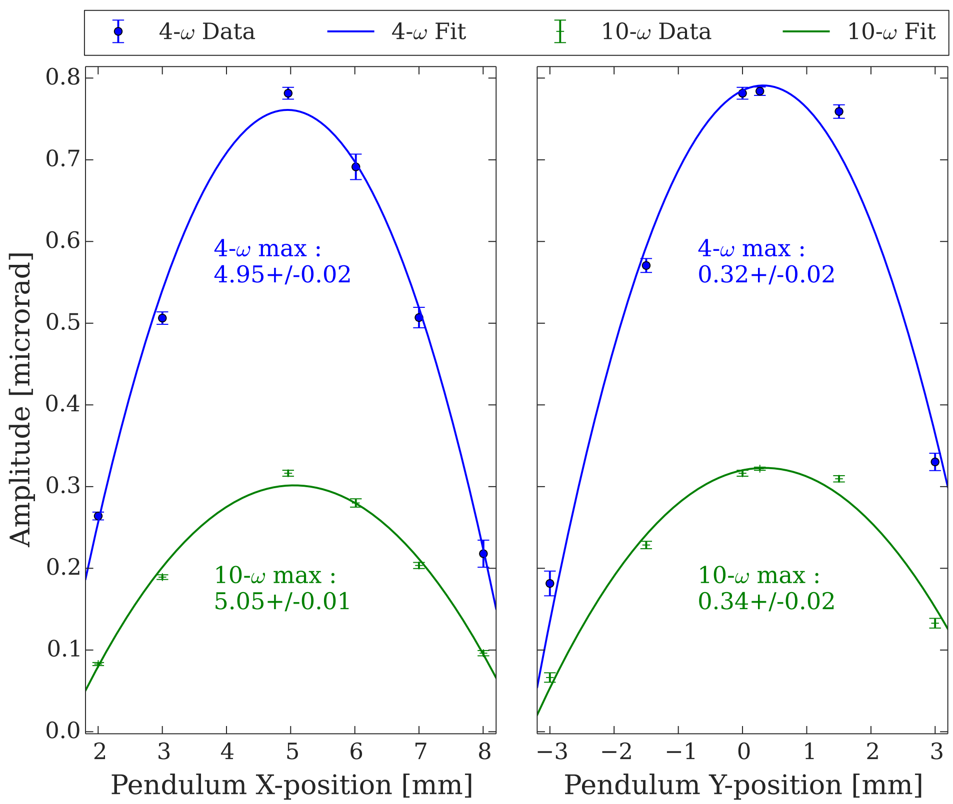

Figure 2.6-1. Gravitational data used to center the spin pendulum prior to data taking.

We increased the number of layers in the shielding screen to 5 layers of 0.010" mu-metal with 0.008" of aluminum spacing between each mu-metal layer. The improved shielding attenuated the attractor-pendulum magnetic coupling enough that only the dipole and quadruple couplings (1st and 2nd harmonics of the turntable rotation rate ω) can be seen above the noise. The 4-ω signal from our gravitational calibration tone is easily resolved. There is no

[1] CENPA Annual Report, University of Washington (2007) p. 38.

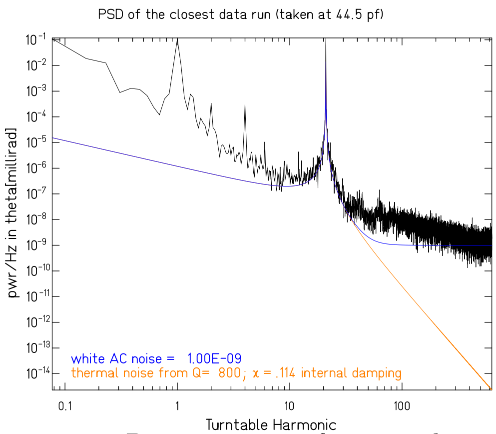

Figure 2.6-2. Power spectrum from our closest run. The curves show the expected thermal noise from our fiber and autocollimator.

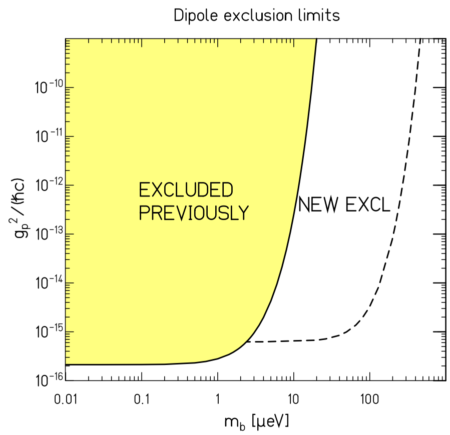

Figure 2.6-3. Prelimanary limits on a new dipole-dipole interaction, compared with previous limits. The previous limits were from 1 year of data while the new limits are from 3 days.

resolved signal at the 10th harmonic, where a new spin-coupled interaction would appear[1] (Fig. 2.6-2). Estimating our total pendulum-attractor separation at 5.8 mm allows us to set preliminary limits on a new spin dipole interaction as shown in Fig. 2.6-2.

2.7 Constraints on long-range, macroscopic spin-dependent forces

E. G. Adelberger, B. R. Heckel, and W. A. Terrano

New low-mass bosons can mediate macroscopic forces of many types. Pseudo-scalar or pseudo-vector particles mediate forces which couple at tree-level to the macroscopic spin of the test bodies. A comprehensive analysis of all possible spin-coupled interactions finds three which produce new spin-dependent forces between stationary, spin-polarized sources[2]. All three (spin-dot-spin, spin-cross-spin, and dipole-dipole) can be mediated by a spin-1 boson with axial and vector couplings g_A and g_V:

$$V_1 = \frac{g_A^2}{4\pi r}(\hat{\sigma}_1 \cdot \hat{\sigma}_2) e^{-r/\lambda} \tag{1}$$

$$V_2 = -\frac{g_A g_V \hbar}{4\pi m_e c r^2}(\hat{\sigma}_1 \times \hat{\sigma}_2 \cdot \hat{r})\left(1 + \frac{r}{\lambda}\right) e^{-r/\lambda} \quad \text{and} \tag{2}$$

$$\begin{aligned} V_3 = & -\frac{(g_A^2 + g_V^2)\hbar^2}{16\pi m_e^2 c^2 r^3}\left[(\hat{\sigma}_1 \cdot \hat{\sigma}_2)\left(1 + \frac{r}{\lambda}\right)\right. \\ & - \left.(\hat{\sigma}_1 \cdot \hat{r})(\hat{\sigma}_2 \cdot \hat{r})\left(3 + \frac{3r}{\lambda} + \frac{r^2}{\lambda^2}\right)\right] e^{-r/\lambda}\ ; \end{aligned} \tag{3}$$

where $r = r_1 - r_2$ and $\lambda = \hbar/(m_b c)$ is the interaction range of a boson of mass m_b.

[1] CENPA Annual Report, University of Washington (2013) p. 41.

[2] B. A. Dobrescu and I. Mocioiu, Jour. of High Energy Phys. **11**, 005 (2006).

To search for these interactions, we used the spin-dipole pendulum[1] and four spin-sources made using the same principles[2]. We looked for torques on the pendulum as its spin direction is rotated relative to the sources. The torques should depend on the locations and orientations of the spin sources as described in Eq. 1-3. Taking data with the spin-sources oriented in several different directions provided, for the first time, simultaneous sensitivity to all three potentials. This work appeared in PRL[3].

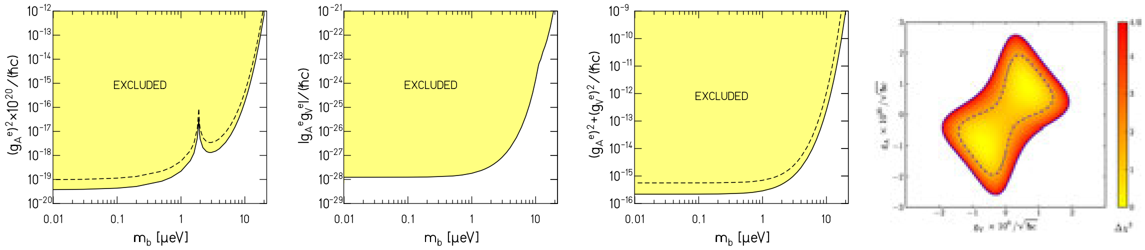

Figure 2.7-1. Exclusion plots, from left to right for the spin-dot-spin, spin-cross-spin and dipole-dipole interactions. The solid line is the exclusion assuming only that one new force exists while the dashed line allows for any possible combination of new spin interactions. The cusp at 20μeV in spin-dot-spin is due to cancellations between the arms of the source. The final plot shows the derived limits on the axial and vector couplings, g_A and g_V, themselves.

2.8 Developments towards a hydrogen-rich equivalence-principle test

B. R. Heckel, J. G. Lee, and W. A. Terrano

The sensitivity of an equivalence-principle style test to new forces depends on the composition difference of the test bodies. The use of hydrogen-rich materials such as polypropylene (PP) can significantly increase the charge-to-mass difference $[\Delta\frac{q}{\mu}]$ on the pendulum[4]: the best current constraints on new long-range forces come from tests using Al-Be test body pairs with $[\Delta\frac{q}{\mu}] = 3.8 \times 10^{-2}$, while PP-Be has $[\Delta\frac{q}{\mu}] = -12.6 \times 10^{-2}$. The material properties of polypropylene pose experimental challenges: the mechanical stability, thermal expansion coefficient and outgassing rate are all worse in thermoplastics than in metals.

The first prototype pendulum showed that differential thermal expansion effects are negligible if the PP is free to expand and contract around its center of thermal expansion[5]. Unfortunately this pendulum was very sensitive to seismic noise. Our second prototype pendulum was modeled on the 8-test body design. The PP is pressed on to the pendulum by a Ti screw and copper end-caps which hold it rigidly in place. This design does not allow for unconstrained expansion and therefore may have more thermal expansion issues.

[1] CENPA Annual Report, University of Washington (2004) p. 7.

[2] CENPA Annual Report, University of Washington (2007) p. 30.

[3] "Limits on Exotic Long-Range Spin-Spin Interactions of Electrons," B. R. Heckel, W. A. Terrano, and E. G. Adelberger, Phys. Rev. Lett. **111**, 151802 (2013).

[4] E. G. Adelberger, J. H. Gundlach, B. R. Heckel, S. Hoedl, and S. Schlamminger, Prog. Part. Nucl. Phys. **62**, 102 (2009).

[5] CENPA Annual Report, University of Washington (2013) p. 43.

This pendulum has successfully been operated at the thermal noise limit, the essential achievement for the use of PP in future equivalence principle tests.

We are looking at potential systematic issues due to thermally-changing gravitational moments. We typically null the q_{21} moment of the pendulum so that its coupling with the uncompensated gravitational field of the lab produces a signal $\theta_{21}^{Pend-Lab} < 2$-nanoradian. Changing the temperature of the apparatus from 20.5°C to 16.5 °C causes a ∼10-nanoradian shift in $\theta_{21}^{Pend-Lab}$. Our long-term temperature stability is on the order of 100 mK, so thermal changes to $\theta_{21}^{Pend-Lab}$ should be less than 0.2 nanoradians over the course of extended data taking. This is much smaller than the residual $\theta_{21}^{Pend-Lab}$, and therefore would not be an important contributor to our systematic error budget.

2.9 Improved limits on long-range parity-odd interactions of the neutron

E. G. Adelberger and T. A. Wagner

Yan and Snow[1] recently inferred bounds on the coupling strength, $g_A^n g_V^{^4\mathrm{He}}$ of long-range, parity-violating interactions of neutrons from an experiment that studied the parity-violating spin-rotation of polarized neutrons transmitted through liquid ^{4}He. Substantially tighter (up to 11 orders of magnitude) limits on several closely related quantities can be found by combining bounds on $|g_A^{\mathrm{n}}|^2$ and on $|g_V|^2$ set by previous experiments to obtain

$$|g_A^n g_V| = \sqrt{|g_A^n|^2 |g_V|^2} \ . \tag{1}$$

It is convenient to define

$$g_V^{\pm} = (g_V^{\mathrm{p}} + g_V^{\mathrm{e}} \pm g_V^{\mathrm{n}})/\sqrt{2} \ , \tag{2}$$

so that $g_V^{^4\mathrm{He}} = 2\sqrt{2} g_V^+$. We take our bounds on $|g_A^{\mathrm{n}}|$ from a Princeton optical-pumping experiment with polarized ^{3}He detector and sources[2,3] that probed the neutron spin-spin interaction

$$V_{12}^{\sigma\cdot\sigma} = \frac{(g_A^n)^2}{4\pi r}(\hat{\sigma}_{\mathbf{1}} \cdot \hat{\sigma}_{\mathbf{2}}) e^{-r/\lambda} \ , \tag{3}$$

because the neutron in ^{3}He carries most of the nuclear spin.

Our bounds on $|g_V|^2$ come from results of equivalence-principle tests[4,5] that tightly constrain Yukawa interactions of the form

$$V_{12} = \frac{(g_V)^2}{4\pi r} e^{-r/\lambda} = V_G(r)\, \tilde{\alpha} \left[\frac{\tilde{q}}{\mu}\right]_1 \left[\frac{\tilde{q}}{\mu}\right]_2 e^{-r/\lambda} \ ; \tag{4}$$

[1] H. Yan and W. M. Snow, Phys. Rev. Lett. **110**, 082003 (2013).

[2] G. Vasilakis, J. M. Brown, T. W. Kornack, and M. V. Romalis, Phys. Rev. Lett. **103**, 261801 (2009).

[3] G. Valilakis, PhD Thesis, Princeton University, 2007.

[4] G. L. Smith, C. D. Hoyle, J. H. Gundlach, E. G. Adelberger, B. R. Heckel, and H. E. Swanson, Phys. Rev. D **61**, 022001-1 (1999).

[5] T. A. Wagner, S. Schlamminger, J. H. Gundlach, and E. G. Adelberger, Class. Quant. Grav. **29**, 184002 (2012).

where, in the second relation (conventionally used to analyze equivalence-principle results[5]), V_G is the Newtonian potential, $\tilde{\alpha}$ is a dimensionless strength to be determined by experiment and a general vector 'charge' of an atom with proton and neutron numbers Z and N can be parameterized as

$$\tilde{q} = \cos\tilde{\psi}[Z] + \sin\tilde{\psi}[N] \ , \tag{5}$$

where $\tilde{\psi}$ characterizes the vector charge with

$$\tan\tilde{\psi} = \frac{g_V^n}{g_V^p + g_V^e} \ . \tag{6}$$

Note that $\tilde{q}^{\pm}$ correspond to 'charge' parameters $\tilde{\psi} = \pm\pi/4$. The results of this analysis for $G_V^+ G_n$ are shown in Fig. 2.9-1. Details and corresponding constraints on $g_V^- g_A^n$ and $g_V^n g_A^n$ may be found in our publication[6].

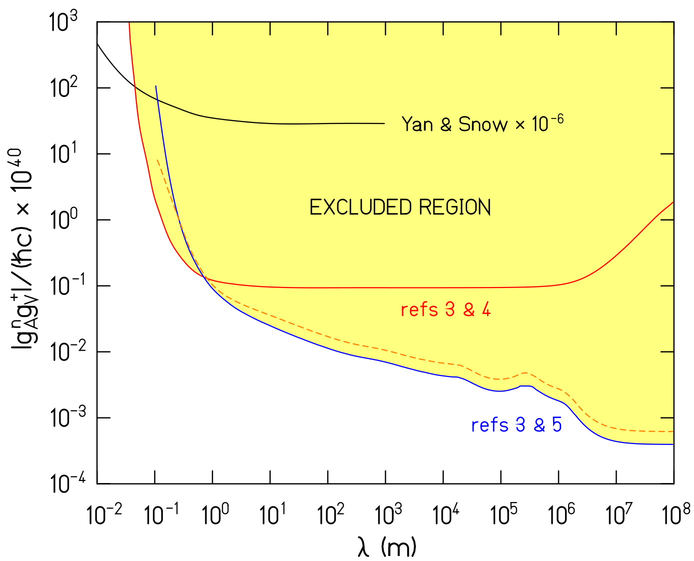

Figure 2.9-1. Comparison of Yan and Snow's 1σ constraints on $|g_A^n g_V^+|$ [1] with those inferred from Princeton neutron spin-spin studies[2] and Eöt-Wash equivalence-principle tests with bodies falling toward a massive ^{238}U laboratory source [4] or in the field of the entire earth[5]. Our constraints shown as solid lines assume that $\tilde{q}^- = 0$. The dashed line shows our constraint with no assumptions about the 'charge' parameter $\tilde{\psi}$. Yan and Snow's upper bounds are divided by 6 orders of magnitude so that they can be displayed on the same scale.

We are indebted to Georg Raffelt for showing how tight bounds on exotic interactions can be obtained by combining the results of gravitational experiments and other data[7]. This work was supported by NSF grant PHY969199.

[6] E. G. Adelberger and T. A. Wagner, Phys. Rev. D **88**, 031101 (2013).
[7] G. Raffelt, Phys. Rev. D **86** 015001 (2012).

Non-accelerator-based weak interactions

2.10 The ^{199}Hg electric-dipole-moment experiment

Y. Chen, B. Graner, B. Heckel, and E. Lindahl

In the summer of 2013, a new round of ^{199}Hg electric-dipole-moment (EDM) measurements was initiated. The current version of the Hg EDM apparatus uses UV laser light to polarize and measure the spin-precession frequency of ^{199}Hg atoms in a stack of 4 vapor cells, 2 of which (the inner pair) have oppositely directed electric fields. A pump-probe sequence is employed, with the electric fields reversed between each pump-probe cycle. A blind frequency offset is added to the inner-cell frequency difference to mask the EDM signal until the analysis of the entire data set is complete. The daily sensitivity of the current apparatus to an EDM is more than 4 times greater than that of the apparatus used in our most recent experiment[1].

EDM data collection is divided into "sequences", groups of 16 days of data distinguished by the ordering and orientation of the 4 vapor cells. Each sequence includes equal numbers of runs with electric-field magnitudes of 6 kV/cm and 10 kV/cm, magnetic field normal and reversed, and slow and fast electric-field ramp rates. The first data sequence showed evidence of a systematic error that was consistent with a small movement of the vapor cells due to forces exerted by the applied electric field. The high-voltage feedthroughs were then redesigned and the vapor cells were better secured to eliminate the systematic error.

The data set with the new high-voltage feedthroughs began in October, 2013. We have completed 4 data sequences and are nearing completion of the fifth. Fig. 2.10-1 shows the EDM measurements taken at 10 kV/cm for the first 4 data sequences. Each run represents one day of data accumulation. A similar data set exists for measurements taken at 6 kV/cm.

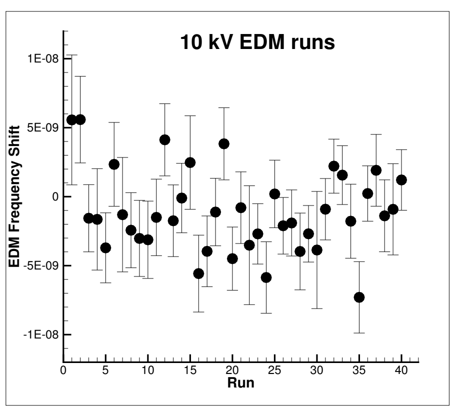

Figure 2.10-1. Angular-frequency Hg EDM results for the first four data sequences.

The statistical error on the current data set is $5.9 \times 10^{-30} e\,\mathrm{cm}$, representing an improvement by a factor of 2.2 over our previous ^{199}Hg EDM result. We anticipate 16 data sequences for the current experiment, which should result in a factor-of-4 improvement over our former results. This project is supported primarily by the NSF (P.I. Heckel).

[1] M. D. Swallows *et al.*, Phys. Rev. A **87**, 012102 (2013).

3 Accelerator-based weak interactions

3.1 Progress towards a precision measurement of the $\beta - \nu$ correlation in ^{6}He β decay

Y. S. Bagdasarova, K. Bailey*, X. Fléchard†, A. García, R. Hong, A. Knecht‡, A. Leredde*, E. Liénard†, P. Müller*, O. Naviliat-Cuncic§, T. P. O'Connor*, M. G. Sternberg, D. W. Storm, H. E. Swanson, F. Wauters, and D. W. Zumwalt

Correlations from beta decay established the $V - A$ nature of the weak interaction over 50 years ago[1]. Exotic scalar and tensor currents, forbidden by the standard model, have only been ruled out at the 5-10% level[2]. The most stringent limits on right-handed tensor currents come from a measurement of the $\beta - \nu$ correlation in ^{6}He performed a half century ago[3]. Limits on scalar currents are roughly half those of tensor currents and have benefited from the use of modern trapping techniques to push down systematics that have plagued past correlation experiments[4]. The goal of the CENPA ^{6}He experiment is to realize similar gains for tensor currents through a precision measurement of the $\beta - \nu$ correlation parameter, $a_{\beta\nu}$, in the pure Gamow-Teller transition of ^{6}He using a magneto-optical trap (MOT).

The relationship between the β-decay rate per solid angle and $a_{\beta\nu}$ is given by the following expression

$$\frac{d\Gamma}{d\Omega} \propto 1 + a_{\beta\nu}\frac{\mathbf{p_e}\cdot\mathbf{p}_\nu}{E_e E_\nu} + b\frac{m}{E_e} \tag{1}$$

where $\mathbf{p_e}$, E_e, $\mathbf{p}_\nu$, and E_ν are the momenta and energy of the β and ν respectively, m is the electron mass, and b is the Fierz interference term. In the Standard Model $b = 0$, while $a_{\beta\nu} = -1/3$ and $+1$ for pure Gamow-Teller and pure Fermi decays respectively. If vector and axial-vector currents were absent and only non-Standard Model tensor and scalar currents were present then one would instead find $a_{\beta\nu} = +1/3$ and -1 for Gamow-Teller and Fermi decays. A general expression for $a_{\beta\nu}$ in terms of the weak couplings is given in Sec. 3.5 along with an overview of experimental limits on scalar and tensor currents.

The ultimate goal of the CENPA ^{6}He experiment is to achieve an uncertainty of 0.1% in the measurement of $a_{\beta\nu}$, which would reveal or limit weak tensor currents at an unprecedented level of $\sim 3\%$. Significant progress has been made over the last year in order to achieve an initial measurement of $a_{\beta\nu}$ at 1%. This represents the current state-of-the-art limit and will guide us towards a future 0.1% measurement.

*Physics Division, Argonne National Laboratory, Argonne, IL.
†LPC-Caen, ENSICAEN, Université de Caen, Caen, France.
‡Paul Scherrer Institute, Villigen, Switzerland.
§Department of Physics and Astronomy and National Superconducting Cyclotron Laboratory, Michigan State University, East Lansing, MI.

[1] R. P. Feynman and M. Gell-Mann, Phys. Rev. **109**, 193 (1958).
[2] N. Severijns, M. Beck, and O. Naviliat-Cuncic, Rev. Mod. Phys. **78**, 991 (2006).
[3] C. H. Johnson, F. Pleasonton, and T. A. Carlson, Phys. Rev. **132**, 1149 (1963).
[4] A. Gorelov *et al*, Phys. Rev. Lett. **94**, 142501 (2005).

^{6}He is produced via the prolific ^{7}Li(d,^{3}He)^{6}He reaction by delivering a 15-μA 18-MeV deuteron beam from the CENPA tandem onto a molten lithium target. Production rates in excess of 10^{10} ^{6}He atoms per second are now achieved routinely providing the world's most intense source of ^{6}He. Details of production are discussed in Sec. 3.2. ^{6}He is pumped away from the target and into a radio-frequency (RF) discharge chamber using a turbomolecular pump. The discharge chamber is used to excite the atoms to the $2^{3}S_{1}$ metastable state, from which they can be laser cooled and trapped within a MOT. Once trapped within the MOT, the atoms are periodically transferred to a second MOT where the background from untrapped ^{6}He atoms is greatly reduced. The dual-MOT laser system is discussed in Sec. 3.3.

A detector system consisting of a plastic-scintillator-backed multi-wire proportional chamber (MWPC) on top, and a position-sensitive multichannel plate detector (MCP) on bottom, surrounds the second MOT chamber. The direction and energy of the β are determined from coincidences between the MWPC and plastic scintillator, which cover $\sim$ 1% of the MOT solid angle. The recoiling $^{6}Li^{+}$ ions are accelerated down towards the MCP by a uniform electric field produced by a stack of cylindrically symmetric electrodes that surround the MOT. Fig. 3.1-1 shows a cross-sectional view of the detection MOT chamber, acceleration electrodes, and detector system.

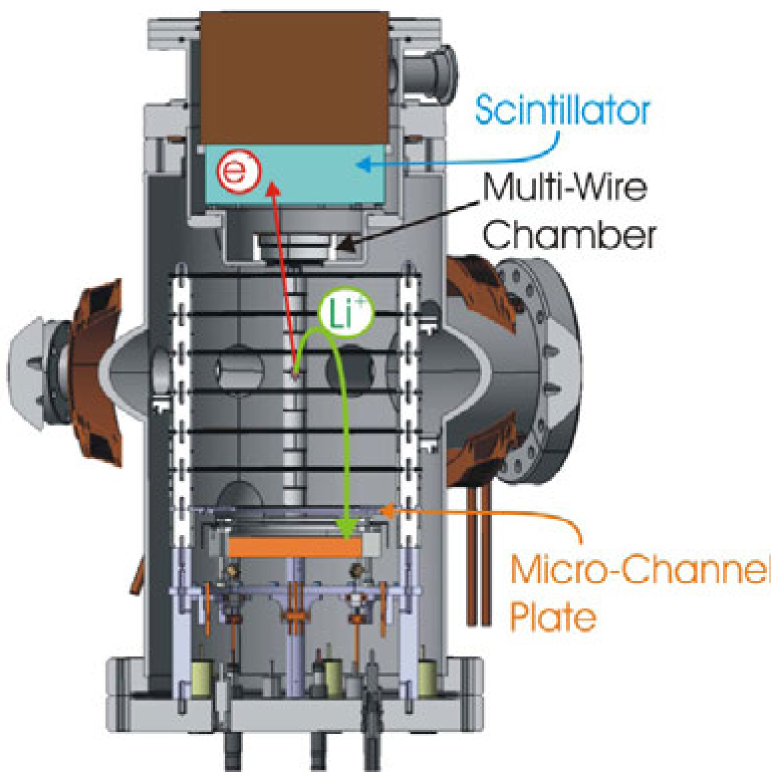

Figure 3.1-1. Cross-sectional view of the detection MOT chamber including the beta detector system (top), the position-sensitive MCP recoil detector (bottom), and the cylindrical electrode stack surrounding the trap region.

The time difference between the prompt β signal and the MCP signal produces a time-of-flight (TOF) measurement of the recoiling nucleus. The TOF signal, the location of the recoil-ion hit on the MCP, and the momentum information of the β combine to fully over-determine the kinematics of the decay. Thus, the angle between the β and ν can be directly determined providing a measure of $a_{\beta\nu}$. The uniform electric field, the MCP detector, and the β-detector system are discussed in Sec. 3.7.

The first β-recoil coincidences from trapped ^{6}He decay were measured in the fall of 2013 at a rate of ~0.15 Hz. Fig. 3.1-2 shows a two-dimensional plot of the measured β energy versus the recoil-ion TOF from the fall run. The data consist of 4250 events, a third of which are from cold laser-trapped ^{6}He atoms. The rest of the events originate from untrapped ^{6}He atoms within the vacuum chamber. The one-dimensional histograms are projections of the β energy and the recoil-TOF spectra with the background-subtracted spectra shown in red. The greatest experimental sensitivity to $a_{\beta\nu}$ is achieved by fitting the shape of the recoil-TOF spectrum to detailed Monte Carlo simulations. The simulations also serve as a laboratory in which to study various experimental and computational systematic uncertainties. Development of the Monte Carlo simulations and the analysis of systematics is discussed in Sec. 3.4.

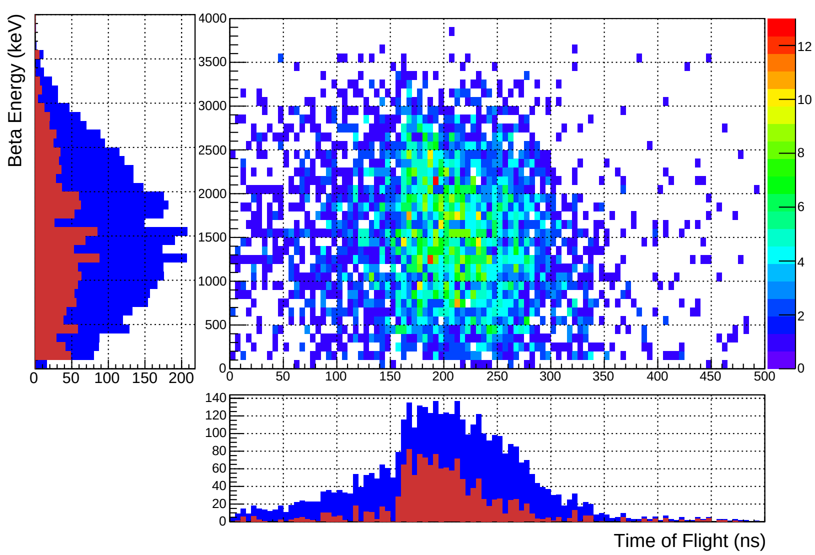

Figure 3.1-2. The β-energy spectrum versus the recoil-ion TOF spectrum along with the one-dimensional projections. The one-dimensional background-subtracted spectra are shown in red, while the full spectrum of the combined trapped and untrapped β-recoil coincidences is shown in blue.

A number of improvements have recently increased the rate of trapped decays and limited the number of background atoms present in the detection chamber, namely the installation of an atomic beam shutter between the first and second MOT, improvements in the ultra-high vacuum system, and a number of upgrades to the laser trapping system discussed in Sec. 3.3. A β-recoil detection rate above 1 Hz is anticipated under the current configuration and should be realized in runs scheduled for the spring of 2014. At such a rate a statistical precision in $a_{\beta\nu}$ of order 1% will be achievable within a week of beamtime. In addition, the ratio of trapped decays to background decays is expected to increase by well over an order of magnitude compared to the data shown in Fig. 3.1-2.

3.2 ^{6}He source developments for the $\beta-\nu$ angular correlation experiment

Y. S. Bagdasarova, K. Bailey*, X. Fléchard†, A. García, R. Hong, A. Knecht‡, A. Leredde*, E. Liénard†, P. Müller*, O. Naviliat-Cuncic§, T. P. O'Connor*, M. G. Sternberg, D. W. Storm, H. E. Swanson, F. Wauters, and D. W. Zumwalt

The ^{6}He source has continued to provide consistent, abundant production for the $\beta-\nu$ angular correlation experiment (Sec. 3.1) via the ^{7}Li(d,^{3}H)^{6}He reaction using 18-MeV deuterons provided by CENPA's tandem Van de Graaff accelerator. With little tuning, ^{6}He production rates exceeding 10^{10} atoms/s are readily achieved. To make the system more robust we have made some alterations to the initial design.

The original source, consisting of a central target containing lithium separated from vacuum by a 2-mil stainless steel foil, was designed for low-beam-current operation with incremental upgrades added later to allow for active cooling of the target due to the 180 W of heating power caused by the 10-μA deuteron beam. Copper cooling lines fed through Swagelok fittings were mounted in contact with the stainless-steel target. Compressed air flowing through the lines provided active cooling to remove heat deposited by the deuteron beam. Over time, these Swagelok mounts began to leak. Efforts to seal these leaks proved temporary as the sealant would routinely crack as the cooling lines expanded and contracted from repeated heating cycles.

The original target was also electrically isolated from the surrounding vacuum chamber to act as a Faraday cup. This was important for our early tests which measured ^{6}He production as a function of energy and beam current. However, the ceramic used in isolating the target as well as the cooling lines presented weaknesses in the structural integrity of the system. Care must be taken when compressing the VCR fittings connecting the cooling lines to the target so that the electrical isolators attached to the lines would not break. We no longer need this electrical isolation, tuning the beam based on production rates and upstream collimator currents instead of beam current on target.

To address these issues, all ceramic isolators have been removed and stainless steel tubes replace the copper cooling lines. This allows welding the tubes directly to the target holding assembly and eliminates any leaks associated with heating or cooling.

The intense deuteron beam, which is typically focused to a 1-mm diameter, causes strong local heating on the stainless-steel foil. Liquid lithium backing the foil helps to cool the foil, but the poor thermal conductivity of stainless steel causes the foil to melt, sometimes within one day of bombardment. Other foil materials are being considered but the chemical reactivity of lithium limits the number of suitable candidates.

---

*Physics Division, Argonne National Laboratory, Argonne, IL.

†LPC-Caen, ENSICAEN, Université de Caen, Caen, France.

‡Paul Scherrer Institute, Villigen, Switzerland.

§Department of Physics and Astronomy and National Superconducting Cyclotron Laboratory, Michigan State University, East Lansing, MI.

To help with this problem, we have installed a two-dimensional rastering magnet. Function generators provide alternating current in both horizontal and vertical directions to paint the beam over a wide surface, with both the amplitude and frequency of rastering as tunable parameters. At the peak magnetic field of 200 Gauss, the beam can be deflected by as much as 3.5 mm on either side. Tests are currently ongoing to determine the efficacy of rastering in decreasing the rate of foil failure.

We are also developing methods of monitoring the foil integrity to better understand how to prevent a rupture. We now leak a small amount of argon gas into the beamline, which is separated from the lithium by the stainless foil. A residual gas analyzer (RGA) attached to the lithium side of the vacuum chamber can sensitively detect partial pressures of argon down to 10^{-12} Torr. A rupture in the foil would provide a path for the argon to reach the RGA and determine that the foil has been compromised. Additionally, we are in the process of mounting optical elements that will allow us to image the foil while the target is installed to periodically monitor its status. Because a large number of neutrons is generated during bombardment, any CCD camera will need to be well-shielded to prevent neutron damage. This work is still ongoing.

In the future, the source may be redesigned to remove the foil altogether, instead using a small aperture to isolate the beamline vacuum from the extracted helium by way of differential pumping.

3.3 Magneto-optical trap status and experimental study of related systematic effects for the ^{6}He experiment

Y. S. Bagdasarova, K. Bailey*, X. Fléchard†, A. García, R. Hong, A. Knecht‡, A. Leredde*, E. Liénard†, P. Müller*, O. Naviliat-Cuncic§, T. P. O'Connor*, M. Sternberg, D. W. Storm, H. E. Swanson, F. Wauters, and D. W. Zumwalt

Laser setup

The ^{6}He beam first passes through a radio-frequency (RF) discharge where a small fraction of the atoms are excited to the 2^3S_1 metastable state. These atoms are then slowed down and focused toward our first magneto-optical trap (MOT) by a transverse cooling beam, a Zeeman slower and a two-dimensional focusing setup, all based on the absorption/emission of 1083-nm laser photons for the $2^3S_1 \to 2^3P_2$ transition. The aim of these stages is to increase the trapping efficiency up to the expected value of 1×10^{-7}. In order to increase the S/B ratio of our experiment, the trapped atoms are periodically pushed by a pulsed laser beam toward a second MOT chamber where the detection setup records $\sim 0.5\%$ of the events coming from the trap. Improvements have been made to improve the MOT-to-MOT transfer and

*Physics Division, Argonne National Laboratory, Argonne, IL.
†LPC-Caen, ENSICAEN, Université de Caen, Caen, France.
‡Paul Scherrer Institute, Villigen, Switzerland.
§Department of Physics and Astronomy and National Superconducting Cyclotron Laboratory, Michigan State University, East Lansing, MI.

the differential pumping between the two MOT chambers. A fast shutter and a 10-cm-long aperture tube with a diameter of 1 cm sit at the exit of the first MOT chamber and help to decrease the conductance and the un-trapped ^{6}He background in the detection chamber.

For low atomic densities, the trap lifetime is limited by collisions with the residual gas, which is dominated by hydrogen. Increasing the lifetime of the trap also increase the S/B ratio, so a getter pump has been added to the detection chamber. With these modifications, we were able to reach a trapping efficiency of about 7×10^{-8}, a transfer efficiency of $\sim 30\%$ and a pressure in the detection chamber of 2.5×10^{-9} Torr.

Since the number of ^{6}He atoms trapped during each cycle is small, the study of some systematic effects related to the trap (position, distribution) becomes very difficult via an optical technique. To monitor the position and the size of our trap-source, we have to switch periodically from ^{6}He to ^{4}He. Due to the isotope shift of the trapping transition, we cannot use a single laser diode for both of them. We decided to use two laser diodes, one locked on the ^{4}He trapping transition ($2^3S_1 \rightarrow 2^3P_2$) via a saturated-absorption-spectroscopy setup, and the other one locked on the same transition for the ^{6}He isotope ($\sim$ 34 GHz above the ^{4}He transition) via a beat-lock technique. Both of them feed the same fiber amplifier. Another laser diode, locked via a saturated-absorption-spectroscopy technique on the $2^3P_2 \rightarrow 3^3S_1$ transition, is used to obtain a much higher optical signal for a small ^{4}He trap. Indeed, the scattering rate of this transition at 706 nm is much higher than the scattering rate of the trapping transition. In this case, a single laser diode is used since the isotope shift of this transition is only 606 MHz. A double pass in an acousto-optic modulator driven by a 303-MHz RF field does the frequency shift to compensate the isotope shift.

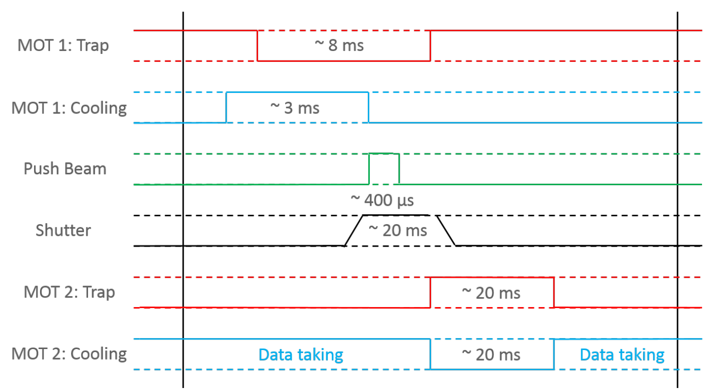

Figure 3.3-1. Time sequence for the laser system during data acquisition. The higher state means *"laser ON"* and the lower state means *"laser OFF"*. The state of the shutter has also been included in this picture. The shutter is open only for a short period of time, just long enough to let the atoms fly from one MOT to the other.

For the data acquisition, the lasers follow a time sequence optimized to increase the number of decays in the second trap. The full sequence is shown in Fig. 3.3-1. It consists of a large detuning of the first MOT laser beam to increase the trapping efficiency, followed by a short low-detuning cooling phase just before the MOT-to-MOT transfer. The same scheme is used for the second MOT laser beam with a short re-capturing period and a long low-temperature phase while useful data are recorded.

MOT properties

With the detection setup added to the second MOT chamber, we were able to detect the ions produced by Penning ionization. Since the trapped helium atoms are in a metastable state, they can easily ionize any other atoms or molecules. The electrode structure has been used to provide a 1.5 kV/cm^{-1} electric field and detect the ions with the MCP.

MOT lifetime By loading the second MOT periodically, we can look at the exponential decay curve due to Penning ionization. The lifetime of the atoms in the MOT is directly related to the Penning-ionization cross section with the different residual gases. One can see in Fig. 3.3-2 that the decay at a pressure of 8.5×10^{-9} Torr leads to a lifetime of about 1 s. The frequency of the time sequence shown previously (Fig. 3.3-1) was thus optimized to increase the β-decay rate of ^{6}He in the detection chamber according to the total efficiency, the ^{6}He lifetime ($t_{1/2} \sim 807$ ms) and the trap lifetime.

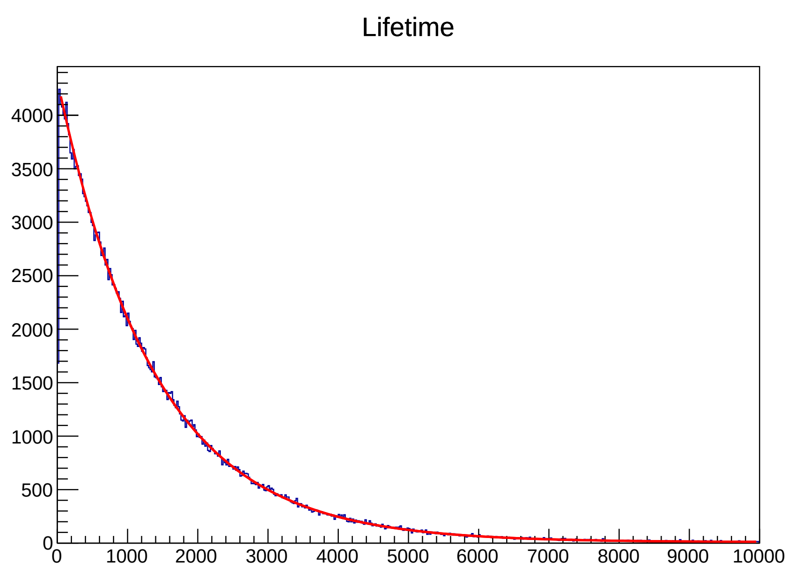

Figure 3.3-2. The number of events is recorded as a function of the time after the trap is loaded. The result is fitted by a simple exponential decay to extract the lifetime of the trap. In this case the lifetime is of about 965 ms.

MOT temperature The trap temperature has also been inferred using the same technique. After the trapping lasers are turned off, the free expansion of the atomic cloud allows us to measure the temperature of the atoms. This technique provides a unique and unperturbed measurement of the trap temperature in contrast to optical techniques. With an appropriate laser power and detuning we were able to reach a cloud temperature as low as 1 mK. For such low temperatures, magnetic interaction between the MOT field and the magnetic moments of helium substates was observed. Instead of a free expansion, three components were evidenced, corresponding to the evolution of the -1, 0 and $+1$ magnetic substate of the metastable helium atoms. While the $m_f = 0$ atoms expand freely, the $m_f = +1$ are accelerated away from the center of the trap and the $m_f = -1$ are confined in the center. The shape of this magnetically trapped atom cloud agrees with the magnetic-field gradient which is twice as strong along the axis of the trapping coils. The width of the cloud along the axis of the trapping coils is then half its width along the two other dimensions.

^{4}He$^+$ time-of-flight / Electric field / Z-position This detection technique, coupled with a pulsed nitrogen laser, which is able to ionize the atoms in the cloud, not only provides useful information about the X and Y positions and widths of the trap but also a relative measurement of the Z position since we can measure the time offlight (TOF) of the ^{4}He$^+$ ions. In fact, the MCP is also slightly sensitive to the UV photons scattered from the Nitrogen laser which allows us to calibrate our TOF spectrum and get rid of any offset. The TOF of the laser-ionized particles is shown in Fig. 3.3-3. The first sharp peak corresponds to the zero time given by the scattered photons. The second peak corresponds to the TOF of the ^{4}He$^+$ ions, and some other species can also be observed with very low statistics at longer TOF.

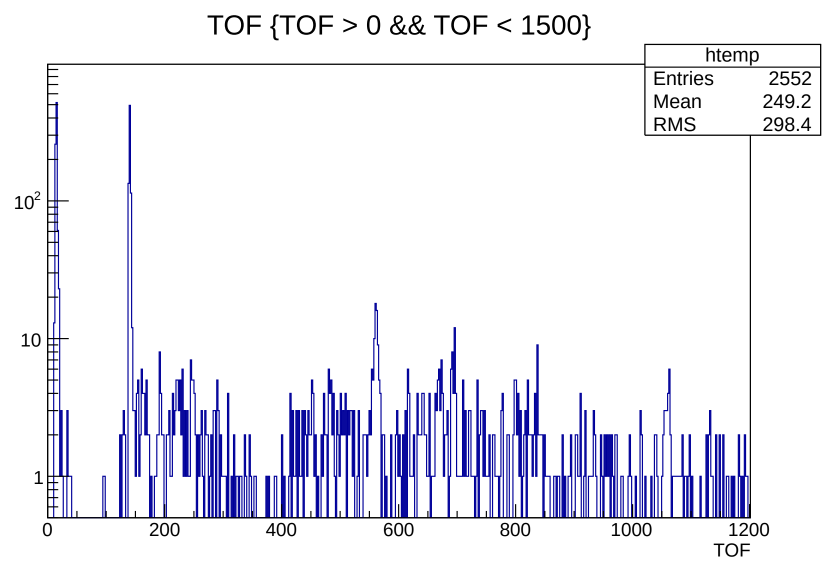

Figure 3.3-3. Time of flight of photoionized atoms in the detection chamber.

Recently, we were also able to detect a ^{6}He cloud in the detection chamber, and we saw our first β-recoil ion coincidences from these trapped atoms.

Perspectives

We are now trying to obtain high, stable trapping efficiency to take the first high-statistic data set. The next planned upgrades are an increase of the thermo-conductivity of the discharge tube to increase the trapping efficiency, further reduction of the ^{6}He background in the detection chamber with a better seal between the shutter and the aperture tube, and a far-detuned guide beam to increase the MOT-to-MOT transfer efficiency.

3.4 Development of Monte Carlo simulation and systematic analysis for the ^{6}He experiment

Y. S. Bagdasarova, K. Bailey*, X. Fléchard†, A. García, R. Hong, A. Knecht‡, A. Leredde*, E. Liénard†, P. Müller*, O. Naviliat-Cuncic§, T. P. O'Connor*, M. G. Sternberg, D. W. Storm, H. E. Swanson, F. Wauters, and D. W. Zumwalt

While making progress in improving the hardware of the ^{6}He experiment, we developed a Monte Carlo simulation program and a data-analysis program to understand the important systematic uncertainties and optimize the experimental setup (Sec. 3.1). The fitting templates for the time-of-flight (TOF) spectra are also generated by the Monte Carlo simulation.

The Monte Carlo simulation program consists of four modules: event generator, β-particle tracker, recoil-ion tracker, and post-processor. The event generator assigns each particle an initial momentum according to three-body decay kinematics (including the Fermi function and radiative corrections) and initial position according to the atom distribution in the magneto-optical trap (MOT). It can also generate events according to ^{207}Bi decay or ^{90}Sr decay, or assign initial positions that are uniformly distributed over the whole chamber. These functions enable us to compare the simulated spectra with those from calibration runs and background runs. The β-particle tracker is a GEANT4 particle tracking program. The Goudsmit-Saunderson model is utilized to simulate multiple-scattering effects for the low-energy electrons. Energy depositions in detectors and the hit positions in the multi-wire proportional chamber (MWPC) are written to an output file. The ion-tracker module follows the ion position and velocity through the electric field to the micro-channel plate detector (MCP) with an adaptive Rungge-Kutta algorithm. The tracker uses an electric-field map generated by COMSOL for the chamber geometry and the applied voltages. Finally, the post-processor reads in the output files from the β-particle tracker and recoil-ion tracker, applies the detector-response functions, e.g. Gaussian broadening of the TOF according to the timing resolutions of the detectors, and writes the detector readings to a final event file. Each module has a command-line interface and can be configured through script files. The whole simulation can run on a computing cluster automatically with the assistance of several shell scripts.

The data-analysis program is designed to analyze data from both Monte Carlo simulation and experiment. It reads in event files and processes the data according to user-specified conditions, and fills histograms with the results. In order to construct TOF fitting templates, two simulations need to be done with $a = +1/3$ and $a = -1/3$ respectively. Then the data analysis program will fill the TOF spectrum for each case and save both as standard templates for fitting. A TOF spectrum from a third simulation or experiment can be fitted as a linear combination of these two templates and the coefficient a can be extracted. Besides the main data analyzer, a FASTER-to-ROOT format converter, a time-sliced histogram builder and

*Physics Division, Argonne National Laboratory, Argonne, IL.
†LPC-Caen, ENSICAEN, Université de Caen, Caen, France.
‡Paul Scherrer Institute, Villigen, Switzerland.
§Department of Physics and Astronomy and National Superconducting Cyclotron Laboratory, Michigan State University, East Lansing, MI.

several other calibration scripts have also been developed. They are used to generate a movie of the atom-loading process in the MOT and to monitor the stabilities of the detectors (Sec. 3.7).

The data analyzer also has several functions to study integrated systematic effects. In short, they plot the extracted a with respect to a change in some condition (like the photomultiplier threshold) or some simulation parameter (like the MOT position). We have been using these functions to study the systematic effects and the correlations between them. A summary of the sensitivity to the systematic effects of the 1% determination of a that have been studied so far is given in Table 3.4-1.

Systematic effect	Sensitivity
PMT Threshold	1.4% per 10 keV
PMT Resolution	<0.1% per 1% change in Res.
MWPC Threshold	<0.5% per 0.5 keV
MWPC Radius	0.5% per mm
MWPC Center	0.5% per mm
MCP Radius	2% per mm
MCP Center	0.5% per mm
MCP Position Resolution	0
MCP Efficiency	0
Electrode Voltage	.2% per V

Table 3.4-1. Sensitivity to selected systematic effects. a.

The Monte Carlo simulation and data-analysis programs are still ongoing projects. A careful comparison between calibration data and simulation is expected to be done within the year of 2014. More functions will be added to the data-analysis program and a more detailed detector-response functions will also be developed for the simulation program.

3.5 Limits on tensor-type weak currents from nuclear and neutron β decays

A. García, R. Hong, and F. Wauters

Recent data in nuclear[1] and neutron[2] decays, including a 5σ shift in the 2012 Particle Data Group's recommended value for the neutron lifetime[3], motivated a new evaluation of the limits on tensor currents from neutron and nuclear β decays[4]. In addition, the quark-level

[1]F. Wauters *et al.*, Phys. Rev. C **82**, 055502 (2010).

[2]D. Mund *et al.*, Phys. Rev. Lett. **110**, 172502 (2013) and M.P. Mendenhall *et al.*, Phys. Rev. C **87**, 032501(R) (2013).

[3]The Review of Particle Physics, J. Beringer *et al.* (Particle Data Group), Phys. Rev. D **86**, 010001 (2012).

[4]F. Wauters, A.García, and R. Hong, Phys. Rev. C **89**, 025501 (2014).

effective field theory framework of Battacharya et al.[1] and recent lattice QCD calculations of the nuclear form factors[1,2,3] allow for a direct comparison of the obtained limits to those from other low-energy probes and the LHC.

We follow the Jackson, Treiman, and Wyld[4] parameterization of the nuclear β decay Hamiltonian in terms of the coupling constants C_i and C_i' for each of the possible vector, axial-vector, tensor and scalar currents. We restrict our analysis to only left-handed components for the standard model currents, i.e. we assume $C_V = C_V'$ and $C_A = C_A'$ and concentrate on searching for non-zero values of $C_S,\ C_S'$ and $C_T,\ C_T'$, where interactions with $C_{S,T} = (-)C_{S,T}'$ couple to left(right)-handed neutrinos. Selecting the most sensitive data in nuclear and neutron decays[4], a 2-D χ^2 surface is constructed by stepping through different values of the two coupling constants of interest (C_T and C_T' or C_T and C_S), at each point minimizing the χ^2 relative to the remaining degrees of freedom. The confidence intervals are obtained by explicitly integrating the probability density surface (p.d.f.).

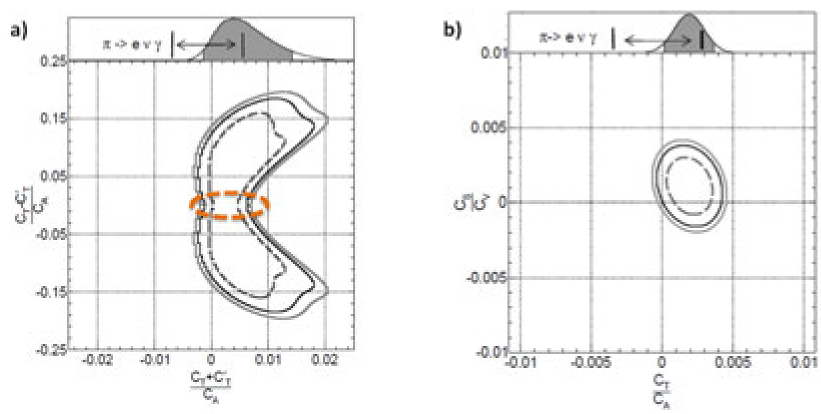

Figure 3.5-1. The 68%, 90%, and 95% confidence contours on scalar and tensor currents from neutron and nuclear β decays are in full agreement with the V-A model. The limits obtained are comparable to those from the radiative pion decay and the LHC (dashed ellipse in panel a).

The 2-D confidence contours are shown in Fig. 3.5-1. These are compared with the limits from radiative pion decay[5] and the LHC[1,6]. Projecting the p.d.f.'s, we find that $-0.14 \times 10^{-2} < (C_T + C_T')/C_A < 1.4 \times 10^{-2}$ and $-0.16 < (C_T - C_T')/C_A < 0.16$ (90% C.L.), while for the case $C_T = C_T'$ the limits are $0.0 \times 10^{-2} < C_T/C_A < 0.4 \times 10^{-2}$. The limits on $(C_T - C_T')$ are dominated by the old ^{6}He experiment of Johnson et al.[7], while those on $(C_T + C_T')$ mainly come from the relative polarization measurements of Carnoy et al.[8], the

[1] T. Bhattacharya *et al.*, Phys. Rev. D **85**, 054512 (2012).
[2] J. R. Green *et al.*, Phys. Rev. D **86**, 114509 (2012).
[3] M. Gonzalez-Alonso and J. Martin Camalich, Phys. Rev. Lett. **112**, 042501 (2014).
[4] J.D. Jackson, S.B. Treiman, and J. Wyld, Phys. Rev. **106**, 517 (1957).
[5] M. Bychkov *et al.*, Phys. Rev. Lett. **103**, 051802 (2009).
[6] V. Cirigliano, Martín González-Alonso, and M.L. Graesser, J. High Energ. Phys. **2013**, 46 (2013).
[7] C.H. Johnson, F. Pleasonton, and T.A. Carlson, Phys. Rev. **132**, 1149 (1963).
[8] A.S. Carnoy *et al.*, Phys. Rev. Lett. **65**, 3249 (1990).

neutron lifetime and the β-asymmetry parameter. At this point one should point out that, although neutron data dominate the limit on left-handed tensor currents, the experimental values for the neutron lifetime form an inconsistent dataset, as discussed by the Particle Data Group[3]. More recent data[1] disagree with the current recommended value of 880.0 $\pm$ 0.9 s.

We also investigated the sensitivity of future 10^{-3}-level correlation measurements. The ^{6}He experiment at CENPA aims is measuring the β-ν correlation of ^{6}He, an observable which is sensitive to the squares of the coupling constants $C_T^{(\prime)}$ and is linear sensitive a tensor interaction coupling to left-handed neutrino's

$$a_{\beta\nu,^6He} \simeq \Big(-\frac{1}{3}+\frac{1}{3}\frac{C_T^2+C_T'^2}{C_A^2}\Big)\Big(1-\langle\frac{m_e}{E}\rangle\frac{C_T+C_T'}{C_A}\Big), \tag{1}$$

with $\langle E\rangle$ the total energy of the β particle and m_e the electron mass. As can be seen in Fig. 3.5-2, a 0.1 % measurement of this parameter will dominate the limits on right-handed tensor couplings, and be as sensitive to left-handed couplings as all current nuclear and neutron decay data combined. An envisaged measurement of b_{Fierz} at the "$\sigma_{b_{Fierz}} = 0.001$" level (on ^{6}He here at CENPA, or on the neutron[2]) has significant discovery potential for left-handed tensor couplings, beyond the reach of future LHC data.

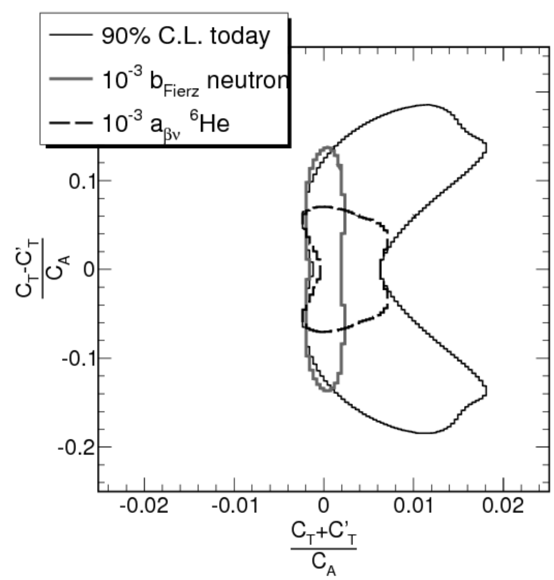

Figure 3.5-2. The projected limits including a future 0.1%-level correlation measurement in neutron or nuclear decays.

[1] A. T. Yue *et al.*, Phys. Rev. Lett. **111**, 222501 (2013).
[2] D. Pocanic *et al.*, arXiv:0810.0251.

3.6 A high-voltage divider for measuring shakeoff electrons from ^{6}He β decay

Y. S. Bagdasarova K. Bailey*, X. Fléchard†, A. García, R. Hong, A. Knecht‡, A. Leredde*, E. Liénard†, P. Müller*, O. Naviliat-Cuncic§, T. P. O'Connor*, M. G. Sternberg, J. Stock¶, D. W. Storm, H. E. Swanson, F. Wauters, and D. W. Zumwalt

The solid angle coverage of the β detector allows detection of approximately 1% of β particles emitted from trapped ^{6}He. Shakeoff electrons are emitted in $\sim$ 10% of β decays with relatively low energy as compared to the β particle. The average energy is on the order of 20 eV with an exponential tail extending to higher energies. The shakeoff electrons are emitted due to the sudden change in charge and momentum of the nucleus. If these shakeoff electrons can be detected with high efficiency in place of the β particles, it may be possible to use the shakeoff electrons to start the time-of-flight (TOF) clock and gain nearly a 10-fold increase in efficiency. Before these new data can be used, additional information on the energy spectrum of the shakeoff electrons is needed.

The primary challenge with this technique is that $\sim$ 3% of the emitted shakeoff electrons have an emission probability that is highly correlated with the energy of the recoil ion creating a nearly 6% systematic shift in the measured value of $a_{\beta\nu}$. In order to correct such systematic effects one must know precisely the energy spectrum of the electrons and the associated detection efficiency, including the spectrum and detection efficiency of the electrons that are highly correlated with the recoil-ion energy. Prior to using this technique to improve the efficiency of the recoil-TOF measurement, it is necessary to demonstrate our ability to measure and understand the shakeoff-electron spectrum. To do this we will perform a shakeoff-electron TOF measurement by reverse biasing the electrode stack in order to detect the shakeoff electron on the multichannel plate detector (MCP), as opposed to the positive recoil ion. From this we can deduce the shakeoff-electron energy spectrum.

To reverse-bias the electrode stack and achieve the desired potential in the chamber a high-voltage divider box was built (see Fig. 3.6-1). The box inputs a voltage of 6 kV and splits it up into increments of 1 kV (i.e. 6 kV, 5 kV, $\cdots$, 1 kV). It does this by passing the

*Physics Division, Argonne National Laboratory, Argonne, IL.
†LPC-Caen, ENSICAEN, Université de Caen, Caen, France.
‡Paul Scherrer Institute, Villigen, Switzerland.
§Department of Physics and Astronomy and National Superconducting Cyclotron Laboratory, Michigan State University, East Lansing, MI.
¶Arrived November, 2013, undergraduate research volunteer, University of Washington.

Figure 3.6-1. A high-voltage divider designed to reverse-bias the electrode stack in order to measure the shakeoff-electron energy spectrum.

current through a series of 2-MΩ resistors until it goes to ground. After each resistor is a connector used to drive the electrode voltages within the chamber. A measurement of the shakeoff-electron energy spectrum from ^{6}He is planned for the spring of 2014.

3.7 Detector development for the ^{6}He experiment

Y. S. Bagdasarova, K. Bailey*, X. Fléchard†, A. García, R. Hong, A. Knecht‡, A. Leredde*, E. Liénard†, P. Müller*, O. Naviliat-Cuncic§, T. P. O'Connor*, M. G. Sternberg, D. W. Storm, H. E. Swanson, F. Wauters, and D. W. Zumwalt

One major upgrade we have made to the β detector is making the light guide longer and wrapping it with multiple layers of Teflon tape. With the previous configuration, we discovered that the gain of the photo-multiplier tube (PMT) drops by more than 90% if the magnetic field of the magneto-optical trap (MOT2) was turned on. This indicates the residual magnetic field is large enough to disable the PMT. Though the gain of the PMT could be recovered by applying a compensation coil, this may introduce another source of instability. After changing to the longer light guide and wrapping it well, there is no obvious photon loss and the residual magnetic field only reduces the gain of the PMT within 8%. Also, an optical fiber was wrapped inside the Teflon layers so that external light pulses can be introduced to the PMT. We set up a gain-monitor system with a LED pulser. The light from the LED is

*Physics Division, Argonne National Laboratory, Argonne, IL.
†LPC-Caen, ENSICAEN, Université de Caen, Caen, France.
‡Paul Scherrer Institute, Villigen, Switzerland.
§Department of Physics and Astronomy and National Superconducting Cyclotron Laboratory, Michigan State University, East Lansing, MI.

sent to the PMT through the optical fiber and also to an internal photodiode. The driver voltage of the LED is stabilized by a NIM module, which maintains a constant output from the photodiode. We measured the photo diode signal and the PMT response and found both of them are stable at the 0.4% level over 15 hours.

The multi-wire proportional chamber (MWPC) was also maintained and optimized in 2013. The gas-handling system maintains a flow rate of 0.5 cfph and the anode board is stable at 2700 V without sparking. We also designed and built new amplifiers for its anode and cathodes. Similar amplifiers were used by the MuSun experiment for the time projection chamber and electron proportional chambers, and we modified the boards and adapted them to the ^{6}He experiment. In this configuration, the MWPC has over 95% detection efficiency of β particles from ^{90}Sr decay and a resolution of 1 mm is expected to be achieved in the central region.

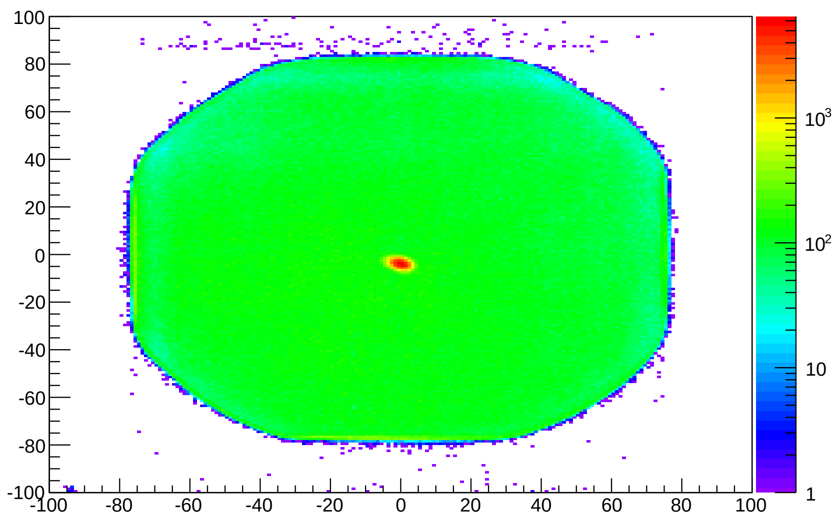

Figure 3.7-1. An image of trapped ^{6}He Penning ions on the MCP after four hours. The axes are labeled in terms of delay-line anode time differences (ns) which correspond to positions on the front plate (40 mm radius).

The electric-field systems for MOT2 were tested over the last year. A potential difference up to 27 kV was successfully applied across the electrodes inside MOT2 and sustained for 16 hours without sparking. With the 1.5 kV/cm electric field in place, we were able to image trapped ^{4}He on the micro-channel plates (MCPs) after ionizing the atoms with a nitrogen laser. We have also detected decay events from trapped ^{6}He in triple coincidence with the scintillator and MWPC over a background of untrapped decays at a rate of about 0.15 Hz for both. Fig. 3.7-1 shows the prominent hotspot formed by the trapped ^{6}He Penning ions on the MCPs during a four-hour run. In the next year, we plan to perform position calibrations for the MCPs using ^{4}He Penning ions as well as a calibration of the absolute field strength and a MOT-MCP distance measurement with photoionized ^{4}He.

4 Precision muon physics

4.1 Overview of the muon physics program

L. P. Alonzi, J. D. Crnkovic, M. Fertl, A. T. Fienberg, A. García, F. E. Gray*, N. S. Froemming, D. W. Hertzog, P. Kammel, J. Kaspar, M. H. Murray, D. J. Prindle, R. A. Ryan, M. W. Smith, H. E. Swanson, and F. Wauters

The Precision Muon Group is involved in fundamental experiments that determine Standard-Model parameters, low-energy effective-field-theory constants, or provide sensitive tests for new physics. With strong CENPA support, the group has grown considerably and, especially in the last year, has carried out a significant number of hardware development projects. The highlights from a very productive year are described in the series of articles that follow. Briefly, we note:

- In 2013 we published the final result of the *MuCap experiment*[1], which is a precision determination of g_P, the weak-pseudoscalar coupling of the proton. The result confirms a fundamental prediction of chiral perturbation theory. We have drafted a technical article about the hydrogen time-projection chamber (TPC) used in the experiment, which is close to submission, and are preparing a long paper about the experiment. Our sabbatical visitor F. Gray deserves credit for spearheading these efforts.

- The *MuSun experiment*, co-led by the UW group, aims to determine the muon capture rate in deuterium to 1.5 %. A well-measured $\mu^- + \mathrm{d} \rightarrow \nu_\mu + \mathrm{n} + \mathrm{n}$ process will provide a clean determination of the low-energy constant arising in the effective-field-theory description of the two-nucleon weak interaction, which is relevant for fundamental astrophysics reactions, such as *pp* fusion and the neutrino breakup reactions in the SNO experiment. Central to the experimental method is a high-resolution TPC, filled with ultrapure gaseous deuterium at cryogenic conditions, which serves as an active target. In 2013 our group significantly upgraded this novel device with the goal of reducing key systematic uncertainties. Several TPC components were replaced by high-Z materials, where stray muons are quickly captured to avoid long-lived background components. With the new grid design the nominal TPC high voltage (HV) was reached for the first time. New cryogenic preamplifiers were designed, tested and installed. They improved the resolution by a factor of 3, which enabled in-situ monitoring of gas impurities at the required part-per-billion level. The new set-up was used in a production run at the

*Visiting faculty, Regis University, Denver, CO.

[1] V. Andreev, *et al.* Phys. Rev. Lett. **110**, 012504 (2013).

Paul Scherrer Institute, which collected good data of limited statistics, due to unusual accelerator problems. A 3-month production run for 2014 was approved. For this run the UW group is preparing a final upgraded TPC, incorporating the experience gained in 2013.

- One of the strongest hints of new physics is the persistent difference between the measurement and Standard-Model prediction for the muon anomalous magnetic moment, $a_\mu = (g-2)/2$. Both are known to ~ 0.5-ppm precision. The current discrepancy $a_\mu(\mathrm{Exp} - \mathrm{Thy})$ exceeds 3 standard deviations and is suggestive, but not yet definitive, of new physics. We co-led the proposal to mount a next-generation muon $g-2$ experiment with a factor-of-4 improved overall precision goal. Fermilab E989 is approved, obtained CD-1 status in 2013, and the project is moving forward rapidly. The Brookhaven superconducting storage ring was dismantled and moved to Fermilab and a new custom building has been prepared. The UW group is involved in the simulation of muon injection into the storage ring, the refurbishment of hundreds of fixed NMR probes used to monitor the precision magnetic field, and the design and construction of the 24 calorimeter stations that will be used to measure the anomalous precession frequency. UW led a successful consortium NSF MRI proposal to support the equipment funds for six domestic universities that will build the detector, electronics, and data-acquisition systems for the precession frequency measurement. We also led a test-beam experiment at SLAC to evaluate the calorimeters and their readout system.

- The hadronic vacuum polarization contribution to a_μ has the largest "theoretical" uncertainty in the SM evaluation. It can be determined using exclusive $\mathrm{e}^+\mathrm{e}^-$ cross-section data and a dispersion relation; thus, the uncertainty is actually experimental. Crnkovic completed his Ph.D. in 2013 and continued to work with Kaspar and Hertzog to obtain final absolute cross-section results on the $\mathrm{e}^+\mathrm{e}^- \to \pi^+\pi^-\pi^0\gamma_{\mathrm{ISR}}$ channel. Here, γ_{ISR} is a hard, initial-state radiated photon that down-shifts the collision energy to permit the 3π cross section to be determined from threshold to above the J/ψ resonance. It is the first such effort using *Belle experiment* data and has required the development of many analysis tools and procedures. We are presently writing a paper summarizing the results.

- The *Mu2e experiment* will perform an ultra-sensitive test of charged-lepton flavor violation using the muon-to-electron conversion process. The smoking-gun signature is a monoenergetic ~ 105-MeV electron in the reaction $\mu^- \to \mathrm{e}^-$ (no neutrinos) in the field of a nucleus, such as aluminum. The branching-ratio sensitivity will be tested to the 10^{-16} level. The process is in competition with ordinary muonic nuclear capture, which can emit protons and neutrons that constitute background in the experiment. The *AlCap experiment* at PSI, led by Kammel, ran in late 2013 with the mission to measure the critical proton spectrum following atomic μ^-Al formation. The results are being analyzed.

$g-2$

4.2 Overview of the $g-2$ experiment

L. P. Alonzi, J. D. Crnkovic, A. García, F. E. Gray*, M. Fertl, A. T. Fienberg, N. S. Froemming, D. W. Hertzog, P. Kammel, J. Kaspar, G. J. Plunkett, M. W. Smith, H. E. Swanson, K. B. Wall

The anomalous magnetic moment of the muon, $a_\mu = (g-2)/2$, can be calculated and measured to sub-ppm precision. The comparison between theory and experiment continues to be one of the most sensitive challenges to the completeness of the Standard Model (SM). The E821 measurement at Brookhaven National Lab (BNL)[1] and the SM theory have uncertainties of 0.54 ppm and 0.42 ppm, respectively. The difference between experiment and theory (Exp − SM) is $(287 \pm 80) \times 10^{-11}$, or a $3.6\,\sigma$ significance[1,2,3]. The previous measurement is highly cited and the discrepancy generates considerable new physics speculation, from supersymmetry (SUSY) to Dark Photons and beyond. To this end we co-lead the development of a next-generation $g-2$ experiment (E989) which has been approved at Fermilab with a precision goal of 0.14 ppm.

The SM uncertainty is dominated by quantum loops involving hadrons, specifically the hadronic vacuum polarization (HVP) and the hadronic light-by-light (HLbL) scattering. The relative uncertainties are 0.35 ppm and 0.22 ppm, respectively. The HVP contribution is obtained from $\mathrm{e^+e^-} \to \mathrm{hadrons}$ cross sections. The optical theorem, cross-sections, and a dispersion relation are used to accurately determine a_μ(HVP). Low-energy cross sections are obtained from experiment and their uncertainty drives the overall error on the HVP contribution. A reduction to a relative uncertainty of ~ 0.25 ppm on the time scale of a new $g-2$ experiment is expected based on upcoming experiments. An update of our group's contribution to these measurements as described below (Sec. 4.8). Crnkovic and Kaspar have been putting final touches on an exhaustive analysis of the exclusive cross section $\mathrm{e^+e^-} \to \pi^+\pi^-\pi^0$ using the initial-state-radiation technique and the large data set from Belle. The HLbL scattering contribution, on the other hand, must be determined from low-energy QCD models or from Lattice QCD calculations; this relatively new approach is becoming a high priority in the lattice community.

The muon anomaly is proportional to the ratio ω_a/ω_p, where ω_a is the anomalous precession frequency of the muon spin in a magnetic field and ω_p is a measure of that average magnetic field carried out using proton nuclear magnetic resonance (NMR). Both frequencies must be determined to 0.1 ppm, including systematic uncertainties. The statistics required exceed those obtained at Brookhaven by a factor of 20 and the new experimental plan can realize this in 1.5 years of data taking. Our UW group is involved in both the ω_a and

*Visiting faculty, Regis University, Denver, CO.

[1]Muon g-2 Collaboration: G.W. Bennett *et al.*, Phys. Rev. D **73** 072003, (2006).
[2]K. Hagiwara *et al.*, J. Phys. **G38**, 085003 (2011).
[3]M. Davier *et al.*, Eur. Phys. J. **C71**, 1515 (2011).

ω_p measurements and we are carrying out systematic-uncertainty studies aimed at properly designing the required measurement hardware.

The E989 experiment has had a remarkably productive year in many aspects. Most notably, the delicate superconducting coils of the BNL storage ring were successfully transported to Fermilab. The highly publicized journey involved highway closures near the labs in New York and Chicago, and a long trip by barge and tug down the eastern seaboard, around Florida, and up through a series of rivers from the Gulf of Mexico to Lamont, IL. The rings arrived in August, 2013, to the welcoming of a huge crowd from the nearby community. Fig. 4.2-1a) shows the coils as they began the last overland leg of the journey in Illinois. Over the past 12 months, the MC-1 Building—“Muon Campus 1”—has been under construction and is about to be awarded beneficial occupancy, see Fig. 4.2-1b). This custom structure has a high degree of temperature and floor stability for the storage ring, dedicated counting and computer rooms, workspace, and necessary utility and cryogenic services. The ring re-assembly is expected to start shortly in the large bay area on the left side of the photo.

In the December, 2013, E989 received CD-1 approval, a major milestone for the project. Design and pre-construction activities have proceeded vigorously since that time with a CD-2/3A review scheduled to be held in late July. Based on the present schedule, the ring should be cold and ready for magnetic shimming in mid-2015, the detector systems would be installed about a year later, and beam into the experiment can be anticipated for late in 2016 or early 2017. In terms of management, Hertzog was re-elected Co-Spokesperson of the experiment, and Swanson is now co-leading the magnetic field team.

Figure 4.2-1. *Left:* Snapshot of the $g-2$ storage ring during the last phase of its journey from Brookhaven to Fermilab. The superconducting coils (shown) and supporting steel yokes and pole pieces, which were transported separately and by conventional carriers, are all now ready for assembly. *Right:* As of March, 2014, the MC-1 building is nearly complete. It will be the home of the new $g-2$ experiment.

While Fermilab is principally responsible for the reassembly of the storage ring and the extensive network of accelerator machines, target, and transfer beamlines to provide the muon beam, the external institutions are leading the development of the required upgraded suite of detectors and associated electronics and the magnetic-field mapping systems. The $g-2$ project work is organized in teams. At UW our large and diverse local group is working on the Ring, Field, and Detector teams.

The Washington group has had a commensurate highly successful year, starting off with obtaining a Major Research Instrumentation (MRI) award from NSF, where UW is the lead institution of a consortium of six domestic and one international partners. The MRI secures all the necessary capital funding for the detector, electronics and DAQ systems related to the measurement of the muon precession frequency, ω_a. For UW, this funding supports the purchase of all PbF_2 crystals, the SiPM readouts, the board fabrication and design, and the mechanical housing. It also partially supports a new senior position necessary to lead much of this intense development effort. Acting Assistant Professor Jarek Kaspar has taken on this key role having already led a test beam run at SLAC in November (Sec. 4.9), with data analyzed by graduate student Fienberg. Kaspar and CENPA engineer Van Wechel are developing and testing new SiPM summing boards (Sec. 4.4) that use next-generation Hamamatsu products. In early 2014, we completed the contract for the purchase of 1055 (our share of the 1325) PbF_2 crystals from the Shanghai SICCAS High Technology Corp. Graduate student Froemming and postdoc Alonzi devoted most of their efforts to simulations that are informing the final design of the beam injection hardware (Sec. 4.7), and the detector gain stability (Sec. 4.5), respectively.

Swanson and Garcia have led a group of students (Smith, Morris), and postdoc Fertl, in several tasks related to the precision field (Sec. 4.3). UW is responsible for repairing, upgrading, and/or replacing the $\sim$ 400 fixed NMR probes that are used to continuously monitor the magnetic field, and we are in charge of the separate DAQ readout of these and other NMR probes in the system (Sec. 4.6). Locally, a large-area dipole was repurposed at CENPA to work as a $g-2$ test magnet. It now has a suitably uniform field of 1.45 T, which is required to test the NMR probes. It is also being used to certify the selection of materials—connectors, chips, capacitors, boards, SiPMs, etc.—that will be located within close proximity to the precision field (Sec. 4.12).

4.3 Progress overview of the UW field team for the muon $g-2$ experiment

M. Fertl, A. García, I. S. Guinn, C. Helling, R. Morris, R. Ortez, R. E. Osofsky, E. A. Shaw, M. W. Smith, R. Morris, and H. E. Swanson

The UW $g-2$ field team is working towards restoring and upgrading the nuclear magnetic resonance (NMR) field-measurement system for the muon storage ring at FermiLab. This system consists of several hundred individual probes, multiplexers to digitally select the probes, pulse amplifiers to excite the NMR resonance and heterodyne receivers to amplify and mix down the free induction decay (FID) signals to a suitable range for the data-acquisition system. We have assembled a small subset of the electronics modules into a working NMR instrument for verifying the operation of the probes. FID waveforms are read out with a digital oscilloscope and downloaded into a computer for frequency extraction (Sec. 4.11). We have developed algorithms for obtaining frequencies from these waveforms which exceed the precision required by the experiment.

The UW test magnet has been operating at 1.45 Tesla for most of the past year. Its field is sufficiently homogeneous to produce FIDs as long as 4 milliseconds with no additional shimming. In addition we have made probe holders with opposing Helmholtz fields to cancel linear gradients and these can achieve 10-ms-long decays. The overall stability of the field is only a few hundred ppm over a few minutes. However the difference in frequency between two independent probes read simultaneously is stable to sub-ppm which allows us to measure susceptibilities of materials destined to be placed within the field of the storage ring. An example showing this capability is discussed in a following article (Sec. 4.12).

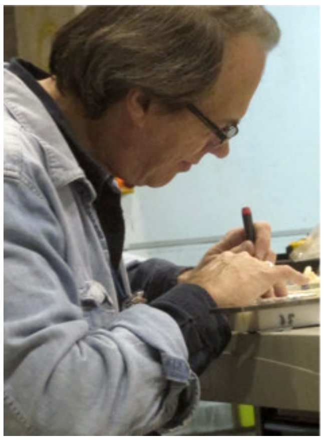

Figure 4.10-1. *Left:* Dave Hertzog improves a prototype $g-2$ calorimeter during a test run at SLAC. *Right:* Erik Swanson checks the UW test magnet containing refurbished NMR probes.

The probes contain an ensemble of protons either from water or petroleum jelly and a tuned coil to excite and detect their free induction decay. We tested over 230 probes used in BNL E821 (the previous $g-2$ experiment). The testing process consisted of inserting the probes into the UW test magnet field and adjusting the magnet current and position of the probe to maximize the amplitude and decay time of the FID signal (Sec. 4.6). These were recorded and formed the basis for comparison in determining the quality of the probes.

Of those tested, 70 provided no signal, indicating either a broken component or evaporation of the sample in the case of water. A subset of probes had shorter coils which gave them less sensitivity to field gradients but a smaller signal as well. Many of the remaining probes had signals that varied as the cable was flexed since the conducting epoxy used in the connections had deteriorated. All in all there were about 100 probes that worked well and these were set aside to be refurbished after non-functioning probes are made operational.

In addition to the above go-no-go tests additional diagnostics were performed on probes considered marginal. The first of these was visual inspection which turned up broken connections and in some cases corrosion from the leaking water sample volume. Others concentrated more on the electronic properties such as inductance, capacitance and Q of the resonant circuit. Our goal was to determine baseline values that would be used when re-building non-working probes and help us understand why probes failed. Measurements used a variety of instruments including a benchtop inductance, capacitance, and resistance (LCR) meter, multimeter, vector impedance meter and a network analyzer. The network analyzer is used to tune the refurbished probe's circuit resonance and impedance as part of our refurbishing procedure.

We have started work on the data-acquisition system (DAQ) for the upcoming $g-2$ experiment. It uses a modern PC, a Struck PCIe (PCI express) interface to a VME crate, and Struck VME waveform digitizers for FID signals. Acquisition software uses the MIDAS framework which is compatible with other DAQ systems in the collaboration. Our frequency extraction algorithms are easily adapted to this framework. A working group has been formed within the collaboration to standardize software versions and share expertise among the community.

4.4 PbF_2 calorimeter with SiPM readout

L. P. Alonzi, A. T. Fienberg, G. C. Harper, D. W. Hertzog, J. Kaspar, D. A. Peterson, G. J. Plunkett, M. W. Smith, T. D. Van Wechel, K. B. Wall, and K. Yai*

After a muon decays into a positron and a neutrino, the positron does not have sufficient energy to fly along the magic orbit in the ring. It curls inward where a *lead fluoride calorimeter*, read out by silicon photo-multipliers (SiPMs), waits for it to report on its energy and the hit time. This year the design of the SiPM readout board was finished, and SiPM candidates were cut down to two finalists. A prototype calorimeter dark-box performed very well during a calorimeter test run at SLAC. Data-analysis techniques were developed to process positron hits and laser calibration data. Finally, systematics studies provided essential feedback to finalize calorimeter design.

Silicon photo-multipliers collect the Čerenkov photons emitted by a positron stopping in lead fluoride. Their operation is not disturbed by strong magnetic fields, their performance can be flexibly fine-tuned to match experiment needs, and dynamic range spans from single counts to many thousands of hits. A preamplifier board designed by CENPA engineers delivers very fast pulses in the couple-of-nsec range to guarantee excellent pulse separation, stellar pulse fidelity, and optimal signal-to-noise ratio. The charge delivered by the SiPM is processed by a two-stage amplifier. The first stage serves as an adder, and is designed around a current-feedback amplifier, because any shunt resistor significantly deteriorates pulse shape. The second stage is a fully differential amplifier that feeds a twinax cable with a $2\,V_{pp}$ signal which maximizes signal-to-noise ratio, and exhibits excellent noise reduction at the same time. Individual electronics components were tested in a 1.5-T magnetic field to verify they will not affect the high quality magnetic field in the $g-2$ ring (Sec. 4.12). It has been a very good year for SiPM development. The CENPA preamplifier board in many aspects transcends the $g-2$ design.

Lead fluoride crystals and SiPMs are housed in a temperature-controlled *calorimeter box.* A cooling concept based on pressurized chilled and dried air blowing directly on the SiPM boards was successfully tested this year. The light-tight box is being designed without any feedthroughs to avoid even the slightest impedance mismatch in cable junctions. Twinax signal cables pass through a chicane in the box wall to maximize noise suppression. The calorimeter box sits on a chariot that runs on rails. Base plates and the rails were inherited from the previous experiment at Brookhaven National Laboratory (BNL). CENPA engineers

*Osaka University Graduate School of Science, Japan.

are designing a chariot which will also house an electronics rack holding custom digitizers and SiPM bias power supplies. The temperature-controlled box is a key to SiPM gain and energy-scale stability.

SiPM gain stability is a major contributor to the experiment systematics and a *laser calibration system* will mitigate this problem. While the calibration system is under development in Italy, a mock-up system has been in use for calorimeter development. It consists of a PicoQuant diode laser at 407 nm, a passive splitter box, and optical fibers feeding laser shots directly into the front face of the crystals. Dedicated laser runs calibrate the energy scale, and shots fired within a run monitor gain stability. The data-analysis technique based on statistical properties of the laser-light was demonstrated to successfully extract the effective number of SiPM pixels fired from digitized traces, and to correct for background noise leakage into light width as well as possibly disentangle laser fluctuations from the intrinsic SiPM response. Proceeding towards a prototype of the final laser system, our group will evaluate dedicated statistical tests to judge calorimeter performance and stability, determining which test will become part of the data-quality decision logic.

The quality of our calorimeter design was thoroughly tested during a *test run at SLAC* (Fig. 4.4-1). Newly developed SiPM readout boards were compared to well-understood PMTs from the MuLan experiment. Details of the test run are covered in a dedicated report (Sec. 4.9). We measured the light yield of the lead fluoride crystals, tested the on-board temperature sensors AD7420, demonstrated the temperature stability of the calorimeter box, and also learned practical lessons in calorimeter operation.

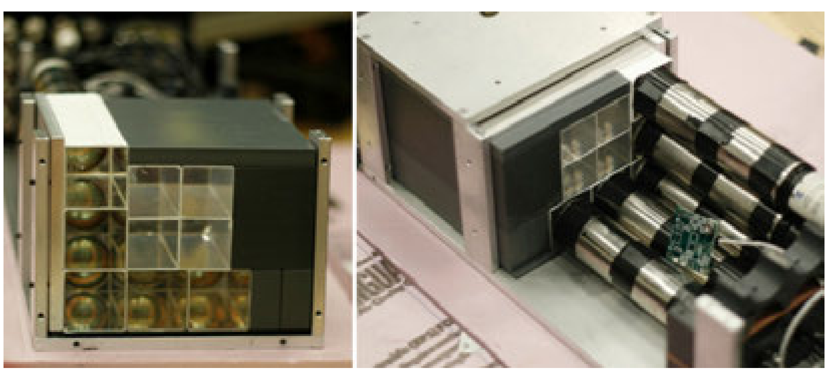

Figure 4.4-1. A calorimeter testbox was used at SLAC to measure the light yield of lead fluoride, and to better understand the SiPM photo-efficiency. A direct comparison between PMT's and SiPM's hit by identical electron beam proved that our design meets $g-2$ requirements.

Several *data-analysis techniques* were developed and tested to successfully process the SLAC data files. New parametric methods are in use in parallel with the pulse-shape template-matching procedures that the previous $g-2$ experiment relied on. In general, answers provided by the different approaches are in good agreement. The new parametric methods handle varying Čerenkov light profiles independently from the static device response. The probability density functions mined from data for two light profiles (an electron beam hit and a laser shot), and two devices (a PMT and a SiPM) are in excellent agreement with simulated predictions. The data analysis keeps evolving to deal with larger data sets and to correct for involved systematic effects.

Both statistical and systematic uncertainties contribute about equally to the $g-2$ result. *Systematic studies* finished this year included an étude on double-pulse resolution and bulk recovery time, and classical pieces on crystal wrapping and optical coupling. The well understood double-pulse stability of the SiPM board provided essential feedback to design more robust op-amp setup. The SiPM bulk recovery time (from a temporary bias-voltage drop) was studied and then mitigated by better preamp board design. As for crystal wrapping, more reflective wrapping increases the number of photons registered by the SiPMs, but the extra photons tend to arrive at later times and undergo more complex optical processes on the PbF_2–air–wrapping boundary that need to be corrected for. Cosmic muons are a useful tool for such a study because they mimic positron hits with an effective energy of 240 MeV. Various optical greases coupling SiPMs to the PbF_2 crystals were tested to maximize the number of detected photons (Sec. 4.10). Our next systematic studies will cross the calorimeter boundary and look at interferences between larger blocks, e.g., the laser calibration system and slow control.

Our calorimeter design is mostly finished. The baseline design will be formalized in the $g-2$ technical design report, and the chariot design will be turned into proper drawings. The SiPM performance will be further improved. In summer, 2014, a prototype calorimeter box housing an 5x5 array of crystals and SiPMs will travel to SLAC for next test run. The goal is demonstrate SiPM performance with the proper high-voltage-bias power supply, 5-channel digitizers in a custom-made μTCA crate, and a prototype of the laser calibration system.

4.5 Software developments and systematic error studies

L. P. Alonzi, A. T. Fienberg, F. E. Gray*, and D. W. Hertzog

This year has involved a major change for the $g-2$ software. We have fully integrated our system into Fermilab's preferred software framework, *ART*[1]. This framework is modular and encompasses everything from GEANT4 simulation to offline analysis. One feature of the framework is the ease of deployment via the CernVM File System (CVMFS)[2]. Due to the CVMFS system we were able to set up our software locally on a cluster at CENPA using 10 lines of code in a bash script. This system makes it easy for new collaborators to contribute.

One of the first tasks we explored was the visualization of the simulated geometry. For this test we implemented a simple muon-decay particle generator and tracked the decay positrons until they struck a calorimeter. Fig. 4.5-1 shows the output of a few selected events.

Building on these simulations we established a connection to the statistical and systematic error budget for the ω_a measurement. First the statistical precision of the simulation was

*Visiting faculty, Regis University, Denver, CO.

[1]See `https://sharepoint.fnal.gov/project/ArtDoc-Pub/SitePages/Support.aspx`.
[2]See `http://cernvm.cern.ch/portal/filesystem`.

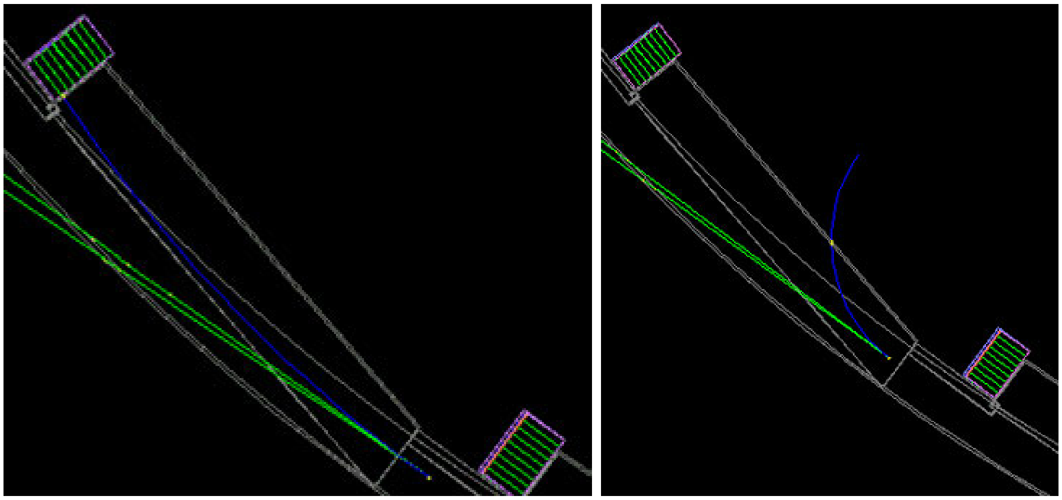

Figure 4.5-1. Two muon-decay events $\mu \rightarrow e^{+}\nu_{e}\overline{\nu}_{\mu}$ are shown, as rendered by GEANT4. The blue (green) line represents the decay positron (neutrino). The left panel shows a high-energy electron (as seen by the large bending radius). The other panel is a lower-energy electron where the bending radius is small enough for the positron to bend in between the calorimeters. The simulation stops once the positron leaves the relevant region or hits the boundary of the calorimeter. The termination criteria are fully configurable.

evaluated and then systematic effects were added. The analysis hinges on fitting a histogram containing the time spectrum of the analyzed events. That distribution can take the following form,

$$N_0 \cdot \exp\left(-t/\tau_\mu \gamma\right) \cdot \left[1 + A\cos\left(\omega_a t + \phi\right)\right]. \qquad (1)$$

The parameters N_0, A, and ϕ are all dependent on the decay-positron energy. The time from the start of the fill is t, the muon lifetime is τ_μ, and the Lorentz boost is γ.

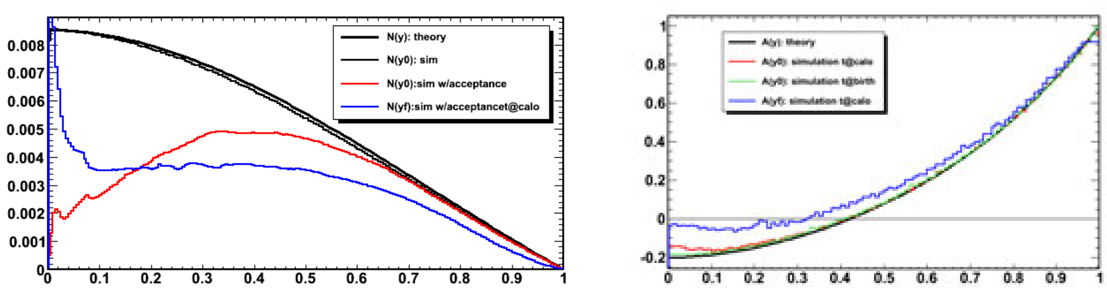

Figure 4.5-2. *Left:* The energy (y) distribution of decay positrons is shown as the theoretical boosted Michel spectrum (smooth black), the positron energy at a decay vertex for realistic beam parameters (black), the energy distribution of the decay positrons y_0 accepted by the detector (red), and the energy deposited into a calorimeter y_f (blue). *Right:* The asymmetry function, A, shows the correlation between the muon spin direction and the decay positron energy (y) in the lab frame. Higher-energy positrons are more strongly correlated with the muon spin and are prioritized in the experimental design and analysis. The horizontal scale is different for each curve and indicated in the legend.

To that end a parameterized simulation technique was developed whereby simulated distributions were parameterized and used to seed a theoretical simulation. Fig. 4.5-2 and Fig. 4.5-3 show the distributions extracted from the simulated data set as a function of the positron energy in the lab frame.

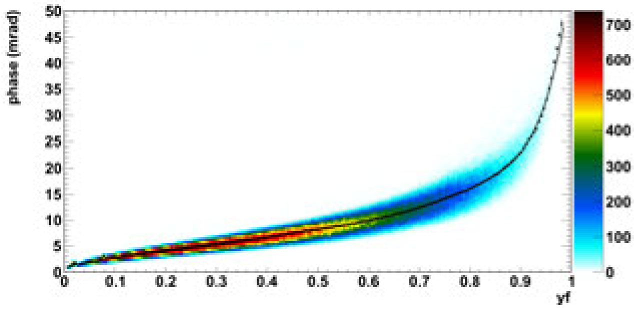

Figure 4.5-3. Positrons of different energy, y, carry a different phase *as measured by the calorimeters* due to different drift times. This plot shows a 2D histogram of the phase shift as a function of the energy measured by the calorimeter y_f. The data points are the profile of the histogram.

Previous work on the statistical power of the $g-2$ experiment technique was limited to a theoretical paper[1]. This paper rigorously treated technique but was unable to account for the acceptance of the detectors, which is a critical feature of the hardware design. With this new simulation we were able to simulate the detector acceptance and recalculate the figure of merit (FOM) for the statistical power of the experiment. Fig. 4.5-4, left panel, shows the FOM for various analysis techniques including the effect of detector acceptance.

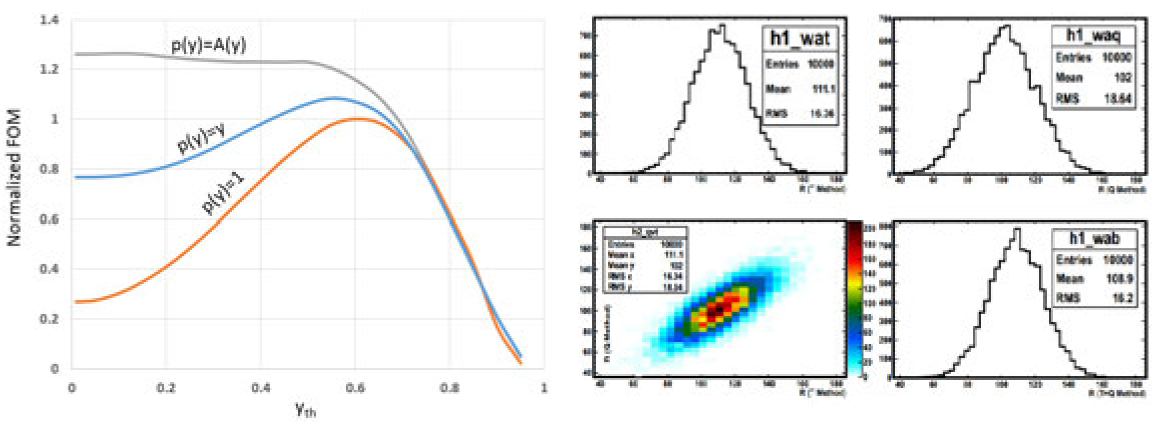

Figure 4.5-4. *Left:* The statistical FOM for different $y_{\rm th}$ event-weighting methods, $p(y)$, is given as a function of analysis positron energy threshold. Using the function $p(y)=1$, as in the T method, maximizes the FOM at a threshold of $y_{\rm th} \approx 0.6$. Weights based on the positron energy can improve the statistical reach of the experiment as shown by the other curves. *Right:* Bootstrap estimate of $\omega_{a;T}$ (upper left), $\omega_{a;Q}$ (upper right), and $\omega_{a;T\oplus Q}$ (lower right). A correlation plot of $\omega_{a;Q}$ versus $\omega_{a;T}$ is shown at lower left.

[1]Muon g-2 Collaboration: G.W. Bennett *et al.*, Nucl. Instrum. Meth. **A579** 1096-1116, (2007).

The next step was to evaluate the improvement in statistical reach by performing a simultaneous analysis using multiple techniques. To study this question we developed a bootstrap simulation[1]. This technique has been used to determine the improvement from a simultaneous analysis of the T and Q methods. The simulated correlation between the two analysis techniques is 0.788 and corresponds to a 1.5% improvement in the statistical reach of the experiment. That result is shown graphically in Fig. 4.5-4, right panel.

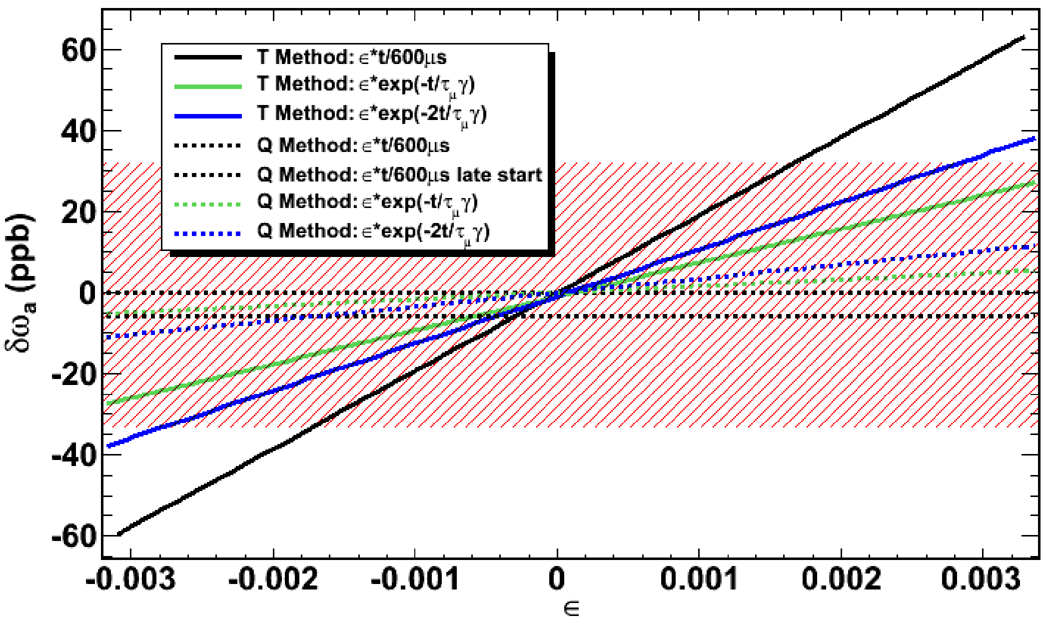

Figure 4.5-5. This plot summarizes the effect of a gain perturbation on the final result of the ω_a measurement. The horizontal axis represents the size of the perturbation with the form of the perturbation shown in the legend. The vertical scale is the change in ω_a in the final result. The cross-hatched region represents the error budget for this systematic effect (30 ppb).

Having firmly established the statistical baseline of our simulation we extended the parameterized simulation to study systematic perturbations in the gain of the calorimeter. To do so we divided the data set into energy slices each about 1.5 MeV. For each slice we prepared the characteristic time spectrum with appropriate statistical fluctuations. That data set is then reduced into the standard final histogram and fit to extract the value of ω_a. We then repeated the process with identical data but introducing a systematic gain shift in the reduction step. The perturbed value of ω_a is extracted and compared to the unperturbed value. The difference between the values is reported in terms of parts per billion (ppb). Fig. 4.5-5 summarizes the results of several different gain perturbations. Based on this study and work from our Italian collaborators we believe we will reach the desired systematic sensitivity laid out in the error budget.

[1] B. Efron and R. J. Tibshirani, An Introduction to the Bootstrap, Chapman & Hall. 1993.

4.6 Further development of the stationary proton nuclear magnetic resonance array for the muon $g-2$ experiment

M. Fertl, A. García, I. S. Guinn, C. Helling, R. Morris, R. Ortez, R. E. Osofsky, E. A. Shaw, M. W. Smith, and H. E. Swanson

A successful measurement of the muon anomalous magnetic moment, $a_\mu = (g-2)/2$, crucially relies on a precise knowledge of the magnetic-field distribution seen by the muons orbiting in the storage ring. While this distribution can be measured with a special magnetic-field mapper several times a week, this trolley has to be retracted into its storage position during muon operation. To track changes of the magnetic field between trolley measurements a stationary array of pulsed proton nuclear magnetic resonance (pNMR) probes is distributed along the outside of the storage ring's vacuum chamber. The magnetic-field team at CENPA has taken the responsibility of refurbishing the pNMR probes, which have formerly been employed in the BNL E821 experiment[1], for their use in the new $g-2$ experiment.

The pNMR probes consist of a serial resonant LC circuit (probe body) inside a cylindrical aluminum shell that acts as one of the electrodes of a capacitor. A solenoid (serial inductor) is wound on a PTFE cylinder, containing the proton sample volume, to excite and pick up the free induction decay (FID) signal. The circuit's resonance frequency is tuned by varying the position of a second PTFE dielectric on the threaded inner conductor of the cylindrical capacitor. A smaller short coil (parallel inductor) is used to match the impedance of the signal cable and the LC circuit. The outer aluminum tube is capped off at the far end of the probe.

About 320 pNMR probes have been checked for functionality in a dedicated test magnet setup at CENPA, see Fig. 4.6-1. Approximately 100 of them were found to perform well while the rest of the probes suffer from at least one of the following difficulties:

- Poor electrical connection between signal cable and pNMR probe body.
- Poor electrical connection between subcomponents of the pNMR probe body.
- Electrical connections broken when opening the pNMR probe for inspection or tuning.
- Water-sample leaks leading to corrosion of the aluminum shell of the probe.

To decide on the best way to refurbish the broken pNMR probes several prototypes based on the original design of the pNMR probes have been built. To resolve the mechanical difficulties, a crimp-type connection between the signal cable and the pNMR probe body has been successfully tested and can replace the conducting-epoxy glue joint used previously. Besides making a low-resistance connection of the cable braid to the outer aluminum shell of the pNMR probe, the crimp connection provides strain relief by including the cable jacket. This increases the mechanical stability of the probes. The crimp approach also proved to be effective in connecting the parallel inductor to the shell of the pNMR probe, again replacing

[1] G. W. Bennett *et al.*, Phys. Rev. D **73**, 072003 (2006).

a conducting-epoxy glue joint. A flux-free soldering procedure based on ultrasound proved useful to connect the inner conductor of the capacitor (made from aluminum) to the serial solenoid. The ultrasonic waves break up the hard oxide layer on the aluminum surface and yield a reliable electrical connection without corroding agents.

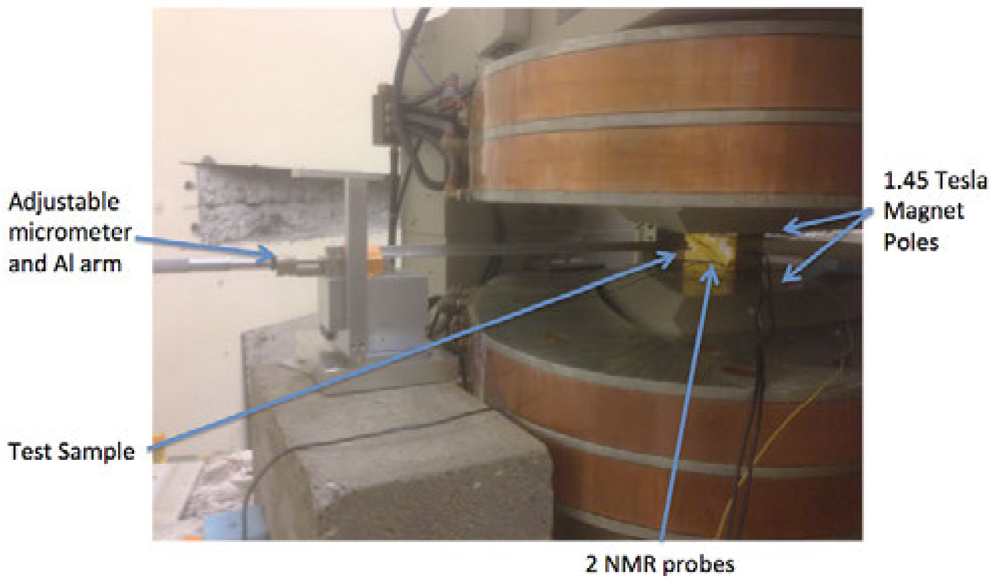

Figure 4.6-1. An analyzer magnet from one of the former CENPA accelerator beam lines serves as a dedicated test setup for the pNMR probes. The magnetic field is 1.45 T, the same as in the $g-2$ ring. Within the magnet pNMR probes are tested for functionality and investigations of different systematic effects can be performed.

To tune the resonant circuit to the frequency of the FID signal (61.74 MHz) the capacitor has to be adjusted. In the former design this involved the repeated removal and installation of the probe's aluminum shell to access the PTFE dielectric. We found that this frequently resulted in the breaking of electrical connections. Milling a slot in the end face of the PTFE cylinder avoids this difficulty. The assembled probe can be frequency-tuned by rotating the PTFE piece inside the aluminum shell with a special tool as shown in Fig. 4.6-2. This allows for easy and reliable tuning without mechanical stress on the pNMR probe body.

In many of the original pNMR probes a mixture of distilled water and copper sulfate was used as a proton sample. Over the course of time the pNMR probes lose their signal due to the evaporation of the water proton sample, and the Cu ions (used to adjust the proton spin-relaxation time) support corrosion of the aluminum shell of the probe. This renders removing the aluminum sleeve very difficult, often breaking the probe as a result.

As an alternative proton sample, petroleum jelly was chosen for its comparable relaxation times and signal strength. More importantly it will not evaporate, greatly extending the overall lifetime of the probe. In order to properly fill the PTFE piece holding the sample, it is, however, necessary to melt the petroleum jelly. To transfer the liquid jelly to the PTFE piece a heated syringe is used to ensure that the jelly remains liquid throughout the process. A hot-air gun is used to heat the PTFE piece holding the proton sample. The hot-air gun keeps the PTFE piece warm enough to maintain a liquid jelly after the transfer, which is important to allow air bubbles, potentially formed during the transfer process, to escape from the sample volume. Gently tapping the encasing PTFE piece accelerates the bubbles' escape. This method allows a consistent uniform filling of the pNMR probes with petroleum jelly.

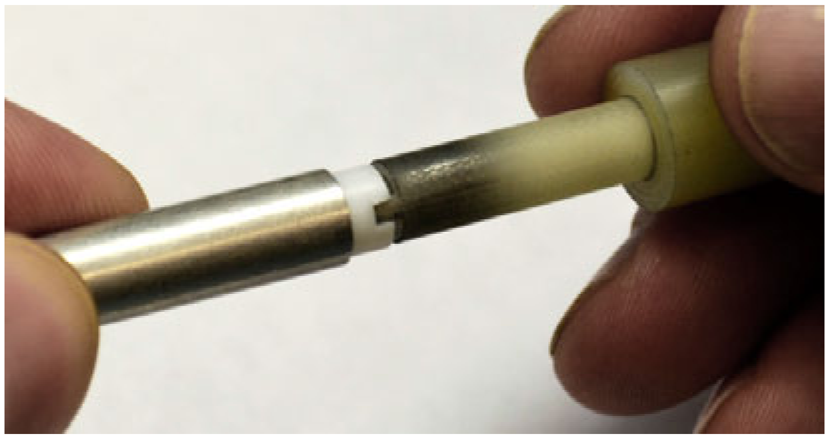

Figure 4.6-2. Tuning of the pNMR probe by screwing the Teflon dielectric in place. A slot was milled in the end face of the Teflon dielectric that can accommodate an adapted screwdriver. Thus the dielectric can be turned inside the probe's aluminum shell.

Changing the proton sample from water to petroleum jelly raises the important question of possible temperature-dependent effects on the spin precession frequency. The diamagnetic shielding effect is well known for water and was taken into account in the last $g-2$ experiment. This triggered measurements to further investigate the differences between the probes filled with a water sample and with a petroleum jelly sample. To do so we built means of heating pNMR probes inside the test magnet. Using a two-channel data-acquisition system allowed us to record the signals of two probes simultaneously. In addition, a Helmholtz coil used for local shimming provided sufficiently long free induction decay signals for the study. The tests to directly compare the influence of temperature on the two types of probes have been performed, but the study is ongoing.

4.7 Optimizing injection efficiency

N. S. Froemming, D. W. Hertzog, and D. L. Rubin*

When muons exit the superconducting inflector magnet and enter the $g-2$ storage ring, they are displaced from the desired orbit by 77 mm. Due to the high uniformity of the ring's magnetic field, injected muons execute uniform circular motion. However, the center of the circle is displaced 77 mm relative to the center of the ring. If this offset is not compensated for, muons will attempt to re-enter the superconducting inflector magnet/cryostat at the end of the first turn, and will be lost. Therefore, an orbit correction must be applied within the first turn if muons are to be stored.

*Cornell University, Ithaca, NY.

The ideal location to apply this orbit correction occurs when the injection orbit first crosses the storage-ring orbit, namely at about 90° downstream. In this region, muons receive a ∼10.8-mrad kick radially outward from a series of pulsed electromagnets, or "kickers," in order to be placed on orbit. The design/effectiveness of the kickers plays a central role in muon-injection efficiency overall, and hence in the experiment. Additionally, muon storage rates and stored beam quality are complicated functions of the input phase-space parameters, the electromagnetic fields experienced by incident muons both inside and outside the ring, the effects of multiple scattering and energy loss in materials traversed during injection, apertures, and several other important factors.

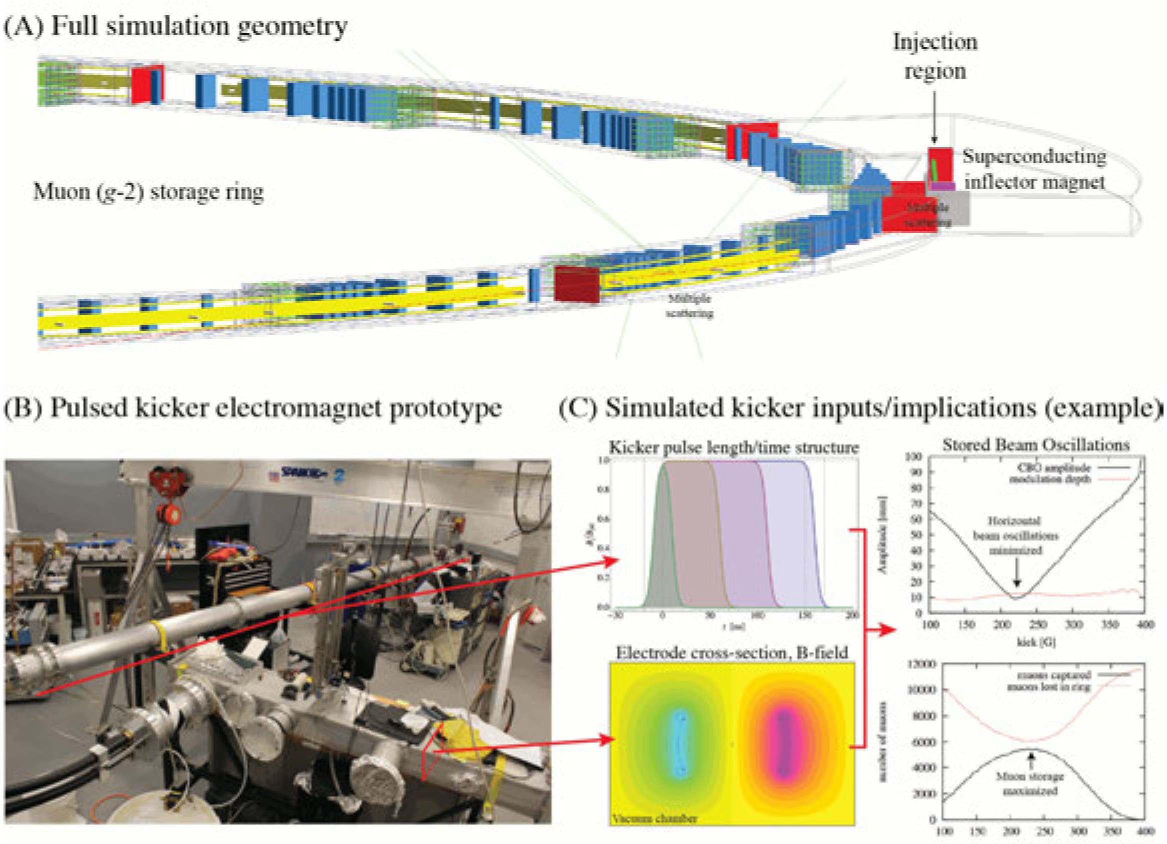

Figure 4.7-1. Muon injection studies. See text for discussion.

The UW group has emerged as a leader in developing/implementing simulation tools that allow various injection schemes to quickly be investigated and optimized. These tools have been developed in close conjunction with Cornell University in Ithaca, NY, with the specific aim of optimizing the kickers and muon injection into the $g-2$ storage ring. A custom particle-tracking simulation tool similar to the one shown in Fig. 4.7-1A (also developed by this author) has been written using Cornell's BMAD library for relativistic charged-particle simulations, and this tool has been used extensively to perform various injection, kicker, and beam-dynamics studies quickly. An example prototype kicker magnet built at Cornell is shown in Fig. 4.7-1B. The kicker parameters serve as inputs to the simulation, as shown in Fig. 4.7-1C. The results of the simulation, some of which are also shown in Fig. 4.7-1C, are then used to assess muon storage efficiency, beam dynamics, and a host of other important quantities. Many studies have been performed in the past, the results of which have guided the design of the muon $g-2$ experiment. More studies will be performed in the future, and the University of Washington will continue to play a leading role.

4.8 Contribution to the muon anomalous magnetic moment from Belle cross section measurements

J. D. Crnkovic, D. W. Hertzog, and J. Kaspar

Cross-section measurements for electron-positron (e^+e^-) annihilation to hadronic final states have several motivations, centering on the non-perturbative nature of Quantum Chromodynamics (QCD). These measurements are a basic element in the study of hadron spectroscopy, providing checks for the development of QCD models, and are used in the calculation of the leading-order Hadronic Vacuum Polarization (LO HVP) contributions to the muon anomalous magnetic moment (a_μ) and the running of alpha ($\alpha(s)$).

Contribution	Absolute Value ($\times 10^{-11}$)	Absolute Error ($\times 10^{-11}$)	Relative Value (%)	Relative Error (%)
QED	116584718.95	0.08	99.993924	0.0003
EW	153.6	1.0	0.000132	0.0410
LO HAD	6923	**42**	0.005938	**72.2653**
NLO HAD	7	26	0.000006	27.6935
TOTAL	116591803	49	100	100

Table 4.8-1. Value and error contributions to the SM prediction of a_μ: Quantum Electrodynamics (QED), Electroweak (EW), next-to-leading-order hadronic (LO HAD), and next-to-order hadronic (NLO HAD). The LO HAD corresponds to the LO HVP contribution, where this result only includes e^+e^- cross sections. The NLO HAD contribution error is dominated by the hadronic light-by-light component.

There is approximately a $3.6\,\sigma$ difference[1] between the world average measurement of a_μ and the SM prediction when exclusively using the e^+e^- cross sections to calculate the LO HVP contribution. Table 4.8-1 shows that the LO HVP contribution is the dominant source of error for the SM prediction of a_μ. The hadronic light-by-light (HLbL) contribution is the second-largest source of error, but this next-to-leading order contribution cannot be directly calculated from measurements.

[1] J. Beringer *et al.* (Particle Data Group), PR **D86**, 010001 (2012) and 2013 update for the 2014 edition (URL: `http://pdg.lbl.gov`).

The a_μ LO HVP contribution is calculated in terms of the e^+e^- cross section measurements via dispersion relations and the optical theorem[1]. The optical theorem relates the imaginary part of the HVP diagram amplitude to the total inclusive cross section of e^+e^- annihilation to hadronic final states. Exclusive cross section measurements are typically made due to experimental limitations, whereby the total inclusive cross section is obtained by summing the individual exclusive cross section measurements. The dispersion integral[1] used to calculate the a_μ LO HVP contribution may be written as,

$$a_\mu^{\text{LO HVP}} = \left(\frac{\alpha m_\mu}{3\pi}\right)^2 \left(\int_{m_{\pi^0}^2}^{E_{\text{cut}}^2} ds \frac{R_{\text{had}}^{\text{data}}(s)\hat{K}(s)}{s^2} + \int_{E_{\text{cut}}^2}^{\infty} ds \frac{R_{\text{had}}^{\text{pQCD}}(s)\hat{K}(s)}{s^2}\right). \tag{1}$$

Here α is the fine structure constant, m_μ is the muon mass, E_{cut} is the energy cutoff where perturbative Quantum Chromodynamics (pQCD) may be used instead of measurements, and m_{π^0} is the neutral pion mass; $\hat{K}(s)$ is a well know integral kernel function that is approximately 0.63 at the pion threshold and asymptotically approaches 1 as s goes to infinity. $R_{\text{had}}(s)$ is the bare (undressed) e^+e^- hadronic inclusive cross section normalized to $\frac{4\pi\alpha(s)^2}{3s}$ (approximated by the tree-level e^+e^- muon-pair production cross section). The $\frac{1}{s^2}$ factor in the integrals from Eq. (1) indicates that the low-energy cross sections (below 3 GeV) are weighted the most in the calculation of the a_μ LO HVP contribution.

The Belle experiment operated at the KEK High Energy Accelerator Research Organization in Tsukuba, Japan. The Belle detector[2] took data at the KEK B-factory, which is an asymmetrical fixed-energy e^+e^- collider that operated at approximately 11.5 GeV in the lab frame: using a 3.5-GeV positron beam, an 8-GeV electron beam, and a 22-mrad crossing angle. The detector was constructed to study CP violation in B-physics, but it has a general-purpose design and a large solid-angle coverage. The experiment collected around 1000 fb^{-1} of data[3] that were primarily taken at the $\Upsilon(4S)$ resonance (10.58 GeV in the center-of-mass (c.m.) frame).

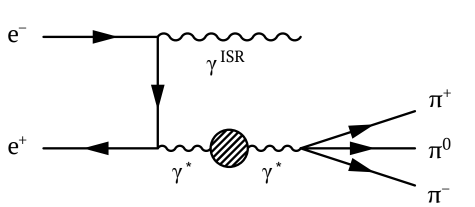

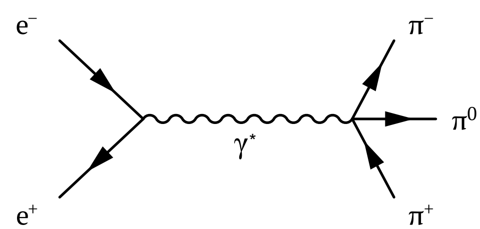

Figure 4.8-1. The leading-order Feynman diagram for the $e^+e^- \to \pi^+\pi^-\pi^0$ process, as measured by the initial-state-radiation method, is given on the left. The tree-level diagram of the same process is given on the right.

The radiative-return method allows the measurement of a cross section as a function of energy in a fixed-energy experiment[4], where the cross section may potentially be measured over a range of energy bins from threshold up to the machine operating energy. Instead of

[1] F. Jegerlehner and A. Nyffeler, Phys. Rept. **477**, 1 (2009) [arXiv:0902.3360 [hep-ph]].
[2] A. Abashian *et al.*, Nucl. Instrum. Meth. A **479**, 117 (2002).
[3] J. Brodzicka *et al.* [Belle Collaboration], PTEP **2012** (2012) 04D001 [arXiv:1212.5342 [hep-ex]].
[4] V. P. Druzhinin, S. I. Eidelman, S. I. Serednyakov and E. P. Solodov, Rev. Mod. Phys. **83**, 1545 (2011).

measuring the e^+e^- annihilation to a hadronic final-state process, the related initial-state-radiation (ISR) process is measured. The ISR effects lead to the emission of photons from the initial e^+e^- system, lowering the effective e^+e^- system c.m. frame energy. The ISR effects are calculable in QED, and these effects can be removed from the measured cross section to produce the desired non-ISR cross section. Fig. 4.8-1 shows the LO ISR and Born Feynman diagrams for e^+e^- annihilation to the $\pi^+\pi^-\pi^0$ hadronic final-state.

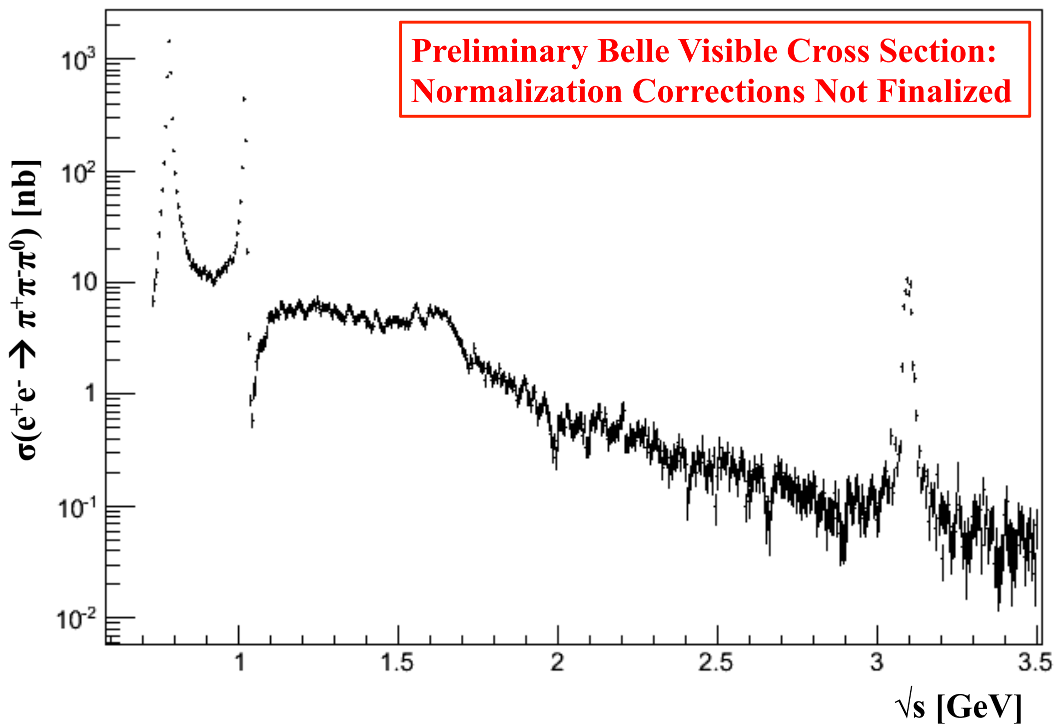

Figure 4.8-2. The preliminary Belle visible cross-section measurement for electron-positron annihilation to the $\pi^+\pi^-\pi^0$ final-state[2,3]. This cross section includes the removal of leading-order ISR effects, but includes higher-order ISR effects. The $\pi^+\pi^-\pi^0$ final state includes the narrow ω, ϕ, and J/ψ resonances, as well as the broad ω' and ω'' resonances.

The Belle experiment has published a number of high-energy cross-section measurements from 3.7 to 6 GeV by the radiative-return method, while it has only published two low-energy radiative-return measurements: the $\phi\pi^+\pi^-$ and $\phi f_0(980)$ final states[1] from 1.5 to 3 GeV. The Belle experiment is in the process of finalizing a cross-section measurement for the $\pi^+\pi^-\pi^0$ final-state[2,3] by the radiative-return method, where Fig. 4.8-2 shows the preliminary visible cross section. The $\pi^+\pi^-\pi^0$ final-state cross section is the second largest component of the a_μ LO HVP value, and one of the largest components of the error.

[1] C. P. Shen *et al.* [Belle Collaboration], Phys. Rev. D **80**, 031101 (2009) [arXiv:0808.0006 [hep-ex]].

[2] 12th International Workshop on Tau Lepton Physics (TAU2012) in Nagoya, Japan, (2012).

[3] 9th International Workshop on e+e- collisions from Phi to Psi (PHIPSI13) in Rome, Italy, (2013).

4.9 PbF_2 calorimeter at SLAC

L. P. Alonzi, A. T. Fienberg, D. W. Hertzog, J. Kaspar, M. W. Smith, K. Wall, and K. Yai*

In November of 2013, the UW-based $g-2$ calorimeter team traveled to SLAC National Accelerator Laboratory's End Station Test Beam facility with a prototype PbF_2 calorimeter. The facility provided an electron beam with energies ranging from 2.5 to 4 GeV, similar to the energies we expect from decay electrons in the final experiment. Scanning over this range of electron energies allowed us to confirm that the resolution and linearity of our PbF_2 calorimeter meet the requirements of the $g-2$ experiment.

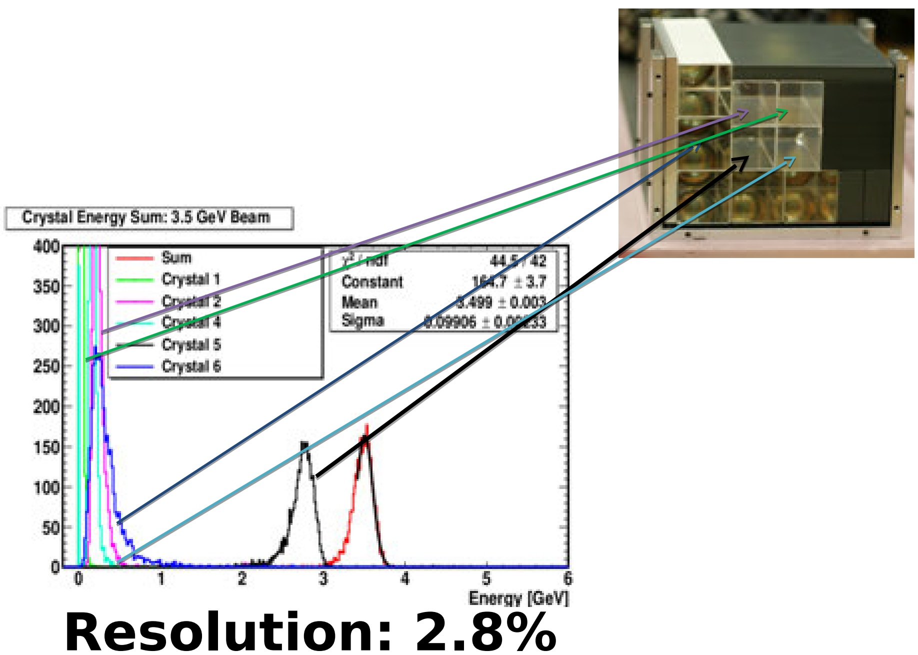

Figure 4.9-1. Energy deposited into the calorimeter by 3.5-GeV electrons hitting the center of each crystal is shown with a histogram of the energy summed across the array. The width of the summed energy histogram gives the relative energy resolution of 2.8 % at 3.5 GeV.

The prototype we constructed was a 3x3 array of crystals, four of which were coupled to Hamamatsu 16-channel silicon photomultipliers (SiPMs) and the remaining five of which were coupled to Electron Tubes photomultiplier tubes. A light-tight housing for this array was constructed by CENPA engineers and featured a cold-air temperature-stabilization system that was required to maintain acceptable SiPM gain stability. Signals from the SiPMs were fed into a pair of Struck 4-channel SIS3350 500MS/s 12-bit digitizers provided by collaborators at the University of Kentucky.

In addition to the detector system itself, we brought a PicoQuant pulsed diode laser and a light-distribution system that interfaced directly with the detector housing via optical

*Osaka University Graduate School of Science, Japan.

cables. This laser system allowed for periodic *in-situ* calibrations of our detectors. The $g-2$ experiment will require a similar, albeit much larger-scale, laser calibration system. Comparing beam data to laser calibrations, we were able to conclude that the PbF_2 yields at least 1.0 pe/MeV at the SiPM, consistent with expectation.

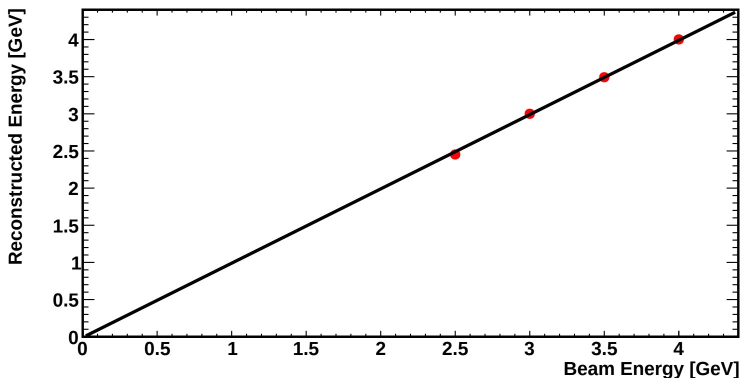

Figure 4.9-2. Excellent calorimeter linearity of the was demostrated by varying the energy of incident particles. The energy was scanned from 2.5 to 4.0 GeV, which is the energy region of interest of the $g-2$ experiment.

The SLAC facility featured a remote controlled x–y table that allowed us to scan the beam over the face of our detector. Provided the beam was close enough to the center of the calorimeter that the shower was contained, our reconstructed energy was independent of the beam position and incident angle (we tested up to 10°). Indeed, by examining the distribution of energy between crystals we were able to locate the beam position to a region smaller than the face of a single crystal. This segmented nature of the detector contributes significantly to its pileup resolution capabilities.

In order to achieve accurate energy measurements and the best resolution, the energy seen by each detector must be summed together on an event-by-event basis. To execute this procedure, each individual photo-detector was calibrated on a universal scale. The calibration constants were obtained by using the x–y table to position our detector so that a 3-GeV beam passed through the center of each of our crystals in turn. Energy proxies were extracted from the digitized traces using a pulse-fitting procedure, and then the energies were normalized to a common scale.

After conducting energy sums across our array, we were able to demonstrate that the energy resolution of our calorimeter exceeds the requirement of 5 % at 2 GeV. In fact, the measurement of 2.8 % at 3.5 GeV (Fig. 4.9-1) suggests a resolution better than 4 % at 2 GeV. An energy scan in the 2.5 – 4.0 GeV range, depicted in (Fig. 4.9-2), demonstrated an excellent linearity of the PbF_2 calorimeter. The calorimeter team is looking forward to another trip to SLAC in July of 2014 where we will test a larger 5x5 array of PbF_2 crystals. We expect the next generation of SiPMs and improved electronics boards designed at CENPA will yield even better performance. Preparing for this upcoming test beam run will be a focus of our group this spring.

4.10 PbF_2 calorimeter systematics study

A. T. Fienberg, D. W. Hertzog, J. Kaspar, G. J. Plunkett, and K. B. Wall

The UW $g-2$ detector group has been engaged in several systematic studies towards the development of the calorimeters. One such study is the investigation of the pure light response of a crystal, in particular how light is propagated and distributed in a crystal and how different reflective or absorptive wrappings affect this distribution. There are two quantities of interest: light yield and pulse width. These quantities correspond to two different extremes of wrapping material. For maximum light yield, the wrapping of choice is white Millipore paper, which allows light to be reflected back inside the crystal. However, the reflections cause the pulse of light to be stretched out in time. Shorter pulse widths are achieved using black Tedlar, which transmits only the initial cone of light and absorbs all reflections. Higher light yield improves the energy resolution of the calorimeter, but shorter pulses can reduce the number of events that overlap in time.

The experimental setup utilizes cosmic-ray muons to produce light inside the crystals. These high-energy particles are the best way to simulate the conditions of the experiment without the use of a particle beam. The cosmic-ray detector consists of a 2×2 array of lead fluoride crystals placed atop a 2×2 array of ET photomultiplier tubes (PMTs) with the entire setup housed inside of a dark box. Each individual crystal is wrapped with either Tedlar or Millipore. Scintillator paddles are placed above and below the setup to establish a trigger for the data-acquisition system and to select only high energy muons that arrive perpendicular to the earth. The data-collection system consists of the raw PMT signals being sent to a Domino Sampling Chip (DRS), developed at Paul Scherrer Institute, which digitizes the signal at 5 GSPS.

We collected a library of cosmic pulses for both wrappings on each crystal. From these libraries we were able to show evidence of the distinct difference in energy observed by the photomultiplier tubes depending on the choice of wrapping. Comparison of the two shows that the observed energy from a crystal wrapped in black Tedlar is about 60 % of that from the same crystal wrapped in white Millipore (see Fig. 4.10-1). This result was consistent across all crystals and PMTs and provides a measure of an important parameter to be used in the final choice of wrapping.

A study on double-pulse resolution was also undertaken at the UW lab to understand events that arrive close in time in the calorimeter. It is important to know if we can resolve the time and energy of an event that arrives in the calorimeter immediately after another event, on the order of a few nanoseconds. Silicon photomultipliers (SiPMs) exhibit a non-trivial decrease in their output gain for events where two particles arrive close in time to each other. It is deterministic and can be corrected for.

In the laboratory, the two-pulse effect is simulated by splitting the output of a 407-nm pulsed diode laser into two channels. One of these channels is then delayed by a variable amount in the range of 5 to 160 ns. The output of the SiPM is digitized using a DRS4 chip.

By observing the two pulses independently as well as together the gain change on the second pulse can be mapped. The quantified result is the function $G2(\Delta t, E_1, E_2)$ where Δt is the difference in time of the two pulses and E_i is the energy of the i^{th} pulse.

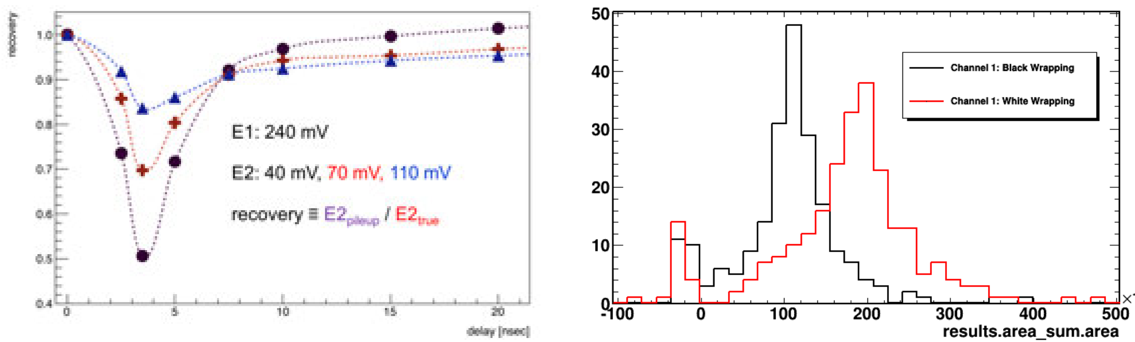

Figure 4.10-1. *Left:* Relative SiPM gain drop experienced by an second event closely following a larger primary one. The gain loss is dependent on time delay and number of photons in the second event. *Right:* Effective number of photons recorded from a crystal wrapped in white paper (black curve) and black foil (red curve). Photons were generated by cosmic muons.

The result of the study is that second-pulse energy reduction depends on Δt and E_2. This energy reduction was mapped out for a range of these parameters as shown in Fig. 4.10-1. The second-pulse energy reduction is smaller at higher values of E_2 as well as at higher values of Δt.

4.11 Frequency extraction studies on free induction decays

M. Fertl, A. García, I. S Guinn, C. Helling, R. Morris, R. Ortez, R. E. Osofsky, E. A. Shaw, <u>M. W. Smith</u>, and H. E. Swanson

The $g-2$ experiment requires very precise and accurate monitoring and measurement of the magnetic field in the storage ring. The fixed nuclear magnetic resonance (NMR) probes are capable of the appropriate precision and accuracy, but we must understand how to extract the necessary values from the data. The data in this case come from the original NMR signal (62 MHz) which is mixed down to a signal at ~ 50 kHz referred to as the free induction decay (FID). The waveform contains oscillations due to precession of the aligned nuclear spins being kicked into the plane transverse to the strong magnetic dipole field. The waveform can be handily approximated by an exponential decay multiplied with a sinusoid. Real data and idealized waveforms are shown in Fig. 4.11-1. The deviations in the real data are due to magnetic-field gradients over the range of the NMR probe. Magnetic-field gradients make frequency extraction a more difficult process.

As a first step towards understanding the values extracted from the data, we test the frequency extraction techniques on the idealized FIDs, for which we know directly the true frequency. We employ several techniques such as zero counting (time domain), centroid calculations (frequency domain), peak fitting (frequency domain), and linear phase fitting

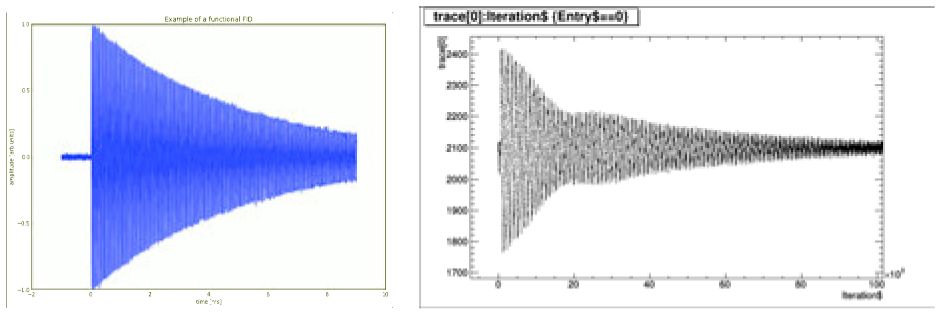

Figure 4.11-1. An example of a simulated free induction decay waveform (left) is compared to a real digitized trace (right).

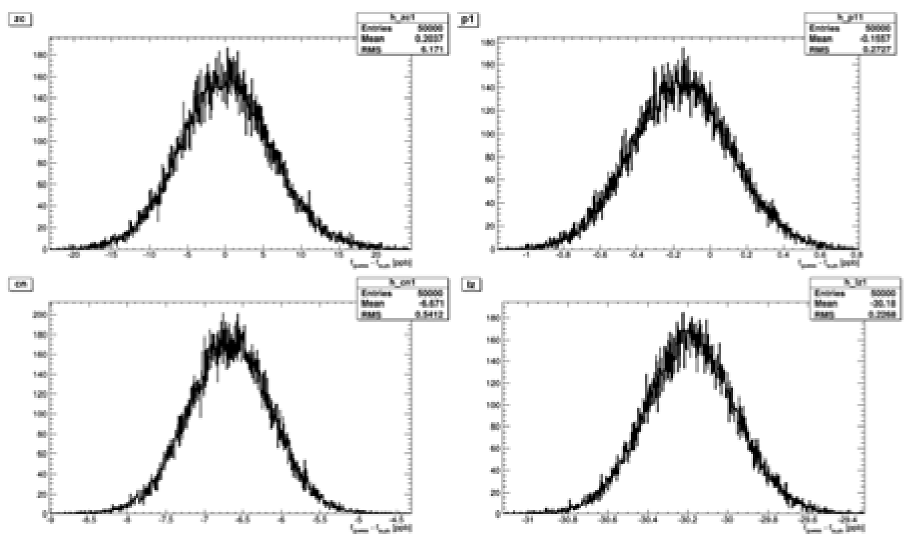

Figure 4.11-2. Frequencies extracted from simulated waveforms are compared for 4 different methods: zero counting (upper left), centroid calculations (lower left), peak fitting (lower right), and linear phase fitting (upper right). The x-scale shows differences from the true (initial) value in ppb units.

(time domain). The zero counting is as simple as counting zero crossings and interpolating the times on the edges. The centroid involves calculating the power of the Fourier transform and calculating the centroid of a symmetric window around the maximum. Another technique fits the power spectrum peak to a Lorentzian peak:

$$F(\omega) = \frac{1}{\pi}\frac{\Gamma/2}{(\omega-\omega_0)^2-(\Gamma/2)^2} \quad . \tag{1}$$

The last technique uses a Hilbert Transform of the original FID to obtain the imaginary, harmonic complement and extracts the phase progression by using $\phi = \arctan(\mathrm{Re}/\mathrm{Im})$. The relative accuracy of the techniques is shown in Fig. 4.11-2. The linear phase fit seems to be the most robust, but all meet the specification of one-part-per-million accuracy from the original 62-MHz NMR signal.

4.12 Magnetic footprint measurements of SiPM electronics

M. Fertl, A. García, I. S. Guinn, C. Helling, R. Morris, R. Ortez, R. E. Osofsky, E. A. Shaw, M. W. Smith, and H. E. Swanson

In the upcoming $g-2$ experiment, the collaboration strives to produce a magnetic field with high homogeneity. In order to determine potential distortions of the field due to silicon photomultiplier (SiPM) detector electronics components we have performed measurements of the effective susceptibility of different electronic components that are being considered for the experiment.

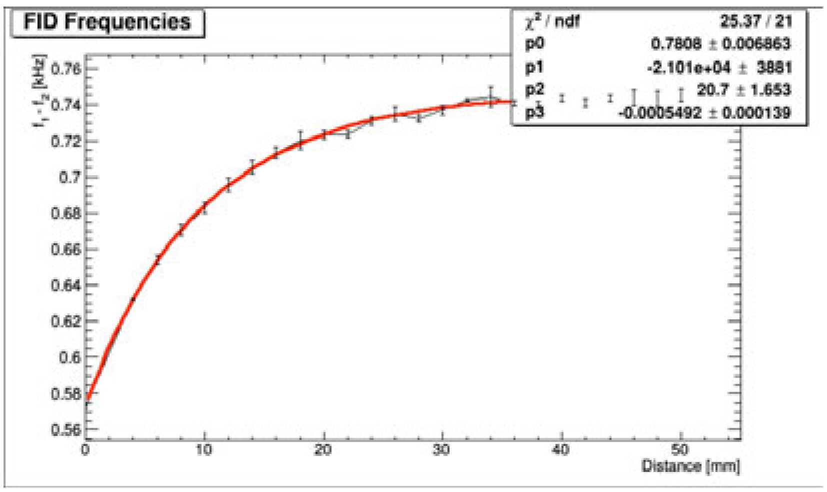

Figure 4.12-1. The CENPA magnet features a strong and uniform magnetic field to judge magnetic properties of electronics components using the free induction decay technique.

Using the fixed nuclear magnetic resonance (NMR) probes from the previous $g-2$ experiment and a sufficiently strong dipole magnet at the University of Washington, pictured in Fig. 4.6-1, we estimate the magnetic characteristics of the electronics board. We take the difference in frequency of two NMR probes separated by 12.7 mm and repeat the measurement over a distance range of 50 mm. The result is a field difference over distance which is modeled nicely by the difference of two dipoles with $\sim 1/r^3$ behavior and a linear background from the aluminum arm.

The initial measurement of $1.48 \times 10^7\,\mu$T mm^2 was larger than the figure of merit. At this point we measured each electronics component that we could be separated out, i.e., the connectors, the connector cables, a bundle of small resistors and capacitors, the empty board itself, the SiPM itself, and finally the large bias and filter capacitor. The large capacitor produced 92 % of the induced magnetic dipole (see Fig. 4.12-1). With this in mind future designs will utilize a capacitor of smaller physical size to reduce the magnetic footprint of the SiPM board. With the susceptibility reduced by a factor of 10, our calculations indicate that the field distortions will meet the demands required for the target accuracy of the $g-2$ experiment.

MuSun

4.13 Overview of the MuSun experiment: Muon capture on deuterium

D. W. Hertzog, P. Kammel, M. H. Murray, D. J. Prindle, R. A. Ryan, and F. Wauters

We are now at the confluence of two exciting developments in the field of muon capture[1]. Based on the novel "active target" technique developed by our collaboration, experiments on hydrogen and the lightest nuclei are approaching sub-percent precision. At the same time, following Weinberg's pioneering approach, effective field theories (EFTs) have been systematically constructed to calculate electro-weak observables in few-body systems. These calculations can provide precise results, including a systematic evaluation of uncertainties. They can also establish quantitative relations between muon capture and electro-weak astrophysical processes of fundamental importance, which have never been measured directly. These include *pp* fusion, which is the primary energy source in the sun and the main sequence stars, and the νd reactions measured at the Sudbury Neutrino Observatory.

Λ_d	year	Method	Reference
392.0±2.3	2011	EFT*	Marcucci, Phys. Rev. C83:014002
399±3	2012	EFT	Marcucci, Phys.Rev.Lett. 108, 052502
383.8-392.4	2012	EFT	Adam, Phys. Lett. B709, 93-100
470±29	1986	Electron	Bardin, Nucl. Phys A453, 591-604
409±40	1989	Neutron	Cargnelli[2]

Table 4.13-1. Recent theoretical and experimental results on the muon-capture rate Λ_d from the doublet state of the μd atom. EFT* denotes a hybrid EFT calculation. "Electron" denotes that the capture rate was measured with the lifetime technique, in contrast with the observation of capture neutrons.

A prime example is the process $\mu + d \to n + n + \nu$ which is the simplest muon capture process on a nucleus. Λ_d denotes the capture rate from the doublet hyperfine state of the muonic deuterium atom in its 1S ground state. The goal of the MuSun experiment is to measure this rate to a precision of better than 1.5%.

In modern calculations the potential-model approach is being replaced by EFT calculations. In 2012 the first self-consistent EFT calculations were published (see Table 4.13-1). The sole unknown low-energy constant (LEC) entering this problem is fixed from the more complicated 3-nucleon system, as present constraints on this quantity from the 2-nucleon system have 100% uncertainties. For the foreseeable future, the MuSun experiment is the only theoretically clean way to determine this important LEC in a simple 2-nucleon system to within 20%, a factor-of-5 improvement. This determination will be essential for calibrating the calculations of the above mentioned astrophysical reactions and for extending the EFT method to more complicated few-body systems. A large improvement in experimental precision is required. As can be seen from Table 4.13-1 the present experimental situation is completely unsatisfactory. MuSun aims to clarify the current tension between experiment

[1]P. Kammel, K. Kubodera, Annu. Rev. Nucl. Part. Sci. **60**, 327 (2010).

[2]Proceedings of the XXIII Yamada Conf. on Nuclear Weak Processes and Nuclear Structure, Osaka, Japan, 1989.

and theory, and provide a benchmark commensurate with the expected precision of ongoing, modern calculations.

The MuSun experiment, shown in Fig. 4.13-1, measures Λ_d with the so-called lifetime technique: $\lambda_{\mu d} = \lambda_{\mu^+} + \Lambda_d$. Incoming muons are detected by muon beam counters (two thin scintillator slabs and a wire chamber) and the electron detector (two cylindrical wire chambers surrounded by a hodoscope consisting of a double layer of scintillator paddles). The conditions of the active target must lead to an unambiguous extraction of Λ_d, independent of muonic atomic-physics complications occurring after the muon stops in deuterium. The transition between the upper μd quartet to the lower μd hyperfine state is slow and, once a $dd\mu$ molecule is formed, muon-catalyzed dd fusion occurs on a time scale of nanoseconds, recycling the muon. Conditions are optimized for T = 31 K and 6.5% liquid hydrogen density. To achieve those, a new high-density cryogenic ionization chamber (CryoTPC) filled with ultra-pure deuterium was developed as an active target to monitor the muon stopping location and muon-catalyzed fusion reactions.

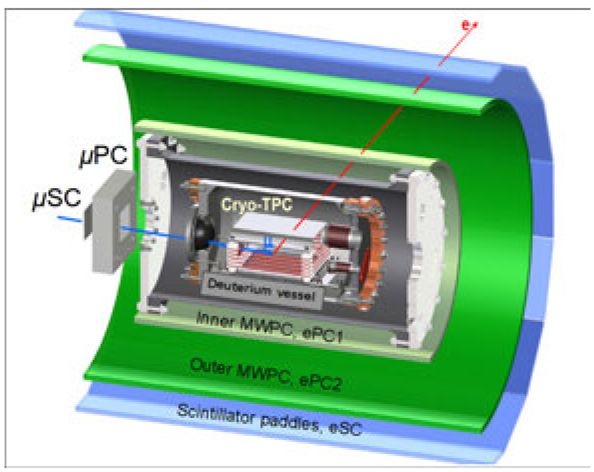

Figure 4.13-1. MuSun CAD model with muon and electron detectors.

MuSun had a first production run in 2011 resulting in $\sim 4 \times 10^9$ fully reconstructed muon-electron pairs, which are being analyzed by UW Ph.D. student Murray. In 2012 the MuSun experiment moved to a new dedicated beam area at the Paul Scherrer Institute. In 2013, the beam line was finally commissioned with new quadrupoles, a fully moveable detector setup and a climate controlled tent to house the detector systems and electronics, and a production run ensued. In preparation for this run, the UW group led key hardware improvements. The TPC was upgraded with high-Z materials as much as possible. New components included a thick silver-coated pad plane, and a Frisch grid, consisting of a tungsten frame and gold plated tungsten wires. Stray muons will be quickly captured in these materials, and thus can be eliminated with time cuts. The new system achieved the required full TPC voltage and took production data for several weeks, but eventually failed during a temperature cycle. A TPC with a composite frame is currently under construction at UW, which should eliminate the thermal mismatch while keeping the excellent performance of the 2013 grid. We also replaced the external preamplifiers with CENPA-built miniature cryogenic preamplifiers working in the insulation vacuum in close proximity to the cold volume of the TPC. The additional risk of operating the electronics in this challenging and hard-to-access environment was justified by a factor-of-3 improved resolution and nearly flawless operation. Our sensitivity for monitoring impurity capture products in-situ using TPC signals was increased to the required ppb level. The statistics accumulated in 2013 were only $\sim 2\times10^9$ muon-electron pairs, primarily because of an unusual extended downtime of the PSI accelerator. For 2014 a long run of 11 weeks was approved (Ph.D. thesis of UW student Ryan), with the goal of collecting $\sim 8 \times 10^9$ decays, half of the experiment's full statistics.

4.14 Cryogenic preamplifiers

F. E. Gray*, P. Kammel, D. A. Peterson, R. A. Ryan, T. D. Van Wechel, and F. Wauters

The MuSun TPC consists of 48 signal pads, each with a separate electronic readout. The first stage in this electronic chain consists of a charge-integrating preamplifier. In 2011, an unoptimized electronic resolution of 30 keV led to an extensive effort to characterize and reduce the noise sources associated with the preamplifier. An improved electronic resolution enables more sophisticated muon-tracking algorithms to be developed and allows the TPC to be used for in-situ monitoring of muon capture on impurities.

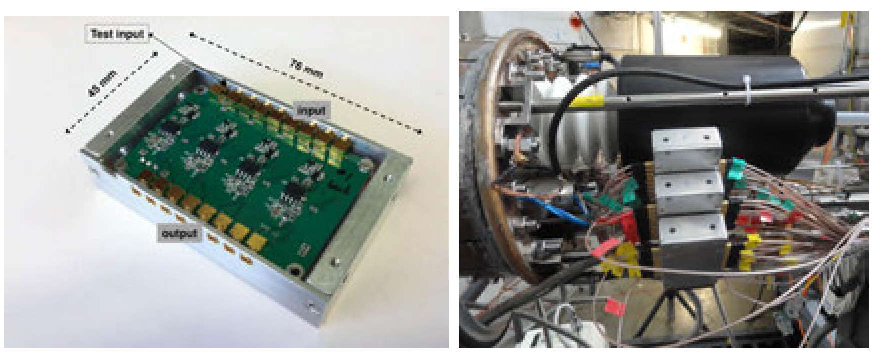

Figure 4.14-1. Left: final preamplifier board, mounted in an aluminum enclosure. Right: half of the preamplifiers mounted symmetrically in either side of the HV feedthrough 20 cm from the TPC.

In 2012, after significant component optimization, four prototype preamplifiers were mounted within the insulating vacuum 30 cm from the TPC flange and cooled via contact with the TPC support rods. Johnson noise was reduced by cooling and lower input capacitance and acoustically induced pickup from the residual cathode field was suppressed with the use of shielded cables. The resolution during this test beam run was improved to 17 keV. However, the cooling power was insufficient to reach the optimal temperature of 140 K and the size of the preamplifiers needed to be further reduced to accommodate 48 channels in the limited space provided by the vacuum volume.

The data collected in the 2012 run motivated further component optimization and in 2013 a final preamplifier was designed in part by Tim Van Wechel and David Peterson. Six boards,

*Visiting faculty, Regis University, Denver, CO.

each containing eight channels, were mounted 20 cm from the TPC flange on a copper cooling block, as shown in Fig. 4.14-1. A new cooling system was designed by PNPI colleagues in which liquid nitrogen boil-off was vented through copper tubing to the cooling blocks. A mock cooling system was designed and installed at CENPA by John Amsbaugh and Doug Will for further testing.

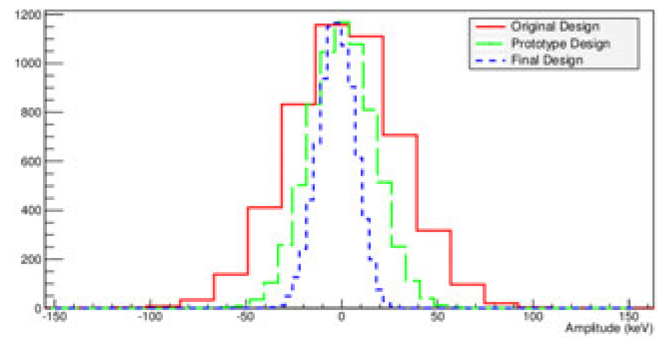

Figure 4.14-2. Amplitude distributions from an injected step pulse of charge over the design iterations. The distributions have been normalized and centered at zero for easy comparison. The RMS of each distribution, in keV, shows the improved electronics resolution.

All 48 channels were installed at PSI and cooled to 140 K for a three-month production data-taking run. The preamplifiers reached a resolution of 10 keV, an overall improvement of a factor of three over the original design, as shown in Fig. 4.14-2. The new design performed reliably throughout the run, with only one channel failing due to rapid cooling and two channel failures due to sparking from a faulty Frisch grid. In future runs, cooling will be slowed to prevent damage and an upgraded grid design will minimize sparking.

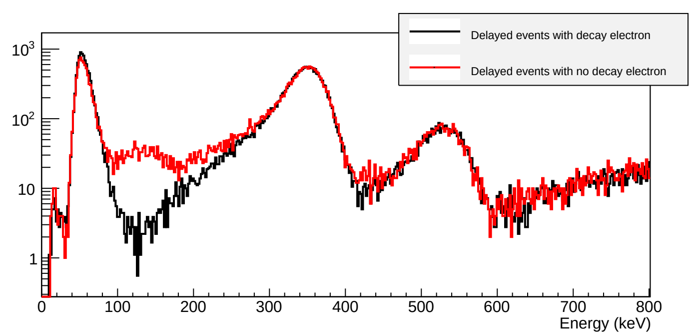

Figure 4.14-3. A delayed energy spectrum in the TPC. Cutting on delay electrons suppresses the capture events. At nominal conditions for the 2013 run, a clear capture signal is present around 100 keV.

During the 2013 production run the zeolite absorbers responsible for cleaning the deuterium gas became saturated, leading to an impurity presence at the level of 20 ppb N_2. Due in part to the improved resolution of the preamplifiers, separation of the large ^{3}He background from the capture recoils was made possible, as demonstrated in Fig. 4.14-3.

4.15 New TPC construction at UW

J. F. Amsbaugh, T. H. Burritt, P. Kammel, R. A. Ryan, and F. Wauters

The operating conditions of the MuSun Time Projection Chamber (TPC) put tight constraints on its design. The materials have to be compatible with cryogenic temperatures, and sub-structures need to have matching coefficients of thermal expansion. Evidently, the design of the cathode, field wires, and Frisch grid has to take into account the high electric fields. Muon physics further restricts what materials can be used. The low, $\mathcal{O}(1\text{ ppb})$, gas-impurity levels which can be tolerated requires low outgassing materials. In addition, muons which are incorrectly identified as D_2 stops will distort the lifetime distribution, as the capture rates on $Z > 1$ elements dramatically differ from the muon-capture rate on the deuteron. For example, the μ^- lifetime in iron is 201 ns, while it is only 78 ns in tungsten. Therefore, it is highly preferable that such muons end up in high-Z materials, so that they disappear out of the lifetime histograms before the lifetime-fit start time.

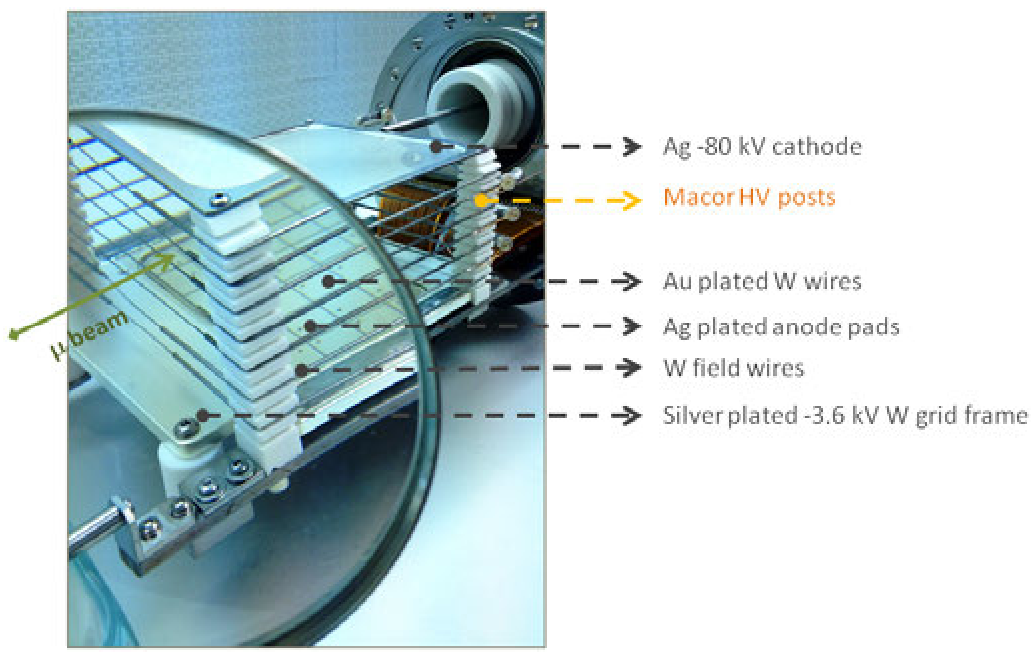

Figure 4.15-1. The MuSun cryo-TPC for the 2013 data run.

For the 2013 data run, the MuSun TPC was upgraded taking these requirements into account (see Fig. 4.15-1). The anode pads were coated with a 40-μm-thick silver layer, the 80-kV cathode consisted of a 100-μm-thick silver foil mounted on a stainless-steel frame, and the field wires were made of pure tungsten. A novel Frisch grid, positioned 1.5 mm above the anode-pad plane, was constructed by soldering tungsten-rhenium wires on a silver plated frame machined from a single piece of tungsten. In contrast to its stainless-steel predecessor, the 2013 Frisch grid could reach its nominal voltage for full charge collection without sparking, which is crucial to protect the cryogenic preamplifiers (Sec. 4.14).

Despite the successful installation and commissioning of the 2013 TPC, during the following long data run several mechanical failure modes were identified. The tungsten field wires turned out to be very fragile, the mounting of the silver cathode was flawed, and most importantly, during a temperature cycle towards the end of the run, some parts of the solder/silver layer peeled off the tungsten grid frame due to the mismatch of the thermal expansion of the materials. It was therefore decided, with the exception of the anode-pad plane, to completely rebuild the TPC with an improved design for the 2014 run. The most critical part is a new Frisch grid. The new design consists of a stainless-steel - tungsten composite frame. The wire soldering and support structures are made of stainless steel. The two cross bars in the wire direction are made of tungsten in order to maintain the tension on the tungsten-rhenium wires at 30 K (Fig. 4.15-2). These bars are hard-soldered on the stainless-steel parts by the PSI detector group. The stringent tolerances on the SS-W interface of $\pm$ 10 μm are achieved with the wire electric-discharge machine (EDM) at the physics workshop.

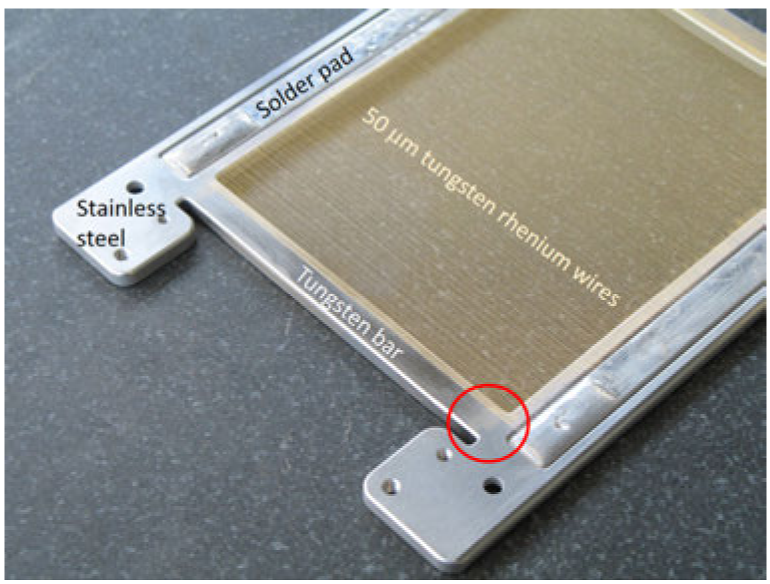

Figure 4.15-2. A close-up of the stainless-steel and tungsten components of the new Frisch grid after they came out of the wire EDM. The tolerances on the interface between the two parts, indicated by the red circle, are $\pm$ 10 μm.

The manufacturing of the new Frisch grid, a joint UW-PSI effort, and the other components (such as a new high-voltage structure), all made in the UW workshops, are well on their way. Installation and commissioning at PSI is planned during May of this year. In parallel, a 2nd TPC will be constructed and commissioned in the MuSun lab at CENPA, where we have built a test setup to mimic realistic conditions. This includes a gas system to fill the TPC up to 10 Bar with purified N_2 gas, a 20-kV high-voltage system, which was implemented by our undergraduate Joseph Toles, a N_2-gas cooling for the preamplifiers and an independent LN_2 cooling system for the TPC.

4.16 Lifetime analysis of the 2011 data

D. W. Hertzog, P. Kammel, M. H. Murray, D. J. Prindle, R. A. Ryan, and F. Wauters

It is crucial to the analysis of the muon lifetime to develop a robust muon-acceptance algorithm that is insensitive to systematic distortions of the decay-time distribution by physical effects and analysis cuts. The primary function of the muon track finder is identifying muons that stop in the fiducial volume of the TPC gas, while rejecting muons that leave this volume. Additionally, the three-dimensional position and timing of muon and other charged-particle tracks in the TPC are used for secondary systematic studies. The efficiency for accepting muon stops must not be coupled to the decay time of the muon. Two examples considered here are the small extra energy deposition by the decay electron, and the large additional pulses due to muon-catalyzed fusion (MCF) products. Additionally, an electronically induced correlation was discovered in the R2011 data.

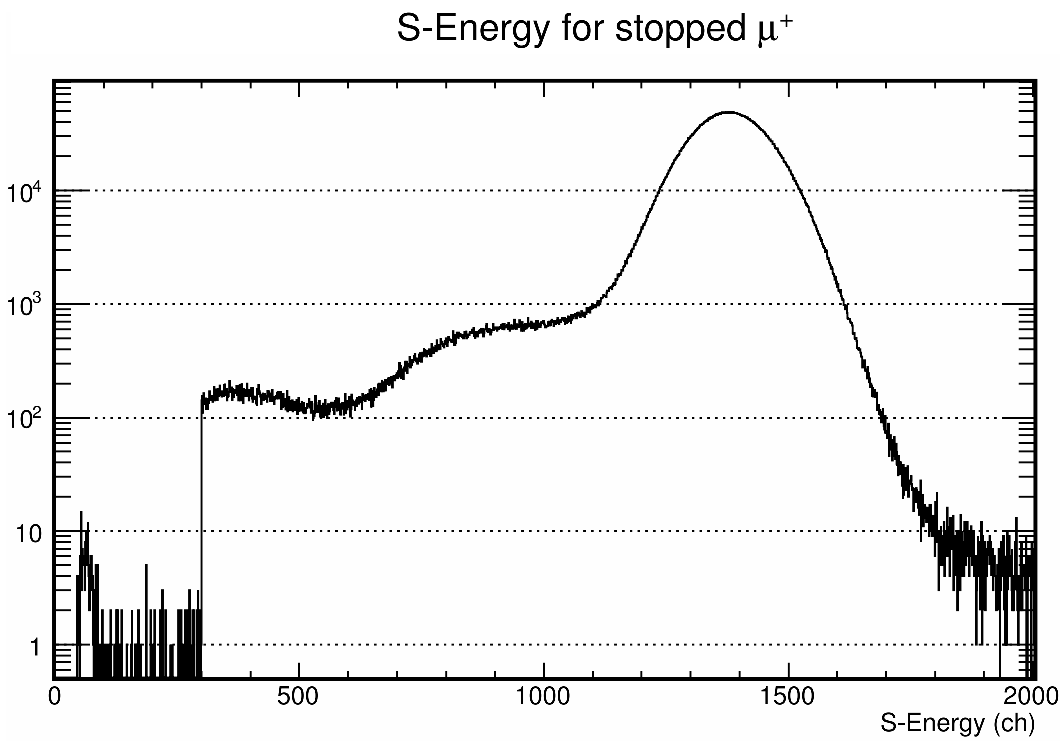

Figure 4.16-1. Distribution of muon S-energy. The nominal cut is at 300 channels. The low-energy shoulder is composed partly of high-angle scattering events and partly of decay-in-flight muons.

Decay-electron tracks may interfere with the acceptance of muon stops. The electron is nearly invisible in the TPC, but the small amount of energy deposited in the stopping pad can push a muon track over an experimental or algorithmic threshold. Events with early decay times, where the electron track most overlaps the drifting cloud of ionized electrons from the muon track, are more likely to be accepted.

We study this effect using stopped μ^+, since the Michel decay mode is nearly identical[1], but the positive muons do not undergo capture or muon-catalyzed fusion as with μ^-. The change in the fitted lifetime as a function of azimuthal angle of the decay electron track provides a way to quantify the interference effect. In addition to the electron track direction, we can enhance the interference by varying the cut on the muon stop energy. To this end, we introduce a quantity called the S-energy, equal to the sum of the stopping pad energy and twice the next-to-last pad energy (Fig. 4.16-1). The electron interference should be largest at the peak of the S-energy distribution, where there is the largest population of muons to be pushed over threshold. An S-energy threshold of 1300 channels enhances the electron interference dramatically (Fig. 4.16-2). However, at the nominal energy cut of 300 channels, there is no dependence of the fitted muon lifetime on the azimuthal angle of the electron track, indicating that MuSun can avoid this systematic effect by choosing a low enough muon energy threshold.

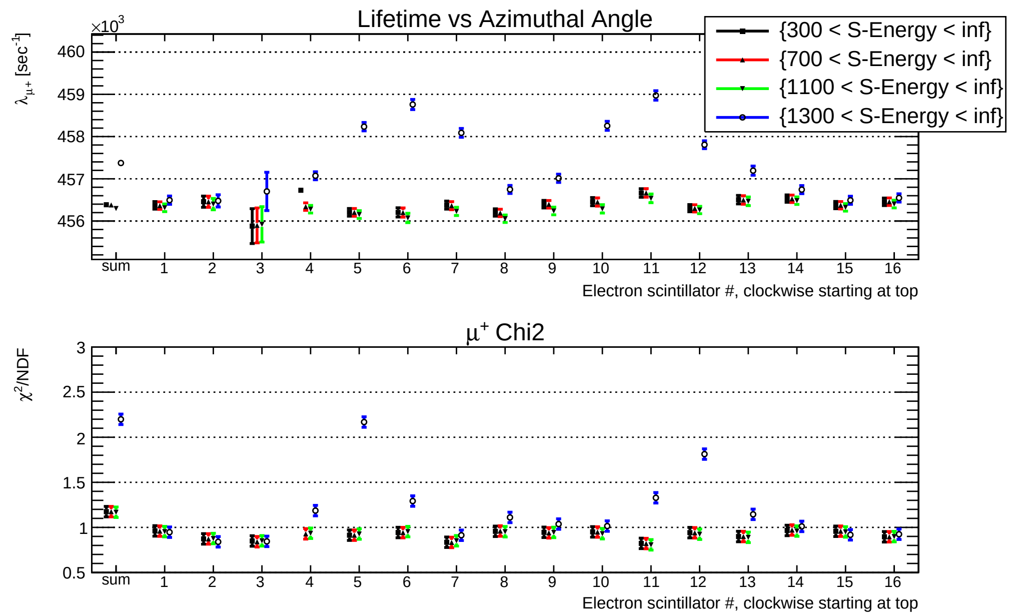

Figure 4.16-2. Measured muon disappearance rate as a function of azimuthal section of the electron detector. Color indicates varying cut on the muon S-energy. At the nominal cut, there is no trend, but cutting in the middle of the S-energy distribution shows a large electron interference effect, strongest in the horizontal directions. The disappearance rate is blinded, both absolutely and with respect to the negative muon disappearance rate.

The next most common process that stopped muons undergo in MuSun is muon-catalyzed fusion, via the reactions $\mu^- dd \to \mu^- + {}^3\text{He} + n$ and $\mu^- dd \to \mu^- + t + p$. Fusion interference is the coupling of the acceptance of a muon stop to the detection of the charged fusion products in the TPC. Misconstruction of the muon energy leads to an effect similar to electron interference, though in this case later decay times are enhanced. On the other hand, misconstruction of the muon stop position due to the longer proton track can alter the acceptance of muon tracks based on the fiducial-volume cut.

---

[1] The behavior of electrons from μ^- decay is nearly identical to that of positrons from μ^+ decay in the MuSun detector. Both are referred to as "electrons" in the text.

In order to calibrate the sensitivity of a muon track finder to the presence of MCF products, we must be able to change the magnitude of fusion interference. Current efforts to accomplish this include Monte Carlo simulation of fusion events, data-driven mixing of fusion waveforms into μ^+ tracks, and artificial contraction of the fiducial volume. Another alternative is a muon track finder based only on the energy deposition on pads far upstream from the stopping point. With such a tracker, the finite range of the fusion products prevents a correlation between fusion products and the acceptance of muon tracks.

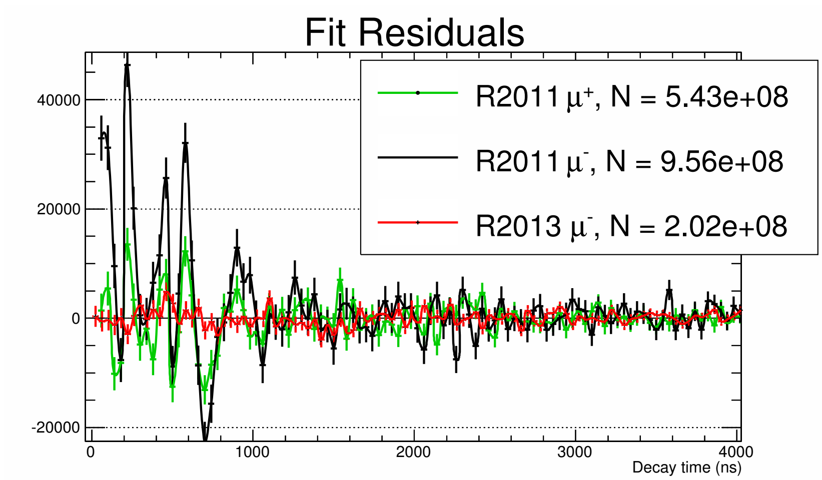

Figure 4.16-3. An anomalous correlation between the muon entrance time and the time of the electron track appears in both μ^+ and μ^- for R2011, but the effect is much smaller in R2013.

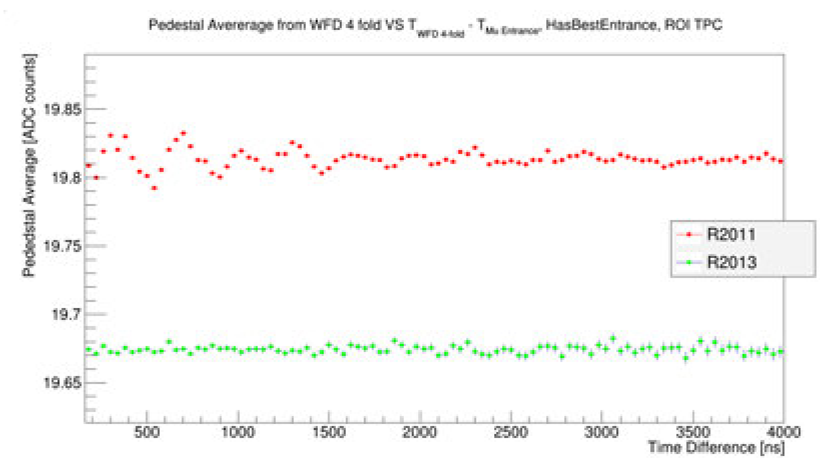

Figure 4.16-4. Electron scintillator waveform pedestals as a function of time after the muon entrance R2011 and R2013. The early oscillation in the (red) R2011 data is absent in the flat (green) R2013 data.

An anomalous correlation between the muon entrance time and the time of the electron track was discovered in the R2011 data. This fluctuation is most visible in the fit residuals from the decay-time distribution and disappears after the first 1.5 microseconds (Fig. 4.16-3) The fluctuation is present in both μ^+ and μ^- data and persists even when only the entrance detectors and the electron scintillator are included in the analysis. In Fig. 4.16-4, a similar early-time oscillation is observed in the waveform baseline of the electron-timing scintillators. In both the electronic baseline and the residuals of the lifetime fit, the effect is not present in the R2013 data at the same magnitude, though further high-statistics analysis will determine if it is completely absent. Many simple hardware changes were made between 2011 and 2013, and the experiment was moved to a different beamline at PSI, so it is unlikely that the specific cause of the anomalous correlation will be determined. However, the triggering algorithm in R2013 was adjusted to record more samples, allowing us to correct for the R2011 pedestal variations using the older data.

4.17 Monte Carlo framework and studies

F. E. Gray*, D. W. Hertzog, P. Kammel, D. J. Prindle, M. H. Murray, R. A. Ryan, and F. Wauters

The MuSun Monte Carlo has progressed to the point where we can run samples of order 10^9 events of μ^+ or μ^- events and check how specific effects modify the measured lifetime.

In the GEANT4 simulation we have moved parameters describing beam conditions and Time Projection Chamber (TPC) gas properties into macros. Gas properties include density and temperature as well as capture and transition rates for the μ^- molecular states. We save the macro in the output as part of the documentation. We also save information for all interesting Geant tracks. This truth information is accessible at all stages of analysis, allowing us to select interesting events as well as check on how well we reconstruct different classes of events.

In the detector response we have improved the simulation of the TPC electronic noise. For studies of order 10^6 events we can add noise from forced-trigger events which captures noise at all relevant frequencies and includes many of the possible correlations. For studies of order 10^9 events we do not have enough forced-trigger events and use a noise model, reproducing the power spectral density of the measured noise. In the 2013 run we had high and low gain ADCs for each channel, increasing the dynamic range. We have added response support for this and are currently verifying the validity. Many run-specific parameters, such as thresholds, pedestals, timing offsets and some gains, are taken from a database allowing us to simulate the 2013 or 2011 run conditions with no changes to the code.

In our first large-event sample test we generated 2×9 μ^- and 2×9 μ^+ events with approximately half of each stopping in the TPC gas. We found the μ^+ lifetime depended on the stop position in the TPC. This was traced to an artifact of the generated noise (the high-pass filter had a transient at the beginning of each sequence) that enabled the Michel positron to extend the cluster to a veto pad even though it deposited negligible energy. This artifact has been fixed and now the μ^+ lifetime is independent of stop position.

*Visiting faculty, Regis University, Denver, CO.

Our immediate future plans include creating 2×9 Geant μ^- events and selecting on the fusion to the proton-triton channel for further processing. This p-t-enhanced sample will help us quantify how much this fusion channel affects the lifetime and, if it is significant, determine how to mitigate the effect. For now we will simulate the TPC conditions from the 2011 run. Running Geant will be done on the Lonestar Linux cluster where we can run 1000 jobs in parallel so the real time is only a few hours.

On a slightly longer time scale we want to understand the TPC response to the highly ionizing fusion products, primarily ^{3}He but also the triton, proton and μ^3He ions. We observe about half of the expected ionization from ^{3}He, presumably mostly due to electron-ion recombination, but the triton and proton signals are much less affected. For now we are not making any strong energy cuts on the fusion products in our event analysis but if we find we need to then we will need to determine a reasonable way to model the recombination. Another tempting project is to add N_2 impurities into the TPC gas.

AlCap

4.18 Charged-particle emission after muon capture, the AlCap experiment

D. W. Hertzog, R. Hong, P. Kammel, M. H. Murray, and F. Wauters

The observation of neutrino flavor oscillation means that lepton number is not fully conserved. However, the predicted charged-lepton flavor violation (CLFV) by a minimal extension of the Standard Model including massive neutrinos is extremely small. Thus, any experimental observation of CLFV is an unambiguous signal of new physics. Various extensions to the Standard Model predict CLFV rates that are within reach of next-generation experiments, probing new physics phenomena both at the grand unified theory (GUT) and the TeV scale[1]. Two new experiments searching for CLFV in the $\mu N \to eN$ process are under construction, Mu2e at FNAL and COMET at J-PARC, both aiming at a sensitivity better than 10^{-16} to improve current limits by a factor of 10000. Both experiments utilize a multi-kW proton beam to produce a high-intensity negative muon beam. The event signature for the CLFV process, $\mu^- + N(A,Z) \to e^- + N(A,Z)$, is a mono-energetic electron with an energy of about 105 MeV, far above the endpoint energy of the Michel spectrum (52.8 MeV).

Candidate electrons are subsequently detected by a cylindrical tracker and an electromagnetic calorimeter. A major background for these detectors arises from muonic capture on the target material, $\mu^- + N(A,Z) \to \nu_\mu + N(A,Z-1)$. This process is often accompanied by the emission of charged particles, neutrons, and photons. In particular, protons with a momentum in the range of the candidate electrons dominate the background for the tracking detector. There are no experimental data in the relevant energy range on charged-particle

[1] Y. Kuno and Y. Okada, Rev. Mod. Phys. **73** 151-202 (2001).

emissions following muon capture on Al and Ti, two candidate target materials. The AlCap experiment is a joint effort by the COMET and Mu2e collaborations, led by the University of Washington and Osaka University, to measure their energy spectrum and yield. These data will serve as an important input for the optimization of the Mu2e and COMET tracking detectors.

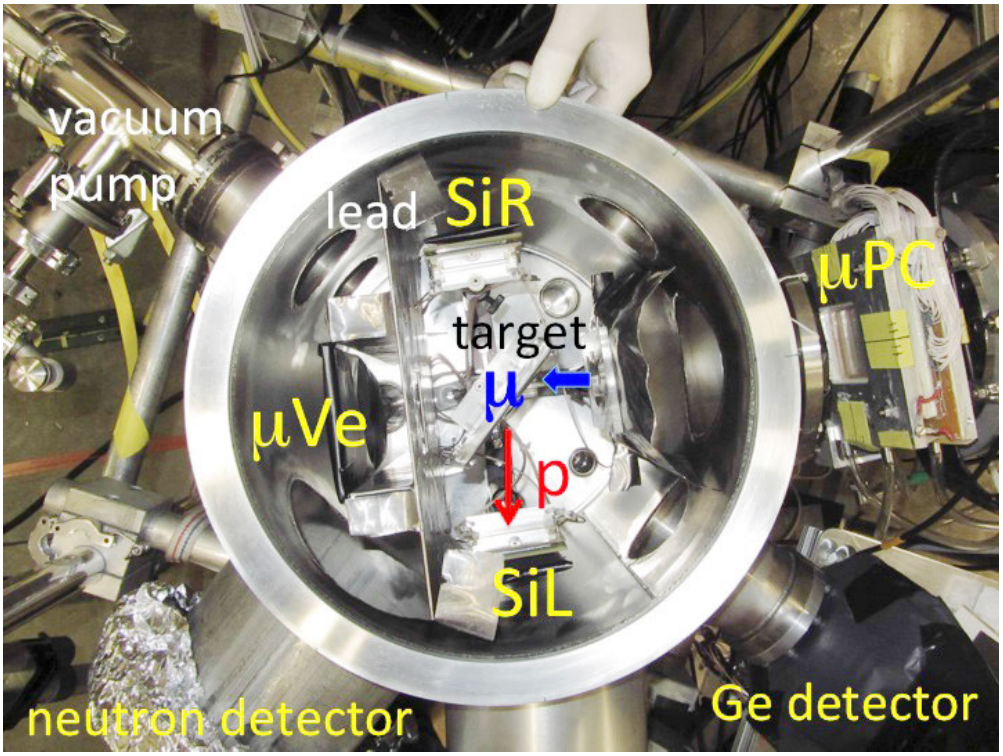

Figure 4.18-1. View into AlCap vacuum chamber.

During 2013 the AlCap detector was built at UW; in July several collaborators from the US and Japan visited our lab for a 2-week work party. In December, 2013, a first experimental run was performed at the πE1 beam line at the Paul Scherrer Institute with the setup shown in Fig. 4.18-1. Low-energy muons were stopped in 50- and 100-μm Al and Si targets inside a vacuum chamber. Charged particles emitted from the foils are detected by silicon detector packages, labeled **SiL**eft and **SiR**ight according to their position relative to the muon beam. Several other detectors, including muon beam counters, a germanium detector, plastic scintillators to detect electrons and neutron detectors, completed the system. The main observable is the spectrum of emitted charged particles dN_c/dE which is used to extract the differential capture rate $d\Lambda/dE$

$$\frac{dN_c}{dE}(E_f) = N_\mu \times \epsilon_C \times \int_0^\infty k(E_f, E_i)\frac{d\Lambda}{dE}(E_i)dE_i \tag{1}$$

The number of muon stops N_μ is optimized and calibrated by observing characteristic muonic X-rays with a high-rate Ge detector, see Fig. 4.18-2. The range distribution is constrained by the symmetry of the setup and directly measured. The detection efficiency ϵ_C will be determined by Monte Carlo and with an active silicon target. During the path through the foil protons lose energy as characterized by the response function $k(E_f, E_i)$. The small 1-3% momentum bin of the beam line allows us to stop several percent of the muons in very thin targets, keeping these distortions small. All materials in the line of sight to the detectors are shielded with lead, where stray muons are short-lived. The Si package consists of a 65-μm-thick ΔE and a 1500-μm-thick E counter to permit particle identification as shown in a first preliminary aluminum capture spectrum, Fig. 4.18-2. The analysis framework and Monte Carlo simulation are nearly finished; the data are currently being analyzed. A second run to increase statistics, measure additional targets and study systematics is being planned.

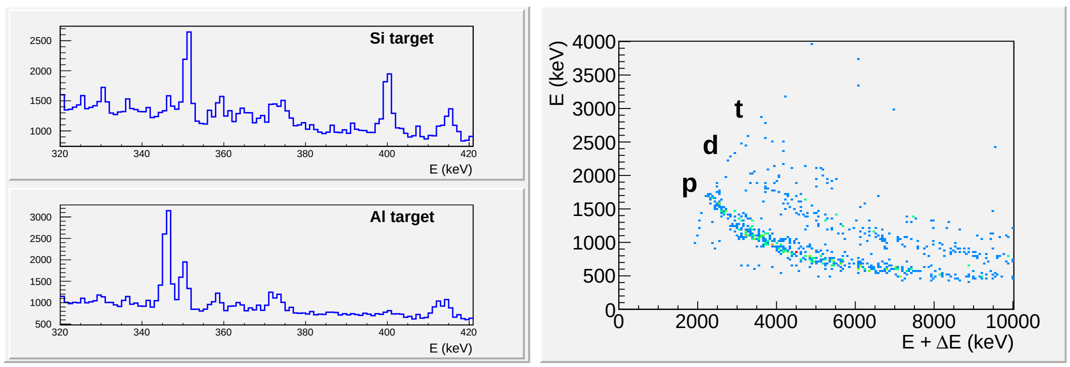

Figure 4.18-2. left: X-ray spectra from silicon (top), and aluminum (bottom). The K_α of silicon (400.2 keV) and aluminum (346.8 keV) are clearly visible; background peaks are from wall materials. right: ΔE vs $E + \Delta E$ scatter plot from 100-μm Al target discriminating between p, d and t capture products.

5 Axion searches

ADMX (Axion Dark Matter eXperiment)[1]

5.1 Status of the ADMX experiment

C. Boutan, M. Hotz, D. Lyapustin, L. J Rosenberg, G. Rybka, A. Wagner, and D. I. Will

The Axion Dark Matter eXperiment (ADMX) is a large-scale RF-cavity search for galactic dark-matter axions. The ADMX collaboration has operated a series of dark-matter axion searches since the mid-1990s, the most recent of which was installed at CENPA beginning in 2010. Installation of the experimental apparatus was completed in late 2013 and operation of the experiment proceeded soon afterward. ADMX is currently searching for dark-matter axions in the range of approximately 10 μeV with a series of cryogenic and amplifier upgrades planned to improve the sensitivity and search rate of the experiment.

Figure 5.1-1. Progress of ADMX experiment site at CENPA. *Left:* Experiment site early 2013, showing clean room with experimental insert, helium liquefaction system, and data acquisition racks. *Right:* Helium liquefaction system commissioned spring of 2013.

The axion was postulated three decades ago to explain why QCD conserves the discrete symmetries P (parity) and CP (charge conjugation times parity). QCD's predictions depend upon a parameter θ. When θ differs from zero, QCD violates P and CP. Since the strong interactions appear to be P- and CP-symmetric in the laboratory, θ must be very small. The upper limit on the neutron electric-dipole moment requires $|\theta| < 10^{-10}$. However, in the Standard Model, P- and CP-violation by the weak interactions feeds into the strong interactions so that the expected value of θ is of order unity. The inability of the Standard Model to account for P- and CP-conservation by the strong interactions is called the "strong CP problem". Peccei and Quinn proposed a solution to this problem in which the Standard Model is modified so that θ becomes a dynamical field and relaxes to zero[2]. The theory's

[1]ADMX is supported by the DOE Office of High-Energy Physics and makes use of CENPA resources by recharge to the cost center.

[2]R. D. Peccei and H. R. Quinn Phys. Rev. Lett. **38**, 1440 (1977).

underlying broken continuous symmetry results in the existence of a new particle called the axion. The axion is the quantum of oscillation of the θ field and has zero spin, zero electric charge, and negative intrinsic parity. So, like the neutral pion, the axion can decay into two photons.

Despite, however, the prodigious predicted local density of dark-matter axions (in the neighborhood of 10^{14}/cc), the expected electromagnetic signal would be extraordinarily weak, around 10^{-23} W in the ADMX apparatus. Our present ADMX Collaboration (with original core institutions Washington, LLNL, Florida, NRAO and Berkeley) constructed and operated a large-scale dark-matter axion experiment that, for the first time, reached sensitivity to plausible dark-matter axions. This experiment consists of a large microwave cavity immersed in a static magnetic field. Nearby galactic-halo axions scatter from the static field and convert into microwave photons within the cavity.

The ADMX detection apparatus is essentially an extraordinarily low-noise radio receiver with a RF cavity forming a tuned tank circuit. A short electric-field probe couples power from the cavity into a cryogenic amplifier which is cooled to near the cavity temperature, around 2 K.

Figure 5.1-2. *Left:* Experiment insert under construction throughout 2013. *Right:* Extraction of ADMX insert after successful commissioning, late 2013.

The last operation of the ADMX experiment, fitted with superconducting quantum interference device (SQUID) amplifiers, completed a scan of the $1.9 - 3.5$ μeV axion-mass range and published the results for conservative estimates of dark-matter density. With further analysis we have since published a search for axions under more interesting models of how dark matter may be distributed in our galaxy[1].

[1] J. Hoskins *et al.*, Phys. Rev. D **84**, 121302(R) (2011).

The motivation for lowering the system noise temperature is clear: (i) for a given axion-photon coupling the scan rate grows inversely as the square of the system temperature and (ii) for a given scan rate the power sensitivity increases as the system temperature drops. In ADMX the system noise temperature is the noise temperature of the amplifier plus the cavity physical temperature. We developed SQUID amplifiers in the 100-1000 MHz range specifically for ADMX and this development allowed more than an order-of-magnitude reduction in system noise temperature.

Over the past year, the ADMX experiment finished a reconstruction effort (Figs. 1 and 2), underwent cold commissioning, and began taking data. ADMX has begun searching for axions in a signal-frequency range of approximately 2 GHz corresponding to a mass of about 10 μeV. Operation of a SQUID amplifier has been demonstrated within the experiment at CENPA, but the sensitivity is currently limited by the physical temperature of the cavity, presently 2 K, maintained by a pumped ^{4}He system. A series of cryogenic upgrades which includes the installation of a pumped ^{3}He system and ultimately a dilution refrigerator will permit the experiment to achieve a physical temperature of 100 mK. Installation of the dilution refrigerator should be completed by late 2014 permitting a nearly a two-order-of-magnitude improvement in axion-search rate.

6 Relativistic Heavy Ions

6.1 UW URHI program overview

T. A. Trainor

The UW URHI program (Event structure or Estruct program, in cooperation with the URHI group at UT-Austin) studies collision processes in high energy nuclear collisions at the RHIC, including yields, spectra and correlations from p-p and A-A collisions. A major result of the program has been establishment of a three-component model of high-energy nuclear collisions including a universal soft component resulting from projectile nucleon dissociation, a hard component arising from large-angle-scattered partons fragmenting to jets, and a nonjet quadrupole. The jet component has been related quantitatively to perturbative QCD (pQCD) predictions in all cases. The nonjet quadrupole, conventionally associated with elliptic flow, has characteristics inconsistent with a hydro interpretation. Estruct results generally contradict conventional claims for formation of a quark-gluon plasma (QGP) or "perfect liquid."

Several Estruct papers have dealt with misidentification of jet structure in spectra and correlations as transverse flows: radial, elliptical and more recently triangular and other "higher-harmonic" flows. Radial flow is identified by fitting p_t spectra with a so-called blast-wave model including radial flow parameter β_t. But the same spectra can be decomposed into soft and hard components with no real evidence of radial flow. The hard component, described quantitatively by a pQCD prediction of jet fragmentation, is the source of β_t in the blast-wave fits. Jet-related angular correlations are identified as flows via naïve Fourier fits to azimuth projections. A recent Estruct paper refutes such claims for "triangular flow[1]."

A common element in the disconnect between Estruct results and QGP claims is misidentification of minimum-bias (MB) jet manifestations (complete hadron fragment contribution from the unrestricted jet spectrum) as manifestations of a flowing dense medium. To better establish the properties of MB jets in p-p and A-A collisions a recent series of studies was undertaken. A universal parametrization of measured jet spectra from the ISR and Sp$\bar{\text{p}}$S describing all jets from p-p collisions below $\sqrt{s} = 1$ TeV has been formulated that describes jet production accurately down to 3-GeV jets (apparent kinematic limit on jet production)[2].

An analysis technique has been developed to isolate a jet-related hard component from trigger-associated (TA) correlations in 200-GeV p-p collisions[3]. The highest-momentum particle in each collision event (trigger hadron) serves as a proxy (with some probability) for a scattered parton. Other hadrons associated with the trigger may then be jet fragments. A two-component model (TCM) of TA correlations derived from the TCM for single-particle p_t spectra is used to isolate the jet-related hard component from a combinatoric soft background[4]. The result has clear similarities to measured jet fragmentation functions.

---

[1] R. L. Ray, D. J. Prindle and T. A. Trainor, Phys. Rev. C **88**, **044920** (2013), arXiv:1308.4367.
[2] T. A. Trainor, arXiv:1403.3685.
[3] T. A. Trainor and D. J. Prindle, arXiv:1310.0408.
[4] T. A. Trainor and D. J. Prindle, Phys. Rev. D **88**, 094018 (2013) , arXiv:1307.1819.

A recent EM calorimeter study of transverse energy E_t production in 200-GeV Au-Au collisions claims that hadron and E_t production actually follow a constituent-quark (CQ) scaling trend representing only soft production, with no significant jet contribution. Examples are provided in which the TCM apparently fails to describe MB cross section distributions on n_{ch} and E_t. A comparison of hadron production at 200 GeV and 2.76 TeV seems to indicate simple proportionality despite a "large increase" in jet production. The two-component model including jet production as a major component is therefore rejected in favor of the CQ model with production arising only from soft string fragmentation. A detailed analysis of the new E_t data and the relation of the TCM to MB distributions refutes such claims[5].

A recent study of mean transverse momentum $\langle p_t \rangle$ vs multiplicity n_{ch} at the LHC for p-p Pb-Pb and p-Pb collisions poses major difficulties for theory Monte Carlos. Principal features include $\langle p_t \rangle$ in p-p collisions rising much faster with n_{ch} than in Pb-Pb collisions and a p-Pb trend intermediate between p-p and Pb-Pb. Given that the $\langle p_t \rangle$ increase in A-A collisions is conventionally attributed to radial flow, are collective effects present in small collision systems at the LHC? The TCM provides a detailed quantitative description of all LHC $\langle p_t \rangle$ data and reveals some interesting new insights into collision mechanisms at the RHIC and LHC[6].

As a follow up to our previous TA analysis of 200-GeV p-p collisions we have undertaken a theoretical program that combines measured fragmentation functions (FFs) from e^+-e^- and p-$\bar{p}$ collisions with the jet spectrum model of Ref. 2 to generate a prediction for the TA hard component as described in (Sec. 6.2), (Sec. 6.3), (Sec. 6.4), and (Sec. 6.5). The goal is to establish a complete description of MB jets in yields, spectra and correlations (angular and TA) for p-p collisions as a preliminary to the same description in A-A collisions. Any description of high energy nuclear collisions must then account for the MB jet contribution before invoking novel processes.

In support of that program we have developed a universal model of jet spectra for all accessible p-p collision energies above 10 GeV and for all jet energies down to a kinematic limit near 3 GeV as described in (Sec. 6.6), (Sec. 6.7), and (Sec. 6.8). Aside from comparisons with published jet spectra we have established that our jet spectrum model combined with p-$\bar{p}$ FFs provides a quantitative description of the hadron spectrum hard component from 200-GeV p-p collisions.

In (Sec. 6.9), (Sec. 6.10), and (Sec. 6.11) we establish that the TCM provides an accurate quantitative description of MB distributions on n_{ch} and E_t. We demonstrate that the TCM combined with an energy scaling trend inferred from RHIC Au-Au data below 200 GeV accurately predicts the hadron production trend for Pb-Pb collisions at 2.76 TeV. We establish the critical role of production fluctuations in MB distributions for detectors with small angular acceptance (PHENIX). And we show that conjectured CQ scaling is not required by E_t measurements, whereas the TCM including strong pQCD jet production is required by other aspects of data.

[5] T. A. Trainor, arXiv:1402.4071.
[6] T. A. Trainor, arXiv:1403.6494.

In (Sec. 6.12) and (Sec. 6.13) we address $\langle p_t \rangle$ vs n_{ch} data from the LHC. We demonstrate that all $\langle p_t \rangle$ data can be represented by a TCM, and that the hard component from *p-p* $\langle p_t \rangle$ data scales with collision energy just as expected from the jet spectrum model described above if the hadron spectrum hard component is fragments from MB jets. We show that the $\langle p_t \rangle$ trend for 2.76-TeV Pb-Pb collisions is remarkably similar to that for Au-Au at 200 GeV except that a "sharp transition" in jet properties observed at 200 GeV occurs for more-peripheral collisions at the higher energy. The $\langle p_t \rangle$ evolution is otherwise consistent with pQCD.

6.2 Trigger-associated analysis of 200-GeV proton-proton collisions

D. J. Prindle and T. A. Trainor

We have analyzed minimum-bias trigger-associated (TA) correlations in 200-GeV p-p collisions primarily to study hard scattering[1]. In this analysis we define the highest y_t particle in the event to be the trigger, all others are associated. The projection onto y_{trig} gives the trigger spectrum weighted by event multiplicity. We use the spectrum two-component model (TCM) to calculate the TA trigger spectrum and find excellent agreement[2]. The trigger spectra are multiplicity dependent only because the relative soft-hard fractions are multiplicity dependent. The raw TA correlation is weighted by the trigger spectrum. We remove this weighting by dividing the 2D TA histogram by the 1D trigger spectrum; A = F/T where the raw 2D TA correlation is called F, T is the 1D spectrum and A is the 2D histogram showing the associated spectrum dependence on y_t. A is shown in Fig. 6.2-1, left panel.

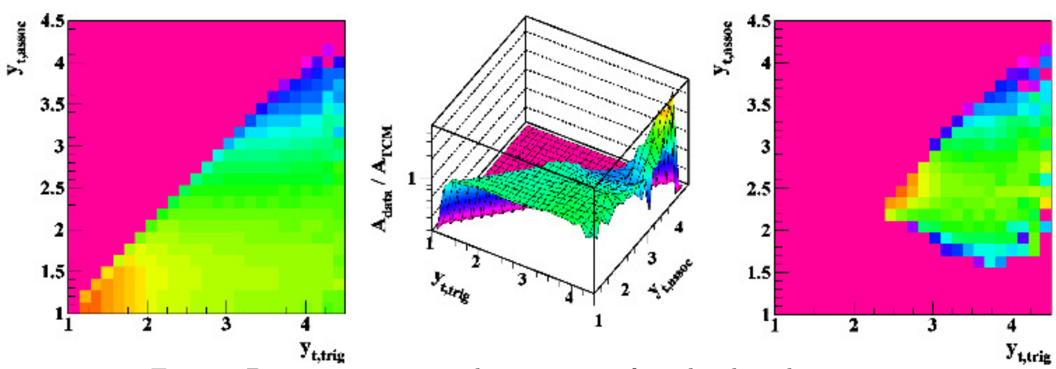

Figure 6.2-1. First: 2D trigger-associated spectrum after dividing by trigger spectrum. Second: Ratio $\mathrm{A_{data}/A_{TCM}}$ showing soft component is quantitatively described by the TCM. Third: Hard component of $\mathrm{A_{data}}$ after subtraction of soft component. All panels are for a particular multiplicity bin. The shape of the hard component is independent of multiplicity.

A is dominated by the soft component. We can calculate the TA correlations in the spectrum TCM model and divide by T to get $\mathrm{A_{TCM}}$. This model describes the soft component quantitatively as demonstrated by the data to model ratio shown in Fig. 6.2-1, middle panel. This gives us confidence to subtract the soft component leaving the hard component, as

[1]CENPA Annual Report, University of Washington (2013) p. 101.
[2]CENPA Annual Report, University of Washington (2013) p. 102.

shown in Fig. 6.2-1, right panel. The soft component falls off quickly with y_t so even if the model is a bit off it only affects the lowest y_t of the hard component.

In isolating the hard component of the TA correlations we verify the hypothesis that the hard component of the spectrum TCM is due to hard scattering. We can study the hard component of TA correlations as a function of angle (comparing with underlying-event studies) and charge dependence (checking charge ordering) as well as multiplicity. Comparing with theoretical calculations based on p-p FFs gives further confidence this hard component is due to hard scattering.

6.3 Partitioning p-p FF ensembles to trigger and associated components

T. A. Trainor

A two-component model (TCM) may be applied to p-p trigger-associated (TA) correlations on transverse rapidity y_t to isolate a 2D hard component (HC) nominally representing hadron fragments from jets. To confirm that interpretation we should predict the TA HC using measured jet fragmentation functions (FFs). The first step is partitioning FFs into trigger and associated components. An FF ensemble $D_u(y|y_{max})$ $[y_{max} = \ln(2E_{jet}/m_\pi)]$ can be partitioned into trigger and associated components by defining a void probability. A trigger (largest rapidity) particle appearing at some rapidity $y = \ln[(E + p)/m_\pi]$ implies a void (no particles with larger rapidity) above that point, with void probability $G_t(y)$ derived from the mean fragment number per p-p collision within the acceptance. The mean number of dijet fragments above y_{trig} within 4π is

$$n_\Sigma(y_{trig}|y_{max}) = \int_{y_{trig}}^{\infty} dy D_u(y|y_{max}). \tag{1}$$

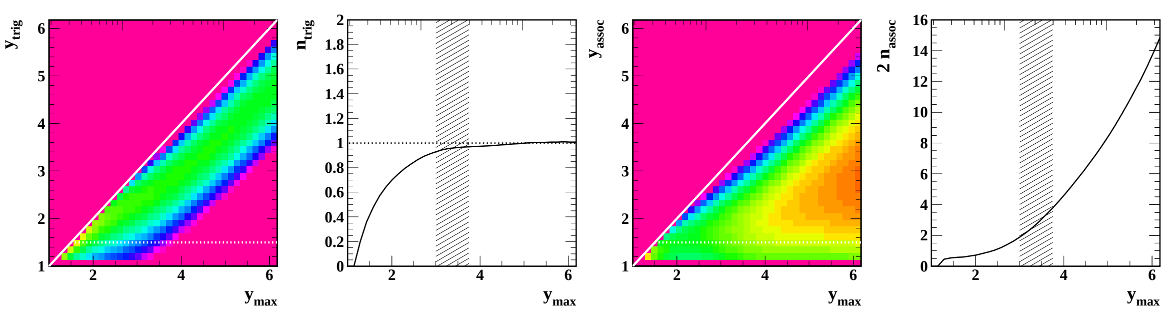

Figure 6.3-1. First: The trigger component of the FF ensemble from LEP/HERA e^+-e^- collisions. Second: Projection of the first panel onto parton rapidity y_{max} to obtain the trigger number ≈ 1. Third: The associated-particle component of the FF ensemble. Fourth: Projection of the third panel onto parton rapidity y_{max} to obtain the associated-particle number $\approx 2n_{ch,j}(y_{max}) - 1$. The hatched bands indicate a lower limit on jet energies.

The void probability is then defined by $G_t(y_{trig}|y_{max}) = \exp[-\kappa\epsilon n_\Sigma(y_{trig}|y_{max})]$, where product $\kappa\epsilon$ includes (a) factor $\epsilon(\Delta\eta) \in [0.5, 1]$ representing the dijet η-acceptance and (b) factor $\kappa \geq 1$ representing effects of non-Poisson correlations. Given trigger (void) probability

$G_t(y)$ we define complementary associated probability $G_a = 1 - G_t$. We obtain trigger and associated FF components $D_t(y_{trig}|y_{max})$ and $D_a(y_{assoc}|y_{max})$ by combining measured $D_u(y|y_{max})$ with factors $G_\alpha(y_\beta|y_{max})$ where α is t or a and β is *trig* or *assoc*. That system is based on fragments from single dijets appearing in hard p-p events. The presence of a soft-spectrum component in hard p-p events introduces additional factors that can be computed. Fig. 6.3-1 (left panels) shows (a) trigger component $D_t(y_{trig}|y_{max})$ and (b) its projection $n_{trig}(y_{max})$ (one trigger per dijet). Fig. 6.3-1 (right panels) shows (c) associated component $D_a(y_{assoc}|y_{max})$ and (d) its projection $2n_{assoc}(y_{max})$. The void probability assumes $\kappa = 1.3$ from TA analysis and $\epsilon(\Delta\eta) \approx 0.65$ for η acceptance $\Delta\eta = 2$. Trigger multiplicity $n_{trig}(y_{max})$ should integrate approximately to 1 and does so for e^+-e^- FFs and $y_{max} > 3$ ($E_{jet} >$ 1.5 GeV). The same method can be applied to partition FFs from p-p or p-$\bar{p}$ collisions.

6.4 Trigger-fragment vs jet-energy conditional distributions

T. A. Trainor

Given a p-p or p-$\bar{p}$ FF ensemble conditional on parton energy partitioned into trigger and associated components a second step is to construct a trigger hadron spectrum reflecting an average over the underlying minimum-bias (MB) parton (jet) spectrum. Fig. 6.4-1 (first panel) shows the 2D joint trigger-parton distribution $F_{tp}(y_{trig}, y_{max})$ obtained as the Cartesian product of the FF trigger component $D_t(y_{trig}|y_{max})$ with pQCD parton spectrum $S_p(y_{max})$. The 2D distribution mode corresponds to 3-GeV partons (gluons) and hadron trigger momenta $\approx$ 1 GeV/c. Near the 2D mode quark and gluon FFs are essentially the same. Fig. 6.4-1 (second panel) shows the marginal projections of $F_{tp}(y_{trig}, y_{max})$ in the first panel compared with other results. The projection onto y_{max} is the parton/jet spectrum model $S_p(y_{max})$ (dash-dotted curve) introduced to construct $F_{tp}(y_{trig}, y_{max})$ and compared to a measured jet spectrum (open squares). The projection onto y_{trig} (solid curve) is the sought-after trigger hadron spectrum $S_t(y_{trig})$ compared with measured spectrum hard component (solid points).

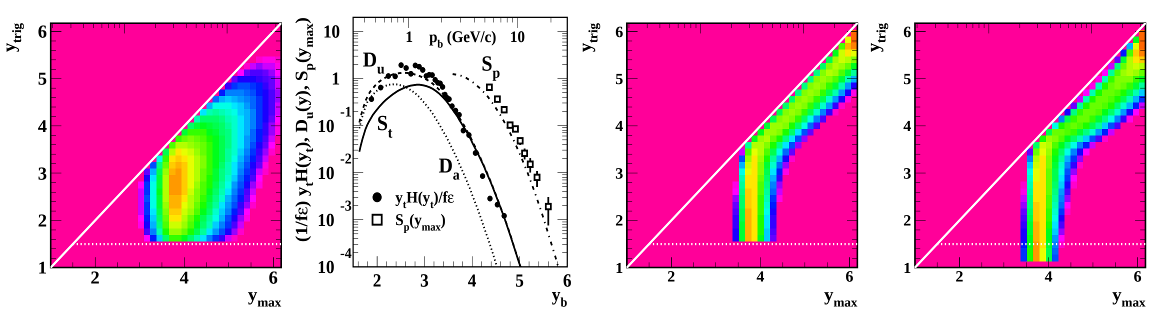

Figure 6.4-1. First: Joint distribution $F_{tp}(y_{trig}, y_{max})$ obtained from measured FFs and jet spectra. Second: Marginal projections of $F_{tp}(y_{trig}, y_{max})$ compared to data. Third: Conditional distribution $D_p(y_{max}|y_{trig})$ for gluon jets from e^+-e^- collisions. Fourth: Conditional distribution $D_p(y_{max}|y_{trig})$ for quark jets from p-$\bar{p}$ collisions.

The next step requires obtaining the distribution of parton/jet rapidity conditional on hadron trigger rapidity $D_p(y_{max}|y_{trig})$ using Bayes' theorem. The first line of

$$\begin{aligned} F_{tp}(y_{trig}, y_{max}) &= D_t(y_{trig}|y_{max})S_p(y_{max}) \\ &= D_p(y_{max}|y_{trig})S_t(y_{trig}) \end{aligned} \quad (1)$$

has been constructed from parametrizations of measured FF ensembles and parton spectra. The second line is an alternative factorization of the 2D joint probability, and we obtained the factor $S_t(y_{trig})$ in the left panels assuming that $D_p(y_{max}|y_{trig})$ is unit-normal on y_{max} (one jet per hadron trigger). We then obtain the required $D_p(y_{max}|y_{trig}) \approx F_{tp}(y_{trig}, y_{max})/S_t(y_{trig})$ as an example of Bayes' theorem. Fig. 6.4-1 (right panels) shows parton spectra $D_p(y_{max}|y_{trig})$ unit-normal on y_{max} for each y_{trig} condition for two systems that can be compared with $D_t(y_{trig}|y_{max})$ approximately unit-normal on y_{trig} for each y_{max} condition. The trigger marginal is broad whereas the parton marginal is a steeply-falling power law. For given parton rapidity the trigger mode lies substantially below the kinematic limit, whereas for given trigger rapidity the parton mode lies just above the kinematic limit. For triggers with $y_{trig} < 3.5$ ($p_{trig} < 2$ GeV/c – most hadron triggers) 3-GeV minijets dominate.

6.5 Predicting the p-p hadron TA hard component from p-p̄ FFs

D. J. Prindle and T. A. Trainor

Conditional and marginal distributions derived from measured fragmentation functions (FFs) and jet spectra can be combined to predict trigger-associated (TA) hard components from *p-p* collisions as follows. The required method to predict the hadron hard component TA conditional distribution is expressed as a convolution integral

$$D_a(y_{assoc}|y_{trig}) = \int dy_{max} D_a(y_{assoc}|y_{max}) D_p(y_{max}|y_{trig}). \quad (1)$$

An ensemble of associated-hadron FF components $D_a(y_{assoc}|y_{max})$ is averaged over a subset of parton rapidities determined by the trigger condition as represented by $D_p(y_{max}|y_{trig})$. For a given y_{trig} condition all associated FFs $D_a(y_{assoc}|y_{max})$ are truncated such that $y_{assoc} < y_{trig}$. The 2D distribution then extends up to the diagonal, whereas the $D_a(y_{assoc}|y_{max})$ do not.

Fig. 6.5-1 (left panels) shows a TA prediction using FFs for light quarks from p-$\bar{p}$ collisions. The effect of the p-$\bar{p}$ FF cutoff near $y = 1.5$ (white dotted line) observed in p-$\bar{p}$ FF data is apparent. The second panel shows a projection onto y_{trig} giving the associated-fragment yield per dijet $2n_{assoc} \equiv 2n_{ch,j}(y_{trig}) - 1$. Generally, gluon FFs manifest substantially larger fragment multiplicities and significantly lower modes on y than light-quark FFs. Higher-energy jets should be predominantly from light (valence) quarks. Lower-energy jets dominated by small-x gluons are similar to quark jets because the effective color charge is reduced.

Fig. 6.5-1 (third panel) shows a measured TA hard component from 200-GeV *p-p* collisions. The dashed and dotted lines show boundaries common to several data conditions. Theory and data histogram amplitudes are similar, indicating that hadrons associated with the measured

TA HC are comparable in number to those expected from the dijet frequency per NSD p-p collision and typical jet fragment number. In the fourth panel a projection of the data in the third panel onto $y_{t,trig}$ is compared with predictions for four systems: e^+-e^- or p-$\bar{p}$ vs quarks (solid) or gluons (dashed). Larger trigger rapidities favor p-$\bar{p}$ FFs and quark jets. Smaller trigger rapidities transition toward e^+-e^- jet trends. In a previous study we used a TCM for p-p single-particle hadron spectra to generate a TA model for all hadrons with which we isolated a TA data hard component. In this study we have used measured FFs and jet spectra to generate a pQCD jet prediction for the measured TA hard component.

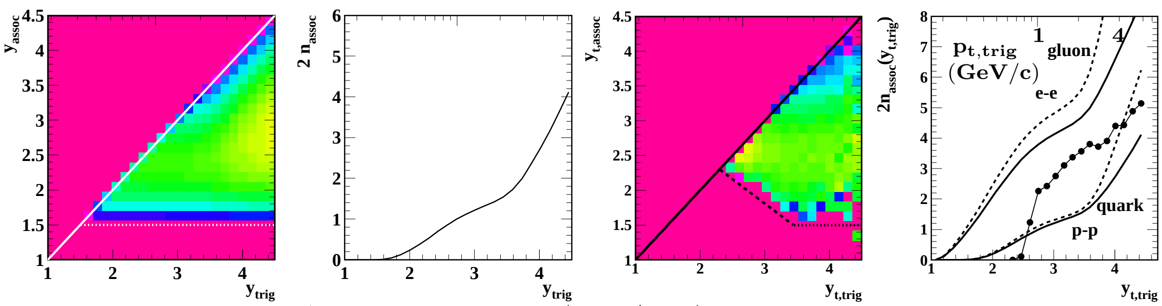

Figure 6.5-1. First: TA hard component $D_a(y_{assoc}|y_{trig})$ for quark jets from p-p collisions. Second: Projection onto trigger rapidity y_{trig}. Third: Measured TA hard component from 200-GeV p-p collisions. Fourth: Projections onto $y_{t,trig}$ and theory-data comparisons.

6.6 Universal model for jet (parton) energy spectra from p-p collisions

T. A. Trainor

The role of low-energy jets in A-A collisions at the RHIC and LHC has been sharply contested in favor of flow manifestations. It is therefore desirable to establish a comprehensive description of low-energy jet systematics based on p-p jet data. Fig. 6.6-1 (first panel) shows R807 and UA1 jet spectra for five p-p collision energies from the ISR and Sp$\bar{\text{p}}$S. Those innovative analyses provided unique access to very low jet energies. Fig. 6.6-1 (second panel) shows the same jet spectra (points) rescaled vertically by factor $[\Delta y_b]^2 = [\log(\sqrt{s}/10\text{ GeV})]^2$ (based on non-eikonal dijet production in p-p and measured jet-correlation energy trends at RHIC) and parton rapidity difference $y_{max} - y_{m0} = \ln(2E_{jet}/3\text{ GeV})$ rescaled horizontally by beam rapidity difference $\Delta y_{max} = y_b - y_{m0} = \log(\sqrt{s}/3\text{ GeV})$ to normalized rapidity u. All jet data for p-p collision energies below 1 TeV fall on a common locus $0.15\exp(-u^2/2\sigma_u^2)$ (solid curve). The parametrized jet (parton) spectrum model conditional on beam rapidity is then

$$S_p(y_{max}|y_b) \equiv \frac{d^2\sigma_j(\sqrt{s})}{dy_{max}d\eta} \quad = \quad p_t\frac{d^2\sigma_j}{dp_t d\eta} = 0.026\Delta y_b^2 \frac{1}{\sqrt{2\pi\sigma_u^2}} e^{-u^2/2\sigma_u^2}, \tag{1}$$

where $\sigma_u \approx 1/7$ is determined empirically from the jet data. All jet production over nine decades is represented by four parameters. Endpoints 10 GeV and 3 GeV are closely related by observed limits on charged-hadron jet production from small-x partons. The result is a universal curve that describes all jet spectrum data for p-p collision energies below 1 TeV.

Fig. 6.6-1 (third panel) shows the ISR and Sp$\bar{\text{p}}$S cross-section data from the first panel plotted in a conventional log-log format, the curves defined by Eq. (1) with beam energies noted. The dotted curve corresponds to $\sqrt{s} = 630$ GeV. The curves extend to $u = 0.9$ corresponding to partons with momentum fraction $x \approx 2/3$ where the kinematic limit of projectile-proton energy is determining. We can then integrate the individual spectrum for each energy to obtain corresponding $d\sigma_j/d\eta(\sqrt{s})$ and multiply those by an empirical expression for the effective 4π η acceptance $\Delta\eta_{4\pi}$ to obtain the energy trend for the total cross section σ_{j0}. Fig. 6.6-1 (fourth panel) shows UA1 measured total cross sections for MB jet production. The curve is defined by integrating Eq. 1 to obtain $\sigma_{j0}(\sqrt{s}) \approx 0.034\Delta y_b^3 \Delta y_{max}$.

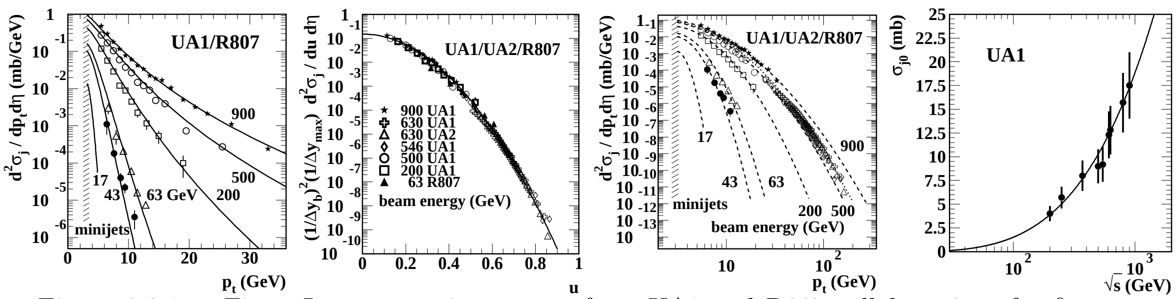

Figure 6.6-1. First: Low-energy jet spectra from UA1 and R807 collaborations for five collision energies. The curves are a universal spectrum model. Second: ISR and Sp$\bar{\text{p}}$S jet spectrum data rescaled to a single universal curve described by Eq. (1). Third: Spectrum data for low- and high-energy jets (including UA2 data) compared to the jet spectrum model. Fourth: Jet total cross sections from UA1 compared to the jet spectrum model.

6.7 p-p jet spectrum collision-energy systematics

T. A. Trainor

In order to predict the absolute yield and spectrum hard component (fragment distribution) from minimum-bias jets in *p-p* collisions we require the jet production rate per non-single-diffractive (NSD) *p-p* collision. Fig. 6.7-1 (first panel) shows the jet differential cross section on η obtained by integrating (Sec. 6.6 Eq. 1)

$$\frac{d\sigma_j}{d\eta} \approx 0.026\Delta y_b^2 \Delta y_{max} \tag{1}$$

which defines the solid curve. The solid points represent jet spectra for four collision energies. The open circle predicts the jet cross section for 7 TeV. Fig. 6.7-1 (second panel) shows the corresponding jet total cross section $\sigma_{j0}(\sqrt{s})$. From comparison of measured total cross sections and jet spectra we infer the energy trend for the effective 4π η acceptance $\Delta\eta_{4\pi} \approx 1.3\Delta y_b$. Combined with Eq. (1) the *p-p* total cross section for jets within 4π is then

$$\sigma_{j0}(\sqrt{s}) = \Delta\eta_{4\pi}\frac{d\sigma_j}{d\eta} \approx 0.034\Delta y_b^3 \Delta y_{max}. \tag{2}$$

plotted as the solid curve. The solid points (UA1 measured total cross sections) are consistent with the energy dependence of Eq. (2). The dashed curves corresponding to $0.13\Delta y_b^2 \Delta y_{max}$ and $0.009\Delta y_b^4 \Delta y_{max}$ provide an indication of the uncertainty in the form of Eq. (2).

Fig. 6.7-1 (third panel) shows parametrizations of several cross-section data trends on p-p collision energy. The inelastic cross section is described by $\sigma_{\text{inel}} = [32 + \Delta y_b^2]$ mb (topmost curve). The other trends are expressed as fractions $\sigma_{\text{SD}} = 0.17\sigma_{\text{inel}}$ and $\sigma_{\text{NSD}} = 0.83\sigma_{\text{inel}}$ (lower curves). At 200 GeV (open circles) $\sigma_{\text{inel}} \approx 41$ mb, $\sigma_{\text{SD}} \approx 7$ mb and $\sigma_{\text{NSD}} \approx 34$ mb. Fig. 6.7-1 (fourth panel) shows the predicted collision-energy trend for the number of dijets per NSD p-p collision $f_{NSD} = dn_j/d\eta = (1/\sigma_{\text{NSD}})d\sigma_j/d\eta$ with value $f_{NSD} \approx 0.029$ for 200-GeV collisions corresponding to $\sigma_{j0} \approx 4$ mb. Asymptotically, f_{NSD} should increase with collision energy as $\ln(\sqrt{s}/3 \text{ GeV})$ (dashed curve). The result in the fourth panel permits us to establish a direct quantitative relation between per-dijet pQCD-predicted fragment yields and momentum distributions and per-NSD-collision hard components from p-p collisions.

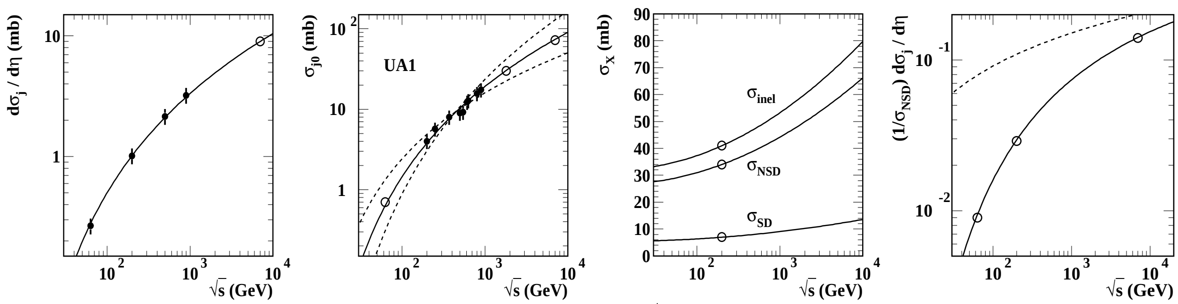

Figure 6.7-1. First: Jet differential cross section $d\sigma_j/d\eta$ vs p-p collision energy. Second: Jet total cross section σ_{j0} vs collision energy. Third: Parametrized p-p cross sections. Fourth: Dijet rate f_{NSD} per unit η and per NSD p-p collision vs collision energy. The solid curves in first, second and fourth panels represent a universal jet spectrum model.

6.8 Predicting the hadron spectrum hard component for p-p collisions

T. A. Trainor

Prediction of jet fragment distributions from p-p or A-A collisions requires a parametrization or model of measured nonperturbative fragmentation functions (FFs). To model p-p collisions we employ available FFs from p-$\bar{p}$ collisions at the Tevatron. Fig. 6.8-1 (first panel) shows FFs for ten dijet energies from 78 to 573 GeV inferred from 1.8-TeV p-$\bar{p}$ collisions (points). The solid curves are explained below. Comparison with parametrized e^+-e^- FF data (dashed curves) indicates that a substantial portion of dijets at lower fragment momenta may be missing from reconstructed p-$\bar{p}$ FFs. Fig. 6.8-1 (second panel) shows the ratio of p-$\bar{p}$ FF data in the first panel to the e^+-e^- FF parametrization for each jet energy, revealing systematic differences. The solid curve is $\tanh[(y - 1.5)/1.7]$ which describes measured p-$\bar{p}$ FFs relative to e^+-e^- FFs for jet energies below 70 GeV. The FF parametrization used for p-p collisions (solid curves, first panel) is the accurate e^+-e^- parametrization modified by the tanh factor.

Fig. 6.8-1 (third panel) shows unit-normal spectrum hard components in the form $H(y_t, n_{ch})/n_h$ from 200-GeV-NSD p-p collision for nine multiplicity classes (spanning the interval $n_{ch}/\Delta\eta \in [2, 25]$) corresponding to more than a factor 100 increase in the non-eikonal dijet rate per p-p collision. The hard component is derived from the normalized y_t spectra by subtracting fixed universal soft-component model $S_0(y_t)$. The HC has a consistent shape independent of n_{ch}

except for a contribution below 0.5 GeV/c ($y_t \approx 2$) for smaller n_{ch}. The dashed curve is unit-normal Gaussian model $H_0(y_t)$. Fig. 6.8-1 (fourth panel) shows hard-component data in the form $y_t H(y_t)$ from 200-GeV-NSD *p-p* collisions (solid points) divided by factor $f_{NSD}\epsilon(\Delta\eta)$, where $\epsilon(\Delta\eta) \in [0.5, 1]$ is the fraction of a detected dijet within acceptance $\Delta\eta$. The result is a 4π per-dijet quantity that can be compared with pQCD predictions. $\bar{D}_u(y)$ (dashed curve) provides a prediction for the HC per dijet into 4π based on a parametrization of measured *p-p* FFs and a universal jet spectrum model. The Gaussian jet (parton) spectrum model defined by Eq. (1) (dash-dotted curve) was derived from Sp$\bar{\text{p}}$S jet spectra (e.g. open squares). The pQCD HC prediction D_u (dashed curve) compares well with the y_t spectrum hard-component data (solid points). If the UA1 jet data are displaced to the left by 1 GeV or reduced by factor 2 they coincide with the parametrized parton spectrum. Either change is within the stated UA1 systematic uncertainties.

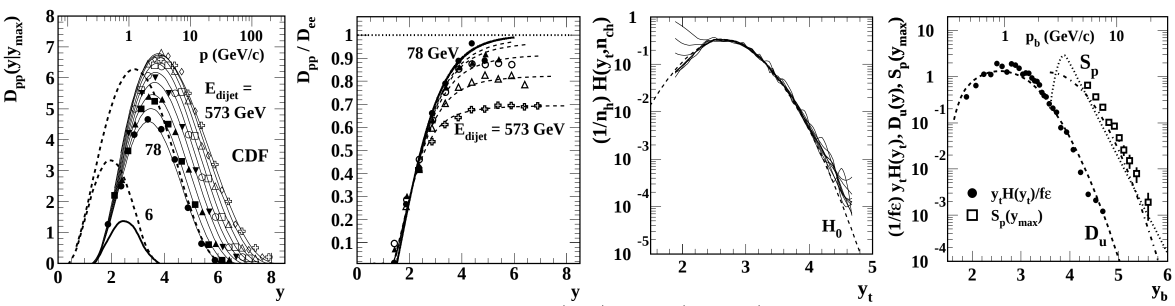

Figure 6.8-1. First: Fragmentation function (FF) data (points) from Tevatron *p*-$\bar{p}$ collisions for several energies. The solid curves represent an FF parametrization. Second: Ratios of *p*-$\bar{p}$ to e^+-e^- FFs showing systematic differences. Third: Hard components from *p-p* collisions for several collision multiplicities n_{ch}. Fourth: Comparison of a pQCD prediction (dashed curve) to a measured 200-GeV *p-p* spectrum hard component (solid points).

6.9 E_t production vs constituent quarks in RHIC Au-Au collisions

T. A. Trainor

In a recent PHENIX paper[1] it is proposed that hadron production trends on centrality from Au-Au collisions reflect so-called "constituent-quark" (CQ) N_{qp} scaling representing soft-only string fragmentation rather than a two-component soft+hard (jets) combination. Fig. 6.9-1 (first panel) shows simulated ratio N_{qp}/N_{part} (points) from Ref. 1. The solid curve is a parametrization. The triangles represent estimates for 200-GeV *p-p* collisions. Fig. 6.9-1 (second panel) shows N_{qp}/N_{part} vs pathlength ν (solid curve) with $(2/N_{part})dn_{ch}/d\eta$ distributions for three energies scaled down by common factor 1.35. The upper dashed line is the conventional TCM for 200 GeV. Ref. 1 concludes from that comparison that CQ scaling explains n_{ch} data without recourse to a TCM dijet contribution. The lower dashed and two other curves show a TCM that also describes peripheral data from 200-, 130- and 62.4-GeV collisions accurately. The substantial differences suggest that detailed comparisons between measured hadron-production trends and the N_{qp} trend for more-peripheral A-A collisions may already falsify the CQM. But that centrality interval is typically de-emphasized at RHIC.

[1] S. S. Adler *et al.* (PHENIX Collaboration), arXiv:1312.667.

Fig. 6.9-1 (third panel) shows ratio $(2/N_{part})dE_t/d\eta$ from Au-Au collisions for three energies vs centrality measured by mean participant pathlength ν. The uncertainties include total point-to-point plus common offset systematic uncertainties. The $\langle E_t\rangle$ centrality trends are described as varying "nonlinearly" with N_{part}, interpreted to imply inconsistency with the participant scaling expected from soft production and therefore apparently requiring hard scattering (dijets) and the TCM. Fig. 6.9-1 (fourth panel) shows ratio $(2/N_{qp})dE_t/d\eta$ vs centrality obtained by dividing the data in the third panel by ratio N_{qp}/N_{part} from the first panel. The ratio data above $\nu = 2$ appear to be constant within systematic uncertainties, suggesting that mid-rapidity hadron production in Au-Au collisions actually occurs by a soft process scaling with the number of CQ participants (QCD strings), not with nucleon participants. Values for 200-GeV *p*-*p* collisions are plotted at $\nu = 1.25$ ($\approx$ NSD N-N collisions). The upper *p*-*p* datum is said to confirm the self-consistency of the CQ analysis and disfavor dijet production. However, the TCM for P_t ($\approx E_t$) production is based on p_t spectrum structure including a hard component (jet fragment distribution) described quantitatively by pQCD. Thus, the relation of the conjectured CQ trend to hadron production is accidental.

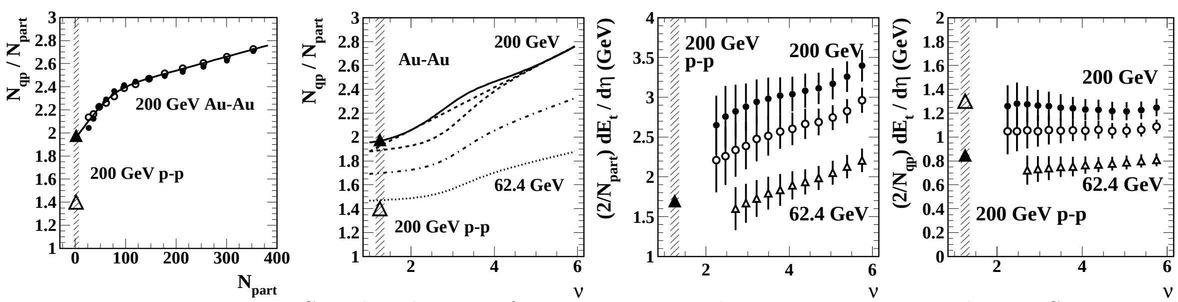

Figure 6.9-1. First: Simulated ratio of constituent quarks to participant nucleons. Second: Ratio comparison with hadron production trends. Third: E_t per-nucleon-participant production vs path length ν. Fourth: The same E_t data in ratio to CQ participant number.

6.10 A TCM description of Au-Au minimum-bias distributions on n_{ch}

T. A. Trainor

In a recent paper[1] it is claimed that the two-component (soft+hard) model (TCM) of hadron production cannot be used to describe minimum-bias (MB) cross-section distributions on charge multiplicity n_{ch} or transverse energy E_t. In fact, a data MB distribution (e.g. on n_{ch}) can be predicted quantitatively from the TCM in the following way. We assume the usual TCM yield expression for the charge yield $(2/N_{part})n_{ch} = n_{pp}[1 + x(\nu - 1)]$, where n_{pp} is the charge yield for *p*-*p* (N-N) collisions, N_{part} is the number of A-A nucleon participants and ν is the mean participant-nucleon path length. The MB distribution on $n_{ch}^{1/4}$ is then

$$\frac{d\sigma}{dn_{ch}^{1/4}} = \frac{[1 + x(\nu - 1)]^{3/4}}{1 + x(\nu - 1) + x\nu/3} \times \frac{d\sigma}{n_{pp}^{1/4} d(N_{part}/2)^{1/4}}, \tag{1}$$

where we have invoked the approximation $\nu \approx (N_{part}/2)^{1/3}$. The first factor (inverse Jacobian) can be derived from the TCM yield expression, and the second factor is a rectangular

[1] S. S. Adler *et al.* (PHENIX Collaboration), arXiv:1312.667.

MB distribution representing participant scaling. If x is constant for all centralities the first factor is approximately a straight line on ν with negative slope ($\approx 1 - 7x\nu/12$).

Fig. 6.10-1 (first panel) shows MB distributions on $n_{ch}^{1/4}$ for (a) participant scaling (dotted lines, $x = 0$) and (b) the TCM describing more-central 200-GeV Au-Au collisions (dashed lines, fixed $x = 0.1$ for all centralities). The sloping dashed line represents Eq. (1). Fig. 6.10-1 (second panel) shows the same distributions in the conventional semilog plotting format, with Jacobian factor $dn^{1/4}/dn = 1/4n^{3/4}$. Fig. 6.10-1 (third panel) shows a comparison between STAR 130-GeV h^- data (solid curve) and the corresponding TCM of Eq. (1) (dashed curve) with constant $x = 0.08$ and $n_{pp} = 2.25/2$ (approximate h^- η density near $\eta = 0$ for 130 GeV). The dotted curve represents participant scaling. This semilog plotting format obscures essential data features relating to the TCM. Fig. 6.10-1 (fourth panel) shows the same distributions in a power-law format. The dotted lines represent participant scaling and the dashed lines (for more-central collisions) represent Eq. (1) with $x = 0.08$. Each distribution integrates to $\sigma_0 = 7.2$ barns. The MB data and TCM agree within systematic uncertainties. The TCM depends only on parameters $n_{pp} \equiv 2.25/2$ and $x = 0.08$.

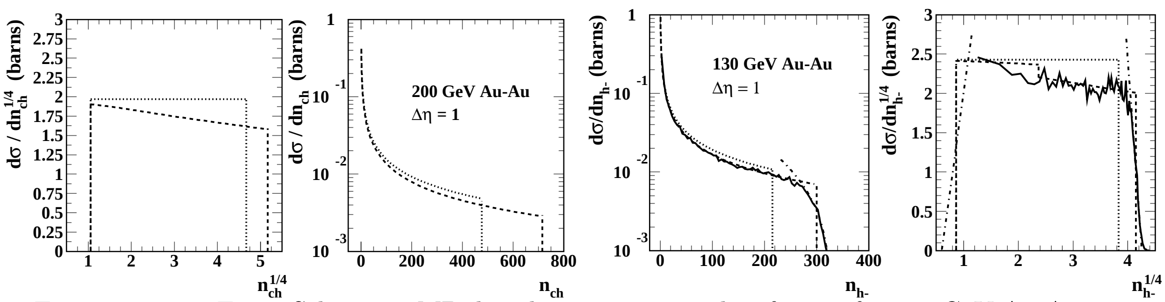

Figure 6.10-1. First: Schematic MB distribution in power-law format for 200-GeV Au-Au. Second: The same in conventional semilog format. Third: Comparison between MB data for 130-GeV Au-Au (solid curve) and TCM models (other curves). Fourth: The same in the power-law format revealing details obscured in the semilog format.

6.11 Energy dependence and fluctuations in minimum-bias distributions

T. A. Trainor

A recent PHENIX paper[1] claims that hadron production must proceed by a soft mechanism (not jets) because the production centrality dependence at 200 GeV and 2.76 TeV are simply proportional whereas jet production increases by a "large factor." Fig. 6.11-1 (first panel) shows the TCM MB distribution for 200-GeV Au-Au collisions with $x \approx 0.1$ for three fluctuation amplitudes (curves) depending on detector acceptance. For the PHENIX EMCal acceptance the fluctuation width (solid curve) is three times larger than the STAR width (dotted curve). The MB distributions can be transformed to production centrality trends by a running integral. Fig. 6.11-1 (second panel) shows the integration results as the solid and dotted curves plotted above $\nu = 4.5$. Corresponding PHENIX and "RHIC average" production data are plotted as open squares and triangles respectively compared to STAR spectrum

[1] S. S. Adler *et al.* (PHENIX Collaboration), arXiv:1312.667.

integrals (solid dots). The exercise demonstrates that the ten-times smaller PHENIX EMCal angular acceptance results in a substantial fluctuation bias for more-central collisions. STAR data show a single most-central point falling slightly above the TCM dash-dotted line.

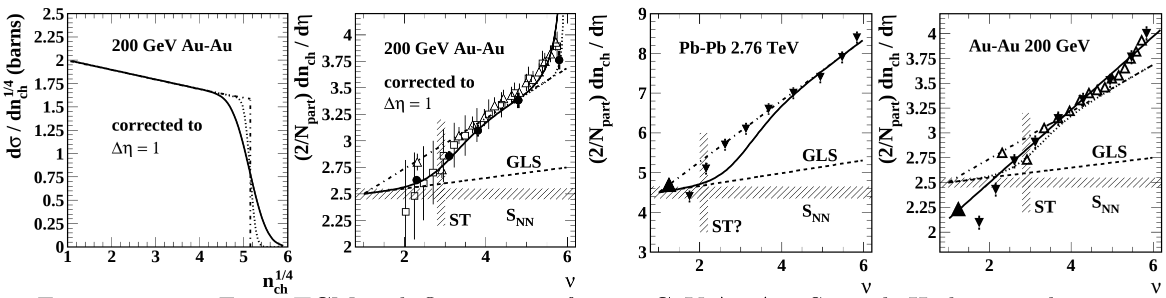

Figure 6.11-1. First: TCM with fluctuations for 200-GeV Au-Au. Second: Hadron production data (points) vs TCM (solid curve) showing fluctuation bias. Third: Production data for 2.76-TeV Pb-Pb (points) vs 200-GeV TCM scaled up in energy. Fourth: Comparison of 2.76-TeV and 200-GeV production data illustrating misleading effects of fluctuation bias.

Fig. 6.11-1 (third panel) shows hadron production data from 2.76-TeV Pb-Pb collisions (inverted triangles) and *p*-*p* collisions (upright triangle). The TCM limiting cases are defined by $1.8\times2.5(1+1.8\times x(\nu-1))$ with $x\approx0.02$ (dashed line) and $x\approx0.1$ (dash-dotted line). The solid curve is the 200-GeV centrality trend inferred from jet-related correlations scaled up in the same way. Given the relation to data the 2.76-TeV hadron production data are *predicted* by a TCM based on the energy dependence of soft and hard production below 200 GeV. The TCM was not adjusted to accommodate the 2.76-TeV data. Fig. 6.11-1 (fourth panel) shows "RHIC average" 200-GeV production data (open triangles) compared to the TCM. The inverted solid triangles are the 2.76-TeV data in the third panel scaled down by factor 2.1. An *apparent* similarity is invoked to claim that particle production must be exclusively due to a soft process inconsistent with the TCM. But the claimed similarity is due to the substantial fluctuation bias in the more-central PHENIX data. The mean slopes (compare solid and dash-dotted lines) are actually very different due to the strong dijet contribution.

6.12 Collision energy dependence of mean $\mathbf{p_t}$ in high-energy p-p collisions

T. A. Trainor

Recent measurements of ensemble-mean p_t $\langle p_t\rangle$ for *p*-*p* collisions at several energies from the LHC[1] when compared to the PYTHIA Monte Carlo based on the eikonal approximation show large discrepancies leading to confusion as to their interpretation. In contrast a two-component (soft+hard) model (TCM) of P_t production is able to describe the data precisely. Fig. 6.12-1 (first panel) shows LHC $\langle p_t\rangle$ data from *p*-*p* collisions at 0.9, 2.76 and 7 TeV (upper points). The curves represent the TCM based on a non-eikonal model derived from *p*-*p* data. Also included are lower-energy data from UA1 (open triangles, open circles) and STAR (solid points) for reference. The curvature of the $\langle p_t\rangle$ vs n_{ch} trends arises because a

[1]B. B. Abelev *et al.* (ALICE Collaboration), Phys. Lett. B **727**, 371 (2013), arXiv:1307.1094.

jet contribution is common to both numerator and denominator of $\langle p_t \rangle$. The trends saturate at the hard-component value $\langle p_t \rangle_h(\sqrt{s})$ for large n_{ch}. Fig. 6.12-1 (second panel) shows

$$\frac{n'_{ch}}{n_s}\langle p_t \rangle(n_s, \sqrt{s}) - \langle p_t \rangle_s \quad \approx \quad x(n_s)\langle p_t \rangle_h(\sqrt{s}) \tag{1}$$

where $\langle p_t \rangle_s = 0.385$ GeV/c is assumed for all cases and $x(n_s) = \alpha\, n_s/\Delta\eta$ with $\alpha = 0.0055$ for $\Delta\eta = 0.6$. The first term of $n'_{ch}/n_s = n'_s/n_s + n_h/n_s$ is adjusted such that the various data sets have a common intercept point (accommodating an incomplete p_t acceptance).

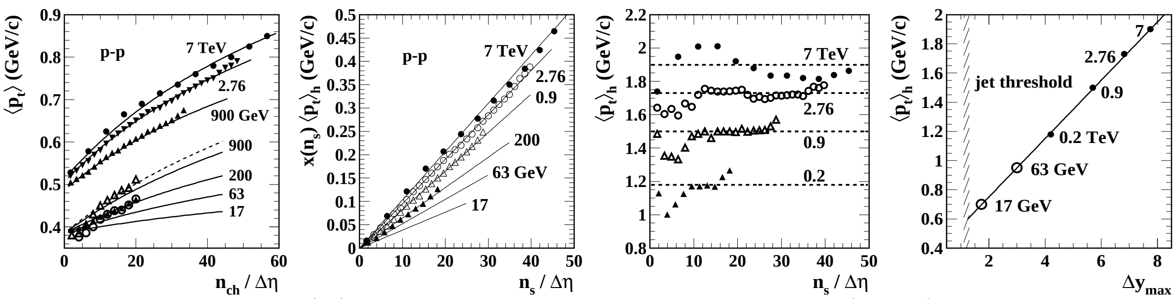

Figure 6.12-1. First: $\langle p_t \rangle$ data for *p-p* collisions at several energies (points) compared to the TCM (curves). Second: The same data adjusted for incomplete p_t acceptance and with soft component subtracted Third: The same data with hard component $\langle p_t \rangle_h(\sqrt{s})$ isolated. Fourth: $\langle p_t \rangle_h(\sqrt{s})$ data vs a measure of the MB jet spectrum width on p-p collision energy.

Fig. 6.12-1 (third panel) shows the $\langle p_t \rangle$ data in the form

$$\frac{1}{x(n_s)}\left(\frac{n'_{ch}}{n_s}\langle p_t \rangle(n_s, \sqrt{s}) - \langle p_t \rangle_s\right) \quad = \quad \langle p_t \rangle_h(\sqrt{s}) \tag{2}$$

for four energies. Most of the $\langle p_t \rangle_h$ values fall in narrow horizontal bands. Fig. 6.12-1 (fourth panel) shows mean values $\langle p_t \rangle_h(\sqrt{s})$ from the third panel (solid points) vs quantity $\Delta y_{max} = \ln(\sqrt{s}/3 \text{ GeV})$. In another study it is shown that MB jet spectrum widths scale with *p-p* collision energy as Δy_{max}. Thus we conclude from the fourth panel that $\langle p_t \rangle_h$ is linearly related to the minimum-bias jet spectrum width. For *p-p* collisions the $\langle p_t \rangle$ vs n_{ch} systematics compel a jet interpretation for the TCM hard component. The soft component remains consistent with a universal phenomenon independent of collision system or energy.

6.13 Mean $\mathbf{p_t}$ systematics for p-Pb and Pb-Pb collisions at the LHC

T. A. Trainor

Recent measurements of ensemble-mean $\langle p_t \rangle$ for *p*-Pb and Pb-Pb collisions at the LHC[1] present major challenges for theory Monte Carlos. No Monte Carlo is able to provide even a qualitative description of the data. Fig. 6.13-1 (first panel) shows 2.76-TeV Pb-Pb $\langle p_t \rangle$ data (solid points). As noted in Ref. 1 $\langle p_t \rangle$ for Pb-Pb collisions increases much less quickly than that for *p-p* collisions. The $\langle p_t \rangle$ increase in A-A collisions is conventionally attributed to

[1] B. B. Abelev *et al.* (ALICE Collaboration), Phys. Lett. B **727**, 371 (2013), arXiv:1307.1094.

radial flow. The hatched band shows the $\langle p_t \rangle_s'$ soft component corresponding to incomplete p_t acceptance. The Glauber linear superposition (GLS) trend (dashed curve) is the A-A $\langle p_t \rangle$ TCM with x and $\langle p_t \rangle_h$ fixed at their 2.76-TeV p-p values. Fig. 6.13-1 (second panel) shows the product $x(\nu)\langle p_t \rangle_h(\nu) = P_{t,h}(\nu)/n_{pp}$ (points) obtained from data in the first panel by

$$x(\nu)\langle p_t \rangle_h(\nu) \;\; = \;\; \frac{1}{\nu - 1}\left(\frac{2}{N_{part}}\frac{n'_{ch}}{n_s}\langle p_t \rangle' - \langle p_t \rangle_s - x_{pp}\langle p_t \rangle_{h,pp}\right). \tag{1}$$

The hatched band shows the p-p value $x_{pp}\langle p_t \rangle_{h,pp} \approx 0.05$ GeV/c. We next isolate the factors.

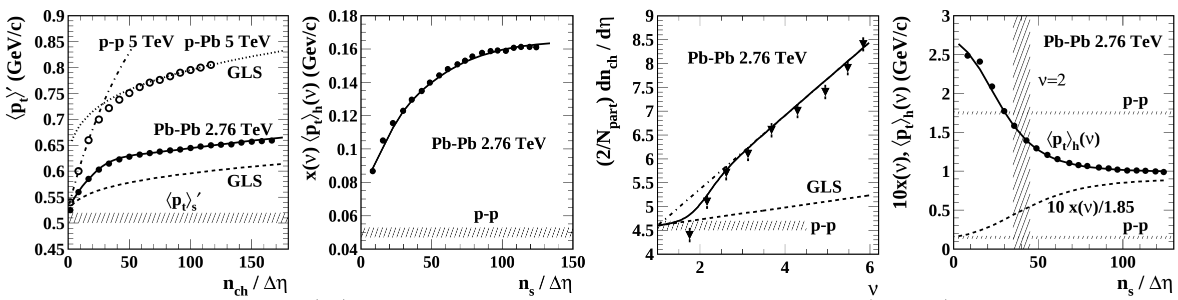

Figure 6.13-1. First: $\langle p_t \rangle$ data for 2.76-TeV Pb-Pb and 5-TeV p-Pb (points), the former compared to a Pb-Pb TCM (solid curve), with GLS references (dashed and dotted curves) and a 5-TeV p-p TCM (dash-dotted curve). Second: Pb-Pb product $x(\nu)\langle p_t \rangle_h(\nu)$ inferred from the first panel with Eq. (1). Third: Hadron production data from 2.76-TeV Pb-Pb collisions (points) compared to the corresponding TCM described by Eq. (2) (solid curve). Fourth: Models for $x(\nu)$ (dashed curve) and $\langle p_t \rangle_h(\nu)$ (solid curve), the latter compared to data (points) inferred from the second panel with Eq. (3).

Fig. 6.13-1 (third panel) shows 2.76-TeV Pb-Pb hadron production data (points) compared to the corresponding production TCM in the general form

$$\frac{2}{N_{part}} n_{ch} \;\; = \;\; n_{pp}[1 + x(\nu)(\nu - 1)], \tag{2}$$

where for 200-GeV Au-Au $n_{pp} \approx 2.5$, $x(\nu) \in [0.015, 0.095]$ and $x(1) = \alpha n_{s,NSD} = 0.015$. For 2.76 TeV the factor $1.85 \approx \ln(2760/10)/\ln(200/10)$ predicts the expected increase in $n_{s,NSD} \approx n_{pp} \rightarrow 4.6$ scaling with small-x partons. The same factor is applied to $x(\nu)$ reflecting non-eikonal jet production in N-N collisions. The functional form of $x(\nu)$ at 2.76 TeV is very similar to that at 200 GeV with the exception that a sharp transition (ST) in jet structure near $\nu = 3$ has shifted down to $\nu \approx 2$ at the higher energy. Eq. (2) with $x(\nu)$ defined below is used here to relate reported n_{ch} values from 2.76-TeV Pb-Pb to fractional cross sections σ/σ_0 and then to Glauber parameters $N_{part}/2$, N_{bin} and $\nu = 2N_{bin}/N_{part}$.

Fig. 6.13-1 (fourth panel) shows the $x(\nu)$ trend (dashed curve) that describes the ALICE hadron production data in the third panel (solid curve) defined by

$$x(\nu) \;=\; 0.028 + 0.141\{1 + \tanh[(\nu - \nu_0)/0.5]\}/2, \tag{3}$$

where $\nu_0 = 2$ estimates the ST for hadron production in 2.76-TeV Pb-Pb collisions. The 2.76-TeV $x(\nu)$ expression is divided by factor 1.85 in the fourth panel for direct comparison with the 200-GeV trend. We can isolate factor $\langle p_t \rangle_h(\nu)$ by dividing the product data in the second panel by $x(\nu)$ from Eq. (3). The result in the fourth panel (solid points) is described by

$$\langle p_t \rangle_h(\nu) \; = \; 1.00 + 1.70\{1 - \tanh[(\nu - \nu_1)/0.42]\}/2 \tag{4}$$

with $\nu_1 = 1.75$ which defines the solid curve through data. The structure of Eq. (2) suggests that of ν N-N encounters the first remains the same as for p-p collisions but subsequent encounters may differ substantially. Note that $\langle p_t \rangle_h(\nu)$ in the fourth panel describes an average over $\nu - 1$ secondary N-N encounters and for peripheral collisions does not extrapolate to the first-encounter p-p value 1.75 GeV/c. The product of Eqs. (3) and (4) gives the solid curve through data in the second panel, and incorporated in the full A-A TCM gives the solid curve through $\langle p_t \rangle$ data in the first panel. Thus, a TCM including strong jet production as the hard component and no radial flow accurately describes 2.76-TeV Pb-Pb $\langle p_t \rangle$ data.

Fig. 6.13-1 (first panel) also shows 5-TeV p-Pb $\langle p_t \rangle$ data (open symbols). As noted in Ref. 1 the p-Pb data increase much faster than the Pb-Pb data for smaller multiplicities but then increase more slowly for larger n_{ch}. The upper GLS curve is the lower GLS curve assuming that constant x increases by factor 2.5 relative to NSD p-p but otherwise jet structure is unchanged in p-Pb collisions relative to p-p collisions. The p-Pb collisions appear to be transparent. The A-A GLS description of p-Pb data with eikonal approximation for larger n_{ch} is good. The p-Pb data appear to make a smooth transition from the non-eikonal p-p trend to the eikonal A-A trend. The transition is located near $n_{ch}/\Delta\eta = 30$.

One can speculate that up to the p-Pb transition point there is only a single N-N collision in peripheral p-Pb and $\nu \equiv 1$. In that case the only way to satisfy the increasing n_{ch} condition is with increased N-N n_s resulting in a large increase in jet production $\propto n_s^2$ due to the non-eikonal interaction as in single p-p collisions. At some value of n_{ch} the probability of producing a single N-N collision with sufficient n_{ch} becomes smaller than the probability of a second N-N binary collision in more-central p-Pb collisions and ν becomes significantly greater than 1. It is then possible to produce more soft hadrons relative to jets by multiple N-N collisions, each with a smaller soft multiplicity n_s and therefore jets $\propto n_s^2$. It is interesting that the transition from non-eikonal to full eikonal behavior seems to occur within a small n_{ch} interval.

7 Other research

7.1 Status of nonlocal quantum communication test

J. G. Cramer

The question we have been investigating is whether the intrinsic nonlocality of standard quantum mechanics is the private domain of Nature, as is generally assumed by the physics community, or whether in special circumstances the nonlocal connection between subsystems can be used to send signals from one observer to another. The basic nonlocal communication (NLC) scheme, as described in the references, is to use the connection implicit in momentum-entangled photon pairs to create a signal as the presence or absence of an interference pattern at the receiving end, depending on whether or not which-way information was extracted at the sending end of the experiment. This work has been reported in CENPA Reports in the past seven years[1,2,3,4,5,6,7].

In the quantum formalism there is an implicit complementarity relation between entanglement and coherence[8] that poses a problem for such communication, since the potential nonlocal signal depends on the presence of both two-photon entanglement and coherence of the waves to produce interference. We have argued[9] that creating a condition between the photon pair in which entanglement and interference were both present only at the 70% level (e.g., $\frac{1}{\sqrt{2}}$), as permitted by the complementarity relation, should permit survival of a nonlocal signal.

Two-particle interferometry is an interesting and intricate quantum problem. Its mathematical treatment is described in some detail in a little-known 1990 paper by Horne, Shimony, and Zeilinger[10], and we have applied this formalism to the current problem. In the past year we have made significant progress in understanding the issues associated with two-particle interference and in resolving the quantum paradox implicit in our proposed NLC experiment. Much of this progress was stimulated by a one-week visit in October 2013 to Prof. Anton Zeilinger's Institute for Quantum Optics and Quantum Information (IQOQI)in Vienna, Austria.

---

[1] CENPA Annual Report, University of Washington (2007) p. 52.
[2] CENPA Annual Report, University of Washington (2008) p. 42.
[3] CENPA Annual Report, University of Washington (2009) p. 41.
[4] CENPA Annual Report, University of Washington (2010) p. 93.
[5] CENPA Annual Report, University of Washington (2011) p. 94.
[6] CENPA Annual Report, University of Washington (2012) p. 89.
[7] CENPA Annual Report, University of Washington (2013) p. 89.
[8] A. F. Abouraddy, M. B. Nasr, B. E. A. Saleh, A. V. Sergienko, and M. C. Teich, Phys. Rev. A **63**, 063803 (2001).
[9] J. G. Cramer, Chapter 18 in *Frontiers of Propulsion Science (Progress in Astronautics and Aeronautics)*, Eds. M. Millis and E. Davis, AIAA (2009).
[10] M. A. Horne, A. Shimony, and A. Zeilinger, *Sixty-Two Years of Uncertainty*, 113-119, Plenum Press, NY (1990).

Zeilinger's group had developed a Sagnac-mode entangled two-photon source[1] that is capable of producing over 10^6 polarization-entangled pairs per second, and in which the entanglement and coherence can be easily set to a desired ratio by the rotation of a half-wave plate. In 2008 they had used this source to perform an experimental test[2] of the complementarity between one- and two-photon interference[3]. This configuration is the equivalent of the momentum-entanglement NLC test that we have been investigating in this work, but it offers the advantage that since there are no D-mirrors, the incident beam can be a single mode throughout its path and the mathematical analysis is more straightforward. The IQOQI one- and two-photon interference test is shown in Fig. 7.1-1.

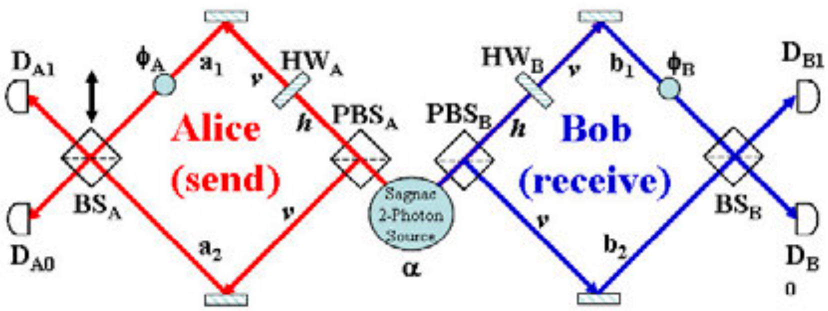

Figure 7.1-1. IQOQI Experiment; polarization-entangled photon pairs are converted to path-entangled pairs by the polarizing beam-splitters and half-wave plates, so that photons on all paths are in the same state v of linear polarization and can interfere. The α parameter of the source determines the degree of two-photon polarization entanglement provided by the source.

Suppose Alice, who controls the left (send) interferometer, wishes to send a nonlocal signal to Bob, who controls the right (receive) interferometer. The source is preset for a particular value of α, which may be $\alpha = 0$ for a Bell state that entangles the uppe/lower and lower/upper paths of the two interferometers, or $\alpha = \pi/4$ for a non-entangled coherent product state, or $\alpha = \pi/8$, which combines entanglement and coherence at 70% each. Alice can control the relative phase on the two paths of her interferometer by varying phase control ϕ_A, and Bob can do the same with ϕ_B. Alice can either attempt to send a signal to Bob by varying ϕ_A or by removing combiner BS_A so that her detectors do a which-way measurement on the two paths. The indication that a nonlocal signal could be achieved would be that the behavior of Bob's interferometer, operated without coincidences with Alice's detectors, depends explicitly on ϕ_A or on the removal of BS_A. It was our hope that with $\alpha = \pi/8$, this might be the case.

To analyze this system, we have applied the methods of Horne, Shimony, and Zeilinger[10] to construct a Mathematica 9 notebook, which may be viewed online at the website: `http://faculty.washington.edu/jcramer/NLS/NLCT.html`. The analysis reproduces the results of the IQOQI experiment[2] and shows that the singles probabilities of detecting a photon in Bob's detectors are: $P(D_{B1}) = \frac{1}{2}[1 + \sin(2\alpha)\sin(\phi_B)]$ and $P(D_{B0}) = \frac{1}{2}[1 -$

[1] A. Fedrizzi, T. Herbst, T. Jennewein, A. Poppe, and A. Zeilinger, Optics Express **15**, 15377 (2007).
[2] A. Fedrizzi, R. Lapkiewicz, X-S. Ma, T. Paterek, T. Jennewein, and A. Zeilinger (2008, unpublished).
[3] G. Jaeger, M. A. Horne, and A. Shimony, Phys. Rev. A **48**, 1023-1027 (1993).

$\sin(2\alpha)\sin(\phi_B)]$. This is the case whether BS_A is in or out of the system, or even if the left-going beam is blocked with a beam stop.. In other words, there is no nonlocal signal in the configuration of Fig. 7.1-1, independent of the value chosen for α and of the beam splitter position. The problem is that while the probability of photon detection in Bob's detectors in coincidence with either of Alice's detectors shows a definite signal, when the two coincidence-dependent probabilities are added to obtain the coincidence-independent singles probabilities, the signal terms cancel and vanish. This is a manifestation of the intrinsic complementarity between one- and two-particle interference[3]. This result suggests that it is Alice's two separate detectors that cause a washout of the signal, and that perhaps directing the two paths to the *same* detector might improve the situation. Therefore, we have analyzed a modification of the IQOQI Experiment that uses a 45° wedge mirror to deflect the a_1 and a_2 paths to the same detector. This is shown in Fig. 7.1-2.

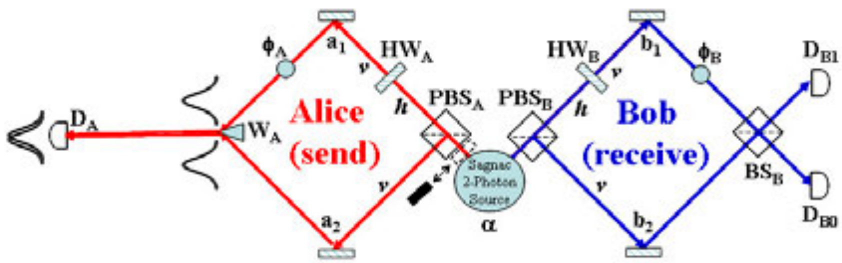

Figure 7.1-2. Modified IQOQI Experiment; paths a_1 and a_2 are directed to the same detector.

This configuration requires a more detailed analysis than the previous one because the wedge reflection places the two beams on slightly different trajectories and one Gaussian tail of each beam is truncated (and lost) at the wedge vertex, so that they are no longer a superposition of identical quantum modes. Therefore, the transport from wedge to detector must be done by integrating Huygens wavelets for the two beams over the effective aperture of the wedge. Fig. 7.1-3 shows the calculated interference pattern on the face of detector D_A for $\alpha = \pi/2$ and $\phi_A = \phi_B = 0$ as measured in coincidence with Bob's detectors D_{B1} and D_{B0}. The probability of singles photon detection for Bob's detectors D_{B1} and D_{B0} is obtained by integrating over these line shapes.

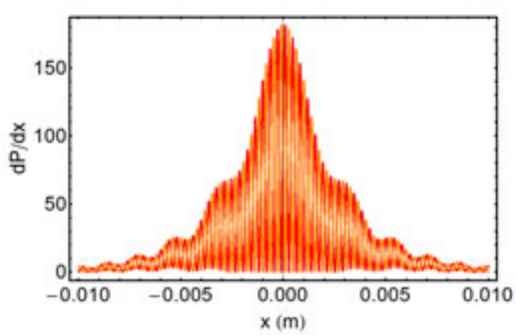

Figure 7.1-3. Profile of intensity patterns on the face of Alice's detector D_A for $\alpha = \pi/2$, $\phi_A = \phi_B = 0$ as measured in coincidence with Bob's detectors D_{B1} (red) and D_{B0} (orange).

We can evaluate the possibility of nonlocal communication in this configuration by plotting the difference in the non-coincident photon detection probabilities in Bob's detectors D_{B1} and D_{B0} as functions of α, ϕ_A, and ϕ_B for the two configurations. This is shown in Fig. 7.1-4. As can be seen from Fig. 7.1-4, there are essentially no differences in Bob's detection probabilities for the configuration of Fig. 7.1-1 and Fig. 7.1-2. The spikes are an artifact of the Mathematica 9 calculation and indicate points at which the numerical integration over the highly oscillatory beam profile on detector D_A had numerical problems. Our conclusion is that no nonlocal signal can be transmitted from Alice to Bob by varying Alice's configuration in any of the ways discussed here. We will continue to test the signaling issue the parameter space of the calculations, but the present conclusion is that Nature is well protected from the possibility of nonlocal signaling.

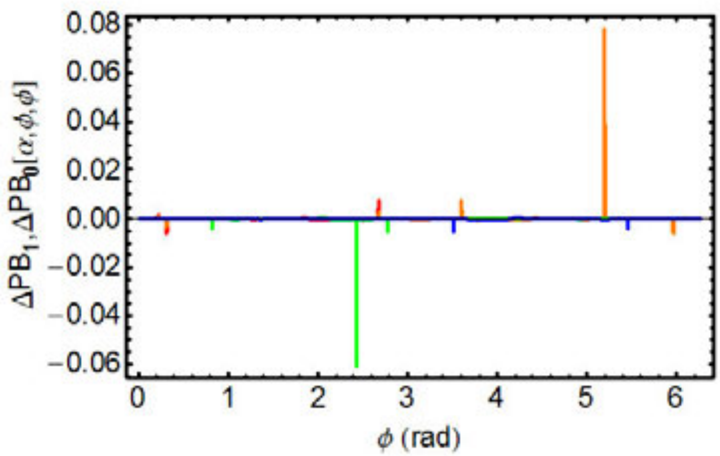

Figure 7.1-4. Configuration difference in non-coincident detection probabilities with $\alpha = \pi/4$ for D_{B1} (red) and D_{B0} (orange) and with $\alpha = \pi/8$ for D_{B1} (green) and D_{B0} (blue).

We would like to thank Anton Zeilinger, Radek Lapkiewicz, and Nick Herbert for very valuable recent contributions to this project.

7.2 Analysis of a wedge quantum interferometer

J. G. Cramer

The previous article (Sec. 7.1) describes the use of a 45° "wedge" mirror to combine interferometer beams at the face of a single detector. Dr. Nick Herbert pointed out to me that such a device had previously been examined as a quantum optics element in a paper by A. Y. Shiekh[1]. In that paper, the author argued that nonlocal communication could be achieved by splitting a laser beam with a 50:50 splitter, then sending one of the beams into a modified Mach-Zehnder interferometer in which the beams were recombined with a wedge mirror after one of the beams had been phase-shifted by 180°. He argued that the combined

[1] A. Y. Shiekh, Electr. Jour. of Theor. Phys. **19** 43 (2008); ArXiv 0710.1367v2 (2008).

beams must cancel to zero amplitude, as they do in the "dark" path of a conventional Mach-Zehnder interferometer. Thus, all photons at the initial splitter must avoid the suppressed path and must take the splitter's other beam path. Thus, it is asserted that by changing the interferometer phase between 0 and π, one should be able to modulate the intensity of the other beam and send a nonlocal signal.

This argument is based on a violation of unitarity in combining the beams and is clearly wrong, but it raises the interesting question of what actually *does* happen in such a situation, which is a simpler version of the modified IQOQI experiment described in the previous article. Fig. 7.2-1 shows a "wedge" interferometer based on this idea. Here the pentaprism reflectors are needed because simple 90° mirror reflections would place the "cut" edges of the half-Gaussian profiles on the outside of the recombined beams instead of rejoining them along the center line.

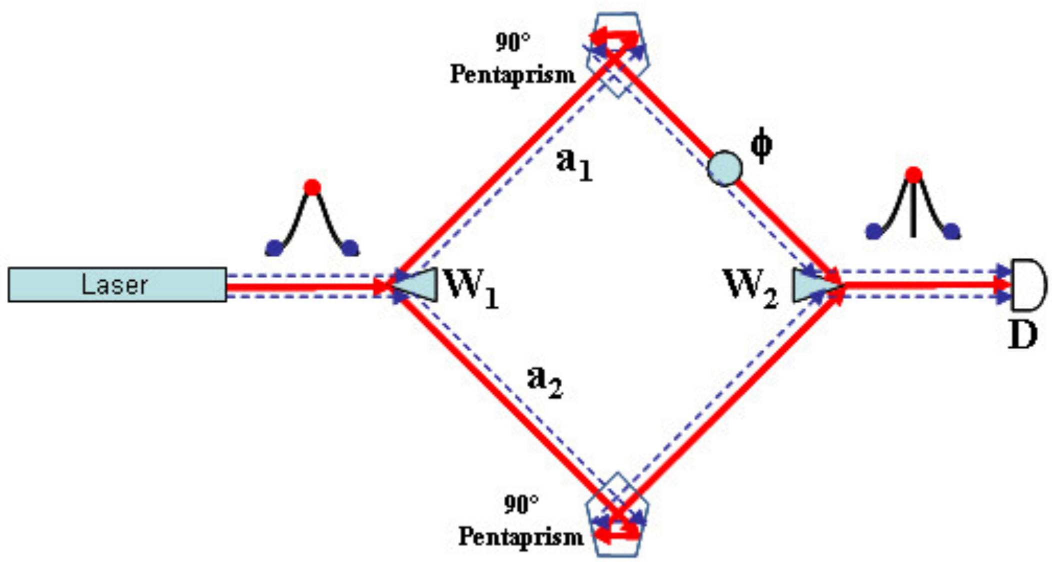

Figure 7.2-1. A Gaussian single-mode laser beam is split into two halves with a 45° wedge mirror, reflected 90° by pentaprisms, recombined with a second wedge mirror, and sent to a detector. The upper beam is shifted in phase by ϕ. Dashed lines and colored dots indicate paths and locations of the tails of the Gaussian lineshapes.

The question of interest is the shape of the interference pattern observed at the detector when the phase ϕ is varied between zero and π. The naive assertion that with $\phi = \pi$ the beams will cancel and vanish is not correct. Splitting a single-mode Gaussian beam into two half-Gaussians produces two multi-mode beams, and their interference pattern is rather complicated. However, it can be calculated by integrating the Huygens wavelets that comprise the two beams over the effective aperture of the second wedge as they are transported to the detector. This has been done in a Mathematica-9 notebook, which may be viewed online at the website: `http://faculty.washington.edu/jcramer/NLS/Wedge/D-Patterns_2.html` .

Fig. 7.2-2 shows the calculated interference patterns for phases of $\phi = 0$, $\phi = \pi$, and $\phi = \pi/2$. As can be seen, when the phase is $\phi = 0$, a Gaussian beam profile with some

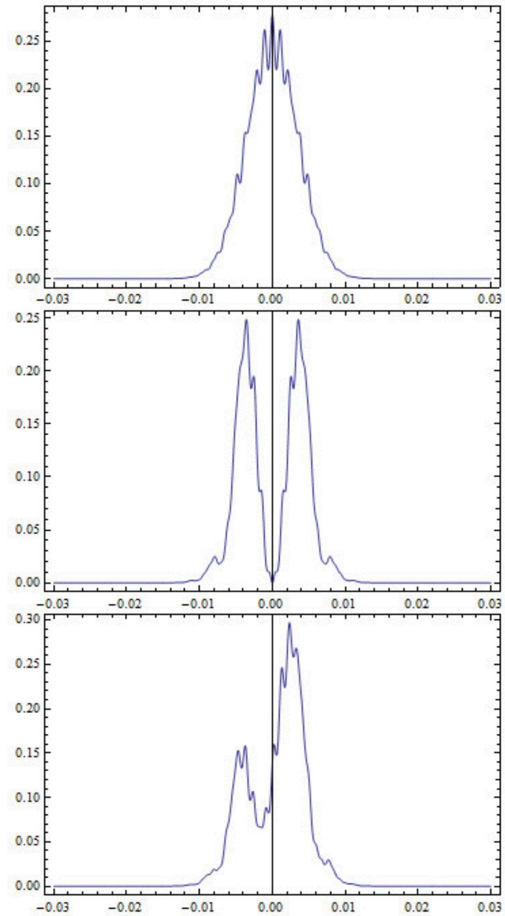

Figure 7.2-2. Calculated line-shape profiles at the detector with phases of $\phi = 0$ (red) , π (green), and $\pi/2$ (blue). All profiles have the same area.

structure from truncation is transported to the detector. When the phase is $\phi = \pi$, the beams indeed cancel along the center line, but constructively reinforce as narrower side peaks to the right and left of the center line. The intermediate case of $\phi = \pi/2$ give some intensity along the center line and produces asymmetric side peaks to the right and left of the center line. The integrals of these line shapes are essentially equal, indicating that no net beam intensity is lost in varying the phase and that, excepts for truncated Gaussian tails, the detector receives all the photons transmitted by the laser. Thus, the Shiekh scheme for nonlocal communication is fatally flawed.

8 Education

8.1 Use of CENPA facilities in education and course work at UW

G. C. Harper and E. B. Smith

CENPA has always maintained a prominent role in broad-scope, practical, hands-on training for both undergraduate and graduate students at the University of Washington. One of the most significant and unique advantages that our students enjoy is direct participation in the ongoing local research at CENPA and in contributions to our off-site collaborations.

We have been increasing our presence in undergraduate and graduate education and since spring 2011 we have provided an accelerator-based laboratory course in nuclear physics. This began as an undergraduate special-topics course in physics, course number 499, and has evolved into Physics 575, Nuclear Physics: Sources, Detectors, and Safety (Sec. 8.2). Another undergraduate classroom application of CENPA facilities included the use of one of our radioactive sources in a radiochemistry course (Sec. 8.3) for activating materials to be used in laboratory experiments.

We continue to provide extensive hands-on training for both undergraduate and graduate students. Our electronics shop is available for use by the students (Sec. 9.4) where they can learn electronic design and assembly. In the student shop (Sec. 9.6) all users are trained in machine-tool operation and safety. Finally, CENPA has a long history of teaching students accelerator and ion-source operation (Sec. 8.4).

8.2 Accelerator-based lab class in nuclear physics

A. García, G. C. Harper, E. B. Smith, and D. I. Will

We have developed a graduate-level lecture and laboratory class for the purpose of teaching aspects of nuclear theory and techniques for nuclear-physics experiments, including student operation of the tandem-accelerator system to achieve beam on an experimental target[1].

The class met twice a week during the spring 2014 quarter, once for a 1-1/2 hour lecture and again in groups for a 1-1/2 hour lab session. The list of subjects we covered were:

1. Atomic nucleus. Basics of nuclear physics, nuclear energy, orders of magnitude.
2. Attenuation of photon radiation. Solid-state detectors (Ge and Si).
3. Ranges of ions and electrons. The weak interaction. Radioactivity and radiation damage and health risks (α, β, γ, and neutron activity).
4. Deciphering a mystery γ spectrum. Gauging the level of radioactivity and assessing health risks.
5. Tandem-accelerator function and ion optics. Tuning beam in CENPA accelerator.

[1] Phys 575, Nuclear Physics: Sources, Detectors, and Safety, http://faculty.washington.edu/agarcia3/phys575.

6. Rutherford back-scattering (RBS). Deciphering a mystery spectrum and the contents of a mystery foil.
7. Fission and fusion. The functioning of reactors.
8. Nuclear astrophysics: nucleosynthesis in stars.
9. Sources of positrons for positron emission tomography.

Nine students attended the Spring 2014 sessions. Students engaged enthusiastically in discussions during lectures and in laboratory sessions.

8.3 Radiochemistry and nuclear-chemistry education program in the UW Department of Chemistry

K. A. Krohn*, D. I. Will, and W. H. Zoller†

The tracer principle using radionuclides is critically important in disciplines ranging from basic chemical and biochemical mechanisms to human medicine, from atmospheric chemistry to geochemistry, and from materials science to cosmology. Several years ago the Howard Hughes Foundation funded nuclear-detection instrumentation for Chemistry 410, a lecture/laboratory course in Radiochemistry and Nuclear Chemistry taught each winter quarter and limited by equipment workstations to 16 students. In order to maintain a fresh course the curriculum is updated each year to reflect the application interests of students. The basic science of radiation detection and the safe handling of isotopes are covered in the first four sessions. The students are then taken to various working laboratories to gain hands-on experience in using radionuclides to answer important science questions.

One trip is to the Washington State Department of Health Laboratory for a practical experiment in counting long-lived α and β emitters. The exercise is done in the context of a realistic dirty-bomb terrorism scenario where the students are presented with an unknown sample wipe test and asked to gauge the magnitude of the threat. A second trip is to the Applied Physics Laboratory to use X-ray fluorescence to analyze an unknown substance.

Protein labeling by radio-iodination is a common method for attaching an exogenous label to important biological molecules. This exercise provides practical experience in handling open sources of radionuclides and teaches the role surveys play in detecting radioactive contamination following the laboratory exercise. Chelation labeling is another approach for attaching a detectable signal to an interesting molecule. We do an experiment using ^{99m}Tc, which is commonly used for medical imaging.

While many radionuclides are commercially available, an even larger number need to be made on demand. The nuclear reactions for this purpose use neutrons or charged particles to induce nuclear reactions. The students gain experience with both methods. We use the UW Medical Center cyclotron to make $^{13}NH_3$ for imaging the heart muscle using positron emission

*Professor of Radiology & Radiation Oncology, Adjunct Professor of Chemistry, University of Washington, Seattle, WA.
†Emeritus Professor, Department of Chemistry, University of Washington, Seattle, WA.

tomography. The students learn basic aspects of cyclotron engineering and medical-imaging instrumentation as well as radiochemical synthesis in a clean room so that the radiopharmaceutical product is safe for human injection. We also make radionuclides using neutrons. Because a reactor is not available at UW, we use the α-Be neutron source from CENPA for this purpose. The neutrons are thermalized by scattering through polyethylene and are used to irradiate different pure elements for neutron-activation analysis and then to identify the composition of an unknown alloy.

8.4 Student training

G. C. Harper, D. R. Hyde, D. A. Peterson, E. B. Smith, and D. I. Will

Students at CENPA receive training in a variety of technical laboratory skills that include accelerator operation, machining, and electronics. Six students received accelerator operation training (a.k.a. "crew training") this last year, in which the students are taught to operate the ion sources and the tandem Van de Graaff accelerator. These students practice generating an ion beam, charging the tandem, and tuning the beam through the accelerator. Frequently, these individuals also gain experience with vacuum systems and cryogenics as dictated by the needs of their experiment.

CENPA student-shop training was received by more than 14 individuals (including staff, RAs, REU students, and undergraduate hourlies) this year, many of whom completed our training course. These students have learned to safely operate a variety of machines including lathes, milling machines, drill presses, saws, grinders, metal shears and breaker, hand tools, and power tools. Several students were trained to use an oxygen/acetylene cutting torch. Additionally, students have been trained on the student-shop NC 2-Axis Trak milling machine in order to make complicated parts for their research projects.

In the electronics shop, instruction in soldering, wiring, and the use of basic electrical and electronic components was given to at least five students.

9 Facilities

9.1 Facilities overview

G. C. Harper, E. B. Smith, and D. I. Will

CENPA constantly updates and improves its facilities and provides the best possible resources and research environment for its users as new experiments emerge and as the demands of research change with time. In addition we maintain high-quality shop services that are available to the faculty, staff, and students.

The computational facilities at CENPA remain at the front edge of technology. As always, personal desktop and portable computers are maintained and the technology kept current. The NPL Data Center (NPLDC), which previously contained a single high performance cluster, ATHENA, now provides the infrastructure to multiple clusters and department appliances (Sec. 9.3).

The laboratory facilities that surround, support, and include the FN tandem Van de Graaff accelerator are constantly evolving, and provide hands-on training for students in operation of the accelerator and ion sources (Sec. 9.2). A graduate physics course using the accelerator to perform nuclear-physics experiments has been developed (Sec. 8.2). Additionally, we have begun an upgrade project to replace the existing control hardware and software used by the accelerator system.

The CENPA electronics shop provides modern surface-mount technology and miniature cable-manufacturing equipment on site and in appropriately clean areas. The shop continues to do custom design work for specialty preamplifiers as well as dedicated multichannel data-acquisition (DAQ) systems. The shop also interacts with the on-campus Washington Technology Center, taking advantage of much of the capital-intensive, high-tech equipment there that is more effectively used as a cost-shared facility. The electronics-shop staff also provides training for students and other staff members (Sec. 9.4).

The CENPA instrument shop (main instrument shop) is manned by three highly skilled instrument makers with vast knowledge of metallurgy, welding, and fabrication (Sec. 9.6). This shop has CNC machines, mills, lathes, and large-capacity machines. The instrument shop can provide engineering for all research projects. The CENPA student shop is headed by an instrument maker who provides safety training and instruction to students, staff, and faculty. This shop includes mills, lathes, drill presses, a laser cutter, and 3D printer.

The ADMX experiment is now fully installed, operational and taking data at the east end of our accelerator tunnel. Their completed pump shed houses two Bauer helium-recovery compressors, a large Edwards roughing pump, and a large Welch pump for the 1-K helium pot. The ADMX group is running a new Linde 1410 helium liquefier successfully at weekly intervals. Initial data suggest 96% of boil-off is reliquefied with the automated purge cycle of the purifier stage being the major helium loss. The liquefier has reduced helium purchases for this experiment from an estimated \$500,000 to about \$20,000 per year.

The MAJORANA and muon groups are now using their new laboratory space in rooms 108 and 110, respectively, for detector testing and development. (Sec. 9.7).

9.2 Van de Graaff accelerator and ion source operations and development

Z. T. Alexander*, G. C. Harper, G. H. Leum†, S. D. MacDonald, J. R. Pedersen, D. A. Peterson, S. S. Sexton‡, E. B. Smith, I. A. Smith§, T. D. Van Wechel, and D. I. Will

The only entry into the tandem this year was made on August 19, 2013, after observing instability at 8.8-MV terminal voltage; which is indicative of possible column resistor failure or disconnection. An internal tank inspection revealed that one resistor shorting wire on bottom string of tube #1 had fallen off requiring re-connection. Some resistors in the top string appeared bent, and were therefore straightened.

ACTIVITY SCHEDULED	**DAYS SCHEDULED**	**PERCENT of TIME**
Ion implantation, deck ion sources	20	6
Nuclear-physics research, accelerator	30	8
Subtotal, ion implant or nuclear-physics research	50	14
Development, maintenance, or crew training	33	9
Grand total	83	23

Table 9.2-1. Tandem Accelerator Operations 1 April, 2013, to 31 March, 2014.

During the 12 months from 1 April, 2013, to 31 March, 2014, the tandem pellet chains operated 348 hours, the sputter-ion-source (SpIS) operated 0 hours, and the direct-extraction-ion source (DEIS) operated 890 hours. Additional statistics for accelerator operations are given in Table 9.2-1.

Ion beams produced using the DEIS this year included 17.0–17.8-MeV ^{2}H for the ^{6}He experiment, 15.2-MeV ^{2}H for a visting experimenter, 2.0-MeV ^{1}H for the Physics 575 class, and 48-keV ^{36}Ar for an implant required for research performed by the fundamental symmetries group. Initial attempts to produce ^{36}Ar^{+} from our duoplasmatron ion source were unsuccessful due to an unexplained, repeated filament breaking issue during positive ion production. It was determined that initial negative ion production with a new filament could be successfully followed by positive ion production from the same filament, making sure the filament experiences vacuum or plasma gases only. We presented the documented details of this unexplained failure at the 2013 Symposium of Northeastern Accelerator Personnel (SNEAP), Sept. 29 - Oct. 1, 2013, in Woods Hole, Massachusetts.

*Departed August, 2013.
†Arrived November, 2013.
‡Arrived October, 2013.
§Arrived May, 2013, departed August, 2013.

9.3 Laboratory computer systems

G. T. Holman

CENPA is a mixed shop of Windows 7, XP, Mac OS X and various Linux distributions. Windows 7 is installed on new systems but we are still running a few Windows XP systems for data-acquisition. In previous years the IT focus was directed toward server consolidation, network security, process documentation and removal of redundant processes. We continue to utilize Xen virtualization to drive most web pages, Elogs, wiki, calendar, tracking, and document servers. The CENPA website and research group web pages are run on a virtual Debian server and utilize the Drupal web framework. The NPL mail server still provides NPL presence but all email is relayed to UW email hardware. This year we synchronized users on multiple Linux and Windows systems to UW active directory via a delegated OU. The delegated drganizational unit (OU) removes the need to run a dedicated domain or LDAP server.

Two Dell 510 20-TB servers (Lisa and Marie) continue to offer user storage, print server capability, and improved backup policy. Linux, Windows and Mac workstations are backed up to the Lisa 20-TB raid farm from which they are written to LTO tape by the Physics Computer Center on a three-month backup retention plan. Lisa runs the Crash Plan Pro backup application which supports all operating systems and provides differential and encrypted backups. Whereas workstations rely on Crash Plan Pro for backups, all servers utilize rsync. Marie provides 20 TB for research, user, and shared group data.

The NPL Data Center (NPLDC) provides critical infrastructure supporting high-performance scientific-computing applications that cannot be efficiently executed on typical commodity server infrastructures (e.g., the Amazon EC2 Cloud). In previous years the space housed a single cluster that was treated as one computational resource, also known as Athena. Today, to meet the wide and highly specialized array of research requirements, the cluster has been separated into two specific cluster instances. The first cluster instance leverages Infiniband interconnects (classified as HPC clusters) and runs the latest open-source Rocks software[1], runs the cvmfs (Cern-VM file system) client, and Frontier local squid cache server. The second cluster that primarily runs single-threaded applications (non-HPC clusters) uses Rocks version 5.4, and most notably runs COMSOL, root[2], and Geant. Both cluster instances use Torque/Maui via dedicated front ends.

Approximately one third of the rack space is dedicated to non-cluster hardware: scratch storage, SQL, elogs, web applications, CAD workstations, and backup storage. These servers constitute over 200 TB of raw disk space.

Our computing and analysis facility consists of:

- The NPL data center as a shared resource with Physics, the Institute for Nuclear Theory (INT), and the Astronomy department.

[1]http://www.rocksclusters.org/
[2]http://root.cern.ch/

- A mix of Linux servers: Debian, Redhat, and Ubuntu distributions.
- One VMS/VAXstation for legacy computing.
- Macintosh systems for the SNO+, KATRIN, MAJORANA, and emiT groups.
- A VAXstation for the linac and vacuum systems control and display system.
- Various Windows XP desktop JAM systems (Java-based software for acquisition and analysis), plus two laptops for transport to other installations.
- A Shorewall Linux-based logical firewall to protect the bulk of CENPA's PCs and servers.
- We provide additional legacy co-location services for the INT and the Physics Nuclear Theory group in the form of one VMS Alphastation 500, which is not directly used by lab personnel.

9.4 Electronic equipment

D. A. Peterson and T. D. Van Wechel

The electronics shop is responsible for the design and construction of new laboratory electronic equipment as well as the maintenance and repair of existing CENPA electronics. Projects undertaken by the electronics shop in the past year include the following:

1. Continued to develop the MAJORANA/Cogent preamplifier. A new front end and post amplifier has been designed and will be ready for testing this month.
2. Designed and built an FPGA-based trigger tester for the Kamland trigger module.
3. Designed and built an eight-channel heat-tape relay box for the KATRIN Tritium Recoil-Ion Mass Spectrometer assembly.
4. Produced quartz and sapphire connector paddles for the MAJORANA connectors.
5. Performing clean-room soldering of the new MAJORANA Vespel connectors.
6. Designed and built several iterations of silicon photomultiplier readout circuits for the $g-2$ project.
7. Built 10 multi-channel preamp boards for the MuSun TPC preamp.
8. Contracted to have 100 additional MuSun cathode preamp circuit boards produced and assembled.
9. Designed and built three amplifiers for the Nanopore project.
10. Designed and built 23-26 GHz voltage-controlled oscillator for Project 8.
11. Designed and built shim heater relay for the Project 8 superconducting magnet.

9.5 Rapid prototyping and fabrication tools

M. D. Turner

Last year[1] we reported on the acquisition of a CNC laser cutter and 3D printer with funding from the University of Washington's Student Technology Fee (STF). Since the installation

[1]CENPA Annual Report, University of Washington (2013) p. 118.

of the laser cutter, about ten students from inside and outside CENPA have been trained and authorized for use of the machine. Besides common applications such as cutting plastics and sheet metal, the system has also been used for niche applications such as pulling quartz fibers, cutting glass and silicon, and engraving instrument panels. The 3D printer has been used for work such as modeling (at a scale of 10^7:1) a bacterial nanopore used for DNA sequencing and creating a low-cost duplicate of a torsion pendulum used for short-range gravity measurements.

We are currently pursuing STF funding for a UV-laser-based micromachining and PCB fabrication system. This system will complement the capabilities of the existing laser cutter and provide our electronics shop with a way to quickly fabricate PCBs on standard and nonstandard substrates.

9.6 CENPA instrument shops

T. H. Burritt, J. H. Elms, D. R. Hyde, and H. Simons

The CENPA instrument shop has given support to CENPA and several UW research groups. Projects completed this year include:

1. Modifications to and redesign of the KATRIN in-beam detector valve and magnet bracing hardware.
2. 8-pin connector for MAJORANA.
3. Design fabrication of the next-generation MuSun TPC detector.
4. Design fabrication of TRIMS ultra-high vacuum components.
5. Fabrication of bearing and chamber for the gravity group.
6. Fabrication of various electrical panels, vacuum equipment, micro parts, and tooling.

The student shop produced several small projects in addition to providing machine-tool training and safety training for the faculty, staff, and students.

1. Manufactured the top and bottom plates for the MuSun TPC project.
2. Made the movable capacitor element and end-cap for the $g - 2$ experiment.
3. Manufactured a UW gas-manifold pump-out-valve support.
4. Produced detector collar for the R-1 project.
5. Small parts for the ^{6}He project.
6. Produced the air manifold for Axion experiment.
7. Made the copper enclosure for MAJORANA experiment.

9.7 Building maintenance and upgrades

C. R. Boutan, M. T. Hotz, D. A. Lyapustin, J. V. Sloan, E. B. Smith, M. D. Turner, and D. I. Will

The pace of maintenance and upgrades has slowed this past year[1]. The new laser cutter is operational. Students from numerous departments have used it successfully. The Axion Dark Matter eXperiment (Sec. 5.1) is taking data at the east of the accelerator tunnel. The parking lot and service drive have been patch-paved where the sewer work was completed last year. All three buildings now have UW campus Wi-Fi throughout. After some startup problems and troubleshooting the new chiller and cooling tower are now running smoothly.

The re-roof of our Van de Graaff accelerator building was funded and has been bid. Pre-construction preparations with the successful bidder commence later this month. Re-roofing should be completed by summers end. The removal of the cyclotron pond and resealing of underground portions of the cyclotron building did not receive funding this year.

Planning has begun for replacement of six individual, oil-filled, single-phase, 2400-Vac stepdown transformers in an ancient underground vault and is scheduled for this fall. One dry, three-phase, air-cooled 208-Vac wye transformer will take the place of the three smaller 2400-Vac-to-120-Vac transformers with wye-wired secondaries. Another dry, three-phase, air-cooled 240-Vac delta transformer will replace the three larger 2400-Vac-to-240-Vac transformers with secondaries wired in delta configuration. Ancient oil-filled switches will also be updated with new, enclosed, dry, switch gear.

Numerous routine and non-routine work orders have been placed and work performed: 82 orders for the Van de Graaff Accelerator Building, 38 orders for the Cyclotron Building and 15 orders for the CENPA Instrument Shop.

[1] CENPA Annual Report, University of Washington (2013) p. 119.

10 CENPA Personnel

10.1 Faculty

Eric G. Adelberger[1]	Professor Emeritus
Hans Bichsel[1]	Affiliate Professor
John G. Cramer[1]	Professor Emeritus
Jason Detwiler	Assistant Professor
Peter J. Doe	Research Professor
Sanshiro Enomoto	Research Assistant Professor; CENPA Fellow
Svenja Fleischer[1]	Research Assistant Professor
Alejandro García	Professor
Fred Gray[2]	Associate Professor
Jens H. Gundlach[1]	Professor
Blayne R. Heckel[1]	Professor; Chair
David W. Hertzog	Professor
C. D. Hoyle[1,3]	Affiliate Assistant Professor
Peter Kammel	Research Professor
Jarek Kaspar	Acting Assistant Professor
Michael L. Miller[1,4]	Affiliate Research Assistant Professor
R. G. Hamish Robertson	Professor; Director
Leslie J Rosenberg[1]	Professor
Gray Rybka	Research Assistant Professor
Stephan Schlamminger[1,5]	Research Assistant Professor
Kurt A. Snover[1]	Research Professor Emeritus
Derek W. Storm[1]	Research Professor Emeritus
Nikolai R. Tolich	Assistant Professor
Thomas A. Trainor	Research Professor
Robert Vandenbosch[1]	Professor Emeritus
William G. Weitkamp[1]	Research Professor Emeritus
John F. Wilkerson[1,6]	Affiliate Professor
Tianchi Zhao[7]	Research Associate Professor

10.2 CENPA External Advisory Committee

Daniel McKinsey[8]	Yale University
Robert McKeown[8]	Jefferson Laboratory
Michael Ramsey-Musolf[8]	University of Massachusetts, Amherst

[1]Not supported by DOE CENPA grant.
[2]Arrived January, 2014, visiting faculty, Regis University, Denver, CO.
[3]Affiliated faculty, Humboldt State University, Arcata, CA.
[4]Affiliated faculty, currently at Cloudant, Inc.
[5]Departed May, 2013, currently at N.I.S.T.
[6]Affiliated faculty, University of North Carolina, Chapel Hill, NC.
[7]Retired December, 2013.
[8]CENPA External Advisory Committee formed January, 2014.

10.3 Postdoctoral Research Associates

L. Peter Alonzi
Jason Crnkovic[1]
Clara Cuesta[2,3]
Martin Fertl[4]
Jarek Kaspar[5]
Andreas Kraft[2,6]
Arnaud Leredde[2,7,8]
Diana Parno
Matthew Sternberg[7]
Krishna Venkateswara[2]
Andrew Wagner[2]
Frederik Wauters

10.4 Predoctoral Research Associates

Yelena Bagdasarova
Laura Bodine
Christian Boutan[2]
Micah Buuck[3]
Ted Cook[2,9]
Aaron Fienberg
Nathan Froemming
Brent Graner
Julieta Gruszko[2]
Ian Guinn[3]
Charles Hagedorn[2]
Ran Hong
Michael Hotz[2]
David Kettler[10]
Luke Kippenbrock
Jared Kofron
John G. Lee[2]
Jonathan Leon
Dmitry Lyapustin[2]
Timothy Major
Eric Martin
Elizabeth McBride[11]
Michael Murray
Rachel Ryan
James Sloan[2,3]
Matthias Smith
William Terrano[2]
Matthew Turner[2]
Todd Wagner[2]
David Zumwalt[2]

[1] Appointed postdoc May, 2013.
[2] Not supported by DOE CENPA grant.
[3] Arrived June, 2013.
[4] Arrived February, 2014.
[5] Appointed Acting Assistant Professor at University of Washington, February, 2014.
[6] Arrived May, 2013.
[7] Arrived September, 2013.
[8] Supported by Argonne National Laboratory.
[9] Graduated June, 2013, currently at Micro Encoder, Inc.
[10] Graduated December, 2013.
[11] Arrived June, 2013, departed September, 2013.

10.5 NSF Research Experience for Undergraduates participants

Rachel Bielajew	University of Michigan	Alejandro García, Advisor
Alexandra Huss	Hamilton College	Nikolai Tolich, Advisor
Hannah LeTourneau	Whitworth University	Jason Detwiler, Advisor
Carisa Miller	University of Albany (SUNY)	Leslie Rosenberg, Advisor

10.6 University of Washington graduates taking research credit

Rachel Morris[1]	Alejandro García, Advisor
Matthew Noakes[2]	Nikolai Tolich, Advisor
Rachel Osofsky[2]	Alejandro García, Advisor
Erik Shaw[2]	Alejandro García, Advisor

10.7 University of Washington undergraduates taking research credit

Amna Al-Qabandi	Nikolai Tolich, Advisor
Shawn Apodaca	Nikolai Tolich, Advisor
Jennie Chen	Blayne Heckel, Advisor
Justin Dubinsky	Nikolai Tolich, Advisor
Cole Helling	Alejandro García, Advisor
Holly Hess	Eric Adelberger, Advisor
Andrew Hillman	Alejandro García, Advisor
Yujung Kim	Alejandro García, Advisor
Eric Lee-Wong	Blayne Heckel, Advisor
Ronaldo Ortez	Alejandro García, Advisor
Gary Joseph Plunkett	David W. Hertzog, Advisor
Jaden Stock	Alejandro García, Advisor
Wei Quan	Nikolai Tolich, Advisor
Thomas Wolowiec	Leslie Rosenberg, Advisor
Alexander Michael Zderic	Svenja Fleicher, Advisor

10.8 Visiting students taking research credit

Holly F. Leopardi[3]	Humboldt State University	C.D Hoyle, Advisor

[1] Arrived June, 2013.
[2] Arrived September, 2013.
[3] Arrived June, 2013, departed August, 2013.

10.9 Professional staff

John F. Amsbaugh	Research Engineer	Design of KATRIN, MuSun
Tom H. Burritt[1]	Shop supervisor	Precision design, machining
Gregory C. Harper	Associate Director	Accelerator, ion sources
Gary T. Holman	Systems Manager	Computer systems
Duncan J. Prindle, Ph.D.	Research Scientist	Heavy ion, muon research
Hendrik Simons[2]	Instrument Maker	Precision mechanical equipment
Eric B. Smith	Research Engineer	Accelerator, ion sources
H. Erik Swanson, Ph.D.	Research Physicist	Precision experimental equipment
Timothy D. Van Wechel	Research Engineer	Analog and digital electronics design
Douglas I. Will	Senior Engineer	Cryogenics, ion sources, buildings

10.10 Technical staff

James H. Elms	Instrument Maker
David R. Hyde	Instrument Maker
David A. Peterson	Electronics Technician

10.11 Administrative staff

Victoria A. Clarkson	Administrator
Robert S. Shupe	Fiscal Specialist 2

10.12 Part-time staff and student helpers

Z. T. Alexander[3]
Grant Leum[4]
Christopher Jantzi[5]
Sean MacDonald
Ronaldo Ortez
Joben Pedersen
Robert Percival[6]
Clifford Plesha
Katleiah Ramos[7]
Samuel Sexton[7]
Isabelle Smith[8]
Frank Sullivan
David Tarazona Gonzalez[9]
Joseph Toles[10]
Kazimir Wall
Skylar Wheaton[3]
Megan Wachtendonk
David Walt
Natasha Woods

[1]Promoted to shop supervisor October, 2013.
[2]Retired December, 2013, began February, 2014, as part-time professional staff.
[3]Departed August, 2013.
[4]Arrived November, 2013.
[5]Arrived December, 2013.
[6]Arrived June, 2013.
[7]Arrived October, 2013.
[8]Arrived May, 2013, departed August, 2013.
[9]Departed May, 2013.
[10]Arrived May, 2013.

11 Publications

Publications and presentations with a date of 2013 or 2014 are included below. Some entries from early 2013 may therefore also appear in the 2013 Annual Report.

11.1 Published papers

1. "Comparison of Modeled and Measured Performance of a GSO Crystal as Gamma Detector," D. S. Parno*, M. Friend, V. Mamyan, F. Benmokhtar, A. Camsonne, G. B. Franklin, K. Paschke, and B. Quinn, Nucl. Instrum. Methods A **728**, 92 (2013); arXiv:1211.3710 [physics.ins-det].

2. "Dead layer on silicon p-i-n diode charged-particle detectors," B. L. Wall*, J. F. Amsbaugh, A. Beglarian, T. Bergmann, H. C. Bichsel, L. I. Bodine, N. M. Boyd, T. H. Burritt, Z. Chaoui, T. J. Corona, P. J. Doe, S. Enomoto, F. Harms, G. C. Harper, M. A. Howe, E. L. Martin, D. S. Parno, D. A. Peterson, L. Petzold, P. Renschler, R. G. H. Robertson*, J. Schwarz, M. Steidl, T. D. Van Wechel, B. A. VanDevender, S. Wüstling, K. J. Wierman, and J. F. Wilkerson, Nucl. Instrum. Methods A **744**, 73 (2014); arXiv:1310.1178 [physics.ins-det].†

3. "Techniques used to search for a permanent electric dipole moment of the ^{199}Hg atom and the implications for CP violation," M. D. Swallows, T. H. Loftus, W. C. Griffith, B. R. Heckel*, E. N. Fortson, and M. V. Romalis, Phys. Rev. A **87**, 012102 (2013).†

4. "Preliminary results of ANAIS-25," J. Amaré, S. Cebrián, C. Cuesta*, E. García, C. Ginestra, M. Martínez, M. A. Oliván, Y. Ortigoza, A. Ortiz de Solórzano, C. Pobes, J. Puimedón, M. L. Sarsa, J. A. Villar, and P. Villar, Nucl. Instrum. Methods A **742**, 187 (2014).

5. "Response of Parylene-coated NaI(Tl) scintillators at low temperature," N. Coron, C. Cuesta, E. García, C. Ginestra, T. A. Girard, P. de Marcillac, M. Martínez, Y. Ortigoza, A. Ortiz de Solórzano, C. Pobes, J. Puimedón, T. Redon, M. L. Sarsa, L. Torres, P. Valko, and J. A. Villar, EPJ Web of Conf. **65**, 02001 (2014).

6. "Slow scintillation time constants in NaI(Tl) for different interacting particles," C. Cuesta*, M. A. Oliván, J. Amaré, S. Cebrián, E. García, C. Ginestra, M. Martínez, Y. Ortigoza, A. Ortiz de Solórzano, C. Pobes, J. Puimedón, M. L. Sarsa, J. A. Villar, and P. Villar, Opt. Mat. **36**, 216 (2013).

7. "Empirical Survey of Neutrinoless Double Beta Decay Matrix Elements," R. G. H. Robertson*, Mod. Phys. Lett. A **28**, No. 8, 1350021 (2013); arXiv 1301.1323.†

An * denotes a CENPA author who is the lead author of or major contributor to a publication.
A † denotes a publication describing work fully or partially supported by the DOE grant.

8. “A Search for Astrophysical Burst Signals at the Sudbury Neutrino Observatory,” B. Aharmim, S. N. Ahmed, A. E. Anthony, N. Barros, E. W. Beier, A. Bellerive, B. Beltran, M. Bergevin, S. D. Biller, K. Boudjemline, M. G. Boulay, B. Cai, Y. D. Chan, D. Chauhan, M. Chen, B. T. Cleveland, G. A. Cox, X. Dai, H. Deng, J. A. Detwiler, M. DiMarco, M. D. Diamond, P. J. Doe, G. Doucas, P.-L. Drouin, F. A. Duncan, M. Dunford, E. D. Earle, S. R. Elliott, H. C. Evans, G. T. Ewan, J. Farine, H. Fergani, F. Fleurot, R. J. Ford, J. A. Formaggio, N. Gagnon, J. TM. Goon, K. Graham, E. Guillian, S. Habib, R. L. Hahn, A. L. Hallin, E. D. Hallman, P. J. Harvey, R. Hazama, W. J. Heintzelman, J. Heise, R. L. Helmer, A. Hime, C. Howard, M. Huang, P. Jagam, B. Jamieson, N. A. Jelley, M. Jerkins, K. J. Keeter, J. R. Klein, L. L. Kormos, M. Kos, C. Kraus, C. B. Krauss, A. Krueger, T. Kutter, C. C. M. Kyba, R. Lange, J. Law, I. T. Lawson, K. T. Lesko, J. R. Leslie, I. Levine, J. C. Loach, R. MacLellan, S. Majerus, H. B. Mak, J. Maneira, R. Martin, N. McCauley, A. B. McDonald, S. R. McGee, M. L. Miller, B. Monreal, J. Monroe, B. G. Nickel, A. J. Noble, H. M. O’Keeffe, N. S. Oblath, R. W. Ollerhead, G. D. Orebi Gann, S. M. Oser, R. A. Ott, S. J. M. Peeters, A. W. P. Poon, G. Prior, S. D. Reitzner, K. Rielage, B. C. Robertson, R. G. H. Robertson, M. H. Schwendener, J. A. Secrest, S. R. Seibert, O. Simard, J. J. Simpson, D. Sinclair, P. Skensved, T. J. Sonley, L. C. Stonehill, G. Tesic, N. Tolich, T. Tsui, R. Van Berg, B. A. VanDevender, C. J. Virtue, B. L. Wall, D. Waller, H. Wan Chan Tseung, D. L. Wark, P. J. S. Watson, J. Wendland, N. West, J. F. Wilkerson, J. R. Wilson, J. M. Wouters, A. Wright, M. Yeh, F. Zhang, and K. Zuber, Astropart. Phys. **55**, 1 (2014).**†**

9. “The Majorana Demonstrator Zero-Neutrino Double-Beta Decay Experiment,” N. Abgrall, E. Aguayo, F. T. Avignone III, A. S. Barabash, F. E. Bertrand, M. Boswell, V. Brudanin, M. Busch, A. S. Caldwell, Y.-D. Chan, C. D. Christofferson, D. C. Combs, J. A. Detwiler, P. J. Doe, Yu. Efremenko, V. Egorov, H. Ejiri, S. R. Elliott, J. Esterline, J. E. Fast, P. Finnerty, F. M. Fraenkle, A. Galindo-Uribarri, G. K. Giovanetti, J. Goett, M. P. Green, J. Gruszko, V. E. Guiseppe, K. Gusev, A. L. Hallin, R. Hazama, A. Hegai, R. Henning, E. W. Hoppe, S. Howard, M. A. Howe, K. J. Keeter, M. F. Kidd, A. Knecht, O. Kochetov, S. I. Konovalov, R. T. Kouzes, B. D. LaFerriere, J. Leon, L. E. Leviner, J. C. Loach, P. N. Luke, S. MacMullin, R. D. Martin, S. Mertens, L. Mizouni, M. Nomachi, J. L. Orrell, C. O’Shaughnessy, N. R. Overman, D. Phillips, A. W. P. Poon, K. Pushkin, D. C. Radford, K. Rielage, R. G. H. Robertson, M. C. Ronquest, A. G. Schubert, B. Shanks, T. Shima, M. Shirchenko, K. J. Snavely, N. Snyder, D. Steele, J. Strain, A. M. Suriano, J. Thompson, V. Timkin, W. Tornow, R. L. Varner, S. Vasilyev, K. Vetter, K. Vorren, B. R. White, J. F. Wilkerson, T. Williams, W. Xu, E. Yakushev, A. R. Young, C.-H. Yu, and V. Yumatov, Adv. High Energy Phys. **2014**, 365432 (2014).**†**

10. “Light Relative Efficiency Factors for ions in BGO and Al_2O_3 at 20 mK,” Y. Ortigoza, L. Torres, N. Coron, C. Cuesta, E. García, C. Ginestra, J. Gironnet, P. de Marcillac, M. Martínez, A. Ortiz de Solórzano, C. Pobes, J. Puimedón, T. Redon, M. L. Sarsa, and J. A. Villar, Astropart. Phys. **50**, 11 (2013).

An * denotes the CENPA lead author of a publication.

A † denotes a publication describing work fully or partially supported by the DOE grant.

11. "Background studies for NaI(Tl) detectors in the ANAIS dark matter project," J. Amaré, S. Borjabad, S. Cebrián, C. Cuesta*, D. Fortuño, E. García, C. Ginestra, H. Gómez, M. Martínez, M. A. Oliván, Y. Ortigoza, A. Ortiz de Solórzano, C. Pobes, J. Puimedón, M. L. Sarsa, J. A. Villar, and P. Villar, AIP Conf. Proc. **1549**, 165 (2013).

12. "Reactor On-Off Antineutrino Measurement with KamLAND," A. Gando, Y. Gando, H. Hanakago, H. Ikeda, K. Inoue, K. Ishidoshiro, H. Ishikawa, M. Koga, R. Matsuda, S. Matsuda, T. Mitsui, D. Motoki, K. Nakamura, A. Obata, A. Oki, Y. Oki, M. Otani, I. Shimizu, J. Shirai, A. Suzuki, Y. Takemoto, K. Tamae, K. Ueshima, H. Watanabe, B. D. Xu, S. Yamada, Y. Yamauchi, H. Yoshida, A. Kozlov, S. Yoshida, A. Piepke, T. I. Banks, B. K. Fujikawa, K. Han, T. O'Donnell, B. E. Berger, J. G. Learned, S. Matsuno, M. Sakai, Y. Efremenko, H. J. Karwowski, D. M. Markoff W. Tornow, J. A. Detwiler, S. Enomoto, and M. P. Decowski, Phys. Rev. D **88**, 033001 (2013).

13. "Combined Analysis of All Three Phases of Solar Neutrino Data from the Sudbury Neutrino Observatory," B. Aharmim, S. N. Ahmed, A. E. Anthony, N. Barros, E. W. Beier, A. Bellerive, B. Beltran, M. Bergevin, S. D. Biller, K. Boudjemline, M. G. Boulay, B. Cai, Y. D. Chan, D. Chauhan, M. Chen, B. T. Cleveland, G. A. Cox, X. Dai, H. Deng, J. A. Detwiler, M. DiMarco, P. J. Doe, G. Doucas, P.-L. Drouin, F. A. Duncan, M. Dunford, E. D. Earle, S. R. Elliott, H. C. Evans, G. T. Ewan, J. Farine, H. Fergani, F. Fleurot, R. J. Ford, J. A. Formaggio, N. Gagnon, J. TM. Goon, K. Graham, E. Guillian, S. Habib, R. L. Hahn, A. L. Hallin, E. D. Hallman, P. J. Harvey, R. Hazama, W. J. Heintzelman, J. Heise, R. L. Helmer, A. Hime, C. Howard, M. Huang, P. Jagam, B. Jamieson, N. A. Jelley, M. Jerkins, K. J. Keeter, J. R. Klein, L. L. Kormos, M. Kos, C. Kraus, C. B. Krauss, A. Krueger, T. Kutter, C. C. M. Kyba, R. Lange, J. Law, I. T. Lawson, K. T. Lesko, J. R. Leslie, J. C. Loach, R. MacLellan, S. Majerus, H. B. Mak, J. Maneira, R. Martin, N. McCauley, A. B. McDonald, S. R. McGee, M. L. Miller, B. Monreal, J. Monroe, B. G. Nickel, A. J. Noble, H. M. O'Keeffe, N. S. Oblath, R. W. Ollerhead, G. D. Orebi Gann, S. M. Oser, R. A. Ott, S. J. M. Peeters, A. W. P. Poon, G. Prior, S. D. Reitzner, K. Rielage, B. C. Robertson, R. G. H. Robertson, R. C. Rosten, M. H. Schwendener, J. A. Secrest, S. R. Seibert, O. Simard, J. J. Simpson, P. Skensved, T. J. Sonley, L. C. Stonehill, G. Tesic, N. Tolich*, T. Tsui, R. Van Berg, B. A. VanDevender, C. J. Virtue, H. Wan Chan Tseung, D. L. Wark, P. J. S. Watson, J. Wendland, N. West, J. F. Wilkerson, J. R. Wilson, J. M. Wouters, A. Wright, M. Yeh, F. Zhang, and K. Zuber, Phys. Rev. C **88**, 025501 (2013).†

14. "Complementarity of dark matter direct detection: the role of bolometric targets," D. G. Cerdeño, C. Cuesta, M. Fornasa, E. García, C. Ginestra, Ji-Haeng Huh, M. Martínez, Y. Ortigoza, M. Peiró, J. Puimedón, L. M. Robledo, and M. L. Sarsa, J. Cosm. Astrop. Phys. **07**, 028 (2013).

An * denotes the CENPA lead author of a publication.
A † denotes a publication describing work fully or partially supported by the DOE grant.

15. "CoGeNT: A search for low-mass dark matter using p-type point contact germanium detectors," C. E. Aalseth, P. S. Barbeau, J. Colaresi, J. I. Collar, J. Leon, J. E. Fast, N. E. Fields, T. W. Hossbach, A. Knecht, M. S. Kos, M. G. Marino, H. S. Miley, M. L. Miller, J. L. Orrell, and K. M. Yocum, Phys. Rev. D **88**, 012002 (2013).

16. "Study of parylene-coated NaI(Tl) at low temperatures for bolometric applications," N. Coron, C. Cuesta, E. García, C. Ginestra, T. A. Girard, P. de Marcillac, M. Martínez, Y. Ortigoza, A. Ortiz de Solórzano, C. Pobes, J. Puimedón, T. Redon, M. L. Sarsa, L. Torres, P. Valko, and J. A. Villar, Astropart. Phys. **47**, 31 (2013).

17. "Limit on Neutrinoless $\beta\beta$ Decay of ^{136}Xe from the First Phase of KamLAND-Zen and Comparison with the Positive Claim in ^{76}Ge," A. Gando, Y. Gando, H. Hanakago, H. Ikeda, K. Inoue, K. Ishidoshiro, R. Kato, M. Koga, S. Matsuda, T. Mitsui, D. Motoki, T. Nakada, K. Nakamura, A. Obata, A. Oki, Y. Ono, M. Otani, I. Shimizu, J. Shirai, A. Suzuki, Y. Takemoto, K. Tamae, K. Ueshima, H. Watanabe, B. D. Xu, S. Yamada, H. Yoshida, A. Kozlov, S. Yoshida, T. I. Banks, S. J. Freedman, B. K. Fujikawa, K. Han, T. O'Donnell, B. E. Berger, Y. Efremenko, H. J. Karwowski, D. M. Markoff W. Tornow, J. A. Detwiler, S. Enomoto, and M. P. Decowski, Phys. Rev. Lett. **110**, 062502 (2013).

18. "Two-component model of 2D trigger-associated hadron correlations on rapidity space $y_{ta} \times y_{tt}$ derived from 1D p_t spectra for p-p collisions at $\sqrt{s} = 200$ GeV," T A. Trainor* and D. J. Prindle, Phys. Rev. D **88**, 094018 (2013) .†

19. "Dijet production, collision centrality and backgrounds in high-energy p-p collisions," T. A. Trainor* Phys. Rev. D **87**, 054005 (2013).†

20. "Azimuth multipoles vs minimum-bias jets in 2D angular correlations on η and ϕ," T. A. Trainor* J. Phys. G **40**, 055104 (2013).†

21. "Challenging the utility of third-order azimuth harmonics in the description of ultra-relativistic heavy-ion collisions," R. L. Ray, D. J. Prindle and T. A. Trainor* Phys. Rev. C **88**, 044920 (2013).†

22. "Performance of Geant4 in simulating semiconductor particle detector response in the energy range below 1 MeV," G. Soti, F. Wauters*, M. Breitenfeldt, P. Finlay, I. S. Kraev, A. Knecht, T. Porobi, D. Zkouck, and N. Severijns, Nucl. Instrum. Methods A **728**, 11 (2013).

23. "Magnetic Dipole Moment of the Doubly-Closed-Shell Plus One Proton Nucleus Sc-49," T. Ohtsubo, N. J. Stone, J. R. Stone, I. S. Towner, C. R. Bingham, C. Gaulard, U. Koester, S. Muto, J. Nikolov, K. Nishimura, G. S. Simpson, G. Soti, M. Veskovic, W. B. Walters, and F. Wauters, Phys. Rev. Lett. **109**, 032504 (2012).

24. "A high-precision mechanical absolute-rotation sensor," K. Venkateswara*, C. A. Hagedorn, M. D. Turner, T. Arp, and J. H. Gundlach, Rev. Sci. Instrum. **85**, 015005 (2014).

An * denotes the CENPA lead author of a publication.
A † denotes a publication describing work fully or partially supported by the DOE grant.

25. "Characteristics of Signals Originating Near the Lithium-Diffused N+ Contact of High Purity Germanium P-Type Point Contact Detectors," E. Aguayo, M. Amman, F. T. Avignone III, A. S. Barabash, P. J. Barton, J. R. Beene, F. E. Bertrand, M. Boswell, V. Brudanin, M. Busch, Y.-D. Chan, C. D. Christofferson, J. I. Collar, D. C. Combs, R. J. Cooper, J. A. Detwiler, P. J. Doe, Yu. Efremenko, V. Egorov, H. Ejiri, S. R. Elliott, J. Esterline, J. E. Fast, N. Fields, P. Finnerty, F. M. Fraenkle, A. Galindo-Uribarri, V. M. Gehman, G. K. Giovanetti, M. P. Green, V. E. Guiseppe, K. Gusev, A. L. Hallin, R. Hazama, R. Henning, E. W. Hoppe, M. Horton, S. Howard, M. A. Howe, R. A. Johnson, K. J. Keeter, M. F. Kidd, A. Knecht, O. Kochetov, S. I. Konovalov, R. T. Kouzes, B. D. LaFerriere, J. Leon, L. E. Leviner, J. C. Loach, Q. Looker, P. N. Luke, S. MacMullin, M. G. Marino*****, R. D. Martin, J. H. Merriman, M. L. Miller, L. Mizouni, M. Nomachi, J. L. Orrell, N. R. Overman, G. Perumpilly, D. G. Phillips II, A. W. P. Poon, K. Pushkin, D. C. Radford, K. Rielage, R. G. H. Robertson, M. C. Ronquest, A. G. Schubert, T. Shima, M. Shirchenko, K. J. Snavely, D. Steele, J. Strain, V. Timkin, W. Tornow, R. L. Varner, K. Vetter, K. Vorren, J. F. Wilkerson, E. Yakushev, H. Yaver, A. R. Young, C.-H. Yu, and V. Yumatov, Nucl. Inst. Meth. Phys. Res. A **701**, 176 (2013).**†**

26. "Performance of the Los Alamos National Laboratory spallation-driven solid-deuterium ultra-cold neutron source," A. Saunders, M. Makela, Y. Bagdasarova, H. O. Back, J. Boissevain, L. J. Broussard, T. J. Bowles, R. Carr, S. A. Currie, B. Filippone, A. García, P. Geltenbort, K. P. Hickerson, R. E. Hill, J. Hoagland, S. Hoedl, A. T. Holley, G. Hogan, T. M. Ito, S. Lamoreaux, C.-Y. Liu, J. Liu, R. R. Mammei, J. Martin, D. Melconian, M. P. Mendenhall, C. L. Morris, R. N. Mortensen, R. W. Pattie, Jr., M. Pitt, B. Plaster, J. Ramsey, R. Rios, A. Sallaska, S. J. Seestrom, E. I. Sharapov, S. K. L. Sjue, W. E. Sondheim, W. Teasdale, A. R. Young, B. VornDick, R. B. Vogelaar, Z. Wang, and Y. Xu, Rev. Sci. Instrum. **84**, 013304 (2013).**†**

27. "Electron capture on ^{116}In and implications for nuclear structure related to double-β decay," C. Wrede*****, S. K. L. Sjue, A. García*****, H. E. Swanson, I. Ahmad, A. Algora, V.-V. Elomaa, T. Eronen, J. Hakala, A. Jokinen, V. S. Kolhinen, I. D. Moore, H. Penttilä, M. Reponen, J. Rissanen, A. Saastamoinen, and J. Äystö, Phys. Rev. C **87**, 031303 (2013).**†**

28. "Precision Measurement of the Neutron Beta-Decay Asymmetry," M. P. Mendenhall, R. W. Pattie, Jr., Y. Bagdasarova, D. B. Berguno, L. J. Broussard, R. Carr, S. Currie, X. Ding, B. W. Filippone, A. García, P. Geltenbort, K. P. Hickerson, J. Hoagland, A. T. Holley, R. Hong, T. M. Ito, A. Knecht, C.-Y. Liu, J. L. Liu, M. Makela, R. R. Mammei, J. W. Martin, D. Melconian, S. D. Moore, C. L. Morris, A. Pérez-Galván, R. Picker, M. L. Pitt, B. Plaster, J. C. Ramsey, R. Rios, A. Saunders, S. J. Seestrom, E. I. Sharapov, W. E. Sondheim, E. Tatar, R. B. Vogelaar, B. VornDick, C. Wrede, A. R. Young and B. A. Zeck, Phys. Rev. C **87**, 032501 (2013).**†**

An ***** denotes the CENPA lead author of a publication.
A **†** denotes a publication describing work fully or partially supported by the DOE grant.

29. "Weak Interaction Studies with ^{6}He," A. Knecht*, Z. T. Alexander, Y. Bagdasarova, T. M. Cope, B. G. Delbridge, X. Fléchard, A. García, R. Hong, E. Linard, P. Mueller, O. Naviliat-Cuncic, A. S. C. Palmer, R. G. H. Robertson, D. W. Storm, H. E. Swanson, S. Utsuno, F. Wauters, W. Williams, C. Wrede, and D. W. Zumwalt, CIPANP 2012 Proceedings, AIP Conf. Proc. **1560**, 636 (2013).†

30. "Decay studies for neutrino physics: Electron capture decays of ^{100}Tc and ^{116}In," A. García*, S. K. L. Sjue, E. Swanson, C. Wrede, D. Melconian, A. Algora, and I. Ahmad, Hyperfine Interactions **223**, 201 (2014).†

31. "Limits on tensor-type weak currents from nuclear and neutron β decays," F. Wauters*, A. García*, and R. Hong, Phys. Rev. C **89**, 025501 (2014).†

32. "Limits on Exotic Long-Range Spin-Spin Interactions of Electrons," B. R. Heckel*, W. A. Terrano, and E. G. Adelberger, Phys. Rev. Lett. **111**, 151802 (2013).†

33. "Measurement of the ν_e and Total ^{8}B Solar Neutrino Fluxes with the Solar Neutrino Observatory Phase III Data Set," B. Aharmim, S. N. Ahmed, J. F. Amsbaugh, J. M. Anaya, A. E. Anthony, J. Banar, N. Barros, E. W. Beier, A. Bellerive, B. Beltran, M. Bergevin, S. D. Biller, K. Boudjemline, M. G. Boulay, T. J. Bowles, M. C. Browne, T. V. Bullard, T. H. Burritt, B. Cai, Y. D. Chan, D. Chauhan, M. Chen, B. T. Cleveland, G. A. Cox, C. A. Currat, X. Dai, H. Deng, J. A. Detwiler, M. DiMarco, P. J. Doe, G. Doucas, M. R. Dragowsky, P.-L. Drouin, C. A. Duba, F. A. Duncan, M. Dunford, E. D. Earle, S. R. Elliott, H. C. Evans, G. T. Ewan, J. Farine, H. Fergani, F. Fleurot, R. J. Ford, J. A. Formaggio, M. M. Fowler, N. Gagnon, J. V. Germani, A. Goldschmidt, J. TM. Goon, K. Graham, E. Guillian, S. Habib, R. L. Hahn, A. L. Hallin, E. D. Hallman, A. A. Hamian, G. C. Harper, P. J. Harvey, R. Hazama, K. M. Heeger, W. J. Heintzelman, J. Heise, R. L. Helmer, R. Henning, A. Hime, C. Howard, M. A. Howe, M. Huang, P. Jagam, B. Jamieson, N. A. Jelley, K. J. Keeter, J. R. Klein, L. L. Kormos, M. Kos, A. Krueger, C. Kraus, C. B. Krauss, T. Kutter, C. C. M. Kyba, R. Lange, J. Law, I. T. Lawson, K. T. Lesko, J. R. Leslie, J. C. Loach, R. MacLellan, S. Majerus, H. B. Mak, J. Maneira, R. Martin, N. McCauley, A. B. McDonald, S. R. McGee, C. Mifflin, G. G. Miller, M. L. Miller, B. Monreal, J. Monroe, B. Morissette, A. W. Myers, B. G. Nickel, A. J. Noble, H. M. O'Keeffe, N. S. Oblath, R. W. Ollerhead, G. D. Orebi Gann, S. M. Oser, R. A. Ott, S. J. M. Peeters, A. W. P. Poon, G. Prior, S. D. Reitzner, K. Rielage, B. C. Robertson, R. G. H. Robertson, E. Rollin, M. H. Schwendener, J. A. Secrest, S. R. Seibert, O. Simard, J. J. Simpson, P. Skensved, M. W. E. Smith, T. J. Sonley, T. D. Steiger, L. C. Stonehill, G. Tesic, P. M. Thornewell, N. Tolich*, T. Tsui, C. D. Tunnell, T. Van Wechel, R. Van Berg, B. A. VanDevender, C. J. Virtue, B. L. Wall, D. Waller, H. Wan Chan Tseung, J. Wendland, N. West, J. B. Wilhelmy, J. F. Wilkerson, J. R. Wilson, J. M. Wouters, A. Wright, M. Yeh, F. Zhang, and K. Zuber Phys. Rev. C **87**, 015502 (2013).†

An * denotes the CENPA lead author of a publication.
A † denotes a publication describing work fully or partially supported by the DOE grant.

34. "Detailed report of the MuLan measurement of the positive muon lifetime and determination of the Fermi constant,"MuLan Collaboration: V. Tishchenko, S. Battu, R. M. Carey, D. B. Chitwood, J. Crnkovic, P. T. Debevec, S. Dhamija, W. Earle, A. Gafarov, K. Giovanetti, T. P. Gorringe, F. E. Gray, Z. Hartwig, D. W. Hertzog*, B. Johnson, P. Kammel*, B. Kiburg, S. Kizilgul, J. Kunkle, B. Lauss, I. Logashenko, K. R. Lynch, R. McNabb, J. P. Miller, F. Mulhauser, C. J. G. Onderwater, Q. Peng, J. Phillips, S. Rath, B. L. Roberts, D. M. Webber, P. Winter*, and B. Wolfe, Phys. Rev. D **87**, 052003 (2013).

35. "Measurement of Muon Capture on the Proton to 1% Precision and Determination of the Pseudoscalar Coupling g_P," V. A. Andreev, T. I. Banks, R. M. Carey, T. A. Case, S. M. Clayton, K. M. Crowe, J. Deutsch, J. Egger, S. J. Freedman, V. A. Ganzha, T. Gorringe, F. E. Gray, D. W. Hertzog*, M. Hildebrandt, P. Kammel*, B. Kiburg*, S. Knaack*, P. A. Kravtsov, A. G. Krivshich, B. Lauss, K. R. Lynch, E. M. Maev, O. E. Maev, F. Mulhauser, C. Petitjean, G. E. Petrov, R. Prieels, G. N. Schapkin, G. G. Semenchuk, M. A. Soroka, V. Tishchenko, A. A. Vasilyev, A. A. Vorobyov, M. E. Vznuzdaev, and P. Winter*, Phys. Rev. Lett. **110**, 012504 (2013).†

36. "Precision Muon Capture at PSI", P. Kammel* representing the MuCap and MuSun collaboration, PoS CD12 (2013) 016.†

37. "Solar Neutrinos: Status and Prospects," W. C. Haxton, R. G. H. Robertson*, and A. Serenelli, Ann. Rev. Astron. Astrophys. **51**, 21 (2013).†

38. "Neutrino mass sensitivity by MAC-E-Filter based time-of-flight spectroscopy with the example of KATRIN," N. Steinbrink, V. Hannen, E. L. Martin*, R. G. H. Robertson, M. Zacher and C. Weinheimer, New Journal of Physics **15**, 113020 (2013); arXiv:1308.0532.†

39. "Energy dependence of moments of net-proton multiplicity distributions at RHIC," H. Bichsel, J. G. Cramer, and the STAR Collaboration[1], Phys. Rev. Lett. **112** (2014) 32302; arXiv: 1309.5681 (2013).†

40. "Neutral pion cross section and spin asymmetries at intermediate pseudorapidity in polarized proton collisions at $\sqrt{s} = 200$ GeV ," H. Bichsel, J. G. Cramer, and the STAR Collaboration[1], Phys. Rev. D **89** (2014) 12001; arXiv: 1309.1800 (2013).†

41. "Fluctuations of charge separation perpendicular to the event plane and local parity violation in $\sqrt{s_{NN}} = 200$ GeV Au+Au collisions at RHIC ," H. Bichsel, J. G. Cramer, and the STAR Collaboration[1], Phys. Rev. C **88** (2013) 64911; arXiv: 1302.3802 (2013).†

42. "Freeze-out Dynamics via Charged Kaon Femtoscopy in $\sqrt{s_{NN}} = 200$ GeV Central Au+Au Collisions," H. Bichsel, J. G. Cramer, and the STAR Collaboration[1], Phys. Rev. **88** (2013) 34906; arXiv: 1302.3168 (2013).†

An * denotes the CENPA lead author of a publication.
A † denotes a publication describing work fully or partially supported by the DOE grant.

[1]See (Sec. 11.7) for collaboration author list.

43. "System Size Dependence of Transverse Momentum Correlations at RHIC," H. Bichsel, J. G. Cramer, and the STAR Collaboration[1], Phys. Rev. C **87** (2013) 64902; arXiv: 1301.6633 (2013).†

44. "Third Harmonic Flow of Charged Particles in Au+Au Collisions at $\sqrt{s_{NN}} = 200$ GeV,"H. Bichsel, J. G. Cramer, and the STAR Collaboration[1], Phys. Rev. C **88** (2013) 14904; arXiv: 1301.2187 (2013).†

45. "Observation of an energy-dependent difference in elliptic flow between particles and antiparticles in relativistic heavy ion collisions," H. Bichsel, J. G. Cramer, and the STAR Collaboration[1], Phys. Rev. Lett. **110** (2013) 142301; arXiv: 1301.2347 (2013).†

46. "Elliptic flow of identified hadrons in Au+Au collisions at $\sqrt{s_{NN}} = 7.7$–62.4 GeV," H. Bichsel, J. G. Cramer, and the STAR Collaboration[1], Phys. Rev. C **88** (2013) 14902; arXiv: 1301.2348 (2013).†

47. "Measurement of J/psi Azimuthal Anisotropy in Au+Au Collisions at $\sqrt{s_{NN}} = 200$ GeV," H. Bichsel, J. G. Cramer, and the STAR Collaboration[1], Phys. Rev. Lett. **111** (2013) 52301; arXiv: 1212.3304 (2013).†

48. "Studies of di-jets in Au+Au collisions using angular correlations with respect to back-to-back leading hadrons," H. Bichsel, J. G. Cramer, and the STAR Collaboration[1], Phys. Rev. C **87** (2013) 44903; arXiv: 1212.1653 (2013).†

49. "J/ψ production at high transverse momenta in p+p and Au+Au collisions at $\sqrt{s_{NN}} = 200$ GeV," H. Bichsel, J. G. Cramer, and the STAR Collaboration[1], Phys. Rev. D **89** (2014) 12001; arXiv: 1309.1800 (2013).†

50. "System size dependence of particle-ratio fluctuations in Pb+Pb collisions at 158A GeV," J. G. Cramer and the NA49 Collaboration[1], Phys.Rev. C **87** (2013) 024902; arXiv: 1204.2130 (2012).†

51. "Improved limits on long-range parity-odd interactions of the neutron", E. G. Adelberger*and T. A. Wagner*, Phys. Rev. D**88**, 031101 (2013).

52. "A reference-beam autocollimator with nanoradian sensitivity from mHz to kHz and dynamic range of 10^7," T. Arp*, C. A. Hagedorn*, S. Schlamminger, and J. H. Gundlach, Rev. Sci. Instrum. **84**, 095007 (2013).

53. "Improved limits on long-range parity-odd interactions of the neutron," E. G. Adelberger and T. A. Wagner, Phys. Rev. D **88**, 031101 (2013).

54. "Hidden Sector Photon Coupling of Resonant Cavities," S. R. Parker, G. Rybka, and M. E. Tobar, Phys. Rev. D **87**, 115008 (2013).

An * denotes the CENPA lead author of a publication.
A † denotes a publication describing work fully or partially supported by the DOE grant.

[1]See (Sec. 11.7) for collaboration author list.

55. "Axions And Other Similar Particles," A. Ringwald, L. J Rosenberg, and G. Rybka, 2014 update to PDG Phys. Rev. D **86**, 010001 (2012).

11.2 Invited talks at conferences

1. "d_2^n and A_1^n: Recent Results and Outlook," D. S. Parno*, Invited talk, Jefferson Lab Users' Group Meeting, Newport News, VA, May, 2013.

2. "The KATRIN Experiment: Status and Outlook," D. S. Parno*, Invited talk, Proceedings of the Sixth Meeting on CPT and Lorentz Symmetry, Indiana University, June, 2013; arXiv:1307.5289 [physics.ins-det].†

3. "The KATRIN Experiment," D. S. Parno*, Invited talk, Perspectives on Fundamental Symmetries and Neutrinos, University of Washington, Seattle, WA, September, 2013.†

4. "KATRIN: Probing the Neutrino Mass," D. S. Parno*, Medium-Energy Particle Physics Seminar, Carnegie Mellon University, October, 2013.†

5. "Looking for Nothing: Experimental Searches for Neutrinoless Double-Beta Decay," J. A. Detwiler*, American Physical Society Division of Nuclear Physics Meeting, Thomas Jefferson National Accelerator Facility, Newport News, VA, October 24, 2013.

6. "Is the Neutrino its Own Antiparticle?" J. A. Detwiler*, Occidental College 125th Anniversary Distinguished Alumni Speaker Series, Los Angeles, CA, April 25, 2013.

7. "Improved isolation of the p-p underlying event based on minimum-bias trigger-associated hadron correlations," T. A. Trainor* and D. J. Prindle, XLIIIrd Symposium on Multiparticle Dynamics (ISMD13), Chicago, IL, September 16-20, 2013.†

8. "Fundamental symmetries with ^{6}He," A. García, National Superconducting Laboratory at Michigan State University, East Lansing, MI, April 3, 2013.

9. "Fundamental symmetries with ^{6}He," A. García, Oak Ridge National Lab, Oak Ridge, TN, August 14, 2013.

10. "Fundamental symmetries with ^{6}He: exchange currents, g_A, and searches for chirality violating interactions," A García, Institute for Nuclear Theory at UW, Workshop on Nuclei and Fundamental Symmetries: Theory Needs of Next-Decade Experiments; Seattle, WA, August 26, 2013.

11. "Fundamental symmetries with ^{6}He," A. García, Invited talk, Perspectives on Fundamental Symmetries and Neutrinos, University of Washington, Seattle, WA, September, 2013.†

An * denotes the CENPA lead author of a publication.
A † denotes a publication describing work fully or partially supported by the DOE grant.

12. “Precision Muon Physics,” D. W. Hertzog, Argonne National Laboratory HEP Division Seminar, April 2, 2013.†
13. “Precision Muon Physics,” D. W. Hertzog, Invited talk; American Physical Society Annual Meeting, Denver, CO, April 14, 2013.†
14. “Low-energy precision experiments,” D. W. Hertzog, Invited talk, Latsis Symposium 2013: Nature at the Energy Frontier, Zurich, Switzerland, June 4, 2013.†
15. “Measurement of the Positive Muon Lifetime and Determination of the Fermi Constant to Part-per-Million Precision,” D. W. Hertzog, Seminar, Cornell University, February 7, 2014.†
16. “Next-Generation Muon g-2 Experiment”, D. W. Hertzog, Colloquium, Texas A&M University, February 27, 2014.†
17. “Precision Muon Capture,” P. Kammel, Seminar, TRIUMF, Vancouver, March, 2013.†
18. “Precision Muon Capture,” P. Kammel, Seminar, SLAC, Stanford, CA, April, 2013.†
19. “Muon Capture: Status and Prospects,” P. Kammel, Invited talk, PSI2013, 3rd Workshop on the Physics of Fundamental Symmetries and Interactions at low energies and the precision frontier, Paul Scherrer Institute, Switzerland, September 9-12, 2013.†
20. “Precision Muon Physics,” P. Kammel, Seminar, Rome, Italy, September, 2013.†
21. “Precision Muon Physics,” P. Kammel, Seminar, Pisa, Italy, February, 2014.†
22. “Solar neutrinos, the physics gold mine,” R. G. H. Robertson, Invited talk, Carolina International Symposium on Neutrino Physics 2013, Columbia, SC, May 19 - 22, 2013.
23. “Fundamental symmetries and neutrinos at CENPA,” R. G. H. Robertson, Invited presentation, DOE Comparative Review, Gaithersburg, MD June 25, 2013.
24. “Fundamental symmetries and neutrinos from 30,000 feet,” R. G. H. Robertson, Invited talk, RHIC Users Group, Brookhaven, NY, June 26, 2013.
25. “Summary - Session Nu3: Absolute neutrino mass,” R. G. H. Robertson, Invited talk, Snowmass Conference, Minneapolis, MN, August 2, 2013.
26. “Neutrino Mass – a long wait for a little weight,” R. G. H. Robertson, Invited talk, Freedman Memorial Symposium, Berkeley, CA, January 11, 2014.
27. “Project 8 – toward a radiometric neutrino mass measurement,” J. Kofron, Invited seminar, UC Berkeley INPA, March 21, 2013.

An * denotes the CENPA lead author of a publication.
A † denotes a publication describing work fully or partially supported by the DOE grant.

28. "The physics laboratory as a heterogenous computing playground," J. Kofron, Invited talk, Erlang Factory, San Francisco, CA, March 6, 2014.

29. "Testing Nonlocal Communication," J. G. Cramer*, Colloquium, Institute for Quantum Communication and Quantum Information, Vienna, Austria, October 3, 2013.†

30. "Exotic Paths to the Stars," J. G. Cramer*, Invited talk, Starship Century Symposium, Center for Human Imagination, University of California at San Diego, San Diego, CA, May 22, 2013; video of talk is available online at: `http://www.starshipcentury.com/blog/videos-of-starship-century-symposium-part-2`.

31. "Tritium-Recoil Ion Mass Spectrometer," L. I. Bodine*, Contributed talk, Workshop on final states, Karlsruhe, Germany, March 5, 2014.†.

32. "Tritium neutrino mass experiments: measuring the molecular dissociation probability," L. I. Bodine, American Physical Society April Meeting, Denver, CO, April, 2013.†

33. "Measuring molecular dissociation in tritium beta decay: validating theory used in neutrino mass experiments," L. I. Bodine, American Physical Society Division of Nuclear Physics Meeting, Newport News, VA, October, 2013.†

34. "Using .NET Tools and FPGAs To Test Einstein's Theories," H. E. Swanson, Invited talk, NIWeek Worldwide Graphical System Design Conference, Austin, TX, August, 2014.

35. "Gravity Experiments and Particle Physics," E. G. Adelberger, Invited talk, Perspectives on Fundamental Symmetries and Neutrinos, University of Washington, Seattle, WA, September, 2013.†

36. "Gravity and Levity: lessons from Stuart on measuring 'nothing' and trying to get it right," E. G. Adelberger, Invited talk, Stuart Freedman Symposium "Measuring 'nothing' and getting it right," Berkeley, CA, January 11, 2014.

37. "Implications of torsion-balance results for some speculations about exotic physics," E. G. Adelberger, Invited talk, 2014 GRANIT workshop, Les Houches, France, March 5, 2014.

38. "Testing quantum gravity speculations with classical experiments," E. G. Adelberger, Invited plenary talk, Spring meeting of the German Physical Society, Hannover, Germany, March 21, 2013.

39. "New Data and New Perspectives from ADMX," G. Rybka, New Perspectives on Dark Matter, Fermilab, IL, April 29, 2014.

An * denotes the CENPA lead author of a publication.
A † denotes a publication describing work fully or partially supported by the DOE grant.

40. "Direct-Detection Searches for Axion Dark Matter," G. Rybka, 13th International Conference on Topics in Astroparticle and Underground Physics, Asilomar, CA, September 8, 2013.

41. "The Future of Direct Neutrino Mass Measurements: Project 8 and Beyond," G. Rybka, Aspen Winter Workshop New Directions in Neutrino Physics, Aspen, CO, February 3-9, 2013.

11.3 Abstracts and contributed talks

1. "The Status of the KATRIN Experiment," D. S. Parno*, American Physical Society April Meeting, Denver, CO, April, 2013.†

2. "Pulse Shape Analysis studies for the MAJORANA DEMONSTRATOR," C. Cuesta* on behalf of the MAJORANA Collaboration, Abstract, XXVI Conference on Neutrino Physics and Astrophysics (Neutrino 2014), Boston, MA, June, 2014.†

3. "Analysis of the ^{40}K contamination in NaI(Tl) crystals from different providers in the frame of the ANAIS project," C. Cuesta*, J. Amaré, S. Cebrián, E. García, C. Ginestra, M. Martínez, M. A. Oliván, Y. Ortigoza, A. Ortiz de Solórzano, C. Pobes, J. Puimedón, M. L. Sarsa, J. A. Villar, and P. Villar, accepted for publication in Int. J. of Mod. Phys. A; arXiv 1403.3580.

4. "The MAJORANA DEMONSTRATOR status and prospects," C. Cuesta* on behalf of the MAJORANA Collaboration, Abstract, 15th Annual Meeting of the Northwest Section of the American Physical Society, University of Washington, Seattle, WA, May, 2014.†

5. "Axion and Dark Matter Searches with the MAJORANA DEMONSTRATOR," J. Gruszko* on behalf of the MAJORANA Collaboration, Abstract, 15th Annual Meeting of the Northwest Section of the American Physical Society, University of Washington, Seattle, WA, May, 2014.†

6. "Design of Low Background Components for the MAJORANA DEMONSTRATOR," I. Guinn* on behalf of the MAJORANA Collaboration, Abstract, 15th Annual Meeting of the Northwest Section of the American Physical Society, University of Washington, Seattle, WA, May, 2014.†

7. "Towards a tritium experiment: Sensitivity to m_ν," R. G. H. Robertson, Contributed talk, Project 8 collaboration meeting, Richland WA, October 14, 2013.

8. "Low-noise preamplifier with forward biased reset for CoGeNT and MAJORANA," J. A. Detwiler, J. Leon*, D. A. Peterson, R. G. H. Robertson, and T. D. VanWechel, Abstract, 15th Annual Meeting of the Northwest Section of the American Physical Society, University of Washington, Seattle, WA, May, 2014.

An * denotes the CENPA lead author of a publication.
A † denotes a publication describing work fully or partially supported by the DOE grant.

9. "The Majorana Demonstrator," C. Cuesta* on behalf of the Majorana Collaboration, Poster presentation, TAUP Young Researcher poster session, 13th International Conference on Topics in Astroparticle and Underground Physics, Asilomar, CA, September, 2013.†

10. "Corrections to Eikonal Approximation for Nuclear Scattering at Low Energies," M. Buuck* and G. A. Miller, Abstract, 15th Annual Meeting of the Northwest Section of the American Physical Society, University of Washington, Seattle, WA, May, 2014.†

11. "Phenomenology of the Final State Distribution," R. G. H. Robertson, Contributed talk, Workshop on final states, Karlsruhe, Germany, March 5, 2014.

12. "Erlang does nuclear physics - controlling medium scale nuclear physics experiments," J. Kofron, Erlang Factory 2013, San Francisco, CA, March 22, 2013.

13. "Signals and detection in Project 8," J. Kofron for the Project 8 Collaboration, American Physical Society DNP Meeting, Newport News, VA, October 25, 2013.

11.4 Papers submitted or to be published

1. "Rare event searches at Canfranc: ANAIS experiment," J. Amaré, S. Cebrián, C. Cuesta*, E. García, C. Ginestra, H. Gómez, M. Martínez, M. A. Oliván, Y. Ortigoza, A. Ortiz de Solórzano, C. Pobes, J. Puimedón, M. L. Sarsa, J. A. Villar, and P. Villar, submitted to Int. J. of Mod. Phys. D.

2. "Laboratory Studies on the Removal of Radon-Born Lead from KamLAND's Organic Liquid Scintillator," G. Keefer, C. Grant, A. Piepke, T. Ebihara, H. Ikeda, Y. Kishimoto, Y. Kibe, Y. Koseki, M. Ogawa, J. Shirai, S. Takeuchi, C. Mauger, C. Zhang, G. Schweitzer, B. E. Berger, S. Dazeley, M. P. Decowski, J. A. Detwiler, Z. Djurcic, D. A. Dwyer, Y. Efremenko, S. Enomoto, S. J. Freedman, B. K. Fujikawa, K. Furuno, A. Gando, Y. Gando, G. Gratta, S. Hatakeyama, K. M. Heeger, L. Hsu, K. Ichimura, K. Inoue, T. Iwamoto, Y. Kamyshkov, H. J. Karwowski, M. Koga, A. Kozlov, C. E. Lane, J. G. Learned, J. Maricic, D. M. Marko, S. Matsuno, D. McKee, R. D. McKeown, T. Miletic, T. Mitsui, M. Motoki, K. Nakajima, K. Nakajima, K. Nakamura, T. O'Donnell, H. Ogawa, F. Piquemal, J.-S. Ricol, I. Shimizu, F. Suekane, A. Suzuki, R. Svoboda, O. Tajima, Y. Takemoto, K. Tamae, K. Tolich, W. Tornow, Hideki Watanabe, Hiroko Watanabe, L. A. Winslow, and S. Yoshida, arXiv:1312.0977 [physics.ins-det], submitted to Nucl. Inst. Meth. Phys. Res. A.

3. "Scintillating bolometers: a key for determining WIMP parameters," D. G. Cerdeño, C. Cuesta, M. Fornasa, E. García, C. Ginestra, C. Marcos, M. Martínez, Y. Ortigoza, M. Peiró, J. Puimedón, and M. L. Sarsa, accepted for publication in Int. J. of Mod. Phys. A; arXiv 1403.3539.

An * denotes the CENPA lead author of a publication.
A † denotes a publication describing work fully or partially supported by the DOE grant.

4. “EURECA Conceptual Design Report,” G. Angloher, E. Armengaud, C. Augier, A. Benoit, T. Bergmann, J. Blümer, A. Broniatowski, V. Brudanin, P. Camus, M. Chapellier, N. Coron, G. A. Cox, C. Cuesta, F. A. Danevich, L. Dumoulin, K. Eitel, A. Erb, A. Ertl, F. von Feilitzsch, D. Filosofovh, E. García, J. Gascon, G. Gerbier, C. Ginestra, J. Gironnet, A. Giuliani, M. Gros, A. Gütlein, D. Hauff, S. Henry, G. Heuermann, J. Jochum, S. Jokisch, A. Juillard, C. Kister, M. Kleifges, H. Kluck, E. V. Korolkova, V. Y. Kozlov, H. Kraus, V. A. Kudryavtsev, J. C. Lanfranchi, P. Loaiza, J. Loebell, I. Machulin, S. Marnieros, M. Martínez, A. Menshikov, A. Münster, X. F. Navick, C. Nones, Y. Ortigoza, P. Pari, F. Petricca, W. Potzel, P. P. Povinect, F. Pröbst, J. Puimedón, F. Reindl, M. Robinson, T. Rolón, S. Roth, K. Rottler, S. Rozov, C. Sailer, A. Salinas, V. Sanglard, M. L. Sarsa, K. Schäffner, B. Schmidt, S. Scholl, S. Schönert, W. Seidel, B. Siebenborn, M.v. Sivers, C. Strandhagen, R. StrauS-S, A. Tanzke, V. I. Tretyak, M. Turad, A. Ulrich, I. Usherov, P. Veber, M. Velazquez, J. A. Villar, O. Viraphong, R. J. Walker, S. Wawoczny, M. Weber, M. Willers, M. Wüstrich, E. Yakushev, X. Zhang, and A. Zöller, accepted for publication in J. Phys. of Dark Univ., ISSN 2212-6864, http://dx.doi.org/10.1016/j.dark.2014.03.004.

5. “Challenging claims of ‘elliptic flow’ by comparing azimuth quadrupole and jet-related angular correlations from Au-Au collisions at $\sqrt{s_{NN}} = 62$ and 200 GeV,” T. A. Trainor*, D. T. Kettler, D. J. Prindle and R. L. Ray, arXiv:1302.0300, submitted to J. Phys. G.†

6. “Ensemble mean p_t vs charged-hadron multiplicities in high energy nuclear collisions,” T. A. Trainor*, arXiv:1403.6494, submitted to Phys. Rev. C.†

7. “Study of scintillation in natural and synthetic quartz and methacrylate,” J. Amaré, S. Borjabad, S. Cebrián, C. Cuesta*, D. Fortuño, E. García, C. Ginestra, H. Gómez, D.C. Herrera, M. Martínez, M. A. Oliván, Y. Ortigoza, A. Ortiz de Solórzano, C. Pobes, J. Puimedón, M. L. Sarsa, J. A. Villar, and P. Villar, submitted to Opt. Mat.; arXiv 1401.3118.

8. “Universal parametrization of jet production based on parton and fragment rapidities,” T. A. Trainor*, arXiv:1403.3685, submitted to Phys. Rev. D.†

9. “Improved isolation of the p-p underlying event based on minimum-bias trigger-associated hadron correlations,” T. A. Trainor* and D. J. Prindle, arXiv:1310.0408, Proceedings of XLIII International Symposium on Multiparticle Dynamics (ISMD), Chicago, IL, September 15-20, 2013.†

10. “Can minimum-bias distributions on transverse energy test hadron production models?,” T. A. Trainor*, arXiv:1402.4071, submitted to Phys. Rev. C.†

11. “A critical review of RHIC experimental results,” T. A. Trainor*, arXiv:1303.4774, Submitted to J. Phys. G.†

An * denotes the CENPA lead author of a publication.
A † denotes a publication describing work fully or partially supported by the DOE grant.

12. "A Search for Astrophysical Burst Signals at the Sudbury Neutrino Observatory," B. Aharmim, S. N. Ahmed, A. E. Anthony, N. Barros, E. W. Beier, A. Bellerive, B. Beltran, M. Bergevin, S. D. Biller, K. Boudjemline, M. G. Boulay, T. H. Burritt, B. Cai, Y. D. Chan, D. Chauhan, M. Chen, B. T. Cleveland, G. A. Cox, X. Dai, H. Deng, J. Detwiler, M. Diamond, M. DiMarco, P. J. Doe, G. Doucas, P.-L. Drouin, C. A. Duba, F. A. Duncan, M. Dunford, E. D. Earle, S. R. Elliott, H. C. Evans, G. T. Ewan, J. Farine, H. Fergani, F. Fleurot, R. J. Ford, J. A. Formaggio, N. Gagnon, J. TM. Goon, K. Graham, E. Guillian, S. Habib, R. L. Hahn, A. L. Hallin, E. D. Hallman, P. J. Harvey, R. Hazama, W. J. Heintzelman, J. Heise, R. L. Helmer, A. Hime, C. Howard, M. A. Howe, M. Huang, P. Jagam, B. Jamieson, N. A. Jelley, K. J. Keeter, J. R. Klein, L. L. Kormos, M. Kos, C. Kraus, C. B. Krauss, A. Krueger, T. Kutter, C. C. M. Kyba, R. Lange, J. Law, I. T. Lawson, K. T. Lesko, J. R. Leslie, I. Levine, J. C. Loach, R. MacLellan, S. Majerus, H. B. Mak, J. Maneira, R. Martin, N. McCauley, A. B. McDonald, S. McGee, M. L. Miller, B. Monreal, J. Monroe, B. Morissette, B. G. Nickel, A. J. Noble, H. M. O'Keeffe, N. S. Oblath, R. W. Ollerhead, G. D. Orebi Gann, S. M. Oser, R. A. Ott, S. J. M. Peeters, A. W. P. Poon, G. Prior, S. D. Reitzner, K. Rielage, B. C. Robertson, R. G. H. Robertson, M. H. Schwendener, J. A. Secrest, S. R. Seibert, O. Simard, D. Sinclair, P. Skensved, T. J. Sonley, L. C. Stonehill, G. Tesic, N. Tolich, T. Tsui, C. D. Tunnell, R. Van Berg, B. A. VanDevender, C. J. Virtue, B. L. Wall, D. Waller, H. Wan Chan Tseung, D. L. Wark, J. Wendland, N. West, J. F. Wilkerson, J. R. Wilson, J. M. Wouters, A. Wright, M. Yeh, F. Zhang, and K. Zuber (SNO Collaboration), Astropart. Phys. (in press).†

13. "Minimum-bias angular and trigger-associated correlations from 200 GeV $p-p$ collisions: jets, flows, centrality and the underlying event," D. J. Prindle*, for the STAR collaboration[1], Proceedings of XLIII International Symposium on Multiparticle Dynamics (ISMD), Chicago, IL, September 15-20, 2013.†

11.5 Reports and white papers

1. "Project 8: Determining neutrino mass from tritium beta decay using a frequency-based method," P. J. Doe, J. Kofron, E. L. McBride, R. G. H. Robertson*, L. J Rosenberg, G. Rybka, S. Doelman, A. Rogers, J. A. Formaggio, D. Furse, N. S. Oblath, B. H. LaRoque, M. Leber, B. Monreal, M. Bahr, D. M. Asner, A. M. Jones, J. Fernandes, B. A. VanDevender, R. Patterson, R.Bradley, and T. Thuemmler," White paper submitted to the Snowmass Conference, 2013; arXiv:1309.7093.†

An * denotes the CENPA lead author of a publication.
A † denotes a publication describing work fully or partially supported by the DOE grant.

[1]See (Sec. 11.7) for collaboration author list.

2. “White paper: CeLAND - Investigation of the reactor antineutrino anomaly with an intense 144Ce-144Pr antineutrino source in KamLAND,” A. Gando, Y. Gando, S. Hayashida, H. Ikeda, K. Inoue, K. Ishidoshiro, H. Ishikawa, M. Koga, R. Matsuda, S. Matsuda, T. Mitsui, D. Motoki, K. Nakamura, Y. Oki, M. Otani, I. Shimizu, J. Shirai, F. Suekane, A. Suzuki, Y. Takemoto, K. Tamae, K. Ueshima, H. Watanabe, B. D. Xu, S. Yamada, Y. Yamauchi, H. Yoshida, T. Banks, B. E. Berger, M. Cribier, P. Decowski, J. A. Detwiler, M. Durero, D. Dwyer, Y. Efremenko, S. Enomoto, V. Fischer, B. K. Fujikawa, J. Gaffiot, V. M. Gelis, H. J. Karwowski, Yu. G. Kolomensky, A. Kozlov, V. N. Kornoukhov, T. Lasserre, J. G. Learned, A. Letourneau, D. Lhuillier, J. Maricic, D. M. Markoff, S. Matsuno, G. Mention, R. Milincic, T. ODonnell, I. S. Saldikov, L. Scola, G. V. Tikhomirov, Ch. Veyssiere, M. Vivier, and S. Yoshida, submitted September 26, 2013, arXiv:1309.6805 [hep-ex].

3. “Neutrino mass hierarchy determination and other physics potential of medium-baseline reactor neutrino oscillation experiments,” A. B. Balantekin, H. Band, R. Betts, J. J. Cherwinka, J. A. Detwiler, S. Dye, K. M. Heeger, R. Johnson, S. H. Kettell, K. Lau, J. G. Learned, C. J. Lin, J. J. Ling, B. Littlejohn, D. W. Liu, K. B. Luk, J. Maricic, K. McDonald, R. D. McKeown, J. Napolitano, J. C. Peng, X. Qian, N. Tolich, W. Wang, C. White, M. Yeh, C. Zhang, and T. Zhao, Snowmass 2013 proceedings, submitted July 28, 2013, arXiv:1307.7419 [hep-ex].

4. “KATRIN: an experiment to determine the neutrino mass from the beta decay of tritium,” R. G. H. Robertson for the KATRIN Collaboration, White Paper for the Snowmass Community Planning Workshops, 2013.

11.6 Book Publications

1. “Exotic Technologies for Interstellar Travel,” John G. Cramer*, Chapter in *Starship Century: Toward the Grandest Horizon*, Eds. James Benford and Gregory Benford, Microwave Sciences (2013), ISBN-13: 978-1-93905-129-5.

11.7 Collaborations

NA49 Collaboration

T. Anticic, B. Baatar, D. Barna, J. Bartke, H. Beck, L. Betev, H. Białkowska, C. Blume, B. Boimska, J. Book, M. Botje, P. Bunčić, P. Christakoglou, P. Chung, O. Chvala, J. Cramer, V. Eckardt, Z. Fodor, P. Foka, V. Friese, M. Gaździcki, K. Grebieszkow, C. Höhne, K. Kadija, A. Karev, V. Kolesnikov, M. Kowalski, D. Kresan, A. Laszlo, R. Lacey, M. van Leeuwen, M. Maćkowiak-Pawłowska, M. Makariev, A. Malakhov, G. Melkumov, M. Mitrovski, S. Mrówczyński, G. Pálla, A. Panagiotou, W. Peryt, J. Pluta,

An * denotes the CENPA lead author of a publication.
A † denotes a publication describing work fully or partially supported by the DOE grant.

D. Prindle, F. Pühlhofer, R. Renfordt, C. Roland, G. Roland, M. Rybczyński, A. Rybicki, A. Sandoval, A. Rustamov, N. Schmitz, T. Schuster, P. Seyboth, F. Siklér, E. Skrzypczak, M. Słodkowski, G. Stefanek, R. Stock, H. Ströbele, T. Susa, M. Szuba, D. Varga, M. Vassiliou, G. Veres, G. Vesztergombi, D. Vranić, Z. Włodarczyk, A. Wojtaszek-Szwarc

STAR Collaboration

L. Adamczyk, J. K. Adkins, G. Agakishiev, M. M. Aggarwal, Z. Ahammed, I. Alekseev, J. Alford, C. D. Anson, A. Aparin, D. Arkhipkin, E. C. Aschenauer, G. S. Averichev, A. Banerjee, D. R. Beavis, R. Bellwied, A. Bhasin, A. K. Bhati, P. Bhattarai, H. Bichsel, J. Bielcik, J. Bielcikova, L. C. Bland, I. G. Bordyuzhin, W. Borowski, J. Bouchet, A. V. Brandin, S. G. Brovko, S. Bültmann, I. Bunzarov, T. P. Burton, J. Butterworth, H. Caines, M. Calderón de la Barca Sánchez, D. Cebra, R. Cendejas, M. C. Cervantes, P. Chaloupka, Z. Chang, S. Chattopadhyay, H. F. Chen, J. H. Chen, L. Chen, J. Cheng, M. Cherney, A. Chikanian, W. Christie, J. Chwastowski, M. J. M. Codrington, G. Contin, J. G. Cramer, H. J. Crawford, X. Cui, S. Das, A. Davila Leyva, L. C. De Silva, R. R. Debbe, T. G. Dedovich, J. Deng, A. A. Derevschikov, R. Derradi de Souza, S. Dhamija, B. di Ruzza, L. Didenko, C. Dilks, F. Ding, P. Djawotho, X. Dong, J. L. Drachenberg, J. E. Draper, C. M. Du, L. E. Dunkelberger, J. C. Dunlop, L. G. Efimov, J. Engelage, K. S. Engle, G. Eppley, L. Eun, O. Evdokimov, O. Eyser, R. Fatemi, S. Fazio, J. Fedorisin, P. Filip, E. Finch, Y. Fisyak, C. E. Flores, C. A. Gagliardi, D. R. Gangadharan, D. Garand, F. Geurts, A. Gibson, M. Girard, S. Gliske, L. Greiner, D. Grosnick, D. S. Gunarathne, Y. Guo, A. Gupta, S. Gupta, W. Guryn, B. Haag, A. Hamed, L-X. Han, R. Haque, J. W. Harris, S. Heppelmann, A. Hirsch, G. W. Hoffmann, D. J. Hofman, S. Horvat, B. Huang, H. Z. Huang, X. Huang, P. Huck, T. J. Humanic, G. Igo, W. W. Jacobs, H. Jang, E. G. Judd, S. Kabana, D. Kalinkin, K. Kang, K. Kauder, H. W. Ke, D. Keane, A. Kechechyan, A. Kesich, Z. H. Khan, D. P. Kikola, I. Kisel, A. Kisiel, D. D. Koetke, T. Kollegger, J. Konzer, I. Koralt, L. K. Kosarzewski, L. Kotchenda, A. F. Kraishan, P. Kravtsov, K. Krueger, I. Kulakov, L. Kumar, R. A. Kycia, M. A. C. Lamont, J. M. Landgraf, K. D. Landry, J. Lauret, A. Lebedev, R. Lednicky, J. H. Lee, M. J. LeVine, C. Li, W. Li, X. Li, X. Li, Y. Li, Z. M. Li, M. A. Lisa, F. Liu, T. Ljubicic, W. J. Llope, M. Lomnitz, R. S. Longacre, X. Luo, G. L. Ma, Y. G. Ma, D. M. M. D. Madagodagettige Don, D. P. Mahapatra, R. Majka, S. Margetis, C. Markert, H. Masui, H. S. Matis, D. McDonald, T. S. McShane, N. G. Minaev, S. Mioduszewski, B. Mohanty, M. M. Mondal, D. A. Morozov, M. K. Mustafa, B. K. Nandi, Md. Nasim, T. K. Nayak, J. M. Nelson, G. Nigmatkulov, L. V. Nogach, S. Y. Noh, J. Novak, S. B. Nurushev, G. Odyniec, A. Ogawa, K. Oh, A. Ohlson, V. Okorokov, E. W. Oldag, D. L. Olvitt Jr., M. Pachr, B. S. Page, S. K. Pal, Y. X. Pan, Y. Pandit, Y. Panebratsev, T. Pawlak, B. Pawlik, H. Pei, C. Perkins, W. Peryt, P. Pile, M. Planinic, J. Pluta, N. Poljak, K. Poniatowska, J. Porter, A. M. Poskanzer, N. K. Pruthi, M. Przybycien, P. R. Pujahari, J. Putschke, H. Qiu, A. Quintero, S. Ramachandran, R. Raniwala, S. Raniwala, R. L. Ray, C. K. Riley, H. G. Ritter, J. B. Roberts, O. V. Rogachevskiy, J. L. Romero, J. F. Ross, A. Roy, L. Ruan, J. Rusnak, O. Rusnakova, N. R. Sahoo, P. K. Sahu, I. Sakrejda, S. Salur, J. Sandweiss, E. Sangaline,

A. Sarkar, J. Schambach, R. P. Scharenberg, A. M. Schmah, W. B. Schmidke, N. Schmitz, J. Seger, P. Seyboth, N. Shah, E. Shahaliev, P. V. Shanmuganathan, M. Shao, B. Sharma, W. Q. Shen, S. S. Shi, Q. Y. Shou, E. P. Sichtermann, R. N. Singaraju, M. J. Skoby, D. Smirnov, N. Smirnov, D. Solanki, P. Sorensen, H. M. Spinka, B. Srivastava, T. D. S. Stanislaus, J. R. Stevens, R. Stock, M. Strikhanov, B. Stringfellow, M. Sumbera, X. Sun, X. M. Sun, Y. Sun, Z. Sun, B. Surrow, D. N. Svirida, T. J. M. Symons, M. A. Szelezniak, J. Takahashi, A. H. Tang, Z. Tang, T. Tarnowsky, J. H. Thomas, A. R. Timmins, D. Tlusty, M. Tokarev, S. Trentalange, R. E. Tribble, P. Tribedy, B. A. Trzeciak, O. D. Tsai, J. Turnau, T. Ullrich, D. G. Underwood, G. Van Buren, G. van Nieuwenhuizen, M. Vandenbroucke, J. A. Vanfossen, Jr., R. Varma, G. M. S. Vasconcelos, A. N. Vasiliev, R. Vertesi, F. Videbæk, Y. P. Viyogi, S. Vokal, A. Vossen, M. Wada, F. Wang, G. Wang, H. Wang, J. S. Wang, X. L. Wang, Y. Wang, Y. Wang, G. Webb, J. C. Webb, G. D. Westfall, H. Wieman, S. W. Wissink, R. Witt, Y. F. Wu, Z. Xiao, W. Xie, K. Xin, H. Xu, J. Xu, N. Xu, Q. H. Xu, Y. Xu, Z. Xu, W. Yan, C. Yang, Y. Yang, Y. Yang, Z. Ye, P. Yepes, L. Yi, K. Yip, I-K. Yoo, N. Yu, Y. Zawisza, H. Zbroszczyk, W. Zha, J. B. Zhang, J. L. Zhang, S. Zhang, X. P. Zhang, Y. Zhang, Z. P. Zhang, F. Zhao, J. Zhao, C. Zhong, X. Zhu, Y. H. Zhu, Y. Zoulkarneeva, M. Zyzak

11.8 Ph.D. degrees granted

A test of the gravitational inverse-square law at short distance, Ted Cook (June, 2013).

Systematic Azimuth Quadrupole and Minijet Trends from Two-Particle Correlations in Heavy-Ion Collisions, David T. Kettler (December, 2013).

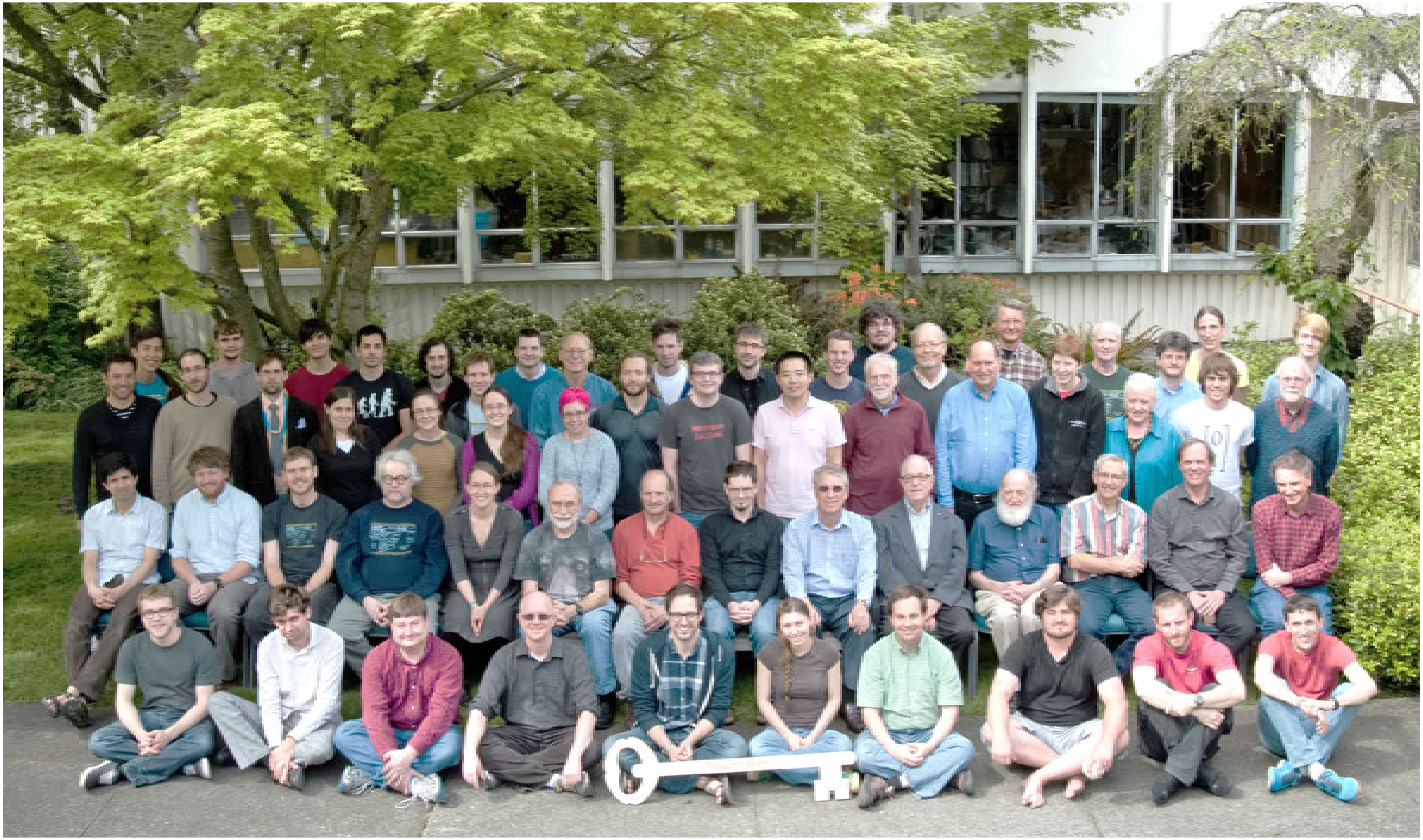

FRONT ROW (L to R): Joben Pedersen, Frederik Wauters, Eric Smith, Gary Holman, Matt Sternberg, Rachel Ryan, Fred Gray, Christian Boutan, Arnaud LeRedde, Jason Detwiler

ROW TWO (L to R): Krishna Venkateswara, Matt Turner, Charlie Hagedorn, John Amsbaugh, Laura Bodine, Doug Will, Tom Burritt, Gray Rybka, Hamish Robertson, John Cramer, Hans Bichsel, Alejandro García, David Hertzog, Jens Gundlach

STANDING (L to R): Jared Kofron, John Lee, Martin Fertl, Matthias Smith, Jim Sloan, Samuel Sexton, Clara Cuesta, David Zumwalt, Yelena Bagdasarova, Aaron Fienberg, Micah Buuck, Diana Parno, Pete Alonzi, David Hyde, Julieta Gruszko, Dmitry Lyapustin, Andreas Kraft, Tim Major, Jarek Kaspar, Ran Hong, Cliff Plesha, Erik Swanson, Ian Guinn, Peter Kammel, Tim Van Wechel, Jim Elms, Luke Kippenbrock, Duncan Prindle, Victoria Clarkson, Peter Mueller, Svenja Fleischer, Kazimir Wall, Derek Storm, Grant Leum

FRONT ROW (L to R): Joben Pedersen, Frederik Wauters, Eric Smith, Gary Holman, Matt Sternberg, Rachel Ryan, Fred Gray, Christian Boutan, Arnaud LeRedde, Jason Detwiler

ROW TWO (L to R): Krishna Venkateswara, Matt Turner, Charlie Hagedorn, John Amsbaugh, Laura Bodine, Doug Will, Tom Burritt, Gray Rybka, Hamish Robertson, John Cramer, Hans Bichsel, Alejandro García, David Hertzog, Jens Gundlach

STANDING (L to R): Jared Kofron, John Lee, Martin Fertl, Matthias Smith, Jim Sloan, Samuel Sexton, Clara Cuesta, David Zumwalt, Yelena Bagdasarova, Aaron Fienberg, Micah Buuck, Diana Parno, Pete Alonzi, David Hyde, Julieta Gruszko, Dmitry Lyapustin, Andreas Kraft, Tim Major, Jarek Kaspar, Ran Hong, Cliff Plesha, Erik Swanson, Ian Guinn, Peter Kammel, Tim Van Wechel, Jim Elms, Luke Kippenbrock, Duncan Prindle, Victoria Clarkson, Peter Mueller, Svenja Fleischer, Kazimir Wall, Derek Storm, Grant Leum